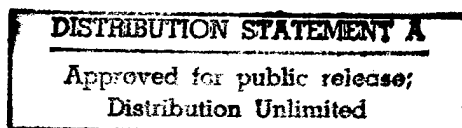


SIMULATION OF WATER WAVES BY BOUSSINESQ MODELS

GE WEI AND JAMES T. KIRBY



RESEARCH REPORT NO. CACR-98-02
MARCH, 1998



CENTER FOR APPLIED COASTAL RESEARCH

Ocean Engineering Laboratory
University of Delaware
Newark, Delaware 19716

DTIC QUALITY INSPECTED 8

19980521 072

REPORT DOCUMENTATION PAGE			Form Approved OMB NO. 0704-0188	
Public reporting burden for this collection of information is estimated to average 1 hour per response, including the time for reviewing instructions, searching existing data sources, gathering and maintaining the data needed, and completing and reviewing the collection of information. Send comment regarding this burden estimate or any other aspect of this collection of information, including suggestions for reducing this burden, to Washington Headquarters Services, Directorate for Information Operations and Reports, 1215 Jefferson Davis Highway, Suite 1204, Arlington, VA 22202-4302, and to the Office of Management and Budget, Paperwork Reduction Project (0704-0188), Washington, DC 20503.				
1. AGENCY USE ONLY (Leave blank)		2. REPORT DATE March 1998		3. REPORT TYPE AND DATES COVERED Technical report
4. TITLE AND SUBTITLE SIMULATION OF WATER WAVES BY BOUSSINESQ MODELS			5. FUNDING NUMBERS DAAL03-92-G-0116	
6. AUTHOR(S) Ge Wei and James T. Kirby				
7. PERFORMING ORGANIZATION NAME(S) AND ADDRESS(ES) UNIVERSITY OF DELAWARE CENTER FOR APPLIED COASTAL RESEARCH OCEAN ENGINEERING LABORATORY NEWARK, DE 19716			8. PERFORMING ORGANIZATION REPORT NUMBER CACR-98-02	
9. SPONSORING / MONITORING AGENCY NAME(S) AND ADDRESS(ES) U.S. Army Research Office P.O. Box 12211 Research Triangle Park, NC 27709-2211			10. SPONSORING / MONITORING AGENCY REPORT NUMBER ARO 30379.60-GS-URI	
11. SUPPLEMENTARY NOTES The views, opinions and/or findings contained in this report are those of the author(s) and should not be construed as an official Department of the Army position, policy or decision, unless so designated by other documentation.				
12a. DISTRIBUTION / AVAILABILITY STATEMENT Approved for public release; distribution unlimited.			12 b. DISTRIBUTION CODE	
13. ABSTRACT (Maximum 200 words)				
14. SUBJECT TERMS			15. NUMBER OF PAGES 202	
			16. PRICE CODE	
17. SECURITY CLASSIFICATION OR REPORT UNCLASSIFIED		18. SECURITY CLASSIFICATION OF THIS PAGE UNCLASSIFIED	19. SECURITY CLASSIFICATION OF ABSTRACT UNCLASSIFIED	20. LIMITATION OF ABSTRACT UL

SIMULATION OF WATER WAVES BY BOUSSINESQ MODELS

GE WEI AND JAMES T. KIRBY

RESEARCH REPORT NO. CACR-98-02
MARCH, 1998

CENTER FOR APPLIED COASTAL RESEARCH
OCEAN ENGINEERING LABORATORY
UNIVERSITY OF DELAWARE
NEWARK, DE 19716
U.S.A.

ACKNOWLEDGMENTS

This work was sponsored by the U.S. Army Research Office through University Research Initiative Grant No. DAAL03-92-G-0116.

ABSTRACT

A new set of time-dependent Boussinesq equations is derived to simulate nonlinear long wave propagation in coastal regions. Following the approaches by Nwogu (1993) and later by Chen and Liu (1995), the velocity (or velocity potential) at a certain water depth corresponding to the optimum linear dispersion property is used as a dependent variable. Further, no assumption for small nonlinearity is made throughout the derivation. Therefore, the resulting equations are valid in intermediate water depth as well as for highly nonlinear waves. Coefficients for second order bound waves and the third order Schrödinger equation are derived and compared with exact solutions.

A numerical model using a combination of second and fourth order schemes to discretize equation terms is developed for obtaining solutions to the equations. A fourth order predictor-corrector scheme is employed for time stepping and the first order derivative terms are finite differenced to fourth order accuracy, making the truncation errors smaller than the dispersive terms in the equations. Linear stability analysis is performed to determine the corresponding numerical stability range for the model. To avoid the problem of wave reflection from the conventional incident boundary condition, internal wave generation by source function is employed for the present model. The linear relation between the source function and the property of the desirable wave is derived. Numerical filtering is applied at specified time steps in the model to eliminate short waves (about 2 to 5 times of the grid size) which are generated by the nonlinear interaction of long waves.

To simulate the wave breaking process, additional terms for artificial eddy viscosity are included in the model equations to dissipate wave energy. The dissipation terms are activated when the horizontal gradient of the horizontal velocity exceeds the specified breaking criteria. Some of the existing models for simulating the process of wave runup are reviewed and we attempt to incorporate the present model to simulate the process by maintaining a thin layer of water over the physically dry grids.

Extensive tests are made to examine the validity of the present model for simulating wave propagation under various conditions. For the one dimensional case, the present model is applied to study the evolution of solitary waves in constant depth, the permanent solution of high nonlinear solitary waves, the shoaling of solitary waves over constant slopes, the propagation of undular bores, and the shoaling and breaking of random waves over a beach. For the two dimensional case, the present model is applied to study the evolution of waves (whose initial surface elevation is a Gaussian distribution) in a closed basin, the propagation of monochromatic waves over submerged shoals of Berkhoff *et al.* (1982) and of Chawla (1995). Results from the present model are compared in detail with available analytical solutions, experimental data, and other model results.

Contents

1	INTRODUCTION	1
1.1	Review of Existing Long Wave Models	2
1.1.1	Nonlinear shallow water model	3
1.1.2	Early Boussinesq models	4
1.1.3	Standard Boussinesq models	6
1.1.4	Extended Boussinesq models	8
1.1.5	Serre models	11
1.1.6	Hamiltonian formulation models	12
1.1.7	Green-Naghdi models	13
1.2	Outline of the Dissertation	15
2	FULLY NONLINEAR BOUSSINESQ EQUATIONS	18
2.1	Introduction	18
2.2	Derivation of Equations	23
2.2.1	Approximation expression for the velocity potential	25
2.2.2	Two-equation model for η and ϕ_α	28
2.2.3	Three-equation model based on η and \mathbf{u}_α	29
2.3	Bound Wave Generation	31
2.4	Evolution of a Slowly Varying Wave Train	38
2.4.1	Solutions for $O(1)$	43
2.4.2	Solutions for $O(\delta)$	45
2.4.3	Solutions for $O(\delta^2)$	48
3	NUMERICAL MODEL	58
3.1	Introduction	58

3.2	Finite Difference Scheme	61
3.2.1	time-differencing	64
3.2.2	Space-differencing	68
3.2.3	Linear stability analysis	69
3.2.4	Convergence	76
3.3	Boundary Conditions	77
3.3.1	Reflecting boundary	78
3.3.2	Absorbing boundary	81
3.3.3	Generating boundary	84
3.4	Wave Generation Inside the Domain	86
3.4.1	Theory	86
3.4.2	Testing results	89
3.5	Numerical Filtering	94
3.5.1	Formulation	96
3.5.2	Comparison	101
4	SIMULATION OF WAVE BREAKING AND RUNUP	104
4.1	Introduction	104
4.2	Simulation of Wave Breaking	105
4.3	Simulation of Wave Runup	110
5	RESULTS AND COMPARISONS	114
5.1	Solitary Wave Evolution over Constant Water Depth	115
5.1.1	Evolution of solitary waves	116
5.1.2	Accuracy of solitary wave with high nonlinearity	120
5.2	Solitary Wave Shoaling Over Constant Slopes	124
5.3	Undular Bore Propagation	135
5.4	Random Wave Propagation Over a Slope	139
5.5	Wave Evolution in a Rectangular Basin	151
5.6	Monochromatic Wave Propagation Over Shoals	158
5.6.1	Case 1: experiment of Berkhoff <i>et al.</i> (1982)	159
5.6.2	Case 2: experiment of Chawla (1995)	166
6	CONCLUSIONS	176

A SOLITARY WAVE SOLUTION FOR EXTENDED BOUSSINESQ MODEL 191**B WAVE GENERATION BY SOURCE FUNCTION** 195

B.1 Source function in continuity equation	196
B.1.1 Case 1: $A = 0$	198
B.1.2 Case 2: $A \neq 0$	199
B.1.3 Solution and choice of source function f	200
B.2 Source function in momentum equation	202

Chapter 1

INTRODUCTION

Accurate prediction of wave transformation in coastal regions still remains a challenge for coastal engineers and scientists, despite the fact that intensive investigation and significant progress have been made for the last fifty years. The complexity of the wave motion in nearshore regions seldom fails to be noticed by anyone who spends some time in the beach. Generated in the deep ocean by wind, waves travel across continental shelves and into coastal areas, where a combination of shoaling, refraction, diffraction and nonlinear interaction takes place, resulting in significant changes to the wave property (*e.g.*, the increase of wave heights and the steepness of wave faces). As these waves propagate towards shores, wave breaking starts to take place in surf zone areas. As a result, wave height decreases dramatically and the corresponding wave energy is transferred into necessary forcing to drive the nearshore circulation and to initialize the process of sediment transport.

In order to describe accurately the propagation of waves, it is necessary to use models based on three dimensional (3-D) spaces, *i.e.* two horizontal coordinates x and y , and one vertical coordinate z . For most of coastal engineering applications, however, it is convenient to construct approximate two dimensional (2-D) models which eliminate the vertical dependency. The reason is that 3-D models in general are quite complex and demand much more computer power to

obtain numerical solutions. In addition, 2-D models are reasonably good approximations to 3-D models under certain conditions, such as small wave amplitude (the linear wave approximation) and small water depth (the long wave approximation). Therefore, a great amount of investigation for the field of coastal engineering and science has been concentrated on deriving 2-D wave equations and on developing the corresponding 2-D numerical models. The existing models include the ray tracing model, the mild-slope model (Berkhoff, 1982), the nonlinear shallow water model (Airy, 1845; Lamb, 1945), the Boussinesq models (Boussinesq, 1872; Peregrine, 1967; Madsen *et al.*, 1991; Nwogu, 1993), the Serre models, the Hamiltonian formulation models, and the Green-Naghdi models. Notice that the ray tracing model and the mild-slope model are based on the linear wave approximation, while the rest of the models mentioned above are based on the long wave approximation. All these models have been shown to be successful in obtaining wave information accurately when applied within their ranges of validity. Since the main objective for this study is to develop a new 2-D wave model which is valid for simulating the transformation of nonlinear long waves in coastal regions, we will begin, in the following, to review some of the existing wave models based on the long wave approximation. The basic assumptions for deriving these models and their ranges of validity will be discussed.

1.1 Review of Existing Long Wave Models

In order to describe different nonlinear long wave models, it is convenient to define three length scales, which include the typical water depth h_0 , the typical wavelength L or the inverse of the typical wavenumber k_0^{-1} , and the typical wave amplitude a_0 . From these three length scales, we can only obtain two independent dimensionless parameters. One is the ratio of wave amplitude to water depth ($\delta = a_0/h_0$), which determines the magnitude of nonlinear effect and thus is

referred to as nonlinearity. The other independent parameter is the ratio of water depth to wave length ($\mu = h_0/L$) or equivalently, the product of wavenumber with water depth ($\mu = k_0 h_0$), which determines the dispersive effect and thus is referred to as dispersion. Depending on the magnitude of these two parameters, various assumptions can be made which will result in different approximate models.

1.1.1 Nonlinear shallow water model

Airy's theory (1845) or the nonlinear shallow water model is the earliest approximate model to describe the propagation of waves in shallow water regions. The basic assumption for the model is that the dispersion effect is negligibly small (*i.e.*, $O(\mu^2) = 0$), however, there is no restriction for the effect of nonlinearity ($O(\delta) = 1$). In deriving the governing equations, the horizontal velocity is assumed to be uniform along the vertical direction and the pressure in the fluid is hydrostatic. Among the approximate long wave models, the set of governing equations for the nonlinear shallow water model has the simplest form. However, the model works quite well for the condition that the ratio of water depth to wavelength is small, such as in surf and swash zone where the water depth is extremely small, or for simulating tidal waves, tsunami, and infra-gravity waves whose wavelengths are quite large. By the inclusion of Coriolis acceleration, the modified nonlinear shallow water model has been applied in the field of geophysical fluid mechanics to obtain solutions to waves whose wavelengths are comparable with the width of the ocean basin.

There have been many numerical models based on the nonlinear shallow water equations. The application of these models for simulating tidal waves is reviewed by Hinwood and Wallis (1975a,b). Recently, Kobayashi and associates (Kobayashi and Watson, 1987; Kobayashi *et al.*, 1989; Kobayashi and Wurjanto,

1992; Karjadi and Kobayashi, 1994) have developed a series of numerical models based on the nonlinear shallow water equations to simulate wave reflection, wave setup, wave breaking and wave runup on different slopes and beaches. Bottom friction is included in the model and numerical dissipation is used to simulate the energy loss due to wave breaking. Özkan and Kirby (1995) applied the nonlinear shallow water equations to investigate finite amplitude shear wave instabilities. Good agreements between numerical results and experimental data have been reported.

Due to the nondispersive property, the resulting linear phase speed from the nonlinear shallow water model is only dependent on the water depth and is not related to the frequency of the wave. This is a rather poor approximation to the exact linear dispersion relation if the water depth is not extremely small, thus greatly limiting the range of validity for the model. Since there are no dispersion terms in the model equations to balance the nonlinear terms, the front face of a wave will steepen continuously even when the wave is propagating over a constant water depth. Therefore, no permanent wave solutions exist for the nonlinear shallow water model, in contrast to other nonlinear long wave models which are described below.

1.1.2 Early Boussinesq models

Another approximate nonlinear long wave model which eliminates the vertical dependency was derived by Boussinesq (1872). Similar to the nonlinear shallow water model, the Boussinesq model involves a set of coupled equations whose dependent variables include the surface elevation η and the depth-averaged velocity \bar{u} or velocity potential $\bar{\phi}$. However, due to the assumption of small, but

not negligible, nonlinearity and dispersion (*i.e.* $O(\mu^2) = O(\delta) < 1$) in the derivation, the resulting Boussinesq model includes an additional term which accounts for the dispersion effect. The forcing and kinematics for the Boussinesq model are fundamentally different from those for the nonlinear shallow water model. In the Boussinesq model, the pressure under the water surface includes a dynamic part as well as a hydrostatic part, and the variation of horizontal velocity with water depth is quadratic instead of uniform. Due to the inclusion of the dispersion term, the corresponding linear dispersion relation for the Boussinesq equations is a second order polynomial expansion to the exact analytical solution. Compared to the nonlinear shallow water model, the Boussinesq model has a larger range of validity in coastal regions, if the nonlinear effect is as small as that of dispersion.

Using the same basic assumptions as those by Boussinesq (1872), Korteweg and de Vries (1895) derived an approximate equation for simulating nonlinear long waves. The equation is referred to as KdV equation and the surface elevation is the only dependent variable. Due to the same assumptions used in the derivation, the KdV equation is considered to be an alternate form of the Boussinesq equations for the study of surface wave propagation. However, the KdV equation is much more popular than the Boussinesq equations in many fields of physics involving waves and has thus attracted a large number of physicists to search for the analytical solution. The proper balance between the effects of nonlinearity and of dispersion in the KdV equation admits permanent wave solutions such as solitary waves and cnoidal waves. In addition, there exists an exact solution to the KdV equation for arbitrary initial conditions by the method of Inverse Scattering Transform (Gardner *et al.*, 1967).

Both Airy's theory and the Boussinesq equations are approximate models for wave propagation in shallow water regions. However, the contradictory

conclusions from the two approaches for the existence of permanent form solutions have puzzled scientists for several decades, until Ursell (1953) showed that the fundamental difference is due to the assumptions in the two models. Ursell (1953) defined a parameter U_r (the Ursell number) as the ratio of nonlinearity to dispersion effects (*i.e.* $U_r = \delta/\mu^2$). The magnitude of the Ursell number U_r determines the range of validity for each model. If U_r is much larger than 1, then the dispersion effect is negligible and the nonlinear shallow water model should be used. On the other hand, if U_r is of $O(1)$, then the effects of nonlinearity and dispersion are of the same order and the Boussinesq model is more valid.

1.1.3 Standard Boussinesq models

Due to the limitations of one horizontal dimension and constant water depth, the early Boussinesq models cannot be applied to most of the real coastal regions where the bottom geometry may vary arbitrarily. Based on perturbation theory, Mei and Le Méhauté (1966) and Peregrine (1967) have derived Boussinesq equations that are valid for variable water depth and for two horizontal dimensions. In derivation of these two sets of Boussinesq equations, the effects of nonlinearity and of dispersion were all assumed to be small and in the same order. However, Mei and Le Méhauté (1966) used the bottom velocity as the dependent variables while the depth-averaged velocity was used in the derivation by Peregrine (1967). Though both sets of equations are regarded as equivalent within the order of approximation in the models, the properties of these two sets of equations are slightly different, as will be shown in Chapter 2 for the comparison of linear dispersion relation. Of these two sets of equations, Peregrine's equations are more widely used by the coastal community and are referred to as the standard Boussinesq equations. Due to the use of depth-averaged velocity, the corresponding continuity equation for the standard Boussinesq model is exact.

Since the derivation of the standard Boussinesq equations, a number of numerical models have been developed and applied for simulating wave propagation in coastal regions. Goring (1978) conducted a series of laboratory experiments to study the transmission and reflection of a solitary wave at a depth transition and showed that results from the standard Boussinesq model agree well with experimental data. Abbott *et al.* (1984) developed a numerical scheme for an alternate form of the standard Boussinesq model, where the volume flux instead of the depth-averaged velocity is used as a dependent variable. The model is shown to be capable of simulating the propagation of short waves in shallow water regions. Liu *et al.* (1985) and Rygg (1988) demonstrated that Boussinesq models give accurate predictions of wave refraction and focusing over a submerged shoal in the laboratory experiment by Whalin (1971).

As shown by Freilich and Guza (1984) and by Elgar and Guza (1985), models based on the frequency domain formulation of the standard Boussinesq equations could be used to predict the evolution of the power spectrum for normally incident waves in coastal regions. The capability of the model for predicting the evolution of bispectrum or third-moment statistics was demonstrated by Elgar and Guza (1986) and by Elgar *et al.* (1990). For a directional wave train, Freilich *et al.* (1993) implemented a parabolic equation method into the model and showed that numerical results agree well with field data. Kirby (1990) showed that an angular spectrum formulation of the standard Boussinesq model gives good predictions of the evolution of a Mach stem measured in the laboratory (Hammack *et al.*, 1989).

1.1.4 Extended Boussinesq models

Despite its success for predicting wave transformation in coastal regions of variable bottom geometry, the standard Boussinesq model is still limited to relatively shallow water areas. McCowan (1987) showed that in order to keep errors in the phase speed less than 5%, the water depth has to be less than about one-fifth of the equivalent deep water wavelength. For many coastal engineering practices, it is desirable to have a general wave model to provide useful wave information for an entire coastal area by utilizing data (which is usually available at the intermediate water depth) as the model input. Due to its limitation to shallow water depth, the standard Boussinesq model is not sufficient to be such a general wave model.

In recent years, extending the range of validity for Boussinesq models to intermediate water depth has been an active area of research. As is known in applied mathematics, an analytical function is better represented by a Padé approximant than by a Taylor series expansion, if the order of expansion is the same. As is known, the linear dispersion relation resulting from the standard Boussinesq equations is a second order Taylor expansion of the exact solution. Working on a generalized wave equation by expanding velocity variables, Whitting (1984) obtained a series of forms of linear dispersion relations, including the regular polynomial expansions (corresponding to Taylor series) and the rational polynomial expansions (similar to Padé approximants). Whitting (1984) demonstrated that the linear dispersion relation based on the rational polynomial formula agree with the exact solution much better than that based on the regular polynomial formula. Though it is not easy to generalize Whitting's equation to the case of two horizontal dimensions and variable water depth, the results suggested that there might exist an alternate form of Boussinesq equations whose linear dispersion relation

is a rational polynomial expansion to the exact solution.

Madsen *et al.* (1991) derived such a set of Boussinesq equations for the case of two horizontal dimensions and constant water depth. The extension to variable water depth was made by Madsen and Sørensen (1992). In the derivation of the extended Boussinesq equations, additional third order terms with adjustable coefficients were added into the momentum equation of the standard Boussinesq equations. Though negligible in the limit of shallow water, these added terms change the properties of linear dispersion and linear shoaling significantly in intermediate water depth. Instead of a polynomial expansion, the linear dispersion from the model becomes a rational polynomial expansion to the exact solution. The adjustable coefficients for the added terms can be determined by several criteria, including the best fit for the linear phase speed, for the linear group velocity, or for the linear shoaling property. Detailed description can be found the corresponding references above.

Instead of directly adding the negligible third order terms to the standard Boussinesq equations, Nwogu (1993) showed another approach of deriving the corresponding extended Boussinesq equations with an improved linear dispersion property. Starting from the original 3-D Euler equations and associated boundary conditions for an incompressible and inviscid fluid, Nwogu (1993) used the horizontal velocities at a reference water depth z_α as the dependent variables. Similar to the derivation of other Boussinesq models, the horizontal velocity is assumed to vary quadratically with water depth and the irrotational condition is employed after the velocity variables are expanded by a power series. The vertical dependency is eliminated by integrating the equations from the bottom to the surface. Compared to the standard Boussinesq equations, Nwogu's equations include extra third order dispersive terms in the continuity equation as well as in the momentum

equations. It is these third order terms that make the resulting linear dispersion relation to be a rational polynomial with an adjustable coefficient α , which is related to the reference depth z_α . Based on the method of least square error for the linear dispersion relation, Nwogu (1993) obtained the optimum value for the coefficient as $\alpha = -0.39$, corresponding to the reference depth of $z_\alpha = -0.531h$, about half of the still water depth.

An alternate form of Nwogu's equations was derived by Chen and Liu (1995), who used the velocity potential, instead of the horizontal velocity, at a certain depth as a dependent variable. The equations were derived from the Laplace's equation which implies the irrotationality of the wave motion. The derivation of Chen and Liu (1995) is much simpler but resulted in the same rational polynomial form of the linear dispersion relation as that from Nwogu (1993).

Although the approaches used by Madsen *et al.* (1991) and by Nwogu (1993) are quite different, the resulting linear dispersion relations from these two sets of extended Boussinesq equations are similar, both of which are a rational polynomial expansion (Padé approximant) to the exact solution. The improved linear dispersion property in intermediate water depth makes the range of validity for the extended Boussinesq models larger than that for the standard Boussinesq model. Numerical models based on the extended equations have been developed and applied to simulate wave propagation using input data from the intermediate water depth (Madsen *et al.*, 1991; Nwogu, 1993; Wei and Kirby, 1995). The numerical model based on the frequency domain formulation was developed by Kaihatu (1994). The agreements between the numerical results and the available experimental data demonstrate that the extended Boussinesq models are capable of simulating the propagation of waves in coastal regions where the water depth can be as deep as about half of the wavelength.

The nonlinear shallow water model and the Boussinesq models described so far are derived using the standard perturbation method, based on power expansions of the velocity (or velocity potential) and the surface elevation. As will be shown below, there are alternate ways to obtain approximate models for nonlinear long wave propagation.

1.1.5 Serre models

For long wave propagation over a constant water depth, Serre (1953) derived a set of approximate equations which are referred to as Serre equations. In the derivation, the horizontal velocity is assumed to be uniform and the vertical velocity varies linearly with water depth. However, different from the derivations of the nonlinear shallow water equations or the Boussinesq equations, the condition of irrotationality is not assumed, though the assumption of inviscid and incompressible fluid is still applied.

Compared to the nonlinear shallow water equations, the Serre equations include dispersion terms which provide a force balance to nonlinear terms. Therefore, the Serre equations admit permanent wave solutions. The closed form solution of solitary waves is given by Su and Gardner (1969) and by Seabra-Santos *et al.* (1987). As will be shown later in Chapter 5, the solitary wave solution from the Serre equations does not compare very well with the exact solution of Tanaka (1986) for the case of high nonlinearity, probably due to the inaccurate assumption of velocity variation with water depth.

An interesting fact is that the Serre equations can be derived on the basis of different (or contradictory) assumptions and methods. Starting from the continuity and Euler equations which govern wave motion in inviscid and incompressible fluid, Su and Gardner (1969) first obtained a general set of integral equations

using a power series expansion for the dependent variables. Then by applying the condition of irrotationality and long wave approximation, the set of integral equations is transformed into the same form of Serre equations. Based on the Laplace's equation and using the standard perturbation method to expand the dependent variables, Mei (1989) derived a set of fully nonlinear Boussinesq equations for constant water depth. Despite the fact that the condition of irrotationality is assumed in the derivation and that the variation of horizontal velocity is quadratic with water depth, the resulting set equations of Mei (1989) is equivalent to that of the Serre equations. As will be described in a later section, the original set of equations derived by Green and Naghdi (1974) based on the theory of fluid sheet is also the same as that of the Serre equations.

The extension of the Serre equations to 2-D horizontal directions and variable water depth was obtained by Seabra-Santos *et al.* (1987). Numerical models based on Serre equations have been developed and applied to simulate the propagation of waves under certain conditions. The transformation of a solitary wave over a shelf was investigated by Seabra-Santos *et al.* (1987) using the corresponding Serre model. Dingemans (1994) showed the comparison of the computed results from a number of nonlinear long wave models including Serre models with experimental data for regular wave shoaling and breaking over an under water bar. In both cases, results from Serre models gave good agreement with experimental data.

1.1.6 Hamiltonian formulation models

The existence of a Hamiltonian for irrotational flow with a free surface lead investigators to derive the corresponding canonical evolution equations for wave propagation based on the Hamiltonian formulation. Broer and associates (Broer,

1974; Broer, 1975; Broer *et al.*, 1976) proposed to write the Hamiltonian as the sum of the kinetic and the potential energy contributions. It is straight forward to represent the potential energy explicitly by the canonical variables of surface elevation and velocity potential at the surface. However, this is not the case for the kinetic energy unless the condition of weak nonlinearity is satisfied. For this reason, the Hamiltonian formulation is restricted to the case of small nonlinear effect.

The linear dispersion relation of the canonical equations derived by Broer is equivalent to that obtained from the Boussinesq equations which use the surface velocity (potential) as a dependent variable. Due to a prediction of negative phase speed for certain short waves, the corresponding model is not suitable for the case in intermediate water depth or when short waves are present. To extend the validity of the Hamiltonian formulation model to a deeper water depth, Van der Veen and Wubs (1993) employed a rational polynomial operator to replace the regular polynomial operator in Broer's formulation. The resulting dispersion relation thus becomes a Padé approximant to the exact solution, similar to that of the extended Boussinesq equations derived by Madsen *et al.* (1991) and by Nwogu (1993). A more complicated formulation of canonical equations was derived by Mooiman (1991), who used a rational polynomial operator with additional property of positive-definiteness. The two coefficients in the operator are determined by the best fit of the linear dispersion relation to the exact solution.

1.1.7 Green-Naghdi models

Approximate governing equations for long wave propagation can also be derived using the theory of fluid sheet originated by Green *et al.* (1974) and by Green and Naghdi (1976). These equations are now commonly referred to as

Green-Naghdi or GN equations. In this approach, the kinematic properties of the velocity field are first assumed to have a certain form. The corresponding coefficients for the velocity field are later determined based on conservation laws for incompressible and inviscid flow. Due to the facts that there are no scaling assumptions for the ratio of wave height to water and that all boundary data are evaluated at the instantaneous free surface, the Green-Naghdi models are fully nonlinear.

The original GN equations derived by Green *et al.* (1974) and by Green and Naghdi (1976) assume a uniform distribution of horizontal velocity and a linear variation of vertical velocity with water depth, which are the same kinematic assumptions as those made in the Serre models. As demonstrated by Kirby (1996), the original GN equations and the Serre equations are exactly the same.

The original GN equations can be extended by assuming a more realistic velocity field. A framework for such an extension has been provided by Shields (1986) and by Shields and Webster (1988, 1989). In this approach, the velocity field is first represented by a combination of certain basis functions. The evolution equations of the basic functions are then obtained based on conservation laws. The mass conservation and the kinematic free surface boundary conditions are satisfied exactly. However, the corresponding Euler equations are satisfied in an approximate sense, using a weak variational formulation in which the basis functions are used as weighting functions. The more number of the basis functions, the more accurate and complicated the model becomes.

Shields and Webster (1988) have shown examples of calculations for solitary and cnoidal waves for GN models up to level three (using up to three basis functions). The convergence rate towards the numerically exact results of wave shape and wave speed from GN models is shown to be greater than that of the

models derived based on the conventional perturbation method. Calculations of wave shoaling in variable water depth are provided by Shields (1986) and good agreement is observed between model results and experiment data of Hansen and Svendsen (1979). Additional example calculations for GN models are provided by Demirbilek and Webster (1992). Webster and Wehausen (1995) applied a GN model to study resonant Bragg reflection of surface waves by undular bed features.

1.2 Outline of the Dissertation

The aim of this study is to construct a comprehensive wave model which is capable of simulating the transformation of waves in coastal regions, including areas in the intermediate water depth and in the surf zone. To accomplish this, we derive a set of fully nonlinear Boussinesq equations with a wide range of variety and develop a high order numerical model to obtain the corresponding solutions. The model is examined extensively by applying it to various cases of wave propagation and the model results are compared with available exact solutions, numerical results, and experimental data.

In Chapter 2, the fully nonlinear Boussinesq equations are derived based on perturbation theory. Following the approaches of Nwogu (1993) and of Chen and Liu (1995), the velocity potential is expanded by a power series in which the dependent variable is the potential at a reference water depth. By substituting the approximate expansion into the original wave equations and by keeping all nonlinear terms, a set of fully nonlinear Boussinesq equations is obtained. Due to the use of the optimum reference water depth and the fact that no assumption of small nonlinearity is made in the derivation, the resulting equations not only improve the linear dispersion property in intermediate water depth but also are valid for cases involving strong nonlinear interaction, such as wave shoaling

prior to breaking. In order to demonstrate the nonlinear properties of the fully nonlinear Boussinesq equations, the coefficients for second order bound waves and the corresponding cubic Schrödinger equation are obtained and compared to the exact solutions obtained by Dean and Sharma (1981) and by Mei (1989).

A high order numerical model for solving the fully nonlinear Boussinesq equations is described in detail in Chapter 3. To ensure that the numerical truncation errors are smaller than the dispersive terms in the equations, the fourth-order Adams-Bashford-Moulton predictor-corrector scheme is employed to step in time, and a combination of second and fourth order finite difference schemes is used to discretize the spatial derivative terms. Based on the method of von Neumann (Hoffman, 1992), the linear stability range of the model is evaluated numerically for the case of one horizontal dimension and constant water depth. The boundary conditions of reflecting, absorbing and generating waves used in the model are described. The linear analytical relation between the source function and the properties of a desirable wave is derived and is applied in the model to generate waves inside the computing domain. To eliminate short waves which are generated by nonlinear interaction and which might cause stability problems, the numerical filter proposed by Shapiro (1970) is employed in the model.

In Chapter 4, the methods of simulating the process of wave breaking in surf zone areas and the process of wave runup over beaches by the present model are described. Following the approach of Zelt (1991), wave breaking is modeled by adding the eddy viscosity terms to the momentum equations to dissipate wave energy. These terms are turned on when the local wave property, such as the spatial derivative of the horizontal velocity or the slope of surface elevation, exceeds a certain criterion. In addition to including the bottom friction terms into the model equations, we propose a method to model the process of wave runup in an

Eulerian system by maintaining a thin layer of water on the physically dry part of the model grids. More research work is needed to solve the problem of instability which occurred at the intersection between the dry and wet grids.

Chapter 5 presents the computational results obtained by the present model for a wide variety of cases of wave propagation. For the one dimensional case, the model is applied to study the evolution of solitary waves over a constant water depth, the permanent form solution of solitary waves with high nonlinearity, the shoaling of solitary waves over constant slopes, the propagation of undular bores in constant water depth, and the shoaling and breaking of random waves over a constant slope. For the two dimensional case, the model is applied to study the evolution of waves in a closed rectangular basin and the transformation of monochromatic waves over submerged shoals. Results from the present model are compared with available analytical solutions, numerical solutions from other models, or experimental data.

The conclusion of this study for developing the fully nonlinear Boussinesq model and comments on future research work are offered in Chapter 6.

Chapter 2

FULLY NONLINEAR BOUSSINESQ EQUATIONS

2.1 Introduction

As stated in Chapter 1, the extended Boussinesq equations derived by Madsen *et al.* (1991) and by Nwogu (1993) increase the range of validity of these models to the intermediate water depth, if linear dispersion properties are used as the criterion for determining the model applicability. Despite the differences in the method of derivation and in the final forms of the governing equations, both of the linear dispersion relations of Madsen *et al.* (1991) and of Nwogu (1993) are Padé approximants to the exact solution, which are a much better representation of the exact dispersion relation than is provided by the polynomial approximations from standard Boussinesq equations. To illustrate this, the linear dispersion relation from Nwogu's equations will be analyzed in detail below.

For wave propagation in one horizontal dimension over a constant water depth, the extended Boussinesq equations derived by Nwogu (1993) are linearized as:

$$\eta_t + hu_{\alpha x} + (\alpha + 1/3)h^3u_{\alpha xxx} = 0 \quad (2.1)$$

$$u_{\alpha t} + g\eta_x + \alpha h^2u_{\alpha xxt} = 0 \quad (2.2)$$

where η is the surface elevation, u_α the horizontal velocity at the reference depth $z = z_\alpha$, h the constant water depth, and α a parameter related to the ratio of z_α/h and is defined as

$$\alpha = \frac{z_\alpha}{h} \left(\frac{1}{2} \frac{z_\alpha}{h} + 1 \right) \quad (2.3)$$

Depending on the choice of reference depth z_α (or, more conveniently, the value of α), we can obtain different sets of governing equations with velocity u_α as the dependent variable. Though these sets of equations are equivalent mathematically to the order of approximation used in the derivation, the corresponding linear dispersion relations are quite different. Assume that a sinusoidal wave with wavenumber k and angular frequency ω propagates in x direction, and that η_0 and $u_{\alpha 0}$ are the amplitudes of the surface elevation η and horizontal velocity u_α . By substituting $(\eta, u_\alpha) = (\eta_0, u_{\alpha 0}) \exp[i(kx - \omega t)]$ into equations (2.1)-(2.2), we obtain the linear dispersion relation

$$\omega^2 = gk^2 h \frac{1 - (\alpha + 1/3)(kh)^2}{1 - \alpha(kh)^2} \quad (2.4)$$

which is to be compared with the exact linear dispersion relation

$$\omega^2 = gk \tanh(kh) \quad (2.5)$$

Figure 2.1 shows the comparison of linear dispersion relations between the exact solution (2.5) and the approximate relation (2.4) for several choices of α values, which are $\alpha = (0, -1/3, -0.39, -0.4, -0.5)$. From equation (2.3), the corresponding ratios of reference depth to still water depth are $z_\alpha/h = (0, -0.423, -0.531, -0.553, -1)$. Notice that the numerator in (2.4) becomes zero for the case of $\alpha = -1/3$, which is equivalent to the linear dispersion relation obtained from the standard Boussinesq equations. The case of $\alpha = -0.4$ corresponds to the exact (2,2) Padé approximant to the exact solution. Though the curve for $\alpha = -0.4$ is

much closer to the exact line than that for $\alpha = -1/3$, there exist better fit curves for other α values. Nwogu (1993) obtained the optimum value as $\alpha = -0.39$, based on the minimum sum of relative error for the phase speed over the range from $kh = 0$ to $kh = 5$.

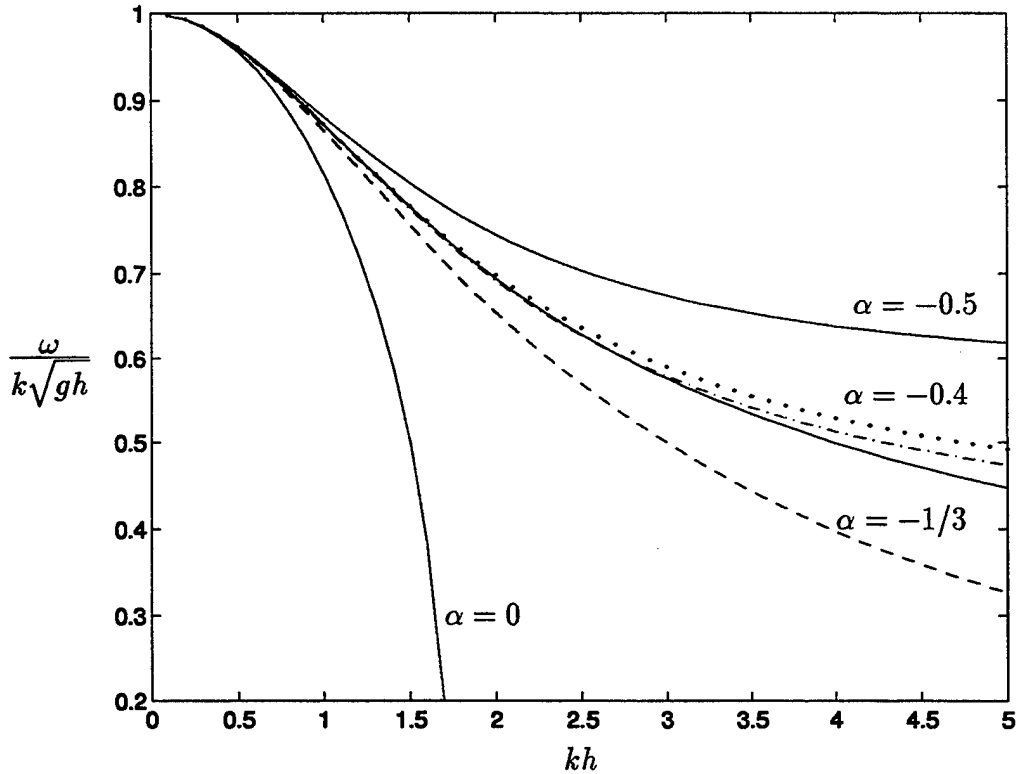


Figure 2.1: Comparison of linear dispersion relations between the exact solution (middle solid line) and those of Nwogu's equations for several values of α : $\alpha = -0.5$ (—); $\alpha = -0.4$ (····); $\alpha = -0.39$ (-··-); $\alpha = -1/3$ (----); $\alpha = 0$ (—).

Despite the improved linear dispersion relations, the extended Boussinesq equations of Madsen *et al.* (1991) and of Nwogu (1993) are still restricted to situations with weakly nonlinear interactions. In many practical cases, however, the effects of nonlinearity are too large to be treated as a weak perturbation to a primarily linear problem. As waves approach a beach, the effects of shoaling

and nonlinear interaction change the wave properties significantly, leading waves to break on most of the gentle natural slopes. The large ratio of wave height to water depth accompanying this physical process makes it inappropriate for using the weakly-nonlinear Boussinesq models, and thus extensions to the models are required in order to obtain a computational tool which is locally valid in the vicinity of a steep, almost breaking or breaking wave crest.

An additional (and less obvious) limitation imposed by weakly nonlinear Boussinesq models occurs in the higher frequency range, which is precisely the range of linear behavior incorporated by the modifications of Madsen *et al.* (1991) and Nwogu (1993). As an illustration, we consider the range of validity for Boussinesq wave models in Figure 2.2, where the horizontal and vertical axes represent dispersive effects ($\mu^2 = (kh)^2$) and nonlinear effects ($\delta = a/h$), respectively. The standard Boussinesq equations are based on the assumption that $\delta, \mu \ll 1$ and $\delta/\mu^2 = O(1)$, after which terms of $O(\mu^4, \delta\mu^2, \delta^2)$ are neglected. The range of validity is thus bounded not only by some arbitrary value for δ and μ^2 , but also by the curve c_1 which represents some value of $\delta\mu^2$. Suppose that the limit of validity for the standard Boussinesq equations corresponds approximately to $\delta = \mu^2 = 0.2$. The value of c_1 is then represented by $\delta\mu^2 = 0.04$, as shown in Figure 2.2. It is apparent that the limit of usefulness of the standard Boussinesq model is not controlled primarily by c_1 , which represents the neglected nonlinear effects in dispersion terms. If we introduce the model extensions of Madsen *et al.* (1991) or Nwogu (1993), however, the implied limit of validity for μ^2 becomes much higher. We see that this extended region is reduced in size by the neglected nonlinear dispersive terms, represented by the region above c_1 .

The extension of the range of validity of the linear models achieved by Madsen *et al.* (1991) and Nwogu (1993) is limited in the nonlinear regime by the

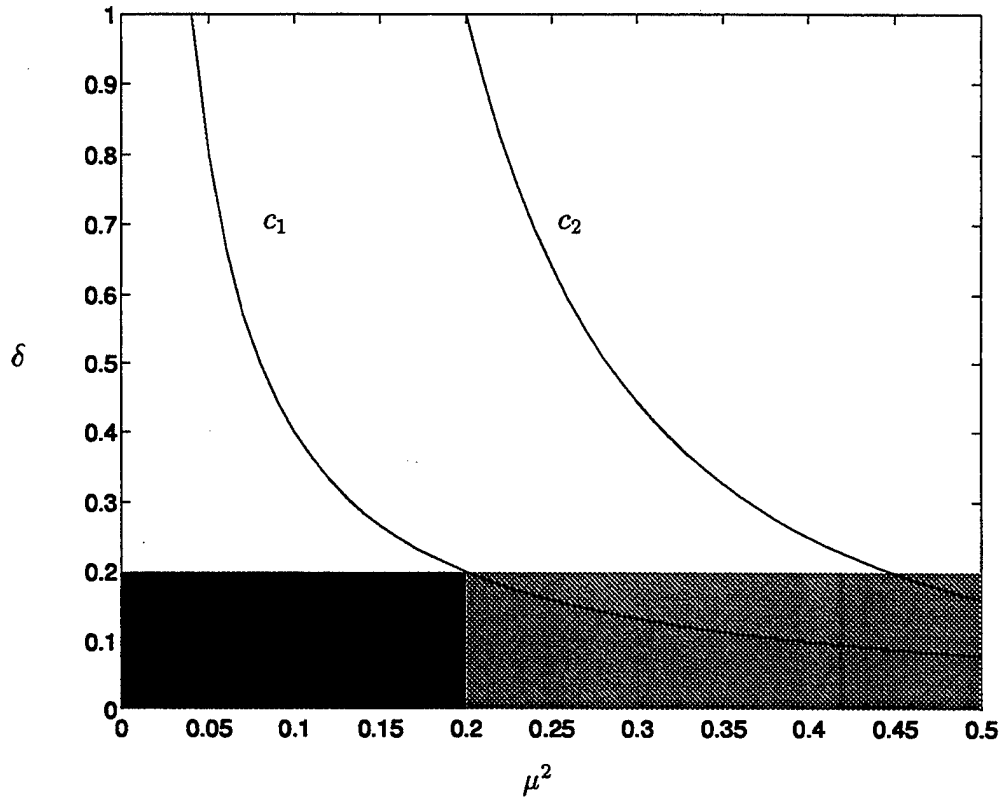


Figure 2.2: Hypothetical limits of validity of approximate long wave models. Dark gray — standard Boussinesq models. Light gray — additional region of validity for extended Boussinesq models of Madsen *et al.* (1991) and Nwogu (1993). Curve c_1 denotes $\delta\mu^2 = .04$. Curve c_2 denotes $\delta\mu^4 = .04$.

fact that the curve c_1 approaches the horizontal axis for large μ^2 values. This places serious constraints on the steepness of waves which are actually allowed in the intermediate water depth. If we, however, introduce a fully nonlinear model within the context of the Boussinesq dispersion approximation, then all terms of $O(\mu^2)$ including $O(\delta\mu^2)$ will be kept and the lowest order nonlinear terms to be neglected is of $O(\delta\mu^4)$. As a result, the validity of range for the fully nonlinear model is enlarged significantly and is formally controlled by the required smallness of $\delta\mu^4$, as illustrated by the curve c_2 . We thus seek to achieve a wider range of

validity for the model over the entire range of water depths.

In Section 2.2, a detailed derivation of the fully nonlinear Boussinesq equations will be given. First, the 3-D governing equation and associated boundary conditions for the incompressible, inviscid and irrotational flow are transferred into dimensionless forms, making the magnitude of each term in the equations explicit by the corresponding parameters. Second, following the approach of Chen and Liu (1995), the velocity potential is approximated by a power series expansion based on a certain water depth. Vertical dependency is eliminated by substituting the approximate expression of velocity potential into the equations. By keeping all nonlinear terms with $O(\mu^2)$, a set of fully nonlinear Boussinesq equations is obtained.

In Section 2.3 and Section 2.4, analytical properties of the fully nonlinear Boussinesq equations will be examined by deriving the coefficients for second order bound waves and the third order Schrödinger equation in a Stokes-type expansion. Comparisons with exact solutions by Dean and Sharma (1981) for bound waves and by Mei (1989) for the Schrödinger equation will be given.

2.2 Derivation of Equations

Two methods can be used to derive the fully nonlinear Boussinesq equations. The first method uses Euler equations and associated boundary conditions for incompressible and inviscid flow, as in the approach of Nwogu (1993) used to derive the extended Boussinesq equations. Velocities are used as variables and the condition of irrotationality is applied after introducing power series expansions to the velocity field. The second method uses Laplace's equation and boundary conditions to begin with the derivation, as in Chen and Liu (1995). In addition to the usual assumptions for incompressible and inviscid fluid, irrotationality is

implied due to the use of Laplace's equation for potential flow. Velocity potential, instead of velocities, is the dependent variable. Though the same set of fully nonlinear Boussinesq model have been derived by both methods, only the second (less complicated than the first) is shown in the following.

To describe the propagation of waves, we first define a 3-D Cartesian coordinate system where x and y are horizontal coordinates and z is the vertical coordinate. The direction of z is upwards and the origin of z is at the still water surface. Then for irrotational wave motion in incompressible and inviscid fluid, the corresponding 3-D governing equation and boundary conditions are:

$$\phi_{zz} + \nabla^2 \phi = 0; \quad -h < z < \eta \quad (2.6)$$

$$\phi_z + \nabla h \cdot \nabla \phi = 0; \quad z = -h \quad (2.7)$$

$$g\eta + \phi_t + \frac{1}{2}[(\nabla \phi)^2 + (\phi_z)^2] = 0; \quad z = \eta \quad (2.8)$$

$$\eta_t + \nabla \phi \cdot \nabla \eta - \phi_z = 0; \quad z = \eta \quad (2.9)$$

where $\phi = \phi(x, y, z, t)$ is the velocity potential, $\eta = \eta(x, y, t)$ the surface elevation, $h = h(x, y)$ the still water depth, $\nabla = (\partial/\partial x, \partial/\partial y)$ the horizontal gradient operator, and subscripts z and t denote partial derivative with respect to z and time t , respectively. Equations (2.7) and (2.9) are the kinematic boundary conditions at the bottom and at the free surface, while equation (2.8) is the dynamic boundary condition at the free surface.

It is convenient to use dimensionless variables for the derivation. Following the approach of Mei (1989), we first assume k_0 , h_0 and a_0 to be the typical wavenumber, the typical water depth and the typical wave amplitude, with which the following dimensionless variables are defined:

$$\begin{aligned} (x', y') &= k_0(x, y), & z' &= \frac{z}{h_0}, & \eta' &= \frac{\eta}{a_0} \\ t' &= k_0(g h_0)^{1/2} t, & \phi' &= \left[\frac{a_0}{k_0 h_0} (g h_0)^{1/2} \right]^{-1} \phi \end{aligned} \quad (2.10)$$

Equations (2.6)-(2.9) are then transformed into dimensionless forms as:

$$\phi_{zz} + \mu^2 \nabla^2 \phi = 0; \quad -h < z < \delta\eta \quad (2.11)$$

$$\phi_z + \mu^2 \nabla h \cdot \nabla \phi = 0; \quad z = -h \quad (2.12)$$

$$\eta + \phi_t + \frac{1}{2} \delta [(\nabla \phi)^2 + \frac{1}{\mu^2} (\phi_z)^2] = 0; \quad z = \delta\eta \quad (2.13)$$

$$\eta_t + \delta \nabla \phi \cdot \nabla \eta - \frac{1}{\mu^2} \phi_z = 0; \quad z = \delta\eta \quad (2.14)$$

where the prime sign for all the dimensionless variables have been dropped for convenience. Notice that the water depth h is also a dimensionless variable (scaled by h_0). Parameters $\mu^2 = (k_0 h_0)^2$ and $\delta = a_0/h_0$ are the scales for the dispersion effect and the nonlinearity effect, respectively.

2.2.1 Approximate expression for the velocity potential

To reduce the dimensionality of the boundary value problem defined by equations (2.11)-(2.14), the velocity potential ϕ is expanded as a power series with respect to $z = -h$:

$$\phi(x, y, z, t) = \sum_{n=0}^{\infty} (z + h)^n \phi_n(x, y, t) \quad (2.15)$$

The corresponding derivatives are given by:

$$\begin{aligned} \nabla \phi &= \sum_{n=0}^{\infty} (z + h)^n \nabla \phi_n + \sum_{n=1}^{\infty} n (z + h)^{n-1} \phi_n \nabla h \\ &= \sum_{n=0}^{\infty} (z + h)^n [\nabla \phi_n + (n + 1) \phi_{n+1} \nabla h] \\ \nabla^2 \phi &= \sum_{n=0}^{\infty} (z + h)^n \nabla^2 \phi_n + 2 \sum_{n=1}^{\infty} n (z + h)^{n-1} [\nabla h \cdot \nabla \phi_n + \nabla \cdot (\phi_n \nabla h)] \\ &\quad + \sum_{n=2}^{\infty} n(n-1) (z + h)^{n-2} \phi_n \nabla^2 h \\ &= \sum_{n=0}^{\infty} (z + h)^n \left\{ \nabla^2 \phi_n + (n+1) [\nabla h \cdot \nabla \phi_{n+1} + \nabla \cdot (\phi_{n+1} \nabla h)] \right\} \end{aligned} \quad (2.16)$$

$$+(n+2)(n+1)\phi_{n+2}\nabla^2 h\} \quad (2.17)$$

$$\begin{aligned} \phi_z &= \sum_{n=1}^{\infty} n(z+h)^{n-1}\phi_n \\ &= \sum_{n=0}^{\infty} (z+h)^n(n+1)\phi_{n+1} \end{aligned} \quad (2.18)$$

$$\begin{aligned} \phi_{zz} &= \sum_{n=2}^{\infty} n(n-1)(z+h)^{n-2}\phi_n \\ &= \sum_{n=0}^{\infty} (z+h)^n(n+2)(n+1)\phi_{n+2} \end{aligned} \quad (2.19)$$

Substituting (2.16) and (2.18) into the bottom boundary condition (2.12) results in:

$$\phi_1 = -\mu^2 \frac{\nabla h \cdot \nabla \phi_0}{1 + \mu^2(\nabla h)^2} = -\mu^2 \nabla h \cdot \nabla \phi_0 + O(\mu^4) \quad (2.20)$$

where $|(\nabla h)^2|$ is assumed to be of $O(\mu^2)$ or smaller, which implies that the slope of bottom geometry should be small. By substituting (2.17) and (2.19) into Laplace's equation (2.11), we obtain the recursion relation:

$$\begin{aligned} \phi_{n+2} &= -\mu^2 \frac{(\nabla^2 \phi_n + (n+1)[\nabla h \cdot \nabla \phi_{n+1} + \nabla \cdot (\phi_{n+1} \nabla h)]}{(n+2)(n+1)[1 + \mu^2(\nabla h)^2]} \\ &= -\mu^2 \frac{(\nabla^2 \phi_n + (n+1)[\nabla h \cdot \nabla \phi_{n+1} + \nabla \cdot (\phi_{n+1} \nabla h)]}{(n+2)(n+1)} + O(\mu^4) \end{aligned} \quad (2.21)$$

$(n = 0, 1, 2, \dots)$

which gives

$$\begin{aligned} \phi_2 &= -\frac{\mu^2}{2} [\nabla^2 \phi_0 + \nabla h \cdot \nabla \phi_1 + \nabla \cdot (\phi_1 \nabla h)] + O(\mu^4) \\ &= -\frac{\mu^2}{2} \nabla^2 \phi_0 + O(\mu^4) \end{aligned} \quad (2.22)$$

$$\begin{aligned} \phi_3 &= -\frac{\mu^2}{6} \{ \nabla^2 \phi_1 + 2[\nabla h \cdot \nabla \phi_2 + \nabla \cdot (\phi_2 \nabla h)] \} + O(\mu^4) \\ &= O(\mu^4) \end{aligned} \quad (2.23)$$

$$\begin{aligned} \phi_4 &= -\frac{\mu^2}{12} \{ \nabla^2 \phi_2 + 3[\nabla h \cdot \nabla \phi_3 + \nabla \cdot (\phi_3 \nabla h)] \} + O(\mu^4) \\ &= O(\mu^4) \end{aligned} \quad (2.24)$$

and so on. Therefore, an expression for ϕ which retains terms to $O(\mu^2)$ is given by

$$\phi = \phi_0 - \mu^2(h+z)\nabla h \cdot \nabla \phi_0 - \mu^2 \frac{(h+z)^2}{2} \nabla^2 \phi_0 + O(\mu^4) \quad (2.25)$$

where $\phi_0 = \phi(x, y, z = -h, t)$ is the value of velocity potential ϕ at the bottom. In practice, we may replace ϕ_0 by the value of the potential at any level in the water column. Any choice will lead to a set of model equations with the same level of asymptotic approximation but with numerically different dispersion properties. Following the approaches of Nwogu (1993) and Chen and Liu (1995), we denote ϕ_α as the value of ϕ at $z = z_\alpha(x, y)$, or

$$\phi_\alpha = \phi_0 - \mu^2(h+z_\alpha)\nabla h \cdot \nabla \phi_0 - \mu^2 \frac{(h+z_\alpha)^2}{2} \nabla^2 \phi_0 + O(\mu^4) \quad (2.26)$$

This expression is then used in (2.25) to obtain an expression for ϕ in terms of ϕ_α :

$$\phi = \phi_\alpha + \mu^2 \left[(z_\alpha - z) \nabla \cdot (h \nabla \phi_\alpha) + \frac{1}{2} (z_\alpha^2 - z^2) \nabla^2 \phi_\alpha \right] + O(\mu^4) \quad (2.27)$$

from which corresponding derivatives for ϕ are obtained as:

$$\begin{aligned} \nabla \phi = \nabla \phi_\alpha + \mu^2 \left\{ \nabla z_\alpha \nabla \cdot (h \nabla \phi_\alpha) + (z_\alpha - z) \nabla [\nabla \cdot (h \nabla \phi_\alpha)] \right. \\ \left. + z_\alpha \nabla z_\alpha \nabla^2 \phi_\alpha + \frac{1}{2} (z_\alpha^2 - z^2) \nabla (\nabla^2 \phi_\alpha) \right\} + O(\mu^4) \end{aligned} \quad (2.28)$$

$$\phi_z = -\mu^2 \left[\nabla \cdot (h \nabla \phi_\alpha) + z \nabla^2 \phi_\alpha \right] + O(\mu^4) \quad (2.29)$$

$$\phi_t = \phi_{\alpha t} + \mu^2 \left\{ (z_\alpha - z) \nabla \cdot (h \nabla \phi_{\alpha t}) + \frac{1}{2} (z_\alpha^2 - z^2) \nabla^2 \phi_{\alpha t} \right\} + O(\mu^4) \quad (2.30)$$

The above forms of the velocity potential ϕ and its derivatives are then used in the governing equations (2.11)-(2.14) to obtain the approximate model equations.

2.2.2 Two-equation model for η and ϕ_α

Integrating (2.11) from $z = -h$ to $z = -\delta\eta$ and applying the kinematic boundary conditions (2.12) and (2.14) gives the continuity equation:

$$\eta_t + \nabla \cdot \mathbf{M} = 0 \quad (2.31)$$

where \mathbf{M} is the volume flux of the fluid which is defined as:

$$\mathbf{M} = \int_{-h}^{\delta\eta} \nabla \phi dz \quad (2.32)$$

Substituting (2.28) into the integral yields

$$\begin{aligned} \mathbf{M} = (h + \delta\eta) & \left\{ \nabla \phi_\alpha + \mu^2 \nabla \left[z_\alpha \nabla \cdot (h \nabla \phi_\alpha) + \frac{z_\alpha^2}{2} \nabla^2 \phi_\alpha \right] \right. \\ & \left. + \frac{\mu^2(h - \delta\eta)}{2} \nabla [\nabla \cdot (h \nabla \phi_\alpha)] - \frac{\mu^2(h^2 - h\delta\eta + \delta^2\eta^2)}{6} \nabla^2 \nabla \phi_\alpha \right\} \end{aligned} \quad (2.33)$$

The expression goes to zero identically as the total depth $(h + \delta\eta)$ goes to zero, which serves as a natural shoreline boundary condition.

By substituting equations (2.28)-(2.30) into equation (2.13), we obtain the Bernoulli equation:

$$\begin{aligned} \eta + \phi_{\alpha t} + \frac{\delta}{2} (\nabla \phi_\alpha)^2 + \mu^2 & \left\{ (z_\alpha - \delta\eta) \nabla \cdot (h \nabla \phi_{\alpha t}) + \frac{1}{2} [z_\alpha^2 - (\delta\eta)^2] \nabla^2 \phi_{\alpha t} \right\} \\ + \delta \mu^2 & \left\{ \nabla \phi_\alpha \cdot [\nabla z_\alpha \nabla \cdot (h \nabla \phi_\alpha) + (z_\alpha - \delta\eta) \nabla (\nabla \cdot (h \nabla \phi_\alpha))] \right\} \\ + \delta \mu^2 & \left\{ \frac{1}{2} [\nabla \cdot (h \nabla \phi_\alpha)]^2 + \delta\eta \nabla \cdot (h \nabla \phi_\alpha) \nabla^2 \phi_\alpha + \frac{1}{2} (\delta\eta)^2 (\nabla^2 \phi_\alpha)^2 \right\} \\ + \delta \mu^2 & \left\{ \nabla \phi_\alpha \cdot \left[z_\alpha \nabla z_\alpha \nabla^2 \phi_\alpha + \frac{1}{2} (z_\alpha^2 - (\delta\eta)^2) \nabla (\nabla^2 \phi_\alpha) \right] \right\} = 0 \end{aligned} \quad (2.34)$$

Equations at the order of approximation of the weakly nonlinear Boussinesq theory may be immediately obtained by neglecting terms of $O(\delta\mu^2)$ or higher. The modified expression for volume flux \mathbf{M} is

$$\mathbf{M} = (h + \delta\eta) \nabla \phi_\alpha + \mu^2 h \nabla \left[z_\alpha \nabla \cdot (h \nabla \phi_\alpha) + \frac{z_\alpha^2}{2} \nabla^2 \phi_\alpha \right]$$

$$+\frac{\mu^2 h^2}{2} \left[\nabla[\nabla \cdot (h \nabla \phi_\alpha)] - \frac{h}{3} \nabla^2 \nabla \phi_\alpha \right] \quad (2.35)$$

and the Bernoulli equation reduces to

$$\eta + \phi_{\alpha t} + \frac{\delta}{2} (\nabla \phi_\alpha)^2 + \mu^2 \left[z_\alpha \nabla \cdot (h \nabla \phi_{\alpha t}) + \frac{1}{2} z_\alpha^2 \nabla^2 \phi_{\alpha t} \right] = 0 \quad (2.36)$$

Equations (2.35) and (2.36) were given previously by Chen and Liu (1995). These results may be compared to the two-equation model of Wu (1981), which uses the depth-averaged value of velocity potential $\bar{\phi}$. The two models of Chen and Liu (1995) and of Wu (1981) are essentially the same within rearrangements of dispersive terms.

2.2.3 Three-equation model based on η and \mathbf{u}_α

For most coastal engineering applications, it is desirable to have velocities instead of velocity potential as the dependent variables. Introducing \mathbf{u}_α as the horizontal velocity vector at the depth $z = z_\alpha$, we have

$$\begin{aligned} \mathbf{u}_\alpha &= \nabla \phi|_{z=z_\alpha} \\ &= \nabla \phi_\alpha + \mu^2 \left[\nabla z_\alpha \nabla \cdot (h \nabla \phi_\alpha) + z_\alpha \nabla z_\alpha \nabla^2 \phi_\alpha \right] + O(\mu^4) \end{aligned} \quad (2.37)$$

which gives

$$\nabla \phi_\alpha = \mathbf{u}_\alpha - \mu^2 \left[\nabla z_\alpha \nabla \cdot (h \mathbf{u}_\alpha) + z_\alpha \nabla z_\alpha \nabla \cdot \mathbf{u}_\alpha \right] + O(\mu^4) \quad (2.38)$$

Substituting (2.38) into (2.33) and retaining terms to $O(\mu^2)$ and to all orders in δ gives the corresponding volume flux

$$\begin{aligned} \mathbf{M} &= (h + \delta \eta) \left\{ \mathbf{u}_\alpha + \mu^2 \left[\frac{1}{2} z_\alpha^2 - \frac{1}{6} (h^2 - h \delta \eta + (\delta \eta)^2) \right] \nabla (\nabla \cdot \mathbf{u}_\alpha) \right. \\ &\quad \left. + \mu^2 \left[z_\alpha + \frac{1}{2} (h - \delta \eta) \right] \nabla [\nabla \cdot (h \mathbf{u}_\alpha)] \right\} + O(\mu^4) \end{aligned} \quad (2.39)$$

By taking the horizontal gradient of (2.34) and then substituting equation (2.38), we obtain the corresponding momentum equation

$$\mathbf{u}_{\alpha t} + \delta(\mathbf{u}_\alpha \cdot \nabla)\mathbf{u}_\alpha + \nabla\eta + \mu^2\mathbf{V}_1 + \delta\mu^2\mathbf{V}_2 = O(\mu^4) \quad (2.40)$$

where

$$\mathbf{V}_1 = \frac{1}{2}z_\alpha^2\nabla(\nabla \cdot \mathbf{u}_{\alpha t}) + z_\alpha\nabla[\nabla \cdot (h\mathbf{u}_{\alpha t})] - \nabla\left[\frac{1}{2}(\delta\eta)^2\nabla \cdot \mathbf{u}_{\alpha t} + \delta\eta\nabla \cdot (h\mathbf{u}_{\alpha t})\right] \quad (2.41)$$

$$\begin{aligned} \mathbf{V}_2 = & \nabla\left\{(z_\alpha - \delta\eta)(\mathbf{u}_\alpha \cdot \nabla)[\nabla \cdot (h\mathbf{u}_\alpha)] + \frac{1}{2}(z_\alpha^2 - (\delta\eta)^2)(\mathbf{u}_\alpha \cdot \nabla)(\nabla \cdot \mathbf{u}_\alpha)\right\} \\ & + \frac{1}{2}\nabla\left\{[\nabla \cdot (h\mathbf{u}_\alpha) + \delta\eta\nabla \cdot \mathbf{u}_\alpha]^2\right\} \end{aligned} \quad (2.42)$$

The Boussinesq approximation of Nwogu (1993) is recovered by neglecting terms of $O(\delta\mu^2)$ or smaller, yielding the expressions

$$\begin{aligned} \mathbf{M} = (h + \delta\eta)\mathbf{u}_\alpha & + \mu^2h\left\{\left(\frac{z_\alpha^2}{2} - \frac{h^2}{6}\right)\nabla(\nabla \cdot \mathbf{u}_\alpha) + \left(z_\alpha + \frac{h}{2}\right)\nabla[\nabla \cdot (h\mathbf{u}_\alpha)]\right\} \\ & + O(\delta\mu^2) \end{aligned} \quad (2.43)$$

and

$$\mathbf{u}_{\alpha t} + \delta(\mathbf{u}_\alpha \cdot \nabla)\mathbf{u}_\alpha + \nabla\eta + \mu^2\left\{\frac{z_\alpha^2}{2}\nabla(\nabla \cdot \mathbf{u}_{\alpha t}) + z_\alpha\nabla[\nabla \cdot (h\mathbf{u}_{\alpha t})]\right\} = O(\delta\mu^2) \quad (2.44)$$

The two versions of fully nonlinear Boussinesq model derived here all have volume flux $\mathbf{M} \rightarrow 0$ at the shoreline, where the total water depth $(h + \delta\eta) \rightarrow 0$. This result is expected on physical grounds and appears in the nonlinear shallow water equations and in the standard Boussinesq models where the depth-averaged velocity is the dependent variable. However, this condition is not automatically satisfied by Nwogu's or other weakly nonlinear Boussinesq model based on a velocity other than the depth-averaged value, making the application of these models problematic at the shoreline. All fully nonlinear variations of any of the possible model systems should recover this condition correctly.

Before applying numerical schemes to obtain approximate solutions to the fully nonlinear Boussinesq equations derived above, we first examine the corresponding analytical properties from the equations. In the following sections, the coefficients for second order bound waves and the third order Schrödinger equation will be derived and compared with exact solutions obtained by Dean and Sharma (1981) and by Mei (1989). Comparison for bound wave coefficients are also made for the fully and weakly nonlinear versions of the present model.

2.3 Bound Wave Generation

One of the important properties for nonlinear wave equations is to generate bound waves at the sum and difference frequencies of the primary waves. The nonlinear transfer of wave energy between the spectral components for a random sea state have been studied extensively by Hasselmann (1962). Starting from equations (2.6)-(2.9), Hasselmann (1962) obtained the transfer coefficients for velocity potential up to fifth order. Using the same equations and perturbation method, Dean and Sharma (1981) also obtained the explicit expressions for the magnitude of the second-order bound waves, which will be used as the exact solution to compare with. To show the validity of the extended Boussinesq equations, Madsen and Sørensen (1992) and Nwogu (1993) derived the corresponding coefficients for these bound waves and compared with exact solutions of Dean and Sharma (1981). As we know, these extended Boussinesq equations are only valid for the weakly nonlinear case. In order to demonstrate the importance of high order nonlinear terms in the fully nonlinear Boussinesq equations, we follow the approach of Nwogu (1993) to derive the corresponding expressions for bound waves and compare with the exact and Nwogu's solutions.

For the case of constant water depth h , the natural choice for vertical length

scale is $h_0 = h$. Therefore, the dimensionless variable for water depth is one and the fully nonlinear Boussinesq equations (2.31)-(2.34) using η and ϕ_α as variables reduce to

$$\begin{aligned} \eta_t &+ \nabla^2 \phi_\alpha + \mu^2 \alpha_1 \nabla^2 (\nabla^2 \phi_\alpha) + \delta \nabla \cdot (\eta \nabla \phi_\alpha) + \delta \mu^2 \alpha \nabla \cdot [\eta \nabla (\nabla^2 \phi_\alpha)] \\ &- \frac{\delta^2 \mu^2}{2} \nabla \cdot [\eta^2 \nabla (\nabla^2 \phi_\alpha)] + \frac{\delta^3 \mu^2}{6} \nabla \cdot [\eta^3 \nabla (\nabla^2 \phi_\alpha)] = 0 \end{aligned} \quad (2.45)$$

$$\begin{aligned} \eta &+ \phi_{\alpha t} + \mu^2 \alpha \nabla^2 \phi_{\alpha t} + \frac{\delta}{2} (\nabla \phi_\alpha)^2 - \delta \mu^2 \left(\eta + \frac{\delta}{2} \eta^2 \right) \nabla^2 \phi_{\alpha t} \\ &+ \delta \mu^2 \left[\alpha - \delta \eta - \frac{1}{2} \delta^2 \eta^2 \right] \nabla \phi_\alpha \cdot \nabla (\nabla^2 \phi_\alpha) \\ &+ \frac{\delta \mu^2}{2} [1 + 2\delta \eta + \delta^2 \eta^2] (\nabla^2 \phi_\alpha)^2 = 0 \end{aligned} \quad (2.46)$$

where η , ϕ_α , δ and μ^2 are the same as defined previously, α and α_1 are constants which are defined as

$$\alpha = \frac{1}{2} z_\alpha^2 + z_\alpha, \quad \alpha_1 = \alpha + \frac{1}{3} \quad (2.47)$$

For the study of a forced second-order sea, only terms up to $O(\delta)$ are useful and must be kept. For convenience, we denote $\phi = \phi_\alpha$ from now on. To $O(\delta)$, equations (2.45) and (2.46) become

$$\begin{aligned} \eta_t &+ \nabla^2 \phi + \mu^2 \alpha_1 \nabla^2 (\nabla^2 \phi) + \delta \nabla \cdot (\eta \nabla \phi) \\ &+ \delta \mu^2 \alpha \nabla \cdot [\eta \nabla (\nabla^2 \phi)] = 0 \end{aligned} \quad (2.48)$$

$$\begin{aligned} \eta &+ \phi_t + \mu^2 \alpha \nabla^2 \phi_t + \frac{\delta}{2} (\nabla \phi)^2 - \delta \mu^2 \eta \nabla^2 \phi_t + \frac{\delta \mu^2}{2} (\nabla^2 \phi)^2 \\ &+ \delta \mu^2 \alpha \nabla \phi \cdot \nabla (\nabla^2 \phi) = 0 \end{aligned} \quad (2.49)$$

To obtain the solution for bound waves, we first expand η and ϕ as

$$\eta = \eta_1 + \delta \eta_2 + \dots \quad (2.50)$$

$$\phi = \phi_1 + \delta \phi_2 + \dots \quad (2.51)$$

where subscripts 1 and 2 denote the primary and the secondary wave components, respectively. Then by substituting the expansions into equations (2.48)-(2.49), we obtain two sets of equations corresponding to different powers of δ . To $O(1)$, we have

$$\eta_{1t} + \nabla^2 \phi_1 + \mu^2 \alpha_1 \nabla^2 (\nabla^2 \phi_1) = 0 \quad (2.52)$$

$$\phi_{1t} + \eta_1 + \mu^2 \alpha \nabla^2 \phi_{1t} = 0 \quad (2.53)$$

which are the linearized forms of the fully nonlinear Boussinesq equations and are exactly the same as those obtained by Nwogu (1993). To $O(\delta)$, we have

$$\eta_{2t} + \nabla^2 \phi_2 + \mu^2 \alpha_1 \nabla^2 (\nabla^2 \phi_2) = -\nabla \cdot (\eta_1 \nabla \phi_1) - \mu^2 \alpha \nabla \cdot [\eta_1 \nabla (\nabla^2 \phi_1)] \quad (2.54)$$

$$\begin{aligned} \phi_{2t} + \eta_2 + \mu^2 \alpha \nabla^2 \phi_{2t} = & -\frac{1}{2} (\nabla \phi_1)^2 + \mu^2 \eta_1 \nabla^2 \phi_{1t} - \frac{\mu^2}{2} (\nabla^2 \phi_1)^2 \\ & - \mu^2 \alpha \nabla \phi \cdot \nabla (\nabla^2 \phi) \end{aligned} \quad (2.55)$$

where terms on the right hand sides represent the nonlinear interaction of the first order free waves η_1 and ϕ_1 . These free waves serve as the forcing terms for second order bound waves η_2 and ϕ_2 . Compared with the corresponding forcing equations obtained by Nwogu (1993), terms with $O(\mu^2)$ on the right hand side of equations (2.54) and (2.55) are extra. As will be shown later, it is these terms which improve the accuracy of bound wave coefficients for the case of large nonlinearity. To obtain the forcing coefficients, we introduce a linear random sea which consists of infinite number of waves with different frequencies and directions

$$\eta_1 = \sum_{n=1}^{\infty} a_n \cos \psi_n \quad (2.56)$$

$$\phi_1 = \sum_{n=1}^{\infty} b_n \sin \psi_n \quad (2.57)$$

$$\psi_n = \mathbf{k}_n \cdot \mathbf{x} - \omega_n t + \xi_n \quad (2.58)$$

where subscript n is the n -th wave component, \mathbf{k}_n the wavenumber vector, \mathbf{x} the horizontal coordinate vector, ω_n the angular frequency, and ξ_n the initial phase

of the wave. Substituting equations (2.56)-(2.58) into equations (2.52) and (2.53) yields

$$\omega_n^2 = k_n^2 \frac{1 - \mu^2 \alpha_1 k_n^2}{1 - \mu^2 \alpha k_n^2} \quad (2.59)$$

$$b_n = \frac{\omega_n a_n}{k_n^2 [1 - \mu^2 \alpha_1 k_n^2]} = \frac{a_n}{\omega_n [1 - \mu^2 \alpha k_n^2]} \quad (2.60)$$

where k_n is the magnitude of wavenumber vector $|\mathbf{k}_n|$, i.e., $k_n = |\mathbf{k}_n|$. Equation (2.59) is the linear dispersion relation of the fully nonlinear Boussinesq equations and equation (2.60) is the corresponding linear relation between the amplitudes of velocity and surface elevation. These two relations are exactly the same as those from the extended Boussinesq equations of Nwogu (1993).

By substituting equations (2.56)-(2.58) into equations (2.54) and (2.55) and by utilizing relations (2.59) and (2.60), we have

$$\begin{aligned} \eta_{2t} + \nabla^2 \phi_2 + \mu^2 \alpha_1 \nabla^2 (\nabla^2 \phi_2) \\ = \frac{1}{4} \sum_m \sum_l a_m a_l [\mathcal{F}_{ml}^+ \sin(\psi_m + \psi_l) + \mathcal{F}_{ml}^- \sin(\psi_m - \psi_l)] \end{aligned} \quad (2.61)$$

$$\begin{aligned} \phi_{2t} + \eta_2 + \mu^2 \alpha \nabla^2 \phi_{2t} \\ = \frac{1}{4} \sum_m \sum_l a_m a_l [\mathcal{G}_{ml}^+ \cos(\psi_m + \psi_l) + \mathcal{G}_{ml}^- \cos(\psi_m - \psi_l)] \end{aligned} \quad (2.62)$$

where

$$\mathcal{F}_{ml}^\pm = \frac{\omega_l k_m^2 \pm \omega_m k_l^2 + (\omega_m \pm \omega_l) \mathbf{k}_m \cdot \mathbf{k}_l}{\omega_m \omega_l} \quad (2.63)$$

$$\begin{aligned} \mathcal{G}_{ml}^\pm = & -\frac{[1 - \mu^2 \alpha (k_m^2 + k_l^2)](\mathbf{k}_m \cdot \mathbf{k}_l)}{\omega_m \omega_l [1 - \mu^2 \alpha k_m^2][1 - \mu^2 \alpha k_l^2]} + \frac{\mu^2 \omega_m^2}{1 - \mu^2 \alpha_1 k_m^2} \\ & \pm \frac{\mu^2 \omega_m \omega_l}{[1 - \mu^2 \alpha_1 k_m^2][1 - \mu^2 \alpha_1 k_l^2]} + \frac{\mu^2 \omega_l^2}{1 - \mu^2 \alpha_1 k_l^2} \end{aligned} \quad (2.64)$$

The expression for \mathcal{F} has exactly the same form as that obtained from Stokes theory by Dean and Sharma (1981), aside from differences in the evaluation

of wavenumbers from the true and the approximate linear dispersion relations. The expression for \mathcal{G} in (2.64) at the first glance is not in the same form as that from Stokes theory. However, after expanding the denominators, we have

$$\mathcal{G}_{ml}^{\pm} = -\frac{[(\mathbf{k}_m \cdot \mathbf{k}_l)]}{\omega_m \omega_l} \pm \mu^2 \omega_m \omega_l + \mu^2 \omega_m^2 + \mu^2 \omega_l^2 + O(\mu^4) \quad (2.65)$$

which is equivalent to the form obtained from Stokes theory after the neglect of $O(\mu^4)$ terms. Notice that the level of approximation in the governing equations is of $O(\mu^2)$, the same as that in equation (2.65).

From equations (2.61) and (2.62), we know that the wavenumber vectors and the frequencies for second order bound waves are the (vector) sum and (vector) difference of those for the first order free waves. After assuming the solution forms for the bound waves and work on some algebra derivation, we obtain the surface elevation as:

$$\eta_2 = \frac{1}{2} \sum_m \sum_l \left\{ a_m a_l \left[G_{ml}^+ \cos(\psi_m + \psi_l) + G_{ml}^- \cos(\psi_m - \psi_l) \right] \right\} \quad (2.66)$$

where, on the right hand side, the first term represents the superharmonic component and the second term represents the subharmonic component. The corresponding coupling coefficients are given by

$$G_{ml}^{\pm} = \frac{1}{4} \frac{\omega_{ml}^{\pm} \mathcal{F}_{ml}^{\pm} - k_{ml}^{\pm} T_{ml}^{\pm} \mathcal{G}_{ml}^{\pm}}{(\omega_{ml}^{\pm})^2 - k_{ml}^{\pm} T_{ml}^{\pm}} \quad (2.67)$$

where the parameters ω_{ml}^{\pm} , k_{ml}^{\pm} , and T_{ml}^{\pm} are defined as

$$\omega_{ml}^{\pm} = \omega_m \pm \omega_l \quad (2.68)$$

$$k_{ml}^{\pm} = |\mathbf{k}_m \pm \mathbf{k}_l| \quad (2.69)$$

$$T_{ml}^{\pm} = k_{ml}^{\pm} \frac{1 - \alpha_1 (k_{ml}^{\pm})^2}{1 - \alpha (k_{ml}^{\pm})^2} \quad (2.70)$$

Given any two of the primary wave components (*i.e.* specified frequencies ω_m and ω_l , and specified directions of \mathbf{k}_m and \mathbf{k}_l), the corresponding superharmonic and subharmonic coefficients G^+ and G^- can be obtained from equation

(2.67) and related formulas. Nwogu (1994) demonstrated that the coefficients obtained from the extended Boussinesq equations agreed with the exact solution better than those from the standard Boussinesq equations. To show the importance of the extra nonlinear terms in the fully nonlinear Boussinesq equations, we obtain the corresponding coefficients for the same wave conditions used by Nwogu (1994) and compare the results between different models. As shown in Figures 2.3, solid curves are the results obtained from the full Stokes theory by Dean and Sharma (1981), dashed curves from the extended Boussinesq model of Nwogu (1994), and dash-dot curves from the present theory with \mathcal{G}_{ml}^{\pm} obtained from (2.64). The two primary wave components used for the calculation are different in frequency by 10%, *i.e.* $\omega_1 = 1.05\omega_0$ and $\omega_2 = 0.95\omega_0$, where ω_0 is the reference center frequency. Two angles between these waves are used for the sample calculation, which are $\Delta\theta = 0^\circ$ and $\Delta\theta = 40^\circ$, respectively, as indicated by the upper and lower sets of curves. The horizontal axis is the ratio of water depth ($h = 1$) to l_0 , the deep water wavelength corresponding to the center frequency ω_0 .

The superharmonic and subharmonic coefficients from both Nwogu's extended Boussinesq model and the present theory give good agreements to those from Stokes theory over the range of specified deep water wavelength. However, the present model provides a more consistent approximation to the full theory except at large values of l_0^{-1} (corresponding to deeper water depth), where the form of error in the Nwogu's theory leads to a fortuitously better prediction. If we used the expression (2.65) instead of (2.64) to obtain the value of \mathcal{G}_{ml}^{\pm} , then the maximum error between the present theory and the full theory is on the order of 2% over the entire range.

Figure 2.4 gives an alternate view for the comparisons of these coefficients

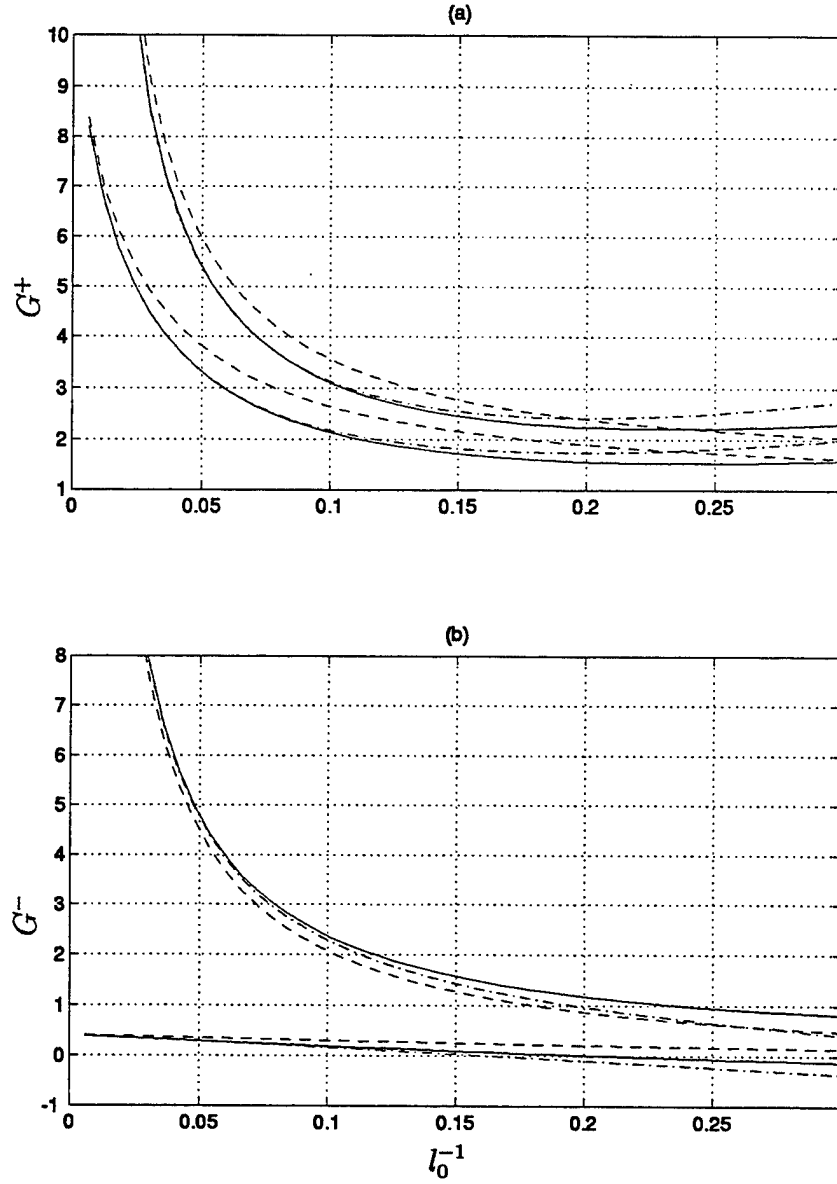


Figure 2.3: Comparisons for bound wave coupling coefficients: (a) superharmonic; and (b) subharmonics. Stokes theory (—); Nwogu's theory (----); present theory (-·-·-). The two primary waves are 10% difference in frequency and at the angles of $\Delta\theta = 0^\circ$ (upper curves) and $\Delta\theta = 40^\circ$ (lower curves).

among different models, following the example plots by Madsen and Sørensen (1993). The frequencies of the primary wave components are varied over a wide range of values but their directions are the same (so that $\Delta\theta = 0^\circ$). The ratios of G^\pm predicted from Nwogu's model and the present theory to that from Stokes theory are calculated and shown in contour plots. Again, results from the present theory are generally more accurate than those from Nwogu's model, except for large value of ω , where Nwogu's model leads to fortuitously better agreement. However, if the expression of \mathcal{G}_{ml}^\pm in (2.65) is used instead of equation (2.64), a much better agreement is obtained between the present theory and Stokes theory, as shown in (e) and (f) of Figure 2.4.

2.4 Evolution of a Slowly Varying Wave Train

It is of great interest for applying nonlinear wave equations to examine the effect of third order nonlinear resonant interaction to a wave train with a narrow band of frequencies and wavelengths. Since Benjamin and Feir (1967) demonstrated that Stokes waves are unstable to periodic side-band disturbances, the nonlinear evolution of a wave train traveling over a long distance for a long time has been studying by a number of investigators, including Zakharov (1968), Benney and Roskes (1969), and Chu and Mei (1971). This nonlinear resonant property is best described by the corresponding evolution equation, whose form is the same as that of the cubic Schrödinger equation in quantum mechanics. For the original 3-D wave propagation problem governed by equations (2.6)- (2.9), Mei (1989) showed detailed derivation for obtaining the Schrödinger equation. In the following, we will derive the corresponding Schrödinger equation for the fully nonlinear Boussinesq equations and compare the model results with Mei's solutions.

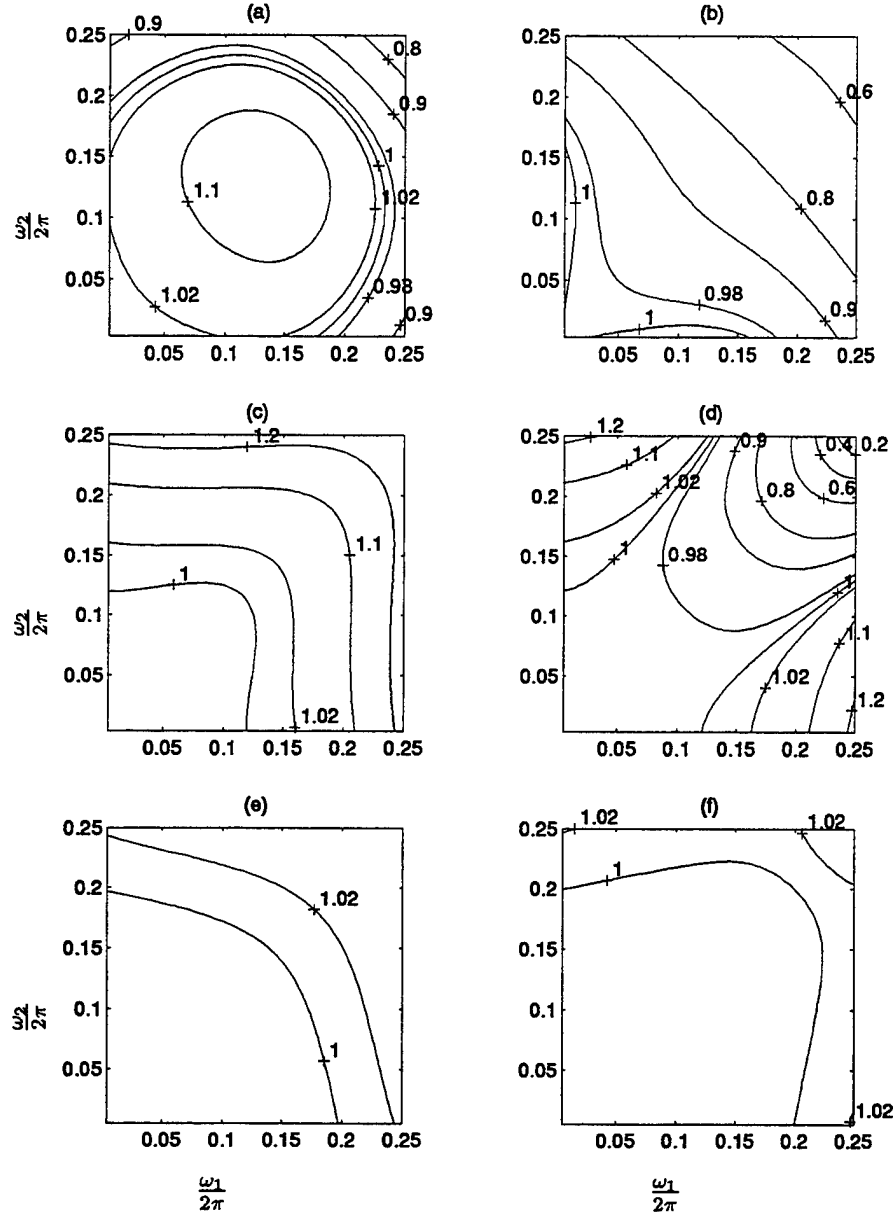


Figure 2.4: Ratio of model predicted G^\pm to value from Stokes theory. (a,c,e) — Superharmonics; (b,d,f) — Subharmonics. $\Delta\theta = 0$. (a,b) — Nwogu equation; (c,d) — Present theory; (e,f) — Present theory with modified \mathcal{G} .

For constant water depth, the fully nonlinear Boussinesq equations are reduced to equations (2.45) and (2.46). In order to derive the corresponding cubic Schrödinger equation, only terms to $O(\delta^2)$ are useful. Thus equations (2.45) and (2.46) are further reduced to ($\phi = \phi_\alpha$)

$$\begin{aligned} \eta_t &+ \nabla^2 \phi + \mu^2 \alpha_1 \nabla^2 (\nabla^2 \phi) \\ &+ \delta \nabla \cdot (\eta \nabla \phi) + \delta \mu^2 \alpha \nabla \cdot [\eta \nabla (\nabla^2 \phi)] \\ &- \frac{\delta^2 \mu^2}{2} \nabla \cdot [\eta^2 \nabla (\nabla^2 \phi)] = 0 \end{aligned} \quad (2.71)$$

$$\begin{aligned} \eta &+ \phi_t + \mu^2 \alpha \nabla^2 \phi_t \\ &+ \frac{\delta}{2} (\nabla \phi)^2 - \delta \mu^2 \eta \nabla^2 \phi_t + \delta \mu^2 \alpha \nabla \phi \cdot \nabla (\nabla^2 \phi) + \frac{\delta \mu^2}{2} (\nabla^2 \phi)^2 \\ &- \frac{\delta^2 \mu^2}{2} \eta^2 \nabla^2 \phi_t - \delta^2 \mu^2 \eta \nabla \phi \cdot \nabla (\nabla^2 \phi) + \delta^2 \mu^2 \eta (\nabla^2 \phi)^2 = 0 \end{aligned} \quad (2.72)$$

Differentiating equation (2.72) with respect to t and subtracting the resulting equation from equation (2.71), we have

$$\begin{aligned} -\phi_{tt} &+ \nabla^2 \phi - \mu^2 \alpha \nabla \phi_{tt} + \mu^2 \alpha_1 g \nabla^2 (\nabla^2 \phi) \\ &+ \delta \nabla \cdot (\eta \nabla \phi) - \delta \nabla \phi \cdot \nabla \phi_t + \delta \mu^2 (\eta \nabla^2 \phi_t)_t \\ &- \delta \mu^2 \alpha (\nabla \phi \cdot \nabla (\nabla^2 \phi))_t - \delta \mu^2 \nabla^2 \phi \nabla^2 \phi_t + \delta \mu^2 \alpha \nabla \cdot [\eta \nabla (\nabla^2 \phi)] \\ &+ \frac{\delta^2 \mu^2}{2} (\eta^2 \nabla^2 \phi_t)_t + \delta^2 \mu^2 [\eta \nabla \phi \cdot \nabla (\nabla^2 \phi)]_t - \delta^2 \mu^2 [\eta (\nabla \phi)^2]_t \\ &- \frac{1}{2} \delta^2 \mu^2 \nabla \cdot [\eta^2 \nabla (\nabla^2 \phi)] = 0 \end{aligned} \quad (2.73)$$

Assume the carrier wave of a wave train propagates in the x direction. To allow slow modulation, we introduce the following multiple scales for independent variables x , y and t

$$\begin{aligned} x &= x + \delta x + \delta^2 x = x + X_1 + X_2 \\ y &= \delta y + \delta^2 y = Y_1 + Y_2 \\ t &= t + \delta t + \delta^2 t = t + T_1 + T_2 \end{aligned} \quad (2.74)$$

where X_1 , X_2 , Y_1 , Y_2 , T_1 , and T_2 are slow variables. The corresponding partial derivative operators are defined as

$$\begin{aligned} ()_x &\rightarrow ()_x + \delta()_{X_1} + \delta^2()_{X_2} \\ ()_y &\rightarrow \delta()_{Y_1} + \delta^2()_{Y_2} \\ ()_t &\rightarrow ()_t + \delta()_{T_1} + \delta^2()_{T_2} \end{aligned} \quad (2.75)$$

and so on for higher order and mixed derivatives. Equations (2.72) and (2.73) are then transformed into

$$\begin{aligned} L_1(\phi) + \delta L_2(\phi) + \delta^2 L_3(\phi) + \delta M_1(\eta, \phi) + \delta N_1(\phi, \phi) \\ + \delta^2 M_2(\eta, \phi) + \delta^2 N_2(\phi, \phi) + \delta^2 M_3(\eta, \phi) = 0 \end{aligned} \quad (2.76)$$

$$\eta + P_1(\phi) + \delta P_2(\phi) + \delta Q(\eta, \phi) + \delta R(\phi, \phi) = 0 \quad (2.77)$$

where L_1 , L_2 , L_3 , P_1 , and P_2 are linear operators which are defined as:

$$L_1() = -()_{tt} + ()_{xx} - \mu^2 \alpha()_{xxtt} + \mu^2 \alpha_1()_{xxxx} \quad (2.78)$$

$$L_2() = -2()_{tT_1} + 2()_{xX_1} - 2\mu^2 \alpha [()_{ttX_1} + ()_{xxtT_1}] + 4\mu^2 \alpha_1()_{xxxX_1} \quad (2.79)$$

$$\begin{aligned} L_3() = & -()_{T_1T_1} - 2()_{tT_2} + [()_{X_1X_1} + 2()_{xX_2} + ()_{Y_1Y_1}] \\ & - \mu^2 \alpha [()_{X_1X_1tt} + 2()_{xX_2tt} + ()_{xxT_1T_1} + 2()_{xxtT_2} + 4()_{xX_1tT_1} + ()_{Y_1Y_1tt}] \\ & + \mu^2 \alpha_1 [4()_{xxxX_2} + 6()_{xxX_1X_1} + 2()_{xxY_1Y_1}] \end{aligned} \quad (2.80)$$

$$P_1() = ()_t + \mu^2 \alpha()_{xxt} \quad (2.81)$$

$$P_2() = ()_{T_1} + \mu^2 \alpha [2()_{xX_1t} + ()_{xxtT_1}] \quad (2.82)$$

and M_1 , N_1 , M_2 , N_2 , M_3 , Q and R are nonlinear terms which are defined as

$$M_1(\eta, \phi) = (\eta \phi_x)_x + \mu^2 (\eta \phi_{xxt})_t + \mu^2 \alpha (\eta \phi_{xxx})_x \quad (2.83)$$

$$N_1(\phi, \phi) = -\phi_x \phi_{xt} - \mu^2 \alpha (\phi_x \phi_{xxx})_t - \mu^2 \phi_{xx} \phi_{xxt} \quad (2.84)$$

$$\begin{aligned} M_2(\eta, \phi) = & [(\eta \phi_x)_{X_1} + (\eta \phi_{X_1})_x] \\ & + \mu^2 [(\eta \phi_{xxt})_{T_1} + 2(\eta \phi_{xX_1t})_t + (\eta \phi_{xxT_1})_t] \end{aligned}$$

$$+\mu^2\alpha[(\eta\phi_{xxx})_{X_1}+3(\eta\phi_{xxX_1})_x] \quad (2.85)$$

$$\begin{aligned} N_2(\phi, \phi) = & -\phi_{X_1}\phi_{xt} - \phi_x\phi_{X_1t} - \phi_x\phi_{xT_1} \\ & -\mu^2\alpha[(\phi_{X_1}\phi_{xxx})_t + (\phi_x\phi_{xxx})_{T_1} + 3(\phi_x\phi_{xxX_1})_t] \\ & -\mu^2(2\phi_{xX_1}\phi_{xxt} + 2\phi_{xx}\phi_{xX_1t} + \phi_{xx}\phi_{xxT_1}) \end{aligned} \quad (2.86)$$

$$M_3(\eta, \phi) = \mu^2 \left\{ \frac{1}{2}(\eta^2\phi_{xxt})_t + (\eta\phi_x\phi_{xxx})_t - (\eta\phi_{xx}^2)_t - \frac{1}{2}(\eta^2\phi_{xxx})_x \right\} \quad (2.87)$$

$$Q(\eta, \phi) = -\mu^2\eta\phi_{xxt} \quad (2.88)$$

$$R(\phi, \phi) = \frac{\mu^2}{2}\phi_x^2 + \mu^2\alpha\phi_x\phi_{xxx} + \frac{\mu^2}{2}\phi_{xx}^2 \quad (2.89)$$

To obtain the evolution equation, we introduce the following perturbation expansions for the unknowns of ϕ and η

$$\phi = \phi_1 + \delta\phi_2 + \delta^2\phi_3 \quad (2.90)$$

$$\eta = \eta_1 + \delta\eta_2 + \delta^2\eta_3 \quad (2.91)$$

where subscripts 1, 2, and 3 denote the first, the second, and the third order wave components, respectively. Substituting the above expansions into (2.76) and (2.77) yields

$$\begin{aligned} L_1(\phi_1) + & \delta L_1(\phi_2) + \delta^2 L_1(\phi_3) + \delta L_2(\phi_1) + \delta^2 L_2(\phi_2) + \delta^2 L_3(\phi_1) \\ & + \delta M_1(\eta_1, \phi_1) + \delta^2 M_1(\eta_1, \phi_2) + \delta^2 M_1(\eta_2, \phi_1) \\ & + \delta N_1(\phi_1, \phi_1) + \delta^2 N_1(\phi_1, \phi_2) + \delta^2 N_1(\phi_2, \phi_1) \\ & + \delta^2 M_2(\eta_1, \phi_1) + \delta^2 N_2(\phi_1, \phi_1) + \delta^2 M_3(\eta_1, \phi_1) = O(\delta^3) \end{aligned} \quad (2.92)$$

$$\begin{aligned} \eta_1 + & \delta\eta_2 + P_1(\phi_1) + \delta P_1(\phi_2) + \delta P_2(\phi_1) \\ & + \delta Q(\eta_1, \phi_1) + \delta R(\phi_1, \phi_1) = O(\delta^2) \end{aligned} \quad (2.93)$$

from which equations of $O(1)$, $O(\delta)$, and $O(\delta^2)$ are obtained. Due to the effect of nonlinear interaction, high order solutions must contain high order harmonics.

Therefore, the solution forms for different order of ϕ and η are assumed to be

$$\phi_n = \sum_{m=-n}^{m=n} \phi_{n,m} E^m \quad (2.94)$$

$$\eta_n = \sum_{m=-n}^{m=n} \eta_{n,m} E^m \quad (2.95)$$

$n = 1, 2, 3, \dots$

where n is the order number, m is the mode number, $\phi_{n,m}$ and $\eta_{n,m}$ are functions of slow variables X_1, X_2, Y_1, Y_2, T_1 and T_2 only. Terms with subscript $(n, -m)$ are the complex conjugates of terms with subscript (n, m) . The quantity of E is a function of fast variables x and t and is defined as

$$E = \exp[i(x - \omega t)], \quad i = \sqrt{-1} \quad (2.96)$$

where ω is the angular frequency of the wave train. Notice that x is a dimensionless variable which has been scaled by the inverse of the typical wavenumber k_0 and the natural choice for k_0 is k — the wavenumber of the wave train.

In the following, we start from lowest order equations and seek solutions to equations of higher order. In the end, we will obtain the corresponding cubic Schrödinger equation which governs the long term evolution of a wave train.

2.4.1 Solutions for $O(1)$

To $O(1)$, equations (2.92) and (2.93) reduces to

$$L_1(\phi_1) = 0 \quad (2.97)$$

$$\eta_1 + P_1(\phi_1) = 0 \quad (2.98)$$

Substituting equations (2.94) and (2.95) for $n = 1$ into (2.97) and (2.98) yields

$$D_1 \phi_{1,1} E + D_1 \phi_{1,-1} E^{-1} = 0 \quad (2.99)$$

$$\eta_{1,1} E + \eta_{1,0} + \eta_{1,-1} E^{-1} - i\omega[1 - \alpha\mu^2](\phi_{1,1} E - \phi_{1,-1} E^{-1}) = 0 \quad (2.100)$$

where

$$D_1 = \omega^2[1 - \alpha\mu^2] - [1 - \alpha_1\mu^2] \quad (2.101)$$

Collecting terms with E , equation (2.99) becomes

$$D_1\phi_{1,1} = 0 \quad (2.102)$$

Notice that terms with E^{-1} will also result in an equation. However, the equation is redundant since it is the complex conjugate of that with E . In the subsequent derivation, all complex conjugate equations will not be considered.

Since the term $\phi_{1,1}$ is not zero in general, equation (2.102) requires $D_1 = 0$ and results in

$$\omega^2 = \frac{1 - \alpha_1\mu^2}{1 - \alpha\mu^2} \quad (2.103)$$

which is the linear dispersion relation for the fully nonlinear Boussinesq equations, the same as that from Nwogu's equations.

To satisfy equation (2.100), we have

$$\eta_{1,1} = i\omega(1 - \alpha\mu^2)\phi_{1,1} \quad (2.104)$$

$$\eta_{1,0} = 0 \quad (2.105)$$

Denoting $\eta_{1,1} = A/2$ (so that $|A|$ is the amplitude of η_1), equation (2.104) results in

$$\phi_{1,1} = -\frac{1}{\omega(1 - \alpha\mu^2)} \frac{iA}{2} \quad (2.106)$$

For convenience, the first order solutions are summarized here

$$\eta_1 = \frac{A}{2}E + \frac{A^*}{2}E^{-1} \quad (2.107)$$

$$\phi_1 = -\frac{1}{2\omega(1 - \alpha\mu^2)}(iAE - iA^*E^{-1}) + \phi_{1,0} \quad (2.108)$$

where A^* is the conjugate gradient of A . The relation between the mean flow potential $\phi_{1,0}$ and A can not be determined at this order.

2.4.2 Solutions for $O(\delta)$

To $O(\delta)$, equations (2.92) and (2.93) reduce to

$$L_1(\phi_2) + L_2(\phi_1) + M_1(\eta_1, \phi_1) + N_1(\phi_1, \phi_1) = 0 \quad (2.109)$$

$$\eta_2 + P_1(\phi_2) + P_2(\phi_1) + Q(\eta_1, \phi_1) + R(\phi_1, \phi_1) = 0 \quad (2.110)$$

Using the first order solutions, we first obtain solution of ϕ_2 from equation (2.109) and then obtain solution of η_2 from (2.110). The two linear terms in (2.109) become

$$L_1(\phi_2) = D_2 \phi_{2,2} E^2 + c.c. \quad (2.111)$$

$$L_2(\phi_1) = 2i\omega(1 - \alpha\mu^2)(\phi_{1,1T_1} + C_g \phi_{1,1X_1}) E + c.c. \quad (2.112)$$

where $c.c.$ denotes complex conjugate, D_2 and C_g (the group velocity) are defined as

$$D_2 = 4\omega^2(1 - 4\alpha\mu^2) - 4(1 - 4\alpha_1\mu^2) = \frac{4\mu^2}{1 - \alpha\mu^2} \quad (2.113)$$

$$C_g = \frac{1 + \alpha\mu^2\omega^2 - 2\alpha_1\mu^2}{\omega(1 - \alpha\mu^2)} \quad (2.114)$$

In the above derivation, the linear dispersion relation (2.103) has been used.

The two nonlinear terms in equation (2.109) are evaluated as

$$\begin{aligned} M_1(\eta_1, \phi_1) &= (\eta_1 \phi_{1x})_x + \mu^2(\eta_1 \phi_{1xxt})_t + \mu^2\alpha(\eta_1 \phi_{1xxx})_x \\ &= 2(\omega^2 - 1 + \alpha\mu^2)(\eta_{1,1}\phi_{1,1}E^2 + \eta_{1,-1}\phi_{1,-1}E^{-2}) \end{aligned} \quad (2.115)$$

$$\begin{aligned} N_1(\phi_1, \phi_1) &= -\phi_{1x}\phi_{1xt} - \mu^2\alpha(\phi_{1x}\phi_{1xxx})_t - \mu^2\phi_{1xx}\phi_{1xxt} \\ &= i\omega(-1 + 2\alpha\mu^2 + \mu^2)(\phi_{1,1}^2E^2 - \phi_{1,-1}^2E^{-2}) \end{aligned} \quad (2.116)$$

By substituting the expressions for L_1 , L_2 , M_1 , and N_1 back into equation (2.109) and collecting for terms with E and E^2 , we have

$$2i\omega(1 - \alpha\mu^2)(\phi_{1,1T_1} + C_g \phi_{1,1X_1}) = 0 \quad (2.117)$$

$$D_2\phi_{2,2} - 2(1 - \alpha\mu^2 - \omega^2)\eta_{1,1}\phi_{1,1} - i\omega[1 - (1 + 2\alpha)\mu^2]\phi_{1,1}^2 = 0 \quad (2.118)$$

Terms with products of $\eta_{1,m}$ and $\phi_{1,m}$ ($m = -1, 1$) indicate nonlinear interaction between the first order waves, which determines the solution of $\phi_{2,2}$. Substituting solutions (2.107) and (2.108) of η_1 and ϕ_1 into equations (2.117) and (2.118) yields

$$A_{1,1T_1} = -C_g A_{1,1X_1} \quad (2.119)$$

$$\phi_{2,2} = -\frac{3iA^2 \mathcal{G}_{2,2}(\mu)}{16\omega \mu^2} \quad (2.120)$$

where $\mathcal{G}_{2,2}(\mu)$ is a function of μ which is defined as

$$\mathcal{G}_{2,2}(\mu) = \frac{1 - (1 + 2\alpha)\mu^2 + \frac{2}{3}(\alpha^2 + \alpha_1)\mu^4}{1 - \alpha\mu^2} \quad (2.121)$$

With the solution for $\phi_{2,2}$, we are now seeking solution for η_2 from equation (2.110), which is rewritten here for convenience

$$\eta_2 + P_1(\phi_2) + P_2(\phi_1) + Q(\eta_1, \phi_1) + R(\phi_1, \phi_1) = 0 \quad (2.122)$$

Each term in the above equation is expanded as

$$\eta_2 = \eta_{2,2}E^2 + \eta_{2,1}E + c.c. + \eta_{2,0} \quad (2.123)$$

$$P_1(\phi_2) = -2i\omega(1 - 4\alpha\mu^2)\phi_{2,2}E^2 - i\omega(1 - \alpha\mu^2)\phi_{2,1}E + c.c. \quad (2.124)$$

$$P_2(\phi_1) = [(1 - \alpha\mu^2)\phi_{1,1T_1} + 2\mu^2\alpha\omega\phi_{1,1X_1}]E + c.c. + \phi_{1,0T_1} \quad (2.125)$$

$$\begin{aligned} Q(\eta_1, \phi_1) &= -\mu^2\eta_1\phi_{1xxt} \\ &= -i\mu^2\omega\eta_{1,1}\phi_{1,1}E^2 + c.c. \\ &\quad -i\mu^2\omega(\eta_{1,-1}\phi_{1,1} - \eta_{1,1}\phi_{1,-1}) \end{aligned} \quad (2.126)$$

$$\begin{aligned} R(\phi_1, \phi_1) &= \frac{1}{2}\phi_{1x}^2 + \mu^2\alpha h^2\phi_{1x}\phi_{1xxx} + \mu^2\frac{1}{2}\phi_{1xx}^2 \\ &= -\frac{1}{2}(1 - 2\alpha\mu^2 - \mu^2)E^2 + c.c. \\ &\quad + (1 - 2\alpha\mu^2 + \mu^2)\phi_{1,1}\phi_{1,-1} \end{aligned} \quad (2.127)$$

By substituting the above expressions back into equations (2.122) and collecting terms with E^0 , E^1 and E^2 , we have

$$\begin{aligned} \eta_{2,0} &+ \phi_{1,0T_1} - i\mu^2\omega(\eta_{1,-1}\phi_{1,1} - \eta_{1,1}\phi_{1,-1}) \\ &+ (1 - 2\alpha\mu^2 + \mu^2)\phi_{1,1}\phi_{1,-1} = 0 \end{aligned} \quad (2.128)$$

$$\eta_{2,1} - i\omega(1 - \alpha\mu^2)\phi_{2,1} + (1 - \alpha\mu^2)\phi_{1,1T_1} + 2\mu^2\alpha\omega\phi_{1,1X_1} = 0 \quad (2.129)$$

$$\begin{aligned} \eta_{2,2} &- 2i\omega(1 - 4\alpha\mu^2)\phi_{2,2} - i\mu^2\omega\eta_{1,1}\phi_{1,1} \\ &- \frac{1}{2}(1 - 2\alpha\mu^2 - \mu^2)\phi_{1,1}^2 = 0 \end{aligned} \quad (2.130)$$

It is apparent that solutions $\eta_{2,0}$ and $\eta_{2,2}$ but not $\eta_{2,1}$ depend on the nonlinear interaction of first order wave components. Substituting the expressions of $\phi_{1,1}$, $\eta_{1,1}$ and $\phi_{2,2}$ into the above equations gives

$$\eta_{2,0} = -\phi_{1,0T_1} - \mathcal{F}_{2,0}(\mu)\frac{|A|^2}{4} \quad (2.131)$$

$$\eta_{2,1} = i\omega(1 - \alpha\mu^2)\phi_{2,1} + \frac{i}{2\omega}A_{T_1} + \frac{\alpha\mu^2}{(1 - \alpha\mu^2)}iA_{X_1} \quad (2.132)$$

$$\eta_{2,2} = \frac{3A^2}{8}\frac{\mathcal{F}_{2,2}(\mu)}{\mu^2} \quad (2.133)$$

where

$$\mathcal{F}_{2,0}(\mu) = \frac{1 - (1 + 2\alpha)\mu^2 + 2\alpha_1\mu^4}{(1 - \alpha_1\mu^2)(1 - \alpha\mu^2)} \quad (2.134)$$

$$\mathcal{F}_{2,2}(\mu) = (1 - 4\alpha\mu^2)\mathcal{G}_{2,2}(\mu) - \frac{\mu^2[1 - (2\alpha + 3)\mu^2 + 2\alpha_1\mu^4]}{3(1 - \alpha_1\mu^2)(1 - \alpha\mu^2)} \quad (2.135)$$

Figure 2.5 shows the comparisons of $\mathcal{F}_{2,0}$ and $\mathcal{F}_{2,2}$ between the present model and the analytical solution of Mei (1989). In shallow water range ($\mu \leq 1$), both results are quite close and approach the same asymptotic values as $\mu \rightarrow 0$. However, in intermediate and deep water where the values of μ increase, discrepancy between two solutions are quite large. For instance, the asymptotic value of $\mathcal{F}_{2,0}$ for the analytical solution is zero as μ approaches infinity. However, the corresponding asymptotic value for the present model is equal to $2/\alpha = -5.13$.

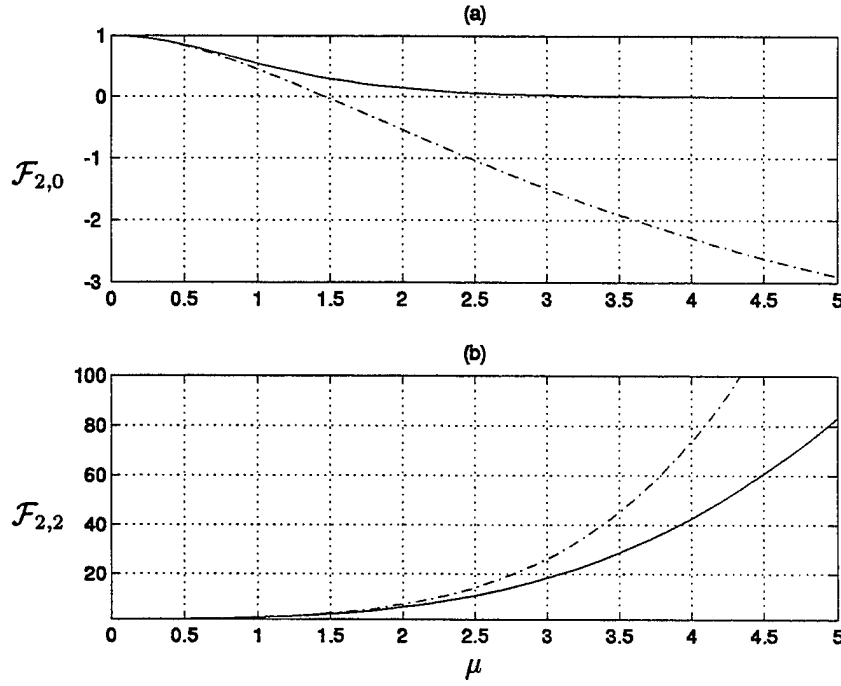


Figure 2.5: Comparisons of nonlinear interaction coefficients $\mathcal{F}_{2,0}$ and $\mathcal{F}_{2,2}$ between the present theory (----) and the analytical solution (—) of Mei (1989).

2.4.3 Solutions for $O(\delta^2)$

To $O(\delta^2)$, equation (2.92) reduces to

$$\begin{aligned} L_1(\phi_3) + L_2(\phi_2) + L_3(\phi_1) + M_1(\eta_1, \phi_2) + M_1(\eta_2, \phi_1) + N_1(\phi_1, \phi_2) \\ + N_1(\phi_2, \phi_1) + M_2(\eta_1, \phi_1) + N_2(\phi_1, \phi_1) + M_3(\eta_1, \phi_1) = 0 \end{aligned} \quad (2.136)$$

The three linear terms in equation (2.136) are evaluated as

$$L_1(\phi_3) = D_3 \phi_{3,3} E^3 + D_2 \phi_{3,2} E^2 + c.c. \quad (2.137)$$

$$L_2(\phi_2) = L_2(\phi_{2,2} E^2) + 2i\omega(1 - \alpha\mu^2)(\phi_{2,1} T_1 + C_g \phi_{2,1} X_1) E + c.c. \quad (2.138)$$

$$\begin{aligned} L_3(\phi_1) = 2i\omega(1 - \alpha\mu^2)(\phi_{1,1} T_2 + C_g \phi_{1,1} X_2 - \frac{i}{2} \omega'' \phi_{1,1} X_1 X_1) E + c.c. \\ - \phi_{1,0} T_1 T_1 + \phi_{1,0} X_1 X_1 + \omega C_g (1 - \alpha\mu^2) \phi_{1,0} Y_1 Y_1 \end{aligned} \quad (2.139)$$

where

$$D_3 = 9\omega^2(1 - 9\alpha\mu^2) - 9(1 - 9\alpha_1\mu^2) = \frac{24\mu^2}{1 - \alpha\mu^2} \quad (2.140)$$

$$\omega'' = \frac{1 + \alpha\mu^2\omega^2 - 3\alpha_1\mu^2}{\omega(1 - \alpha\mu^2)} \quad (2.141)$$

The first and second nonlinear terms in (2.136) become

$$\begin{aligned} & M_1(\eta_1, \phi_2) + M_1(\eta_2, \phi_1) \\ &= (\eta_1\phi_{2x} + \eta_2\phi_{1x})_x + \mu^2(\eta_1\phi_{2xxt} + \eta_2\phi_{1xxt})_t + \mu^2\alpha(\eta_1\phi_{2xxx} + \eta_2\phi_{1xxx})_x \\ &= -(1 - \alpha\mu^2 - \omega^2)(\eta_{2,0}\phi_{1,1} - \eta_{2,1}\phi_{1,-1})E \\ &\quad - 2(1 - 4\alpha\mu^2 - 4\omega^2)\eta_{1,-1}\phi_{2,2}E + T(E^{\pm 3}, E^{\pm 2}, E^{-1}) \end{aligned} \quad (2.142)$$

where $T(E^{\pm 3}, E^{\pm 2}, E^{-1})$ represents terms with $E^{\pm 3}$, $E^{\pm 2}$ and E^{-1} , which are not needed for obtaining the cubic Schrödinger equation. The third and fourth nonlinear terms in (2.136) become

$$\begin{aligned} & N_1(\phi_1, \phi_2) + N_1(\phi_2, \phi_1) \\ &= -(\phi_{1x}\phi_{2x})_t - \mu^2\alpha(\phi_{1x}\phi_{2xxx} + \phi_{2x}\phi_{1xxx})_t - \mu^2(\phi_{1xx}\phi_{2xx})_t \\ &= 2i\omega(1 - 5\alpha\mu^2 + 4\mu^2)\phi_{1,-1}\phi_{2,2}E + T(E^{\pm 3}, E^{\pm 2}, E^{-1}) \end{aligned} \quad (2.143)$$

The last three nonlinear terms in (2.136) become

$$\begin{aligned} M_2(\eta_1, \phi_1) &= i\mu^2\omega(\eta_{1,-1}\phi_{1,1} - \eta_{1,1}\phi_{1,-1})_{T_1} \\ &\quad - i\alpha(1 - \alpha\mu^2)(\eta_{1,-1}\phi_{1,1} - \eta_{1,1}\phi_{1,-1})_{X_1} \\ &\quad + i\eta_{1,1}\phi_{1,0X_1}E + T(E^{\pm 2}, E^{-1}) \end{aligned} \quad (2.144)$$

$$\begin{aligned} N_2(\phi_1, \phi_1) &= -(1 + \mu^2 - 2\alpha\mu^2)(\phi_{1,1}\phi_{1,-1})_{T_1} \\ &\quad - \omega(1 - \alpha\mu^2)\phi_{1,1}\phi_{1,0X_1}E + T(E^{\pm 2}, E^{-1}) \\ M_3(\eta_1, \phi_1) &= -\frac{1}{2}\mu^2(1 - \omega^2)(2\eta_{1,-1}\phi_{1,1} - \eta_{1,1}\phi_{1,-1})\eta_{1,1}E \\ &\quad - 4\mu^2\eta_{1,1}\phi_{1,1}\phi_{1,-1}E + T(E^{\pm 2}, E^{-1}) \end{aligned} \quad (2.145)$$

Substituting all the above terms into equation (2.136) and collecting terms with E , we have

$$\begin{aligned}
& 2i\omega(1 - \alpha\mu^2)(\phi_{2,1T_1} + C_g\phi_{2,1X_1}) \\
& + 2i\omega(1 - \alpha\mu^2)(\phi_{1,1T_2} + C_g\phi_{1,1X_2} - \frac{i}{2}\omega''\phi_{11X_1X_1}) \\
& - 2(1 - 4\alpha\mu^2 - 4\omega^2)\eta_{1,-1}\phi_{2,2} \\
& - (1 - \alpha\mu^2 - \omega^2)(\eta_{2,0}\phi_{1,1} - \eta_{2,2}\phi_{1,-1}) \\
& + 2i\omega(1 + 2\mu^2 - 5\alpha\mu^2)\phi_{1,-1}\phi_{2,2} \\
& - \frac{1}{2}(1 - \omega^2)(2\eta_{1,-1}\phi_{1,1} - \eta_{1,1}\phi_{1,-1})\eta_{1,1} \\
& + 4i\mu^2\omega\eta_{1,1}\phi_{1,1}\phi_{1,-1} \\
& + i\eta_{1,1}\phi_{1,0X_1} - \omega(1 - \alpha\mu^2)\phi_{1,1}\phi_{1,0X_1} = 0
\end{aligned} \tag{2.146}$$

Substituting solution forms of η_1 , η_2 , ϕ_1 and $\phi_{2,2}$, equation (2.146) becomes

$$\begin{aligned}
& A_{T_2} + C_g A_{X_2} - \frac{i}{2}\omega'' A_{X_1X_1} \\
& + \frac{i\omega}{16} \frac{\mathcal{P}_1(\mu)}{\mu^4} |A|^2 A - \mathcal{P}_2(\mu) \frac{i}{2\omega} \phi_{1,0T_1} A + i\phi_{1,0X_1} A = 0
\end{aligned} \tag{2.147}$$

where $\mathcal{P}_1(\mu)$ is the coefficient representing nonlinear interaction between wave components $\eta_{1,m}$, $\eta_{2,m}$, $\phi_{1,m}$, and $\phi_{2,m}$ ($m = -1, 0, 1, 2$), and $\mathcal{P}_2(\mu)$ is related to the nonlinear interaction between a wave component (η_1 , ϕ_1) and a current component ($\phi_{1,0}$). These two coefficients are defined as

$$\begin{aligned}
\mathcal{P}_1(\mu) = & \frac{[3\mathcal{F}_{2,2}(\mu) - 2\mu^2\mathcal{F}_{2,0}(\mu)][1 - (1 + 2\alpha)\mu^2 + (\alpha^2 + \alpha_1)\mu^4] + 8\mu^4 + \mu^6}{(1 - \alpha\mu^2)(1 - \alpha_1\mu^2)} \\
& + \frac{6\mathcal{G}_{2,2}(\mu)[1 - (1 + 5\alpha)\mu^2 + 2(\alpha^2 + \alpha_1)\mu^4]}{1 - \alpha_1\mu^2}
\end{aligned} \tag{2.148}$$

$$\mathcal{P}_2(\mu) = \frac{1 - (1 + 2\alpha)\mu^2 + (\alpha^2 + \alpha_1)\mu^4}{(1 - \alpha\mu^2)^2} \tag{2.149}$$

Now we should obtain the relation between $\phi_{1,0}$ and A so that equation (2.147) has only one unknown A . To do that, we first collect terms with E^0 in equation (2.136), which results in

$$\begin{aligned}
& - \phi_{1,0T_1T_1} + \phi_{1,0X_1X_1} + \omega C_g(1 - \alpha\mu^2)\phi_{1,0Y_1Y_1} \\
& + i(1 - \alpha\mu^2)(\eta_{1,-1}\phi_{1,1} - \eta_{1,1}\phi_{1,-1})_{X_1} + i\mu^2\omega(\eta_{1,-1}\phi_{1,1} - \eta_{1,1}\phi_{1,-1})_{T_1} \\
& - (1 + \mu^2 - 2\alpha\mu^2)(\phi_{1,1}\phi_{1,-1})_{T_1} = 0
\end{aligned} \tag{2.150}$$

Substituting the solution forms of η_1 and ϕ_1 yields

$$\begin{aligned}
\phi_{1,0T_1T_1} & - \phi_{1,0X_1X_1} + \omega C_g(1 - \alpha\mu^2)\phi_{1,0Y_1Y_1} \\
& = \omega^3 \frac{\mathcal{Q}_1(\mu)}{\mu^2} (|A|^2)_{X_1} - \frac{\omega^2}{4} \frac{\mathcal{Q}_2(\mu)}{\mu^2} (|A|^2)_{T_1}
\end{aligned} \tag{2.151}$$

where

$$\mathcal{Q}_1(\mu) = \left(\frac{1 - \alpha\mu^2}{1 - \alpha_1\mu^2} \right)^2, \quad \mathcal{Q}_2(\mu) = \frac{1 - (1 + 2\alpha)\mu^2 + 2\alpha_1\mu^4}{(1 - \alpha_1\mu^2)^2} \tag{2.152}$$

To obtain relation between $\phi_{1,0}$ and A , we assume that $(\)_{Y_1} = 0$, which implies there is no slow variation in the y direction. We also introduce a new set of coordinates as

$$\xi = X_1 - C_g T_1 = \frac{1}{\delta}(X_2 - C_g T_2), \quad \tau = \delta T_1 = T_2 \tag{2.153}$$

which gives

$$(\)_{T_1} = -C_g(\)_{\xi} + O(\delta), \quad (\)_{X_1} = (\)_{\xi} \tag{2.154}$$

$$(\)_{T_2} = (\)_{\tau} - \frac{C_g}{\delta}(\)_{\xi}, \quad (\)_{X_2} = \frac{1}{\delta}(\)_{\xi} \tag{2.155}$$

$$(\)_{T_1T_1} = C_g^2(\)_{\xi\xi} + O(\delta), \quad (\)_{X_1X_1} = (\)_{\xi\xi} \tag{2.156}$$

Then equation (2.151) becomes

$$\phi_{1,0\xi\xi} = \frac{\omega^2 [2\omega\mathcal{Q}_1(\mu) + C_g\mathcal{Q}_2(\mu)]}{4\mu^2(1 - C_g^2)} (|A|^2)_{\xi} + O(\delta) \tag{2.157}$$

which is integrated once with respect to ξ and becomes

$$\phi_{1,0\xi} = S(\tau) - \frac{\omega^2 [2\omega Q_1(\mu) + C_g Q_2(\mu)]}{4\mu^2(1 - C_g^2)} |A|^2 + O(\delta) \quad (2.158)$$

Substituting (2.158) into (2.146) and using new coordinates, we obtain a nonlinear cubic equation with a single variable A as:

$$-iA_\tau - \frac{\omega''}{2} A_{\xi\xi} + \beta |A|^2 A + \gamma A = 0 \quad (2.159)$$

where

$$\beta = \beta_1 + \beta_2 \quad (2.160)$$

$$\beta_1 = \frac{1}{16\omega} \frac{\mathcal{P}_1(\mu)}{\mu^2} \quad (2.161)$$

$$\beta_2 = -\frac{\omega}{8\mu^2} \frac{[2\omega + C_g \mathcal{P}_2(\mu)][2\omega Q_1(\mu) + C_g Q_2(\mu)]}{1 - C_g^2} \quad (2.162)$$

$$\gamma = \frac{S(\tau)}{2\omega} [2\omega + C_g \mathcal{P}_2(\mu)] \quad (2.163)$$

The last term in equation (2.159) can be eliminated by introducing

$$A = B \exp \left(-i \int \gamma d\tau \right) \quad (2.164)$$

which results in the classic nonlinear cubic Schrödinger equation

$$-iB_\tau - \frac{\omega''}{2} B_{\xi\xi} + \beta |B|^2 B = 0 \quad (2.165)$$

Though the form of equation (2.165) is exactly the same as that of Mei (1989), the expressions of ω'' and β are different. The variations of ω'' and β with μ from $\mu = 0$ (shallow water limit) to $\mu = 5$ (very deep water) are shown in Figures 2.6(a) and 2.7(b). The ratios of the present model results to the analytical solutions are also shown in the accompanying plots (b) in the same figures. For small values of μ , both the analytical solutions and the present model results

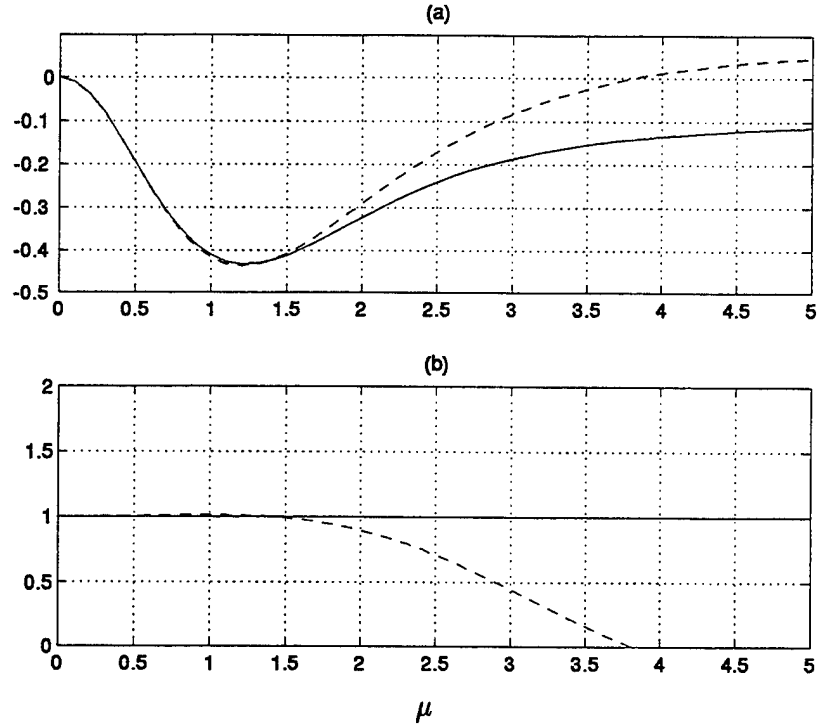


Figure 2.6: Comparisons of ω'' between the analytical solution (—) and present model results (----): (a) actual values; and (b) the ratio of model result to analytical solution.

compare quite well. However, the differences between the two models increase as the water depth becomes deeper.

As demonstrated by Mei (1989) from the derived cubic Schrödinger equation, the sign of the product for ω'' and β is essential to the stability of uniform Stokes waves. From the analytical solutions, the values of ω'' are always negative. However, the value of β changes sign from negative to positive at around $\mu = 1.36$, which is the critical value for the product $\omega''\beta$ to change sign from positive to negative. Therefore, Stokes waves in the range of $\mu \leq 1.36$ are always stable. For the range of $\mu > 1.36$, however, the side-band disturbance of certain frequencies can increase exponentially with time and hence the corresponding Stokes waves are unstable.

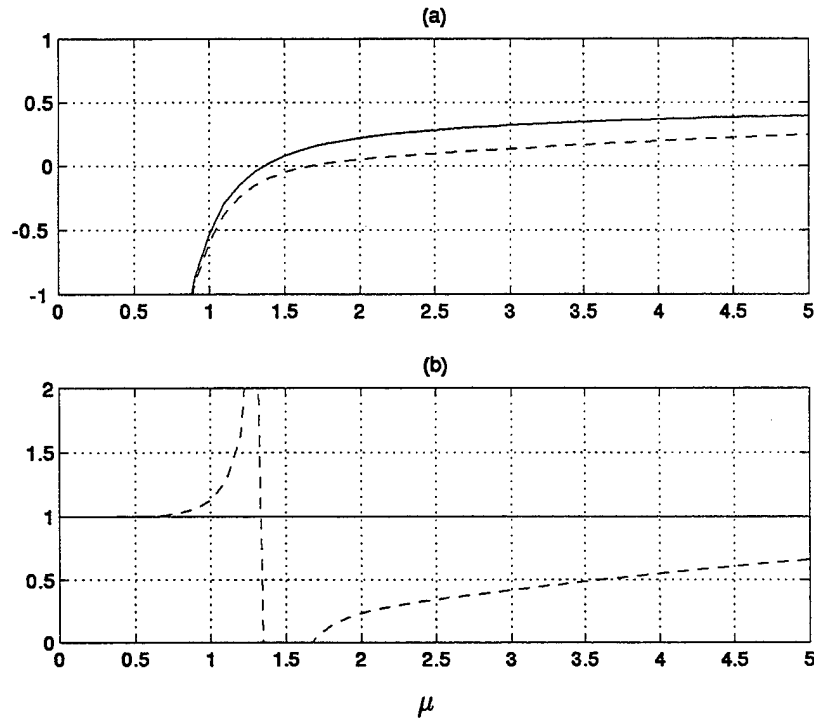


Figure 2.7: Comparisons of β between analytical solution (—) and present model results (---): (a) actual values; and (b) the ratio of model result to analytical solution.

As for the present model, the value of ω'' is negative from $\mu = 0$ to about $\mu = 3.7$ then becomes positive for the rest of water depth. The value of β , on the other hand, change sign from negative to positive around $\mu = 1.57$. Therefore, the values for the product of $\omega''\beta$ are positive in two ranges, one is from $\mu = 0$ to $\mu = 1.57$ and the other is from $\mu = 3.7$ to $\mu = 5$. In the remaining range of $\mu = 1.57$ to $\mu = 3.7$, the product of $\omega''\beta$ is negative. Using the present model, the stability range for Stokes waves will be within $\mu < 1.57$, a reasonable approximation to the analytical value of $\mu = 1.36$. Due to the opposite signs of ω'' for $\mu > 3.7$ between the present model and the exact solution, we should not conclude that Stokes waves are stable in this range.

The value of β is the sum of two parts, i.e., β_1 and β_2 . The first part β_1

is related to the interaction between wave components, while the second part β_2 is related to the interaction of wave and current components. Figures 2.8 and 2.9 show the comparisons of these two coefficients between analytical solutions and the results from the present model. The variation of β_1 from the present model follows the exact solution closely for small value of μ and then start to deviate in the intermediate water depth where $\mu > 2$. The relative error between the present model and the exact solution can be as large as 40%. The variation of β_2 , on the other hand, compares quite well with the exact solution for the whole range of μ . The reason for these different behaviors for β_1 and β_2 comparing with exact solution is not known at the present and should be pursued for future study.

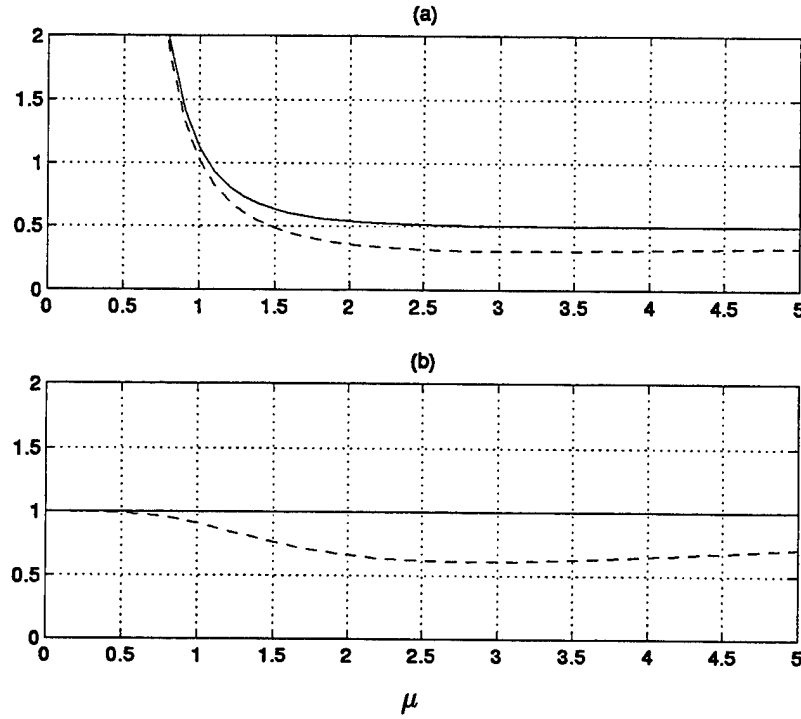


Figure 2.8: Comparisons of β_1 between analytical solution (—) and present model results (---): (a) actual values; and (b) the ratio of model result to analytical solution.

From the above derivation of the cubic Schrödinger equation, it is apparent

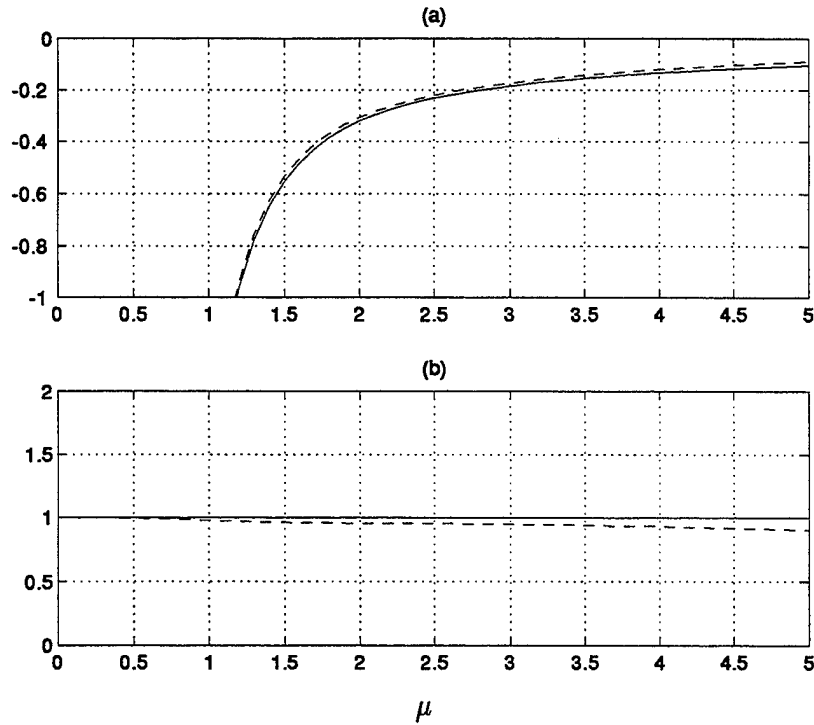


Figure 2.9: Comparisons of β_2 between analytical solution (—) and present model results (---): (a) actual values; and (b) the ratio of model result to analytical solution.

that the nonlinear properties from the fully nonlinear Boussinesq equations do not agree well with the analytical solution in intermediate water depth ($\mu = 2 \sim 5$), despite the fact that the corresponding linear dispersion property has been improved significantly over the same range of μ values. Nevertheless, the present model is still quite accurate for predicting nonlinear properties in shallow water areas. For most cases of wave propagation in coastal regions, large nonlinear interaction usually takes place in surf zones where wave breaking takes place and where the water depth is quite small. The fully nonlinear Boussinesq equations thus are valid for describing the shoaling of weakly nonlinear waves in intermediate water depth and the propagation of strong nonlinear waves in surf zones where wave breaking dominates.

The reason for the poor comparison of nonlinear properties between the present model and the exact solution may be due to the approximation for the velocity field used in the present model, which is only accurate to $O(\mu^2)$. Following a similar approach of using velocity potentials at different depth as dependent variables and keeping terms up to $O(\mu^4)$, Gobbi and Kirby (1996) derived a new set of fully nonlinear Boussinesq equations with fourth order dispersion. The resulting nonlinear properties are better than those of the present model compared with the exact solutions.

Chapter 3

NUMERICAL MODEL

3.1 Introduction

The fully nonlinear Boussinesq equations derived in the previous Chapter are coupled hyperbolic partial differential equations which involve three variables (surface elevation η , horizontal velocities u and v) and derivatives with respect to x , y and t up to third-order. No analytical methods have been developed so far to solve the equations for real coastal engineering applications. Instead, numerical models are developed to obtain the approximate solutions to wave propagation problems. Due to the wide variety of schemes available to discretize the equations, a number of different numerical models have been developed by investigators over the past three decades since digital computers became available for computation.

For the Boussinesq equation system, finite-differencing of the first order derivative terms to second-order accuracy leads to leading order truncation error terms whose forms are mathematically the same as those of dispersive terms appearing in the model equations. These terms are eliminated consistently in the limit as $\Delta x, \Delta y, \Delta t \rightarrow 0$, but usually are large enough in magnitude to interfere with the solution at typical grid resolutions. The characteristics of any Boussinesq models are defined by the accuracy for discretizing the first order terms and by the treatment to the truncation errors. In the following, a brief description for

selected Boussinesq models is given, with emphasis on the discretization methods and the truncation errors.

Peregrine (1967) employed a numerical method to solve the standard Boussinesq equations for simulating wave propagation in 1-D horizontal space. Solitary wave shoaling and reflection over a constant slope were studied by a simple second-order finite difference scheme, which is forward in time and center in space, plus one extra corrector for solving the continuity equation to obtain the surface elevation η . Since truncation errors have the same forms as those of the dispersive terms (third-order derivatives), small time step Δt and small grid size Δx had to be used in order to obtain accurate results. At each time step, a system of tridiagonal element equations were solved to obtain velocity u from the momentum equation. The use of tridiagonal matrix is typical for Boussinesq models since it stabilizes the numerical scheme yet does not affect solution speed.

Abbott *et al.* (1973) developed a more complicated numerical model (the SYSTEM 21) for Boussinesq equations whose momentum variable is, instead of depth-averaged velocity, the mass flux. Since its development, this model has been under constant modifications by McCowan (1978, 1981) and by Abbott *et al.* (1981, 1984). In this approach, the differential equations are discretized by using a time-centered implicit scheme with variables defined on a space-staggered rectangular grid. Though the finite difference scheme used in the model is only second order, the final overall scheme is third-order accurate due to the use of some special techniques, including the back-substitution of truncation errors for some specific terms. The mass flux variables at a new time step are obtained by solving a system of tridiagonal matrix equations, which is similar to that used by Peregrine (1967). The latest version of this model was used by Madsen *et al.* (1991, 1992) to solve the newly derived extended Boussinesq equations whose

linear dispersion property is improved in the intermediate water depth.

Another scheme to solve the standard Boussinesq equations was developed by Rygg (1988). In this method, the governing equations were rearranged so that velocity derivatives with respect to time become two additional variables. A staggered Arakawa-C grid is used for spatial derivatives and a second order predictor-corrector scheme is used for time stepping. The use of an implicit method of solving for the velocity derivatives by tridiagonal matrix is essential for the stability of the scheme. Since only second order schemes are employed to discretize the first order derivative terms, the resulting truncation errors have the same form as the dispersive terms in the equations. In order to obtain meaningful results from the model, small values of grid size and time step must be used.

Mooiman (1990) developed a numerical model for the Boussinesq equations which were derived as canonical equations for an approximate Hamiltonian for water wave motion. The fourth-order Runge-Kutta method is used for time stepping. For spatial derivatives, first order terms are discretized by a fourth order finite difference scheme while second or higher order terms are discretized by a second order finite difference scheme. With the combination of the fourth and second order schemes, the forms of truncation errors will not be the same as those of dispersive terms in the equations. Therefore, there is no need for back-substitution of truncation errors for typical grid resolutions. A system of space-staggered rectangular grids is employed for discretizing spatial derivatives for all variables and the velocity components are obtained by solving tridiagonal matrix equations resulted from the momentum equations.

Nwogu (1993) used an iterative Crank-Nicolson scheme for discretizing the extended weakly-nonlinear Boussinesq equations described in the previous Chapter. The original Crank-Nicolson scheme, which is accurate to second order for

discretizing the first order temporal and spatial derivatives, was used in the predictor stage to obtain the predicting values at the new time step. With these predicting quantities, the estimate of the lowest order truncation errors resulted from the second order scheme are obtained and substituted back into the equations in the corrector stage. The use of back-substitution makes the overall scheme developed by Nwogu (1993) to be accurate to third order.

3.2 Finite Difference Scheme

In this study, we seek to reduce all differencing errors to a size that is small relative to all retained terms in the model equations. We therefore adopt a scheme where the spatial differencing in first order terms is done to fourth-order accuracy, leading to a truncation error of $O(\Delta x^4/\mu^2)$ relative to the model dispersive terms at $O(\mu^2)$. In contrast, the dispersive terms themselves are finite-differenced only to second-order accuracy, leading to errors of $O(\Delta x^2)$ relative to the actual dispersive terms. Finally, the system of equations is written in a form that makes the application of a higher-order time-stepping procedure convenient. We utilize a fourth-order Adams-Bashforth-Moulton (Press *et al.*, 1992) predictor-corrector scheme to perform this updating.

It is convenient to use dimensional variables for the development and the application of the numerical model. Therefore, from now on, all the variables used in the model will have their usual dimensions. In order for the model to be capable of simulating wave propagation for real applications, additional terms are needed for the model equations. These terms account for the generation of waves by source function inside the domain, the energy dissipation due to the use of sponge layers, due to the process of wave breaking, and due to the existence of bottom friction. Each of these additional term will be described in details in

later sections of this Chapter. After adding these terms, the dimensional model equations based on (2.39) and (2.40) are rearranged as

$$\eta_t = E(\eta, u, v) + \gamma E_2(\eta, u, v) + f(x, y, t) \quad (3.1)$$

$$\begin{aligned} [U(u)]_t &= F(\eta, u, v) + [F_1(v)]_t + \gamma[F_2(\eta, u, v) + F^t(\eta, u_t, v_t)] \\ &\quad + F_{br} + F_b + F_{sp} \end{aligned} \quad (3.2)$$

$$\begin{aligned} [V(v)]_t &= G(\eta, u, v) + [G_1(u)]_t + \gamma[G_2(\eta, u, v) + G^t(\eta, u_t, v_t)] \\ &\quad + G_{br} + G_b + G_{sp} \end{aligned} \quad (3.3)$$

where η is the surface elevation, u and v are the horizontal velocities at depth $z = z_\alpha$ in x and y directions, respectively, subscript t denotes partial derivative with respect to time t , γ is a control parameter allowing us to choose the model to be fully nonlinear ($\gamma = 1$) or weakly nonlinear ($\gamma = 0$). The quantities U , V , E , F , F_1 , G and G_1 are functions of η , u , and v and are defined as

$$U = u + h[b_1 h u_{xx} + b_2 (hu)_{xx}] \quad (3.4)$$

$$V = v + h[b_1 h v_{yy} + b_2 (hv)_{yy}] \quad (3.5)$$

$$\begin{aligned} E &= -[(h + \eta)u]_x - [(h + \eta)v]_y \\ &\quad - \left\{ a_1 h^3 (u_{xx} + v_{xy}) + a_2 h^2 [(hu)_{xx} + (hv)_{xy}] \right\}_x \\ &\quad - \left\{ a_1 h^3 (u_{xy} + v_{yy}) + a_2 h^2 [(hu)_{xy} + (hv)_{yy}] \right\}_y \end{aligned} \quad (3.6)$$

$$F = -g\eta_x - (uu_x + vv_y) \quad (3.7)$$

$$G = -g\eta_y - (uv_x + vv_y) \quad (3.8)$$

$$F_1 = -h[b_1 h v_{xy} + b_2 (hv)_{xy}] \quad (3.9)$$

$$G_1 = -h[b_1 h u_{xy} + b_2 (hu)_{xy}] \quad (3.10)$$

The quantities E_2 , F_2 , G_2 , F^t and G^t are high order dispersive terms which are defined as

$$E_2 = - \left\{ \left[a_1 h^2 \eta + \frac{1}{6} \eta (h^2 - \eta^2) \right] (u_{xx} + v_{xy}) \right\}_x$$

$$\begin{aligned}
& - \left\{ \left[a_2 h \eta - \frac{1}{2} \eta (h + \eta) \right] [(hu)_{xx} + (hv)_{xy}] \right\}_x \\
& - \left\{ \left[a_1 h^2 \eta + \frac{1}{6} \eta (h^2 - \eta^2) \right] (u_{xy} + v_{yy}) \right\}_y \\
& - \left\{ \left[a_2 h \eta - \frac{1}{2} \eta (h + \eta) \right] [(hu)_{xy} + (hv)_{yy}] \right\}_y
\end{aligned} \tag{3.11}$$

$$\begin{aligned}
F_2 &= - \left\{ \frac{1}{2} (z_\alpha^2 - \eta^2) [u(u_x + v_y)_x + v(u_x + v_y)_y] \right\}_x \\
& - \left\{ (z_\alpha - \eta) [u[(hu)_x + (hv)_y]_x + v[(hu)_x + (hv)_y]_y] \right\}_x \\
& - \frac{1}{2} \left\{ [(hu)_x + (hv)_y + \eta(u_x + v_y)]^2 \right\}_x
\end{aligned} \tag{3.12}$$

$$\begin{aligned}
G_2 &= - \left\{ \frac{1}{2} (z_\alpha^2 - \eta^2) [u(u_x + v_y)_x + v(u_x + v_y)_y] \right\}_y \\
& - \left\{ (z_\alpha - \eta) [u[(hu)_x + (hv)_y]_x + v[(hu)_x + (hv)_y]_y] \right\}_y \\
& - \frac{1}{2} \left\{ [(hu)_x + (hv)_y + \eta(u_x + v_y)]^2 \right\}_y
\end{aligned} \tag{3.13}$$

$$F^t = \left\{ \frac{1}{2} \eta^2 [(u_t)_x + (v_t)_y] + \eta [[h(u_t)]_x + [h(v_t)]_y] \right\}_x \tag{3.14}$$

$$G^t = \left\{ \frac{1}{2} \eta^2 [(u_t)_x + (v_t)_y] + \eta [[h(u_t)]_x + [h(v_t)]_y] \right\}_y \tag{3.15}$$

The quantity $f(x, y, t)$ is the source function term for generating waves inside the computing domain and will be described in detail in Section 3.4. The quantities F_{br} and G_{br} are terms related to wave breaking in x and y directions, respectively, which will be described in Section 4.2; F_b and G_b are terms due to bottom friction, which are important for the simulation of wave runup and will be described in Section 4.3; F_{sp} and G_{sp} are terms due to the existence of sponge layer, which is used for absorbing boundary conditions and will be described in detail in Section 3.3.2.

The constants a_1, a_2, b_1, b_2 are used here for the convenience of comparing four different model equations for the same numerical scheme. For the fully non-linear Boussinesq equations and extended Boussinesq equations of Nwogu (1993), these constants are defined as:

$$a_1 = \frac{1}{2} \beta^2 - \frac{1}{6}, \quad a_2 = \beta + \frac{1}{2}, \quad b_1 = \frac{1}{2} \beta^2, \quad b_2 = \beta \tag{3.16}$$

where $\beta = z_\alpha/h = -0.531$ is a dimensionless parameter related to the reference water depth z_α at which the horizontal velocity is chosen as a dependent variable. Using the constants defined in (3.16) and setting $\gamma = 1$ in equations (3.2) and (3.3) will result in the fully nonlinear Boussinesq model, while the extended Boussinesq model of Nwogu (1993) can be recovered by setting $\gamma = 0$. In order for the model to be equivalent to the standard Boussinesq model derived by Peregrine (1967), the velocity variables u and v in equations (3.1)-(3.3) must be first replaced by the depth-averaged velocity variables \bar{u} and \bar{v} . Then the corresponding parameters must be defined as:

$$\gamma = 0, \quad a_1 = 0, \quad a_2 = 0, \quad b_1 = \frac{1}{6}, \quad b_2 = -\frac{1}{2} \quad (3.17)$$

Finally, the nonlinear shallow water model can be obtained by using the depth-averaged velocity and by setting

$$\gamma = a_1 = a_2 = b_1 = b_2 = 0 \quad (3.18)$$

3.2.1 Time-differencing

The arrangement of cross-differentiated and nonlinear time derivative terms on the right hand sides of equations (3.2)-(3.3) makes the resulting set of left-hand sides purely tridiagonal. This technique has been employed in all the existing Boussinesq models to stabilize the scheme. The governing equations are finite-differenced on a centered grid in $x = (i-1)\Delta x$, $y = (j-1)\Delta y$, and $t = (n-1)\Delta t$, where i and j are indices for spatial grids in x and y direction and n is the index for time step. Level $(n+1)$ refers to the new time step at which values of η , u and v are to be obtained. Level (n) refers to the present time step at which information is known. Level $(n-1)$ and $(n-2)$ are the past time steps at which all the values of η , u and v are also known. With the known information at the three time levels (n) , $(n-1)$ and $(n-2)$, we obtain the corresponding values

in the new time level $(n + 1)$ by using the third order explicit Adams-Bashforth predictor scheme, which is given by

$$\eta_{i,j}^{n+1} = \eta_{i,j}^n + \frac{\Delta t}{12} [23(E')_{i,j}^n - 16(E')_{i,j}^{n-1} + 5(E')_{i,j}^{n-2}] \quad (3.19)$$

$$\begin{aligned} U_{i,j}^{n+1} = U_{i,j}^n + \frac{\Delta t}{12} [23(F')_{i,j}^n - 16(F')_{i,j}^{n-1} + 5(F')_{i,j}^{n-2}] \\ + \frac{\Delta t}{12} [23(F_{1t})_{i,j}^n - 16(F_{1t})_{i,j}^{n-1} + 5(F_{1t})_{i,j}^{n-2}] \end{aligned} \quad (3.20)$$

$$\begin{aligned} V_{i,j}^{n+1} = V_{i,j}^n + \frac{\Delta t}{12} [23(G')_{i,j}^n - 16(G')_{i,j}^{n-1} + 5(G')_{i,j}^{n-2}] \\ + \frac{\Delta t}{12} [23(G_{1t})_{i,j}^n - 16(G_{1t})_{i,j}^{n-1} + 5(G_{1t})_{i,j}^{n-2}] \end{aligned} \quad (3.21)$$

where

$$E' = E + \gamma E_2 + f(x, y, t) \quad (3.22)$$

$$F' = F + \gamma(F_2 + F^t) + F_{br} + F_b + F_{sp} \quad (3.23)$$

$$G' = G + \gamma(G_2 + G^t) + G_{br} + G_b + G_{sp} \quad (3.24)$$

The reason for separating $(F_1)_t$ and $(G_1)_t$ in the right hand sides of equations (3.20) and (3.21) will be explained shortly. All information on the right hand sides of (3.19)-(3.21) is known from the previous calculations. The values of $\eta_{i,j}^{n+1}$ are straightforward to obtain from the expression. The evaluation of horizontal velocities at the new time level, however, requires simultaneous solution of tridiagonal matrix systems which are linear in the unknowns at level $(n + 1)$. The classic Double Sweep Algorithm is used here to solve horizontal velocities. For any given grid index j in y direction, the unknown values of $u_{i,j}^{n+1}$ ($i = 1, 2, \dots, M$) are obtained through the solution of a tridiagonal matrix. Similarly, $v_{i,j}^{n+1}$ ($j = 1, 2, \dots, N$) could be obtained. The matrices involved are constant in time and may be pre-factored, inverted and stored for use at each time step.

After the predicted values of $\{\eta, u, v\}_{i,j}^{n+1}$ are evaluated, we obtain the corresponding quantities of $F_{i,j}^t$ and $G_{i,j}^t$ at all four time levels $(n + 1)$, (n) , $(n - 1)$,

$(n - 2)$. We only need to compute the corresponding values of the remaining quantities in $\{E', F', G'\}_{i,j}$ at time step $(n + 1)$. Then we apply the fourth-order Adams-Moulton method to compute $\{\eta, u, v\}$ at time level $(n + 1)$:

$$\eta_{i,j}^{n+1} = \eta_{i,j}^n + \frac{\Delta t}{24} [9(E')_{i,j}^{n+1} + 19(E')_{i,j}^n - 5(E')_{i,j}^{n-1} + (E')_{i,j}^{n-2}] \quad (3.25)$$

$$\begin{aligned} U_{i,j}^{n+1} = U_{i,j}^n + \frac{\Delta t}{24} [9(F')_{i,j}^{n+1} + 19(F')_{i,j}^n - 5(F')_{i,j}^{n-1} + (F')_{i,j}^{n-2}] \\ + \frac{\Delta t}{24} [9(F_{1t})_{i,j}^{n+1} + 19(F_{1t})_{i,j}^n - 5(F_{1t})_{i,j}^{n-1} + (F_{1t})_{i,j}^{n-2}] \end{aligned} \quad (3.26)$$

$$\begin{aligned} V_{i,j}^{n+1} = V_{i,j}^n + \frac{\Delta t}{24} [9(G')_{i,j}^{n+1} + 19(G')_{i,j}^n - 5(G')_{i,j}^{n-1} + (G')_{i,j}^{n-2}] \\ + \frac{\Delta t}{24} [9(G_{1t})_{i,j}^{n+1} + 19(G_{1t})_{i,j}^n - 5(G_{1t})_{i,j}^{n-1} + (G_{1t})_{i,j}^{n-2}] \end{aligned} \quad (3.27)$$

From the arrangement of the model equations, we see that there are some time derivative terms on the right hand side (*i.e.* u_t , v_t , F_{1t} and G_{1t}). For convenience, we define the quantity w as

$$w = \{u, v, F_1, G_1\} \quad (3.28)$$

The corresponding time derivative w_t is evaluated from the known values of w at various time steps. For the predictor stage, we have

$$(w_t)_{i,j}^n = \frac{1}{2\Delta t} [3w_{i,j}^n - 4w_{i,j}^{n-1} + w_{i,j}^{n-2}] + O(\Delta t^2) \quad (3.29)$$

$$(w_t)_{i,j}^{n-1} = \frac{1}{2\Delta t} [w_{i,j}^n - w_{i,j}^{n-2}] + O(\Delta t^2) \quad (3.30)$$

$$(w_t)_{i,j}^{n-2} = \frac{-1}{2\Delta t} [3w_{i,j}^{n-2} - 4w_{i,j}^{n-1} + w_{i,j}^n] + O(\Delta t^2) \quad (3.31)$$

For the corrector stage, w_t at four time steps are evaluated according to

$$(w_t)_{i,j}^{n+1} = \frac{1}{6\Delta t} [11w_{i,j}^{n+1} - 18w_{i,j}^n + 9w_{i,j}^{n-1} - 2w_{i,j}^{n-2}] + O(\Delta t^3) \quad (3.32)$$

$$(w_t)_{i,j}^n = \frac{1}{6\Delta t} [2w_{i,j}^{n+1} + 3w_{i,j}^n - 6w_{i,j}^{n-1} + w_{i,j}^{n-2}] + O(\Delta t^3) \quad (3.33)$$

$$(w_t)_{i,j}^{n-1} = \frac{-1}{6\Delta t} [2w_{i,j}^{n-2} + 3w_{i,j}^{n-1} - 6w_{i,j}^n + w_{i,j}^{n+1}] + O(\Delta t^3) \quad (3.34)$$

$$(w_t)_{i,j}^{n-2} = \frac{-1}{6\Delta t} [11w_{i,j}^{n-2} - 18w_{i,j}^{n-1} + 9w_{i,j}^n - 2w_{i,j}^{n+1}] + O(\Delta t^3) \quad (3.35)$$

Although the values of w at three time levels (n) , $(n - 1)$ and $(n - 2)$ for the same corrector stage remain unchanged, the corresponding time derivatives w_t at these time levels are related to the new corrected values of w at the time level $(n + 1)$. Therefore, the quantities F^t and G^t , which contain nonlinear products involving u_t and v_t , have to be updated for all four time steps during each corrector computation. However, that is not the case for quantities F_{1t} and G_{1t} . By substituting (3.29)-(3.31) into (3.20)-(3.21), the predictor scheme for momentum equations reduced to

$$U_{i,j}^{n+1} = U_{i,j}^n + \frac{\Delta t}{12} \left[23(F')_{i,j}^n - 16(F')_{i,j}^{n-1} + 5(F')_{i,j}^{n-2} \right] + 2(F_1)_{i,j}^n - 3(F_1)_{i,j}^{n-1} + (F_1)_{i,j}^{n-2} \quad (3.36)$$

$$V_{i,j}^{n+1} = V_{i,j}^n + \frac{\Delta t}{12} \left[23(G')_{i,j}^n - 16(G')_{i,j}^{n-1} + 5(G')_{i,j}^{n-2} \right] + 2(G_1)_{i,j}^n - 3(G_1)_{i,j}^{n-1} + (G_1)_{i,j}^{n-2} \quad (3.37)$$

By substituting (3.32)-(3.35) into (3.26)-(3.27), the corrector scheme for momentum equations reduce to

$$U_{i,j}^{n+1} = U_{i,j}^n + \frac{\Delta t}{24} \left[9(F')_{i,j}^{n+1} + 19(F')_{i,j}^n - 5(F')_{i,j}^{n-1} + (F')_{i,j}^{n-2} \right] + (F_1)_{i,j}^{n+1} - (F_1)_{i,j}^n \quad (3.38)$$

$$V_{i,j}^{n+1} = V_{i,j}^n + \frac{\Delta t}{24} \left[9(G')_{i,j}^{n+1} + 19(G')_{i,j}^n - 5(G')_{i,j}^{n-1} + (G')_{i,j}^{n-2} \right] + (G_1)_{i,j}^{n+1} - (G_1)_{i,j}^n \quad (3.39)$$

Therefore, it is not necessary to compute time derivatives for quantities F_1 and G_1 . We only need to update the values of F_1 and G_1 at the time level $(n + 1)$ for corrector stage.

3.2.2 Space-differencing

The model equations (3.1)–(3.3) involve first and higher order spatial derivative terms with respect to x and y . To accomplish the goal of eliminating truncation errors which have the same mathematical forms as those of dispersive terms in the equations, a standard five-point difference scheme is used to discretize the first order derivative terms, while a three-point scheme is used for second or higher order derivative terms. Specifically, for any given grid index j ($j = 1, 2, \dots, N$) in y direction, the five-point finite difference scheme in x direction with truncation error of order $O(\Delta x^4)$ is given by

$$(w_x)_{1,j} = \frac{1}{12\Delta x} (-25w_{1,j} + 48w_{2,j} - 36w_{3,j} + 16w_{4,j} - 3w_{5,j}) \quad (3.40)$$

$$(w_x)_{2,j} = \frac{1}{12\Delta x} (-3w_{1,j} - 10w_{2,j} + 18w_{3,j} - 6w_{4,j} + w_{5,j}) \quad (3.41)$$

$$(w_x)_{i,j} = \frac{1}{12\Delta x} [8(w_{i+1,j} - w_{i-1,j}) - (w_{i+2,j} - w_{i-2,j})] \quad (3.42)$$

$(i = 3, 4, \dots, M-2)$

$$(w_x)_{M_1,j} = \frac{1}{12\Delta x} (3w_{M,j} + 10w_{M_1,j} - 18w_{M_2,j} + 6w_{M_3,j} - w_{M_4,j}) \quad (3.43)$$

$$(w_x)_{M,j} = \frac{1}{12\Delta x} (25w_{M,j} - 48w_{M_1,j} + 36w_{M_2,j} - 16w_{M_3,j} + 3w_{M_4,j}) \quad (3.44)$$

where $M_k = M - k$ ($k = 1, 2, 3, 4$). The three-point difference scheme for second order derivatives with truncation error of order $O(\Delta x^2)$ is

$$(w_{xx})_{1,j} = \frac{1}{(\Delta x)^2} (2w_{1,j} - 5w_{2,j} + 4w_{3,j} - w_{4,j}) \quad (3.45)$$

$$(w_{xx})_{i,j} = \frac{1}{(\Delta x)^2} (w_{i+1,j} - 2w_{i,j} + w_{i-1,j}) \quad (3.46)$$

$(i = 2, 3, \dots, M_1)$

$$(w_{xx})_{M,j} = \frac{1}{(\Delta x)^2} (2w_{M,j} - 5w_{M_1,j} + 4w_{M_2,j} - w_{M_3,j}) \quad (3.47)$$

The corresponding finite-difference schemes in y direction are similar to those in x direction and thus are not listed here.

The finite-difference scheme for the mixed derivatives in x and y with truncation error to second order $O(\Delta x^2, \Delta y^2, \Delta x \Delta y)$ is given by

$$(w_{xy})_{1,1} = \frac{1}{4\Delta x \Delta y} [9w_{1,1} + 16w_{2,2} + w_{3,3} - 12(w_{1,2} + w_{2,1}) + 3(w_{1,3} + w_{3,1}) - 4(w_{2,3} + w_{3,2})] \quad (3.48)$$

for corner points, and

$$(w_{xy})_{1,j} = \frac{1}{4\Delta x \Delta y} [-3(w_{1,j+1} - w_{1,j-1}) + 4(w_{2,j+1} - w_{2,j-1}) - (w_{3,j+1} - w_{3,j-1})] \quad (3.49)$$

$$(j = 2, 3, \dots, N-1) \quad (3.50)$$

for boundary points, and

$$(w_{xy})_{i,j} = \frac{1}{4\Delta x \Delta y} (w_{i+1,j+1} + w_{i-1,j-1} - w_{i-1,j+1} - w_{i+1,j-1}) \quad (3.51)$$

$$(i = 2, 3, \dots, M-1; j = 2, 3, \dots, N-1)$$

for interior points. The corresponding expressions for other corner points and boundary points are similar to the above expressions and thus are not listed here.

3.2.3 Linear stability analysis

As described in previous sections, the numerical scheme to discretize the fully nonlinear Boussinesq equations is quite complex. To gain some insight into the model, we apply the method of von Neumann to perform linear stability analysis for the model, for the case of constant water depth and one dimensional flow only.

The linearized version of the fully nonlinear Boussinesq equations or the extended Boussinesq equations of Nwogu are exactly the same. For the case of 1-D flow and constant water depth, these equations are reduced to

$$\eta_t = E = -hu_x - \alpha_1 h^3 u_{xxx} \quad (3.52)$$

$$U_t = F = -g\eta_x \quad (3.53)$$

where

$$U = u + \alpha h^2 u_{xx} \quad (3.54)$$

$$\alpha_1 = \alpha + 1/3 \quad (3.55)$$

Notice that due to the differences in formulation, the stability ranges for the predictor scheme alone and for the corrector scheme alone are not the same. The stability range also varies according to the number of corrector scheme used for each time step. During our model computation, the number of corrector scheme used for each time step is not constant but depended on the iteration error and the chosen criterion. For simplicity, we only perform the stability analysis for the most common case in the model computation, which corresponds to using one predictor and one corrector for each time step. For the predictor scheme, the corresponding expressions for discretizing equations (3.52) and (3.53) are

$$\eta_j^{(n+1)*} = \eta_j^n + \frac{\Delta t}{12} [23E_j^n - 16E_j^{n-1} + 5E_j^{n-2}] \quad (3.56)$$

$$U_j^{(n+1)*} = U_j^n + \frac{\Delta t}{12} [23F_j^n - 16F_j^{n-1} + 5F_j^{n-2}] \quad (3.57)$$

where the superscript $(n+1)*$ is the newly-obtained predictor value, (n) , $(n-1)$, and $(n-2)$ are three time steps at which the values of η and u are known. At any spatial and temporal coordinates ($x = (j-1)\Delta x$ and $t = (n-1)\Delta t$), we can write η and u by their Fourier components as:

$$\eta_j^n = \eta_0 \exp[i(kj\Delta x - \omega n\Delta t)] \quad (3.58)$$

$$u_j^n = u_0 \exp[i(kj\Delta x - \omega n\Delta t)] \quad (3.59)$$

where $i = \sqrt{-1}$ is the unit imaginary number, k and ω are the corresponding wavenumber and angular frequency. From definitions (3.58) and (3.59), we have

$$\begin{aligned} U_j^n &= u_j^n + \alpha h^2 \frac{u_{j+1}^n - 2u_j^n + u_{j-1}^n}{\Delta x^2} \\ &= \left[1 - \frac{4\alpha h^2}{\Delta x^2} \sin^2\left(\frac{k\Delta x}{2}\right) \right] u_j^n \end{aligned} \quad (3.60)$$

$$\begin{aligned} (u_x)_j^n &= \frac{8(u_{j+1}^n - u_{j-1}^n) - (u_{j+2}^n - u_{j-2}^n)}{12\Delta x} \\ &= \frac{i \sin(k\Delta x)}{3\Delta x} [4 - \cos(k\Delta x)] u_j^n \end{aligned} \quad (3.61)$$

$$(\eta_x)_j^n = \frac{i \sin(k\Delta x)}{3\Delta x} [4 - \cos(k\Delta x)] \eta_j^n \quad (3.62)$$

$$\begin{aligned} (u_{xxx})_j^n &= \frac{(u_{j+2}^n - u_{j-2}^n) - 2(u_{j+1}^n - u_{j-1}^n)}{2\Delta x^3} \\ &= -\frac{4i \sin(k\Delta x)}{(\Delta x)^3} \sin^2\left(\frac{k\Delta x}{2}\right) u_j^n \end{aligned} \quad (3.63)$$

Then equations (3.56) and (3.57) become

$$\eta_j^{(n+1)*} = \eta_j^n + 46pu_j^n - 32pu_j^{n-1} + 10pu_j^{n-2} \quad (3.64)$$

$$u_j^{(n+1)*} = u_j^n + 46q\eta_j^n - 32q\eta_j^{n-1} + 10q\eta_j^{n-2} \quad (3.65)$$

where

$$p = -\frac{ih\Delta t}{24\Delta x} \sin(k\Delta x) \left[\frac{4 - \cos(k\Delta x)}{3} - \frac{4\alpha_1 h^2}{\Delta x^2} \sin^2\left(\frac{k\Delta x}{2}\right) \right] \quad (3.66)$$

$$q = -\frac{ig\Delta t}{24\Delta x} \sin(k\Delta x) \left[\frac{4 - \cos(k\Delta x)}{3} \right] r^{-1} \quad (3.67)$$

$$r = 1 - \frac{4\alpha h^2}{\Delta x^2} \sin^2\left(\frac{k\Delta x}{2}\right) \quad (3.68)$$

The corrector scheme for equations (3.52) and (3.53) is

$$\eta_j^{n+1} = \eta_j^n + \frac{\Delta t}{24} [9E_j^{(n+1)*} + 19E_j^n - 5E_j^{n-1} + E_j^{n-2}] \quad (3.69)$$

$$U_j^{n+1} = U_j^n + \frac{\Delta t}{24} [9F_j^{(n+1)*} + 19F_j^n - 5F_j^{n-1} + F_j^{n-2}] \quad (3.70)$$

where the superscript $(n + 1)$ refers to the newly-obtained corrector value, and $(n + 1)^*$ is the predictor or the previous corrector value. Employing the same definitions as those in the predictor stage, *i.e.*, expressions (3.58)-(3.59) and (3.66)-(3.68), then equations (3.69) and (3.70) become

$$\eta_j^{n+1} = \eta_j^n + 9pu_j^{(n+1)*} + 19pu_j^n - 5pu_j^{n-1} + pu_j^{n-2} \quad (3.71)$$

$$u_j^{n+1} = u_j^n + 9q\eta_j^{(n+1)*} + 19q\eta_j^n - 5q\eta_j^{n-1} + q\eta_j^{n-2} \quad (3.72)$$

Since only one corrector stage for each time step is considered here, the corresponding scheme is equivalent to the direct substitution of $\{u, \eta\}^{(n+1)*}$ from (3.64) and (3.65) into equations (3.71) and (3.72), which results in

$$\eta_j^{n+1} = r_1\eta_j^n + r_2\eta_j^{n-1} + r_3\eta_j^{n-2} + 28pu_j^n - 5pu_j^{n-1} + pu_j^{n-2} \quad (3.73)$$

$$u_j^{n+1} = r_1u_j^n + r_2u_j^{n-1} + r_3u_j^{n-2} + 28q\eta_j^n - 5q\eta_j^{n-1} + q\eta_j^{n-2} \quad (3.74)$$

where

$$r_1 = 1 + 414pq, \quad r_2 = -288pq, \quad r_3 = 90pq \quad (3.75)$$

We follow the method employed by Twizell (1984) to determine the stability range for the multiple time step scheme. First, equations (3.73) and (3.74) are combined into a single matrix equation as

$$Z^{n+1} = AZ^n \quad (3.76)$$

where Z^{n+1} and Z^n are six element vectors which are defined as

$$Z^{n+1} = \{\eta_j^{n+1}, u_j^{n+1}, \eta_j^n, u_j^n, \eta_j^{n-1}, u_j^{n-1}\}^T \quad (3.77)$$

$$Z^n = \{\eta_j^n, u_j^n, \eta_j^{n-1}, u_j^{n-1}, \eta_j^{n-2}, u_j^{n-2}\}^T \quad (3.78)$$

and A is the amplification matrix which is defined as

$$A = \begin{pmatrix} r_1 & 28p & r_2 & -5p & r_3 & p \\ 28q & r_1 & -5q & r_2 & q & r_3 \\ 1 & 0 & 0 & 0 & 0 & 0 \\ 0 & 1 & 0 & 0 & 0 & 0 \\ 0 & 0 & 1 & 0 & 0 & 0 \\ 0 & 0 & 0 & 1 & 0 & 0 \end{pmatrix} \quad (3.79)$$

With the definition of A , we then can determine the stability range by the condition that the magnitudes of all the six eigenvalues of A should not be greater than 1. For any given values of p and q , matrix A has six eigenvalues λ_k ($k = 1, 2, 3, 4, 5, 6$). These eigenvalues are a function of the ratio of water depth to grid size $h/\Delta x$, the Courant number $C_r = \sqrt{gh}\Delta t/\Delta x$ and the dimensionless wavenumber $k\Delta x$. The numerical scheme is stable only if the moduli of all eigenvalues $|\lambda_k|$ are not greater than one. Instead of finding the analytical expression, it is more convenient to obtain the stability range numerically. Figure 3.1 shows the variations of $|\lambda_k|$ for $h/\Delta x = 1$, $C_r = (0, 2)$ and $k\Delta x = (0, \pi)$. From Figure 3.1, it is apparent that only the first two of the six eigenvalue moduli $|\lambda_1|$ and $|\lambda_2|$ can exceed one for certain values of $h/\Delta x$, C_r and $k\Delta x$. These two eigenvalues are complex conjugate and therefore their moduli are exactly the same. In the following, it is sufficient to study the variation of $|\lambda_1|$ for different values of $h/\Delta x$, C_r and $k\Delta x$ in greater detail.

To be more accurate in accessing the stability range, we choose five cross sections corresponding to $k\Delta x = k\pi/10$ ($k = 1, 2, 3, 4, 5$) from Figure 3.1(a) to make a 2-D plot which is shown in Figure 3.2(a). For fixed values of $h/\Delta x$ and C_r , it is apparent from Figure 3.1(a) and Figure 3.2(a) that $|\lambda_1|$ reaches its maximum value when $k\Delta x = \pi/2$ (the kink solid line in 3.2(a)). Therefore, the numerical scheme will be stable for other $k\Delta x$ values if $|\lambda_1| \leq 1$ at $k\Delta x = \pi/2$. Figure 3.2(b)

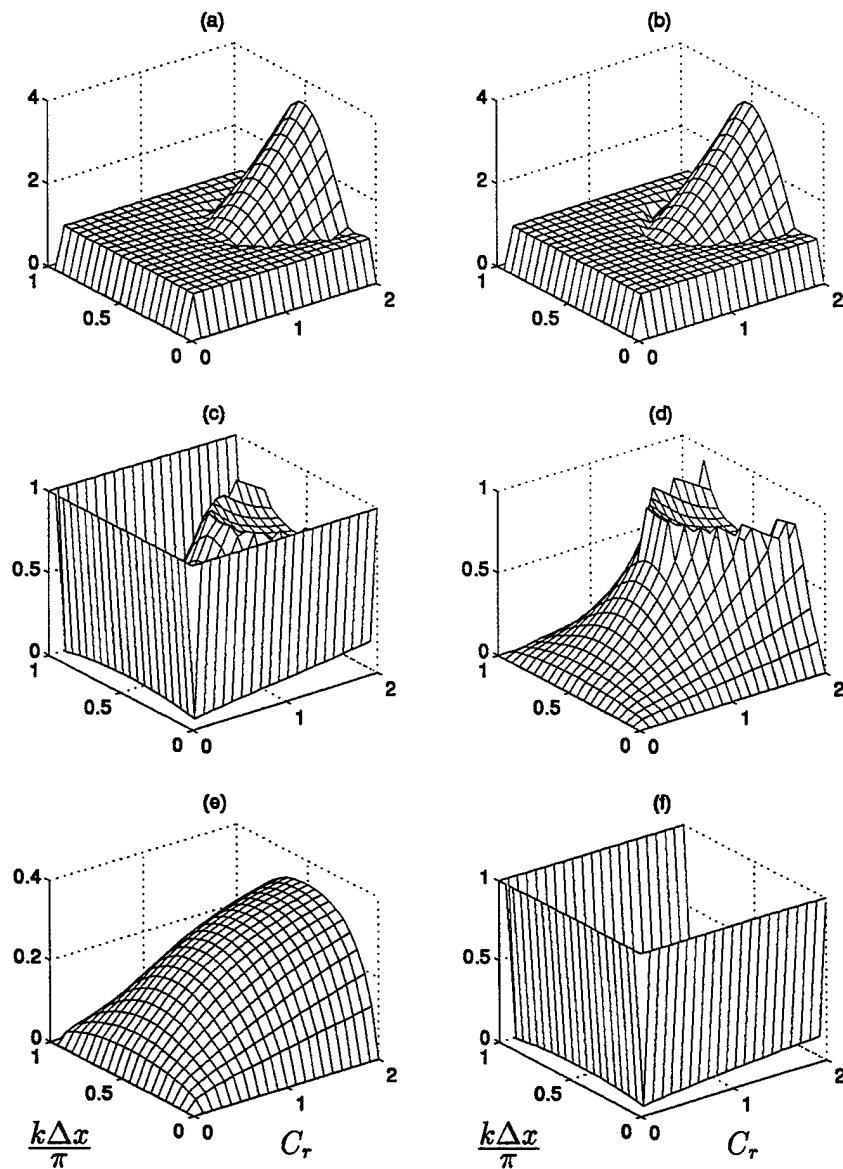


Figure 3.1: Variations of six eigenvalue moduli μ_k ($k = 1, 2, 3, 4, 5, 6$) with Courant number C_r and dimensionless wavenumber $k\Delta x$ for a fixed value of $h/\Delta x = 1$.

shows the variation of $|\lambda_1|$ with Courant number C_r for a fixed value of $k\Delta x = \pi/2$ and for several values of $h/\Delta x = 0.1, 1, 2, 5, 10$. From Figure 3.2(b), it seems that the stability range of the scheme is proportional to the value of $h/\Delta x$. However, further evaluation showed that the variation of $|\lambda_1|$ with C_r for $h/\Delta x = 0.01$ was quite close to that for $h/\Delta x = 0.1$. Therefore, we conclude that the scheme of using one predictor and one corrector is stable if $C_r \leq 0.8$, regardless the values of $k\Delta x$ and $h/\Delta x$.

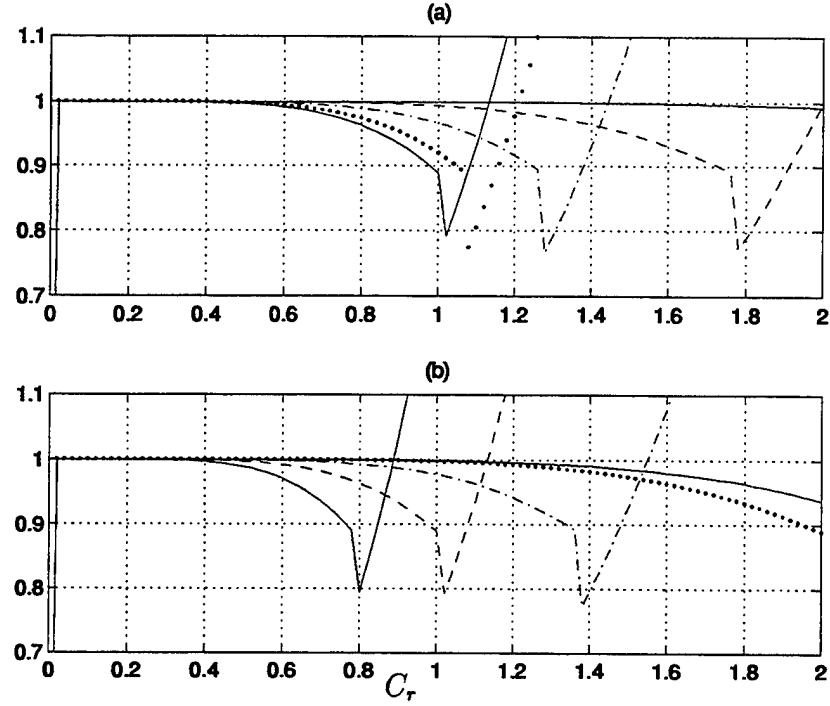


Figure 3.2: Variation of eigenvalue modules $|\mu_1|$ with Courant number C_r . In (a), $h/\Delta x = 1$ and $k\Delta x = \pi/10$ (smooth —), $\pi/5$ (----), $3\pi/10$ (-...), $2\pi/5$ (....), $\pi/2$ (kink —). In (b), $k\Delta x = \pi/2$ and $h/\Delta x = 0.1$ (kink —), 1 (----), 2 (-...), 5 (....), 10 (smooth —).

In real model applications where nonlinear effects are not negligible, the stability criterion evaluated above is not guaranteed to be accurate. Nevertheless,

it provides an estimation for the stability range for the numerical scheme.

3.2.4 Convergence

Linear stability analysis in the previous section shows that the numerical scheme for using one predictor and one corrector at each time step is stable if Courant number $C_r \leq 0.8$. In the real computation, however, the corresponding corrector formula is used several times until the iteration error between two successive results reaches a required limit. There are many methods to evaluate the error and we employed a combination of both absolute and relative errors for the model.

Denoting f to be any one of the dependent variables, *i.e.*, $f = \{\eta, u, v\}$, then the relative error Δf between two successive iterations is given by

$$\Delta f = \frac{\sum_{i=1, j=1}^{i=M, j=N} |f_{i,j}^{n+1} - f_{i,j}^*|}{\sum_{i=1, j=1}^{i=M, j=N} |f_{i,j}^{n+1}|} \quad (3.80)$$

f^{n+1} and f^* denote the current and previous iteration results, respectively. The corrector step is iterated if any of the Δf 's exceeds 10^{-3} (or 10^{-4} for cases of high nonlinearity). For the case of cold start or other situations where a zero denominator will result, absolute error (the numerator in the above expression) is used instead of relative error.

For weakly nonlinear case, the scheme typically requires no iteration unless problems arise from boundaries, or inappropriate values for Δx , Δy or Δt are used. For strong nonlinear case, however, more iterations are required for the model to converge. Further analysis showed that the iterated results oscillated around the desired solution. To increase the convergence rate, we applied an relaxation

technique to the iteration stage. Writing the previous and current iterated values as $f_{i,j}^*$ and $f_{i,j}$, then the adjusted value $f_{i,j}^r$ for relaxation is given by

$$f_{i,j}^r = (1 - R)f_{i,j} + Rf_{i,j}^* \quad (3.81)$$

where R is the relaxation coefficient which is in the range of $(0, 1)$. The adjusted value $f_{i,j}^r$ always lies in between $f_{i,j}^*$ and $f_{i,j}$. In all the model computations, we used the value of $R = 0.2$ which gives quite satisfactory results.

3.3 Boundary Conditions

Boundary conditions are vital for the numerical models to carry out the computation. No matter how valid are the model equations and how accurate are the finite difference scheme to discretize the equation terms, the model will not provide reasonable results if inappropriate boundary conditions are used. The three most commonly used boundary conditions are wave reflecting, wave absorbing and wave generating. A typical computational domain is shown in Figure 3.3, where waves travel into the domain from the left boundary at $x = 0$ ($i = 1$) and then propagate out of the domain from the right boundary at $x = x_L$ ($i = M$). The left and right boundaries are therefore referred to as wave generating (incident) condition and wave absorbing (radiation) condition, respectively. The top and bottom boundaries located at $y = 0$ ($j = 1$) and $y = y_L$ ($j = N$) are vertical walls which fully reflect waves back into the domain and are referred to as wave reflecting condition. In the following, these boundary conditions will be examined in more details.

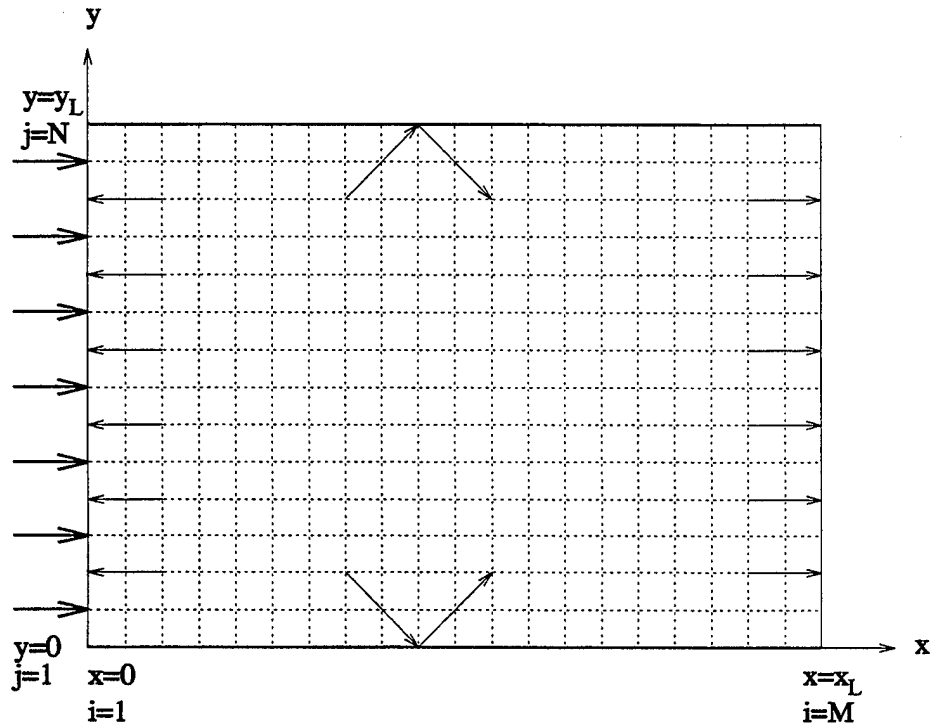


Figure 3.3: Definition sketch of typical boundary conditions.

3.3.1 Reflecting boundary

This case corresponds to a vertical wall placed in a wave field. Based on physical grounds, the horizontal velocity at the direction normal to the wall should be zero everywhere at the wall from the bottom to the water surface. However, this condition can not be satisfied by any Boussinesq models which assume a quadratic variation of horizontal velocity with water depth. Instead, we derive the corresponding boundary condition based on the principle that the water volume flux across the vertical wall is zero. For convenience, the continuity equation of the Boussinesq model is rewritten here

$$\eta_t + \nabla \cdot \mathbf{M} = 0 \quad (3.82)$$

where η is the surface elevation, \mathbf{M} is the horizontal volume flux vector. For the weakly nonlinear case, we have

$$\mathbf{M} = (h + \delta\eta)\mathbf{u} + \mu^2 a_1 h^3 \nabla(\nabla \cdot \mathbf{u}) + \mu^2 a_2 h^2 \nabla[\nabla \cdot (h\mathbf{u})] \quad (3.83)$$

where $\mathbf{u} = (u, v)$ is the horizontal velocity vector.

Assume Ω to be the fluid domain and $\partial\Omega$ the boundary. Integrating equation (3.82) over Ω results in

$$\frac{dV}{dt} = - \int_{\partial\Omega} \mathbf{M} \cdot \mathbf{n} dS \quad (3.84)$$

where \mathbf{n} is the outward normal vector for the reflecting boundary, dS is an element of length along $\partial\Omega$, and V is the total excess volume of water in the domain. Assume dA to be an element of area, then we have

$$V = \int_{\Omega} \eta dA \quad (3.85)$$

If the domain is completely enclosed by impermeable walls, we require that the rate of change of the excess volume be zero. This requirement is then satisfied by the condition

$$\mathbf{M} \cdot \mathbf{n} = 0; \quad \mathbf{x} \in \partial\Omega \quad (3.86)$$

which is the corresponding reflecting boundary condition for Boussinesq models. For Boussinesq models using the depth-averaged velocity $\bar{\mathbf{u}}$ as a dependent variable, condition (3.86) can be simplified as

$$\bar{\mathbf{u}} \cdot \mathbf{n} = 0; \quad \mathbf{x} \in \partial\Omega \quad (3.87)$$

Unfortunately, the velocity $\mathbf{u} = (u, v)$ in the present model equations is not simply related to \mathbf{M} and thus condition (3.87) is apparently not a complete statement. Consider, for instance, the case of a wall parallel to the x axis and located at

$y = y_L$, as shown in Figure 3.3. The water depth h is assumed to be constant in the neighborhood of the wall. Then condition (3.86) is equivalent to

$$M_y = (h + \delta\eta)v + \mu^2 h^3 \left(\alpha + \frac{1}{3}\right) [u_{xy} + v_{yy}] = 0 \quad (3.88)$$

where M_y is the y component of \mathbf{M} ($\mathbf{M} = M_x \mathbf{i} + M_y \mathbf{j}$). It is apparent that setting $v = 0$ only covers a portion of the condition in (3.88). However, if we consider the leading order terms in the mass conservation equation, we have

$$\eta_t + hu_x + hv_y = O(\delta, \mu^2) \quad (3.89)$$

This may be differentiated with respect to y to obtain

$$(\eta_y)_t + h[u_{xy} + v_{yy}] = O(\delta, \mu^2) \quad (3.90)$$

Substituting equation (3.90) into equation (3.88) yields

$$(h + \delta\eta)v - \mu^2 h^2 \left(\alpha + \frac{1}{3}\right) (\eta_y)_t = O(\delta\mu^2, \mu^4) \quad (3.91)$$

Therefore, to the accuracy of the weakly nonlinear Boussinesq models, the overall boundary condition (3.88) is satisfied by additionally imposing $\eta_y = 0$, which can be generalized as

$$\nabla\eta \cdot \mathbf{n} = 0; \quad \mathbf{x} \in \partial\Omega \quad (3.92)$$

Condition (3.92) is consistent with the usual physical notion of total reflection at a vertical barrier. For fully nonlinear Boussinesq models, we still use the same combined boundary conditions (3.87) and (3.92) for reflecting walls. Notice that these conditions are not accurate to the order of approximation for the fully nonlinear model equations.

For the velocity component u_T tangent to the boundary, we require

$$\frac{\partial u_T}{\partial n} = 0; \quad \mathbf{x} \in \partial\Omega \quad (3.93)$$

This last condition essentially imposes a free-slip condition for the flow along the bounding wall, which is not inconsistent with the inviscid flow being considered. This last condition would not seem to be required by the kinematic constraints on the system, but it has been used repeatedly in the literature (Rygg, 1988), and we have not been able to stabilize the computational scheme without imposing it.

In summary, for the case of a vertical wall parallel to x axis and located at $y = y_L$ as shown in Figure 3.3, the boundary conditions used in the model are

$$v = 0; \quad \eta_y = 0; \quad u_y = 0; \quad y = y_L \quad (3.94)$$

Then the corresponding finite difference schemes are

$$v_{i,N} = 0 \quad (3.95)$$

$$u_{i,N} = \frac{1}{25}(48u_{i,N_1} - 36u_{i,N_2} + 16u_{i,N_3} - 3u_{i,N_4}) \quad (3.96)$$

$$\eta_{i,N} = \frac{1}{25}(48\eta_{i,N_1} - 36\eta_{i,N_2} + 16\eta_{i,N_3} - 3\eta_{i,N_4}) \quad (3.97)$$

$$(i = 1, 2, \dots, M)$$

where $N_k = N - k$ ($k = 1, 2, 3, 4$). Similar expressions can be obtained for walls at other locations.

3.3.2 Absorbing boundary

The second commonly used boundary condition is referred to as radiating or open boundary, where all wave energy arriving from within the computing domain should be absorbed completely without reflection back to the domain. Treatment of this boundary is a problem of major interest in the modeling community, and we utilize some fairly well established techniques for the case considered here.

A perfect radiation boundary should not allow any wave reflection back to the domain. For the case where the wave phase speed C and the propagation direction θ at the boundary $x = x_L$ are known, the radiation condition at is

$$\eta_t + C \cos(\theta) \eta_x = 0 \quad (3.98)$$

The above equation is equivalent to the radiation condition derived by Sommerfeld (1949) from the potential flow theory. However, since the present model is essentially dispersive, there exists no single phase speed C which fully characterizes the system. Further, in two-dimensional applications, the wave direction θ is generally not known *a priori*. To treat the first problem, the phase speed C is usually specified by the long wave limit, *i.e.*, $C = \sqrt{gh}$. However, there exist potential problems for offshore boundary where water depth is close or less than zero, resulting in small or imaginary phase speeds.

To solve the second problem of wave direction at the boundary, Engquist and Majda (1977) derived an approximate radiation boundary condition based on parabolic approximation. Assuming the principle propagation direction of waves at the boundary is close to the x -axis, the approximate radiation boundary condition is

$$\eta_{tt} + C \eta_{xt} - \frac{C^2}{2} \eta_{yy} = 0 \quad (3.99)$$

which corresponds to the imposition of a parabolic approximation on equation (3.98).

The above approximate radiation condition inevitably introduces wave reflection along the boundaries and can eventually cause the blowup of the model. To eliminate the problem of wave reflection, Israeli and Orszag (1981) proposed the concept of sponge layer in the region near radiation boundary. Basically, energy dissipation terms are added into the momentum equations so that wave amplitudes are reduced significantly at the radiation boundary. These energy

dissipation terms corresponding to sponge layer in equations (3.2) and (3.3) are defined as

$$F_{sp} = -w_1(x, y)u + (w_2(x, y)u_x)_x + (w_2(x, y)u_y)_y + w_3(x, y)\sqrt{\frac{g}{h}}\eta \quad (3.100)$$

$$G_{sp} = -w_1(x, y)v + (w_2(x, y)v_x)_x + (w_2(x, y)v_y)_y + w_3(x, y)\sqrt{\frac{g}{h}}\eta \quad (3.101)$$

where $w_i(x, y)$ ($i = 1, 2, 3$) are spatial functions which specify the magnitude of dissipation effect by sponge layers in the domain. The first terms on right hand sides of equations (3.100) and (3.101) are equivalent to linear friction, which are referred to as “Newtonian cooling” by Israeli and Orszag (1981). The second terms are analogous to linear viscous terms in Navier-Stokes equations and are referred to as “viscous terms”. The third terms are combined linear friction with radiation, which are referred to as “sponge filter”. Israeli and Orszag (1981) demonstrated by examples that sponge filter is the best among the three dissipation terms for open boundary conditions. However, from our numerical experiments, we found that applying “Newtonian cooling” alone is sufficient to absorb wave energy for radiation boundary.

There are no preferred forms for the sponge layer function $w_i(x, y)$ ($i = 1, 2, 3$). In the area where there is no need for energy dissipation, the values of $w_i(x, y)$ are set to zero. In the area close to the radiation boundary where energy dissipation is needed, nonzero values of $w_i(x, y)$ should be specified. To eliminate possible reflection from the sponge layer, the value of $w_i(x, y)$ should increase gradually from the domain to the boundary. Assume that there is only one sponge layer located on the right end of the domain (*i.e.* from $x = x_S$ to $x = x_L$) and the sponge layer function $w_i(x, y)$ is only a function of x

$$w_i(x, y) = c_i f(x) \quad (3.102)$$

where c_i ($i = 1, 2, 3$) are constant coefficients corresponding to the three terms in (3.100) and (3.101), and $f(x)$ is a smooth monotonically increasing function

varying from 0 to 1 when x varies from x_S to x_L . The values of c_i are determined by the specific problem. The definition of function $f(x)$ is usually given by given by

$$f(x) = \begin{cases} \frac{\exp[(x_P)^N - 1]}{\exp(1) - 1} & x_S < x < x_L \\ 0 & 0 < x < x_S \end{cases} \quad (3.103)$$

where x_P is the transferring coordinate which is defined by

$$x_P = \frac{x - x_S}{x_L - x_S} \quad (3.104)$$

Though the value of N can be arbitrary (1, 2, 3, ...), we choose $N = 2$ in the model for all the computations. The width of the sponge layer (*i.e.* $x_L - x_S$) is usually taken to be two or three times of the dominant wave length. Similar expressions can be obtained for sponge layers on three other ends of the domain. The final representation of functions $w_i(x, y)$ ($i = 1, 2, 3$) are the summation of all sponge layers.

3.3.3 Generating boundary

In most model applications, the incident wave conditions are given. For a regular wave, these conditions include the wave height and the wave period. For a random wave train, the corresponding time series of surface elevation or the power spectrum at the incident boundary are known. With this information, it is possible to generate the desired wave by specifying surface elevation η , horizontal velocity components u and v at the incident boundary if the effects of nonlinearity and reflection are negligible.

For the propagation of monochromatic waves in one dimensional flow, Nwogu (1993) used the linearized relation derived from the extended Boussinesq

equations to compute horizontal velocity at the generating boundary $u_I(x=0, t)$ from the given surface elevation $\eta_I(x=0, t)$, which is given by

$$u_I = \frac{\omega}{kh_0[1 - (\alpha + 1/3)(kh_0)^2]} \eta_I \quad (3.105)$$

where k is the wavenumber and h_0 is the water depth. For the simulation of a random wave train, condition (3.105) is applied to each of the Fourier components to obtain the corresponding velocity. The corresponding time series of u_I is then obtained by the method of linear superposition.

In many practical applications, the effect of wave reflection from the domain back to the incident boundary is not negligible. One commonly used method to account for these reflecting waves is to apply radiation boundary (3.98) with negative phase speed in the incident boundary. Denote η_I to be the incident wave propagating in positive x direction and η_R the reflected wave traveling in opposite direction. Assume that the magnitude of the phase speed for these two waves is the same and is denoted by C , then from radiation condition (3.98) we have

$$(\eta_I)_t + C(\eta_I)_x = 0 \quad (3.106)$$

$$(\eta_R)_t - C(\eta_R)_x = 0 \quad (3.107)$$

The actual surface elevation is related to the incident wave and the reflected wave by

$$\eta = \eta_I - \eta_R \quad (3.108)$$

Combining equations (3.106), (3.107) and (3.108), we obtain the following boundary condition for the incident boundary with strong wave reflection

$$\eta_t - C\eta_x - 2(\eta_I)_t = 0 \quad (3.109)$$

This is exactly the same as that used by Nwogu (1993) in his model. As stated in previous section, however, the phase speed C for the reflecting wave is generally not known *a priori*. In order to apply condition (3.109), approximate phase

speed C has to be used. The inaccurate evaluation of phase speed will inevitably generate non-existing waves around the boundary. Not only do these waves affect the accuracy of the computing wave field but may also cause the blowup of the model. For two dimensional case, the problem becomes more severe due to the directions of reflecting waves are also unknown.

3.4 Wave Generation Inside the Domain

Comparing to radiation condition (3.98), the sponge layer works quite well for dissipating the energy of radiating waves. However, simply adding a sponge layer at incident wave boundary will also dissipate the incident wave energy. The possible solution for using sponge layers to dissipate radiating waves only is to generate waves inside the computational domain, instead of on the boundary. Such an approach has been documented previously by Larsen and Dancy (1983) who used a somewhat ad-hoc source mechanism where water mass is added and subtracted along a straight source/sink line inside the computing domain. Sponge layers are placed in the ends of the domain to effectively dissipate the wave energy of outgoing waves with arbitrary frequencies and propagating directions.

3.4.1 Theory

The problem we are solving is an initial boundary value problem. It would be desirable to develop the corresponding boundary conditions for Boussinesq models which can provide a combination of wave generation, wave absorption, and wave reflection effects. However, the problem of providing a well-posed boundary value problem for these equations is essentially unsolved. In particular, providing absorbing conditions which will work for the entire range of modeled frequencies

is complicated, due to the wide range of phase speed variation (in both amplitude and direction) at the boundary.

In recognition of the difficulties imposed by this approach to model operation, we follow the lead of a number of previous Boussinesq model developers and, instead, generate waves using an internal source mechanism. Larsen and Dancy (1983) proposed a method based on the balance of mass flux to add and subtract water along a straight line inside the computing domain. This approach was demonstrated to work well in a staggered-grid differencing scheme, where water is essentially being added to or drained from a single grid block. In applying this technique to the Boussinesq model on an unstaggered grid, however, we found that use of a single source line caused high frequency noise, leading to the blowup of the model. Therefore, we use, instead, a spatially distributed mass source $f(x, y, t)$ added to the mass conservation equation (3.1). The exact expression of $f(x, y, t)$, which will be shown below, is determined by the characteristics of the waves to be generated.

Assume that in a domain with constant water depth of h , we want to generate a plane wave with amplitude a_0 , wavenumber k , and angular frequency ω . The angle between the propagation direction of the wave and x -axis is θ , as shown in Figure 3.4. Without losing generality, we assume the center line of the source region is parallel to y -axis. Then the source term in equation (3.1) is defined as

$$f(x, y, t) = D \exp[-\beta(x - x_s)^2] \sin(\lambda y - \omega t) \quad (3.110)$$

where β is the shape coefficient for the source function, x_s is the central location of the source, D is the magnitude of the source function, and $\lambda = k \sin(\theta)$ the wavenumber of the plane wave in y direction.

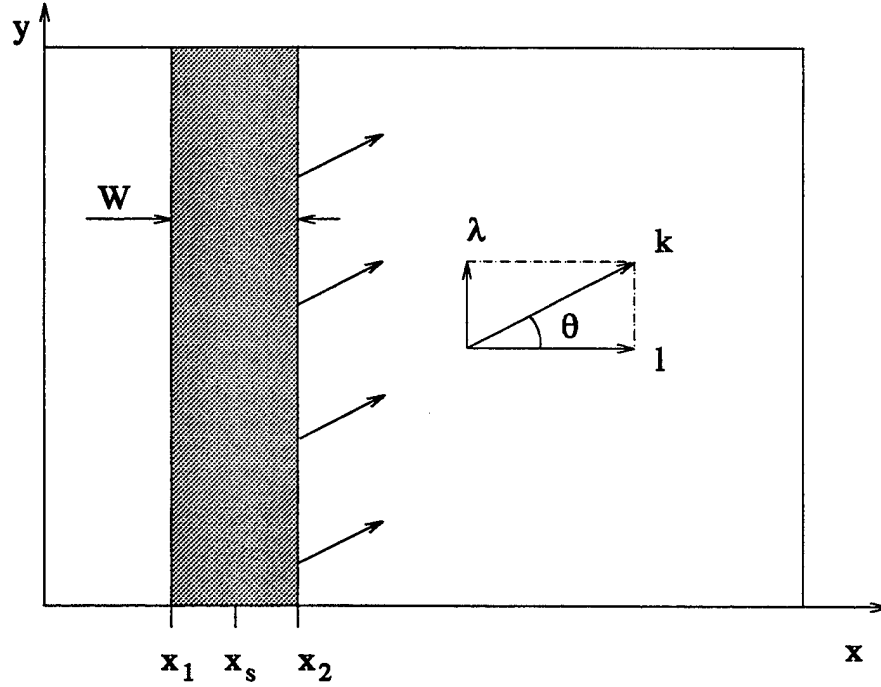


Figure 3.4: Source function definition in the computing domain.

By eliminating nonlinear terms in equations (3.1)-(3.3), the analytical solution for $f(x, y, t)$ can be determined with Green's function. A detailed derivation is included in Appendix B and in Wei and Kirby (1997). Here only we only show the the final results of derivation. The magnitude D of source function is given by

$$D = \frac{2a_0 \cos(\theta)(\omega^2 - \alpha_1 g k^4 h^3)}{\omega^2 k I [1 - \alpha(kh)^2]} \quad (3.111)$$

where h , a_0 , k and ω have been defined above, g is the gravitational acceleration, $\alpha = -0.390$ is the optimized value for the best linear dispersion relation, $\alpha_1 = \alpha + 1/3$, and I is an integral constant which is defined as:

$$I = \int_{-\infty}^{\infty} \exp(-\beta x^2) \exp(-ilx) dx = \sqrt{\frac{\pi}{\beta}} \exp(-l^2/4\beta) \quad (3.112)$$

where $l = k \cos(\theta)$ is the wavenumber in x direction.

In theory, the shape coefficient β can be any number. Large β value is generally preferred since the corresponding source region is narrower. However, the model with a too narrow source region may be inaccurate a poor finite difference representation of the source function. By trial and error, it was found that good results were obtained when the width of the source function W equals to about half of the wavelength L , *i.e.*

$$W = \delta \frac{L}{2} \quad (3.113)$$

where δ is a constant of order $O(1)$. The width of source function W is defined as the distance between two coordinates x_1 and x_2 where the corresponding height of the source function is equal to $\exp(-5) = 0.0067$ times of the maximum height D . Therefore, the values of x_1 and x_2 are the roots which satisfy the quadratic equation

$$\beta(x - x_s)^2 = 5 \quad (3.114)$$

from which we obtain

$$x_{1,2} = x_s \pm \sqrt{\frac{5}{\beta}} \quad (3.115)$$

$$W = |x_2 - x_1| = 2\sqrt{\frac{5}{\beta}} \quad (3.116)$$

From equations (3.113) and (3.116), the shape coefficient β is related to wavelength L and δ as

$$\beta = \frac{80}{\delta^2 L^2} \quad (3.117)$$

3.4.2 Testing results

To verify the wave generating theory described above, we apply the numerical model to generate several types of waves in a 1-D domain of constant water

depth. The domain is bounded by two vertical walls, as shown in Figure 3.5. The horizontal length is $L_x = 50$ meters (m) and the water depth is $h = 0.5$ m . The center of the source region is located at $x_s = 25$ m , which is also the center of the computing domain. To absorb wave energy, two sponge layers of width 5 m are placed at both ends of the domain.

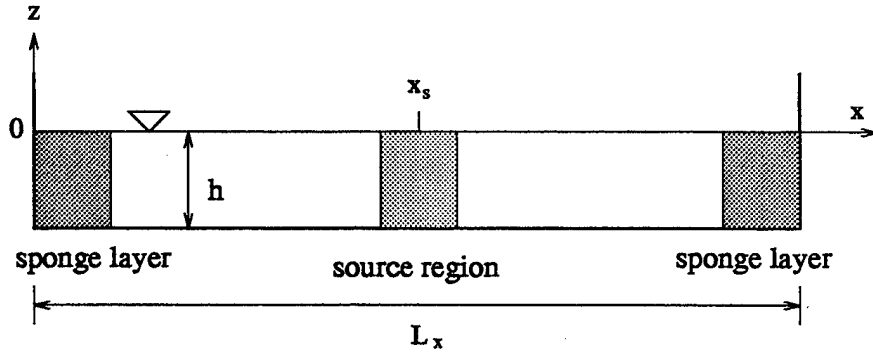


Figure 3.5: Definition sketch of one dimensional domain for verifying the theory of wave generation.

The first wave to be generated is monochromatic with wave period $T = 1$ second (s) and wave height $H = 0.05$ m , which is appropriate to many of those waves generated by laboratory experiments. The grid size is $\Delta x = 0.02$ m and the time step is $\Delta t = 0.02$ s . The corresponding depth to grid size value is $h/\Delta x = 25$ and the Courant number $C_r = 2.21$. These parameters are, according to the trend in Figure 3.2 (b) of linear stability calculation, in the stable range. This is verified directly by the fact that no stability problem was encountered for the model to run for over 100 wave periods. The coefficient for source region width in (3.113) is specified as $\delta = 0.3$, making the source region width contain 19 grid points. Figure 3.6 shows the spatial profiles of surface elevation η at various time $t/T = (2, 10, 20, 40, 100)$.

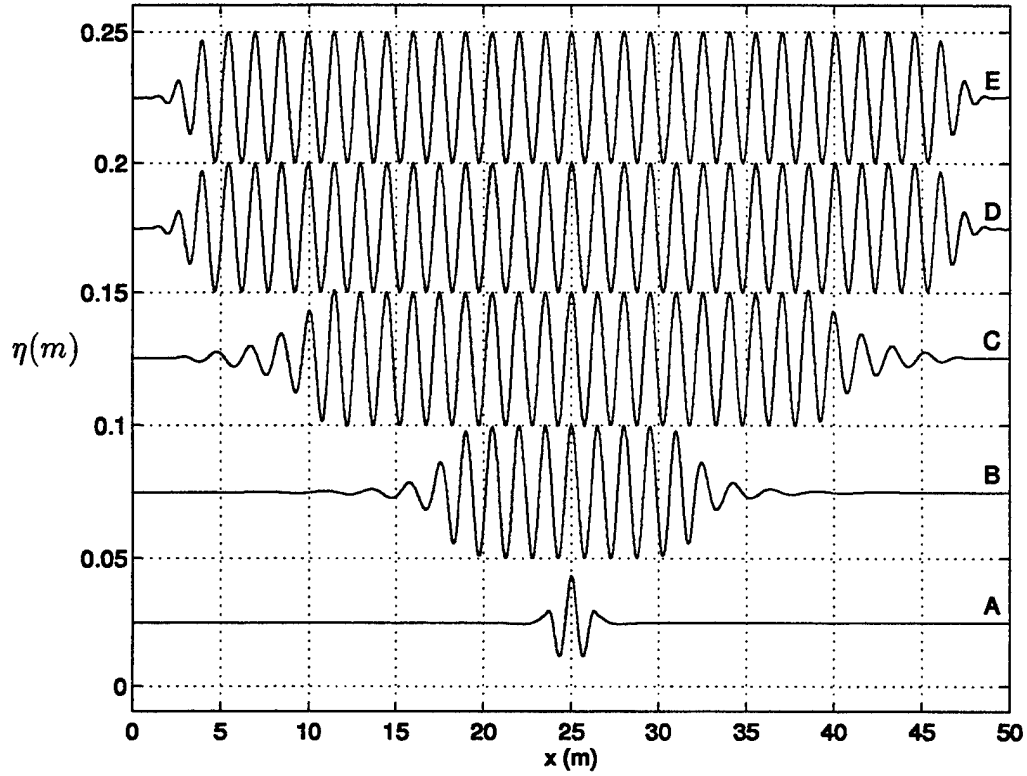


Figure 3.6: Spatial profiles of surface elevation at $t = 2$ s (A), 10 s (B), 20 s (C), 40 s (D), 100 s (E).

At the very beginning (*i.e.*, $t/T = 2$), there are only a few waves being generated around the source region. As time increases, more waves are generated and then propagate out of the source region. When waves arrive in the sponge layer regions at the two ends of the domain, wave height decreases due to the absorption of wave energy by the sponge layers. The effect of wave reflection from the sponge layers back into the domain is negligible. Around time $t/T = 40$, the model reaches quasi steady state, as shown in the figure that the two profiles of η at time $t/T = 40$ and time $t/T = 100$ are very similar. The wave crests and troughs outside source region at time $t/T = 40$ and time $t/T = 100$ are very close to the dashed grid lines whose vertical distances are 0.05 m, the same value

as the target wave height. Further quantitative analysis shows that the relative error between the target and the generated wave heights is less than 0.2%. The magnitude of discrepancy between these two wave heights is mainly depended on the grid size Δx and the width coefficient of the source function δ .

From linear wave theory, a random wave train can be decomposed into many monochromatic wave components whose wave periods and wave heights are determined from the corresponding power spectrum. To generate a desirable random wave train, each of these wave components should be generated correctly. To examine applicability of the model for generating a random wave train, we apply the model to generate three other monochromatic waves whose periods are $T = (0.5, 1.5, 2.0)$ s. In order to mimic the actual generation for a random wave train, all parameters (except for wave periods) for these three cases are kept the same as those in previous one with $T = 1$ s. We ran the model for five thousand time steps (or *i.e.*, 100 seconds) and there were no problems. Results of the spatial profiles of η at $t = 100$ s for all four cases are shown in Figure 3.7. By simply looking at these profiles, the generated wave heights are quite close to the target wave height of 0.05 m.

A more accurate estimation for the height of generated waves is to check the coordinates of crests and troughs for the corresponding wave. For the case of $T = 0.5$ s, the generated wave height is somewhat higher than the target one (about 1.4%). The reason is mainly due to relatively large values of grid size and time step for such a short wave whose wavelength is 0.49 m. The generated wave heights for $T = 1.0$ s and $T = 1.5$ s are very close to the target value of 0.5 m, all within 0.2 % error range. For $T = 2.0$ s, the generated wave height is about 0.484 m, equivalent to 3.2% less than the target one. Further analysis shows that it is caused by the insufficient length of the sponge layers (the corresponding

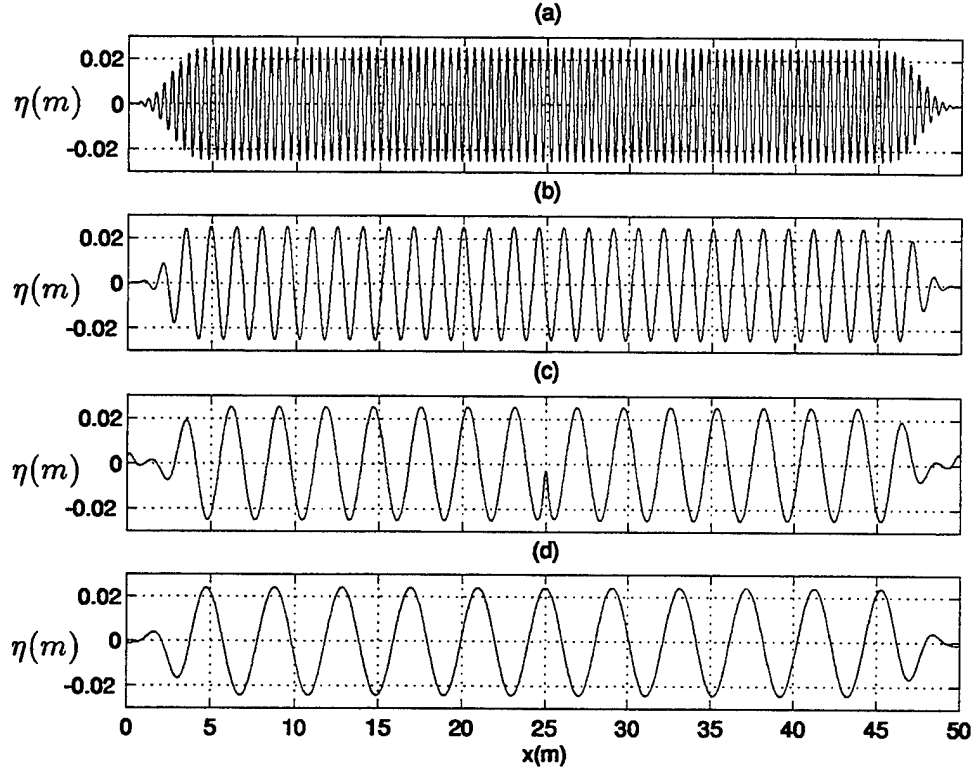


Figure 3.7: Spatial profiles of surface elevation at $t = 100$ s: (a) $T = 0.5$ s; (b) $T = 1.0$ s; (c) $T = 1.5$ s; (d) $T = 2.0$ s.

wavelength for this case is about 4.1 m). For instance, by increasing sponge layer length from 5 m to 6 m, the error is reduced to 0.4% .

For a random wave train with peak period $T = 1$ s, the energy at the frequencies corresponding to $T = 0.5$ s and $T = 2.0$ s is small compared to the peak value. The relatively large error for the two spectrum ends will have much less effect on the total energy spectrum. Therefore, the use of a fixed grid size Δx , time step Δt and width coefficient of source function δ determined from the peak wave is justified.

In the computation described above, only the linearized version of the

model was used, which is consistent with the proposed theory of wave generation. In real applications, however, nonlinear terms have to be included into the model equations for simulating the effect of nonlinear interaction. With the inclusion of the nonlinear terms, the corresponding wave fields will be different from the previous ones. We run the model for the case of $T = 1.0$ s using both the weakly and the fully nonlinear versions of the model. Figure 3.8 shows the spatial profiles of η obtained from the weakly and fully nonlinear models, comparing with results from the linear model. The wave heights across the domain obtained from the linear model is quite constant, as shown in Figure 3.8(a). However, that is not the case for the weakly and fully nonlinear models. Due to nonlinear interaction, the resulting variation wave heights (wave crests and troughs) over the domain exhibit slowly modulation, as shown in Figure 3.8(b) and (c). The modulation to wave height of a sinusoidal wave train propagating over constant water depth has been observed from laboratory and field experiments.

To further illustrate the effect of nonlinear interaction to the sinusoidal wave train, we obtain time series of surface elevation at three locations from these three Boussinesq models (*i.e.*, linear, weakly nonlinear, and fully nonlinear). Figure 3.9 shows the comparison of time series of surface elevation from $t = 40$ s to $t = 45$ s. Again, a clean sinusoidal wave train is apparent for the results obtained from the linear model at the three locations, as shown by solid lines. The surface elevations obtained from the other two nonlinear models, however, show small deviations from the desirable sinusoidal wave.

3.5 Numerical Filtering

Due to nonlinear terms in the model equations, high frequency waves are generated during the evolution process. These super-harmonic waves could have

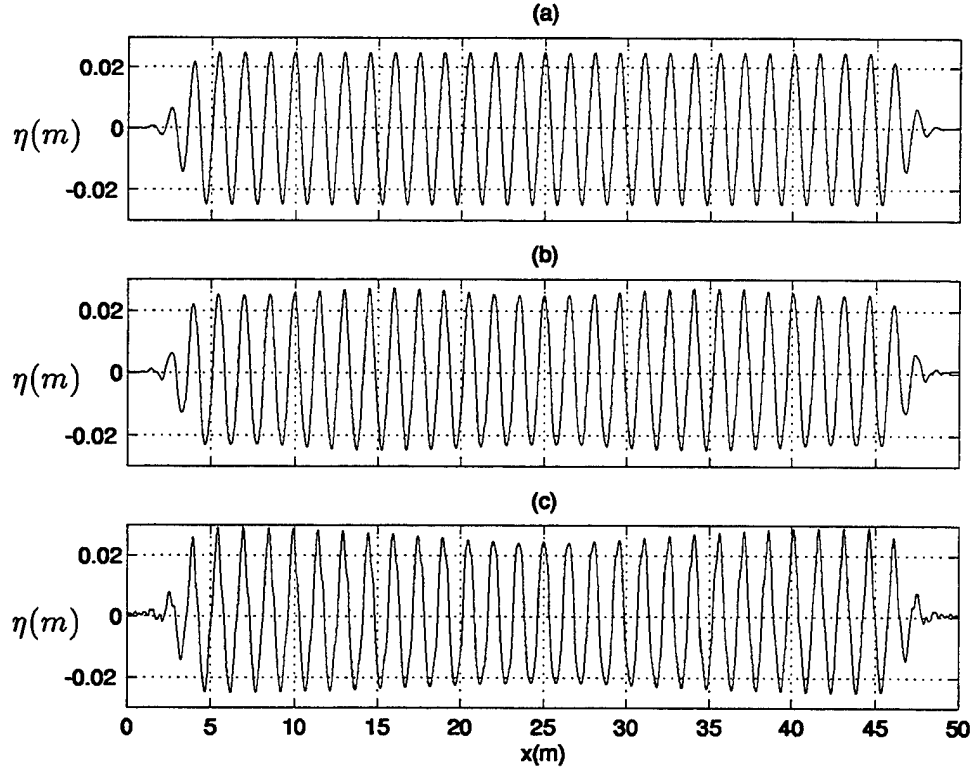


Figure 3.8: Spatial profiles of surface elevation at $t = 100$ s: (a) linear model; (b) weakly nonlinear model; (c) fully nonlinear model.

very short wavelengths whose minimum value is $2\Delta x$ for a fixed grid resolution Δx . Despite the improved linear dispersion property for the present Boussinesq model in intermediate water depth, the depth to wavelength ratios for these short waves are too large for the model to be valid. The magnitude of these short waves usually are amplified rapidly once they are generated, causing the eventual blowup of the model.

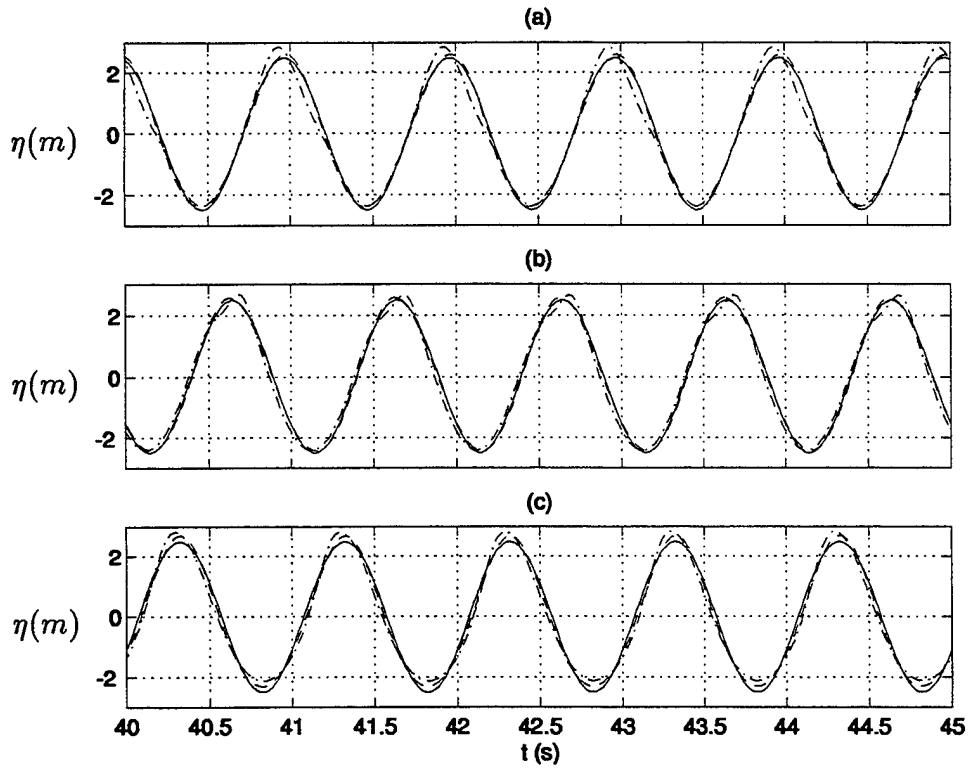


Figure 3.9: Comparison of time series of surface elevations at locations (a) $x = 10 m$; (b) $x = 15 m$; and (c) $x = 20 m$ for three Boussinesq models: linear model (—), weakly nonlinear model (----), and fully nonlinear model (-·-·-). The center of the source is at $x_s = 25 m$.

3.5.1 Formulation

To eliminate these short wave components which pose potential stability problems, numerical filtering proposed by Shapiro (1970) is employed in the model. Based on the method of weighted averages, Shapiro (1970) derived a system of filter formula, ranging from low to high orders. For the one dimensional case, the general form of a numerical filter is given as

$$Z_j^* = a_0 Z_j + a_1 (Z_{j+1} + Z_{j-1}) + \cdots + a_N (Z_{j+N} + Z_{j-N}) \quad (3.118)$$

where $Z = \{\eta, u\}$ represents the original values which consist of long and short wave components, $Z^* = \{\eta, u\}^*$ represents the new values with short wave being filtered out, subscripts $j, j \pm 1, j \pm 2, \dots, j \pm N$ are grid indices where values of Z^* and Z are used for filter evaluation, a_0, a_1, \dots, a_N are weighted coefficients which is determined by the characteristics of the filter.

The property of a filter is determined by the response function R which is defined as the ratio of the smoothed amplitude Z_j^* to the unsmoothed amplitude Z_j . Using the Fourier component to represent the original value Z results in

$$Z_{j+n} = Z_j \exp(ink\Delta x) \quad (3.119)$$

where n is an integer, $i = \sqrt{-1}$ is the unit imaginary number, k is the wavenumber, and Δx is the grid size. From equation (3.119) we have

$$Z_{j+n} + Z_{j-n} = 2Z_j \cos(n\theta); \quad \theta = k\Delta x \quad (3.120)$$

Using equation (3.120), the response function for the filter (3.118) becomes

$$R = \frac{Z_j^*}{Z_j} = a_0 + 2a_1 \cos(\theta) + \dots + 2a_N \cos(N\theta) \quad (3.121)$$

For an ideal low pass filter, the corresponding response function R should be zero for the undesirable short waves and be one for the long waves. For the filter expressed by (3.118) which uses $2N + 1$ surrounding points for weighted averages, the response function R is depended on the actual values of a_0, a_1, \dots , and a_N . As shown by Shapiro (1970), there exist an optimum response function R in (3.121) which is the most accurate representation of an ideal low pass filter. The optimum response function is given by

$$R = 1 - \sin^{2N} \left(\frac{k\Delta x}{2} \right) = 1 - \sin^{2N} \left(\frac{\pi}{L/\Delta x} \right) \quad (3.122)$$

where $L = 2\pi/k$ is the wavelength. Using trigonometric function to transfer the products of sin and cos functions in equation (3.122) into summation terms,

the corresponding coefficients a_n ($n = 0, 1, \dots, N$) in (3.121) are straightforward to obtain. For instance, if $N = 4$ (corresponding to the filter used in the model), we have

$$\begin{aligned} R &= 1 - \sin^8\left(\frac{\theta}{2}\right) \\ &= \frac{1}{256} (186 + 112 \cos(\theta) - 56 \cos(2\theta) + 16 \cos(3\theta) - 2 \cos(4\theta)) \end{aligned} \quad (3.123)$$

Then the corresponding filtering formula is given by

$$\begin{aligned} Z_j^* &= \frac{1}{256} [186Z_j + 56(Z_{j+1} + Z_{j-1}) - 28(Z_{j+2} + Z_{j-2}) \\ &\quad + 8(Z_{j+3} + Z_{j-3}) - (Z_{j+4} + Z_{j-4})] \end{aligned} \quad (3.124)$$

The optimum filters for other N values could be obtained in a similar way. The variations of R with $L/\Delta x$ for $N = 1, 2, 4, 8$ are shown in Figure 3.10. For the shortest wave whose wavelength is $L = 2\Delta x$, the response function R is equal to zero for all N , indicating that this wave is eliminated completely, regardless the number of points used for the optimum filters. As wavelength L increases, the value of R increases and approaches one in the limit of $L \rightarrow \infty$. Therefore, there is less filtering effect on long waves. The transition length from $R = 0$ to $R = 1$ is depended on the number of points N used in the filter. The large the value of N , the shorter the transition length for R . For a given wavelength (for instance, $L/\Delta x = 5$), the filter which uses more points for weighting averages has less filtering effect on the wave.

For accurate simulation, at least 10 grid points are needed for the representation of one wavelength. For a wave whose wavelength is about 10 times of grid size, there will be 10% wave height loss if we applying the lowest order filter with $N = 1$. This loss is equivalent to twenty percent energy loss and is not tolerable. Choosing high order filter with too large value of N ($N \geq 4$), on the

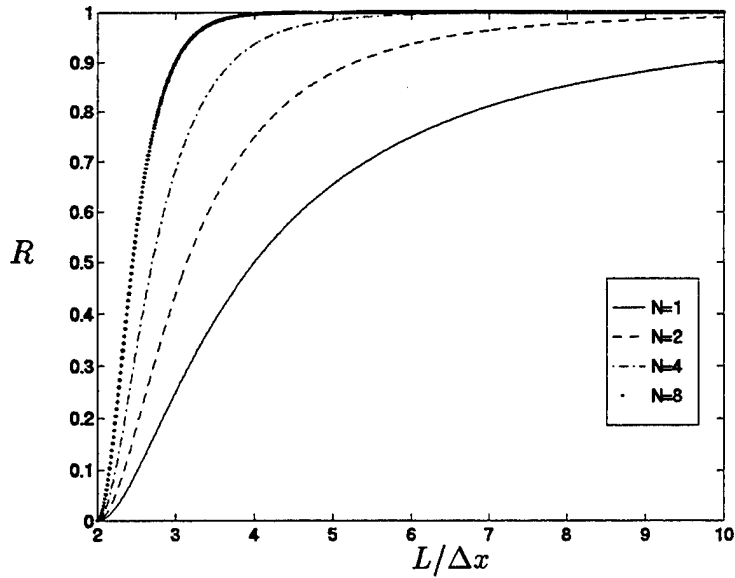


Figure 3.10: Response functions of the 1-D filter for $N = 1, 2, 4, 8$.

other hand, will allow the existence of some short waves whose wavelength is a little greater than $2\Delta x$. In the present model, the numerical filter with $N = 4$ is employed. This filter reduce the energy for short waves with wavelengths less than 6 grid points and admits less than 0.01 percent of wave height loss for waves whose wavelengths are equal to or large than 10 grid sizes.

It is straightforward to obtain the corresponding filtering formula for the 2-D case by applying equation (3.124) to the x direction first and then to the y direction. However, it is cumbersome to write the formula and inconvenient to code it in the program. The reason is that the corresponding filter formula contains a total number of $9 \times 9 = 81$ points for weighting average. To solve the problem, the 1-D formula (3.124) is applied twice in the model code, first to the x direction and then to the y direction. The corresponding response function for

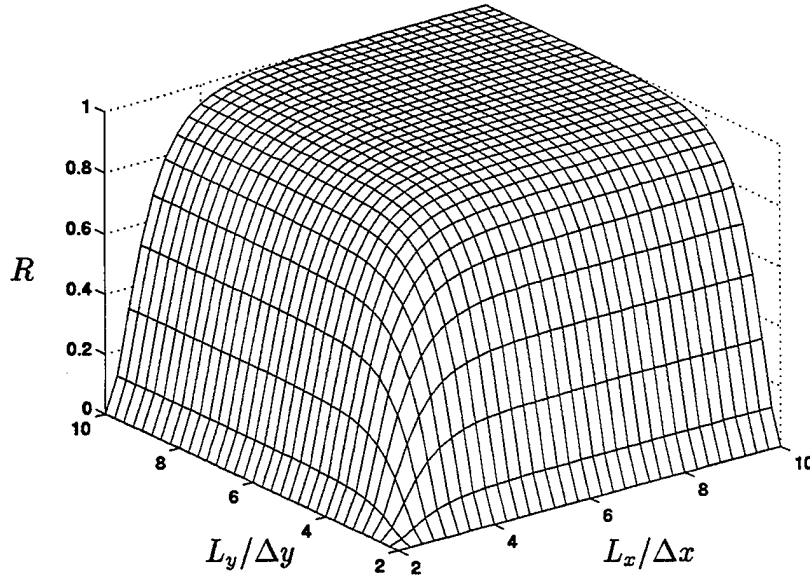


Figure 3.11: Response function of the 2-D filter for $N_x = 4$, $N_y = 4$.

the 2-D filter given by

$$R = \left[1 - \sin^8 \left(\frac{l\Delta x}{2} \right) \right] \left[1 - \sin^8 \left(\frac{\lambda\Delta y}{2} \right) \right] \quad (3.125)$$

$$= \left[1 - \sin^8 \left(\frac{\pi}{L_x/\Delta x} \right) \right] \left[1 - \sin^8 \left(\frac{\pi}{L_y/\Delta y} \right) \right] \quad (3.126)$$

where l and λ are the wavenumbers in x and y directions, respectively, and $L_x = 2\pi/l$ and $L_y = 2\pi/\lambda$ are the corresponding wavelengths. Figure 3.11 shows the variation of the response function R for the 2-D filter with the ratios of wavelengths to grid sizes $L_x/\Delta x$ and $L_y/\Delta y$. For waves whose wavelength in x direction (L_x) is twice of the grid size Δx , the corresponding response function R is zero for all values of $L_y/\Delta y$. This is also true for interchanging x and y . Waves with $L_x/\Delta x = 2$ or $L_y/\Delta y = 2$ are eliminated completely by applying the filter. For waves with large wavelengths, the corresponding response function R increases, indicating that the effect of filtering is reduced.

3.5.2 Comparison

To show the effect of numerical filtering, we apply the model for a simple case of wave propagation in a rectangular basin bounded by four vertical walls (more results for this case will be given in Chapter 5). The basin dimension is $10\text{ m} \times 10\text{ m}$ and the water depth across the domain is constant with $h = 0.5\text{ m}$. A Gaussian hump of water with zero velocity everywhere is placed in the center of the basin initially and then released. Because of gravitational forcing, waves will be generated and propagate in the basin. Though there is neither analytical solution nor experiment data to compare with, the computed surface elevation at any given time should be symmetric about the two lines which are parallel to the wall and crossing the center of the basin, due to the symmetry of the basin and of the initial condition. The surface elevation is also symmetric about the two diagonal lines across the basin.

We run the weakly nonlinear version of the present model for two cases, one with the numerical filter (3.124) applying for every 100 time steps and the other without using any filters. For meaningful comparison, all the parameters used in the model are kept the same for these two runs. The grid size is $\Delta x = 0.1\text{ m}$, the time step is $\Delta t = 0.02\text{ s}$, and the maximum time step for the model to run is 2501 (a time lapse of 50 seconds). Figure 3.12 shows the two resulting cross sections of surface elevation at the time step $it = 2501$ and at the $y = 5.0\text{ m}$. The solid line is the result using the 2-D numerical filter ($N = 4$) for every 100 time step and the dashed line corresponds to the case without using any filters. Though the overall shapes for the two lines are quite similar, careful examination shows that the solid line is quite symmetric about the center $x = 5\text{ m}$. However, the dashed line exhibits small deviations from the symmetry, as evident for the surface elevations at the locations around the center $x = 5\text{ m}$, near $x = 2\text{ m}$ and

$x = 8 \text{ m}$, and close to the boundaries (*i.e.*, $x = 0$ and $x = 10 \text{ m}$).

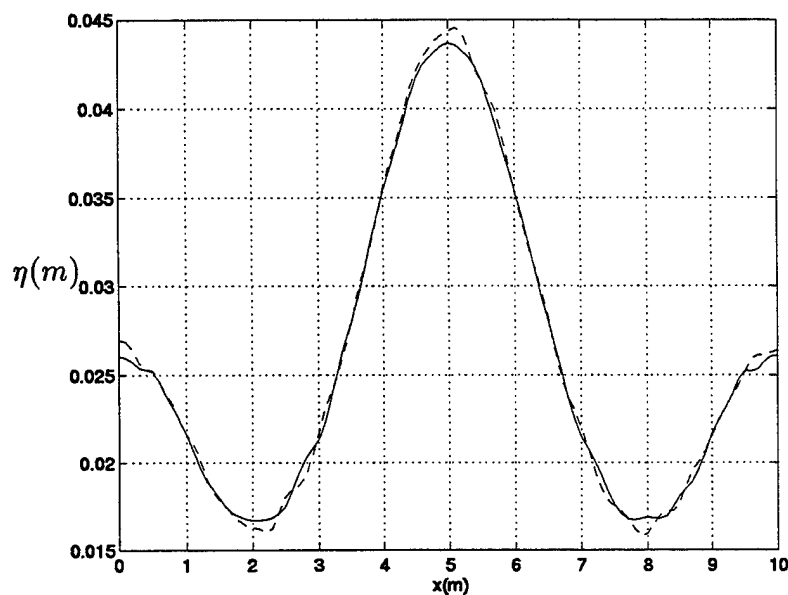


Figure 3.12: Comparison of surface elevation at time step $it = 2501$ and $y = 5.0 \text{ m}$: applying filter for every 100 time steps (—); without using any filters (----).

An alternate way to examine the symmetry of surface elevation is to plot the corresponding spatial profile for the entire domain, as shown in Figure 3.13 (a) and (b) for the contour plots of computed η at the time step $it = 2501$. On the first look, these two plots seem to be quite identical. However, careful examination reveals that the contours in Figure 3.13(b) are not as symmetric as those in Figure 3.13(a), see the contours around the center of the domain. Without applying numerical filters, the symmetry of model results will be distorted by those short waves whose wavelengths are close to two grid sizes.

Despite its advantage, the use of numerical filter in the model computation should be kept to a minimum. Every time when the filter (3.124) is applied, a fraction of energy for the long waves is also lost. The accumulating effect of the

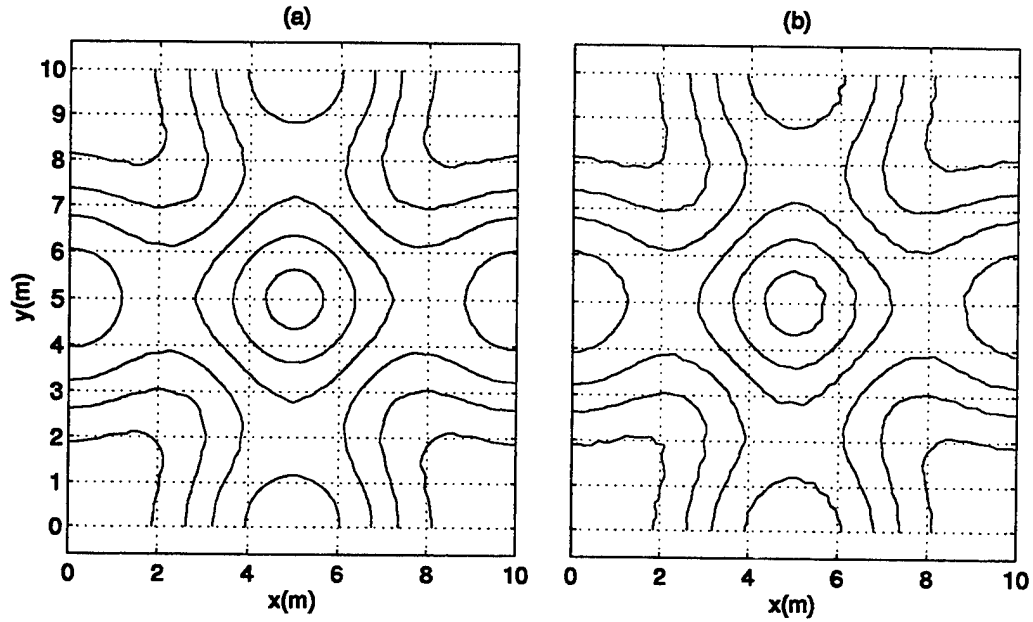


Figure 3.13: Surface elevation profiles at time step $it = 2501$: (a) applying numerical filter for every 100 time step; (b) no numerical filter is used.

loss is not negligible if the numerical filter is employed too frequently (*e.g.*, every time step). It is recommended that the filter be used once for about every 100 time steps (or about two wave periods).

Chapter 4

SIMULATION OF WAVE BREAKING AND RUNUP

4.1 Introduction

The importance of wave breaking in nearshore processes cannot be over emphasized. As waves propagate into surf zone areas, wave height keeps increasing and the wave front face steepens, which eventually causes waves to break. In the process of breaking, wave height decreases dramatically and the corresponding wave energy is transferred into necessary forcing to drive nearshore circulation and to initiate sediment transport.

It has been known that the breaking of obliquely incident waves is responsible for the generation of longshore currents along a straight beach. The driving force for longshore currents was referred to as radiation stress by Longuet-Higgins and Stewart (1964), due to its similarity to radiation pressure in the field of electromagnetics. Based on the concept of radiation stress, a number of nearshore circulation models have been developed. The success of these models, however, depends greatly on the accuracy of simulating wave breaking (location, surface elevation, *etc.*) by short wave models.

Despite the difficulty in mathematical description for discontinuity of surface elevation, research work on wave breaking has been advanced significantly. Reviews on the subject of wave breaking on beaches were provided by Galvin

(1972) and by Peregrine (1983). Most of the research work has been concentrated on the initialization of wave breaking for given wave conditions. Based on the ratio of wave height to water depth, the magnitude of particle velocity in a wave crest with that of wave phase speed, or the curvature of surface elevation, a number of empirical formulas have been proposed and verified by experiment results.

The problem of wave runup is essential for the design of breakwaters and for the prediction of floods caused by storms or tsunamis. In a swash zone, as waves move up and down the beach face, the corresponding shoreline boundary location changes constantly, making it difficult to describe by mathematical formula and by numerical treatment. Due to relatively small water depth in swash zones, bottom friction is no longer negligible. However, depending on the empirical formula chosen for the model and the corresponding friction coefficient for the beach bottom, the calculation of bottom friction varies significantly.

In this study, we attempt to simulate the processes of wave breaking and wave runup by including additional terms in the model equations. With the already improved linear dispersion property in intermediate water depth and the improved property for large nonlinear waves, the inclusion of breaking and runup would make the model valid in general coastal environments.

4.2 Simulation of Wave Breaking

The early models to simulate wave breaking are based on the nonlinear shallow water wave equations. Due to the non-dispersive property, these models predict, prior to wave breaking, the continuous steepening of the front face of a wave. Two numerical approaches to simulate wave breaking have been reported in the literature. In the first approach, the turbulent bore due to breaking was replaced by a discontinuity in the physical variables and by jump conditions which

conserve mass and momentum (Whitham, 1958). In the second approach, the Lax-Wendroff scheme was utilized to discretize the model equations, assuming that numerical dissipation is equivalent to the effect of wave breaking. The second approach has been used by many investigators, among which are Abbott *et al.* (1984), Hibberd and Peregrine (1979), Packwood (1980), and Kobayashi *et al.* (1989). Compared to Boussinesq breaking models which will be discussed below, shallow water wave models are easy to apply. However, these models are restricted to the areas of extremely shallow water and in general cannot provide a realistic prediction of the actual location of wave breaking and associated characteristics.

Observing the similarity between broken wave propagation and hydraulic jumps, Heitner and Housner (1970) proposed a breaking model which includes an eddy viscosity term into the Boussinesq equation to dissipate wave energy due to breaking. The eddy viscosity is expressed in terms of a mixing length and a velocity scale, which is related to the turbulent kinetic energy. This approach is originated by Von Neumann and Richtmyer (1950) for the analysis of gas dynamics. Wave energy loss is limited to the front face of waves where the change of wave properties (*i.e.*, the horizontal gradient of horizontal velocity) exceeds a certain criteria.

Similar approaches based on the eddy viscosity formula have been used by a number of investigators to extend Boussinesq models to the surf zone. Tao (1983) combined the eddy viscosity with a transport equation for the turbulent kinetic energy. Karambas and Koutitus (1992) used an algebraic closure with eddy viscosity proportional to the local water depth times the linear long wave celerity. Zelt (1991) implemented the eddy viscosity formula in a Lagrangian Boussinesq model to study the runup of breaking and non-breaking solitary waves over constant slopes. Good agreements between numerical results and experimental data

were obtained.

A different approach for simulating wave breaking is based on the concept of surface rollers proposed by Svendsen (1984). Deigaard (1989) is the first to apply the concept of the surface roller for simulating wave breaking. Arguing that the local energy dissipation for wave breaking is dependent on the vertical gradient of the horizontal velocity profile rather than horizontal gradient, Schäffer *et al.* (1993) modified and applied the roller model to the extended Boussinesq equations derived by Madsen *et al.* (1992). During the process of wave breaking, a surface roller is generated on the front face of a wave and transported with the wave phase speed, which is larger than the depth-averaged velocity. The non-uniform distribution of horizontal velocity with water depth results in additional convective terms in the momentum equations. These terms play the role of dissipating wave energy during the breaking process. Wave height variations in surf zone areas predicted by the model for the 1-D case have been shown by to be in good agreement with experimental data. The extension of the roller model to the 2-D case for directly calculating wave-induced currents is described by Sørensen *et al.* (1994) and Madsen *et al.* (1994).

Another wave breaking model, which is more closely related to the physical aspects of processes in surf zone areas than the eddy viscosity model and the roller model, was proposed by Yu and Svendsen (1995). Realizing that potential flow theory is not sufficiently valid in surf zone areas, Yu and Svendsen (1995) derived a set of depth-integrated governing equations directly from the Navier-Stokes equations. The velocity variables are split into a potential part and a rotational part. Compared to the Boussinesq equations derived from potential theory, additional convective terms were obtained from the rotational part of velocity. It is these terms that dissipate energy in the process of wave breaking.

Preliminary results from this vorticity model for 1-D wave propagation showed promising results.

Of the three wave breaking models for Boussinesq equations, we chose the eddy viscosity model for simulating wave breaking. Despite of some unphysical assumptions made in the eddy viscosity model, numerical calculation showed that it is capable of predicting reasonably accurate wave height variations and associated properties in surf zone areas. Though physically more accurate, the numerical implementations for the roller model and the vorticity model is quite complicated. In order to evaluate the dissipation terms, additional empirical parameters are required to estimate the roller shape, the roller location, and the distribution of rotational velocity components. Obviously, these approximation made the overall models to be less accurate.

Following the approach of Heitner and Housner (1970) and of Zelt (1991), the corresponding energy dissipation terms in the right hand sides of equations (3.2) and (3.3) are given by

$$F_{br} = (\nu_b u_x)_x + (\nu_b u_y)_y \quad (4.1)$$

$$G_{br} = (\nu_b v_x)_x + (\nu_b v_y)_y \quad (4.2)$$

where u and v are the x and y components of horizontal velocity \mathbf{u}_α , respectively. The notion ν_b is the eddy viscosity which is defined as

$$\nu_b = -B\delta^2(h + \eta)^2 \nabla \cdot \mathbf{u}_\alpha \quad (4.3)$$

where B is a coefficient related to the local shape of the waves and the corresponding critical value for wave breaking to take place, δ is the coefficient of mixing length, whose value is determined empirically. In the computation which will be shown in Chapter 5, we use it as a constant, *i.e.* $\delta = 2$. Zelt (1991) used velocity

gradient to determine wave breaking and defined the critical value of velocity gradient as $u_x^* = -0.3\sqrt{g/h}$. Using the leading order relation (linear and long wave) from the model equations, the critical value for velocity gradient is equivalent to the slope of surface elevation $\eta_x^* = -0.3$. To avoid the abrupt change in eddy viscosity which might cause instability in numerical computation, the coefficient B is given by

$$B = \begin{cases} 1 & \text{if } \nabla \cdot \mathbf{u} \leq 2u_x^* \\ \left(\frac{\nabla \cdot \mathbf{u}}{u_x^*} - 1\right) & \text{if } 2u_x^* < \nabla \cdot \mathbf{u} \leq u_x^* \\ 0 & \text{if } \nabla \cdot \mathbf{u} > u_x^* \end{cases} \quad (4.4)$$

We have applied this simple eddy viscosity model to simulate the shoaling and breaking of 1-D regular and random waves and compared with two experiments. For the case of regular waves, the experiment was conducted in a wave flume in Delft Hydraulic where the a bar-type geometry was seating on the flat bottom (Dingemans, 1994). For the case of random waves, the experiment was conducted in a wave flume in Kyoto University in which the bottom geometry consists of a constant water depth and a constant slope (Mase and Kirby, 1992). The agreement between the model results and the data from these two experiments are quite good. The case of random waves will be shown in Chapter 5.

We have also applied the model to simulate the case of 2-D wave breaking. However, the comparisons between the model results and experimental data in the breaking zone are not as good as those for 1-D case. The reason maybe due to the localization of the breaking terms in the model which are activated only when the local properties of the wave exceed the breaking criterion. While in reality, the breaking of a wave crest at a given location can affect the breaking of its neighboring points and spread across the crest. More research work is needed for implementing 2-D breaking model.

4.3 Simulation of Wave Runup

Unlike wave breaking, there exist analytical solutions to shallow water equations for wave runup under very special conditions. Using coordinate transformation, Carrier and Greenspan (1958) obtained exact expressions for the runup of nonbreaking periodic waves over constant slopes. Following the approach of Carrier and Greenspan, Synolakis (1986) obtained solutions based on linear and nonlinear theory, including solitary runup over constant slopes. The extension of analytical solutions to 2-D case was given by Thacker (1981), who obtained the required bottom geometry and initial surface elevation for predefining solution forms of velocity.

Analytical solutions are useful tools for studying wave runup problems and for verifying numerical models. However, these solutions are not valid when wave breaking occurs, which is, unfortunately, the most general case for wave propagation over a beach.

For the problem involving wave breaking and wave runup, numerical simulation is the only method being used at present. For shallow water wave equations, a widely used numerical scheme is based on mass conservation to determine the shoreline grid. Dividing the dry land cells and wet cells, the shoreline grid changes constantly and has to be determined at each time step. Combining with upwind or other low order numerical schemes to discretize equation terms, this kind of runup models has less stability problems and works quite well. Liu *et al.*, (1995) applied such a model to study solitary wave runup on a circular island and numerical results were shown to be in good agreement with experimental data.

However, for numerical models based on Boussinesq equations, it is difficult to adapt the same approach as used by the shallow water wave model for moving

shoreline. In all Boussinesq models, velocity or mass flux are obtained from a system of tridiagonal matrix equations. A varying number of grid points at each time step due to the changing shoreline location makes it inconvenient for applying tridiagonal matrix solution. In addition, Boussinesq equations include dispersive terms with third-order derivative, which are in same form as truncation errors if low order numerical schemes are used to discretize all equation terms.

The difficulty for determining the shoreline location in an Eulerian system has lead a number of investigators to develop runup models based on a Lagrangian coordinate description. For Boussinesq equations written in a Lagrangian system, the movement of individual fluid particles in a domain is computed at each time step. There is no special treatment for particles at the shoreline and thus the corresponding numerical scheme is simplified. Heitner and Housner (1970) applied a Lagrangian model to study tsunami runup problem. Pedersen and Gjevik (1983) and Zelt (1991) used a similar approach to simulate solitary wave runup over slopes. Good agreement between numerical results and experimental data have been reported.

In order to preserve the Eulerian description for Boussinesq equations and to overcome the difficulty for varying the number of grid points at each time step, several approaches have been proposed. Tao (1983) developed a runup model based on the so called slot-technique, in which artificial slots with width between 0.01 to 0.001 times the grid size are added into the computational domain. With modification, Madsen *et al.* (1994) applied the method to the extended Boussinesq equations for simulating runup.

Casulli and Cheng (1992) proposed a method which includes dry cells in the computing grids by specifying zero total water depth at the dry cells. In this study, we attempt to modify the approach of Casulli and Cheng (1992) by

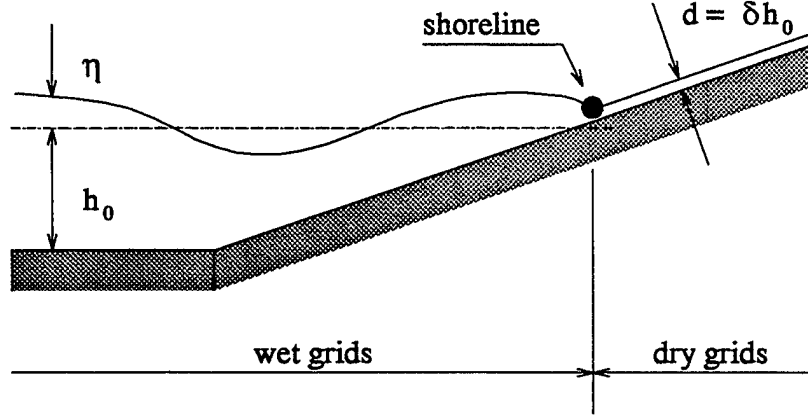


Figure 4.1: Definition sketch of runup model based on a thin layer of water.

specifying a minimum thickness of water for physically dry cells, instead of giving zero to water depth. The reason for the modification is due to singularity for friction computation if zero water depth is used. This thin layer of water should remain almost motionless due to the balance between gravitational force and bottom friction. Figure 4.1 shows the definition sketch for the runup model.

Since the effect of bottom friction is no longer small during the process of wave runup, the corresponding bottom friction terms are included in most of the runup models. The following is a bottom friction formula for 1-D depth-averaged turbulent flow:

$$F_{bottom} = -\frac{K}{h + \eta} \bar{u}|\bar{u}| \quad (4.5)$$

where K is the bottom friction coefficient, $h + \eta$ the total water depth, and \bar{u} the depth-averaged velocity. Expression (4.5) has been implemented in runup models by a number of investigators, including Heitner and Housner (1970), Packwood and Peregrine (1981), and Zelt (1991). In this study, we utilize the same formula as (4.5) in the Boussinesq model. The corresponding terms in the right hands side

of equations (3.2) and (3.3) are given by

$$F_b = -\frac{K}{h + \eta} \sqrt{u^2 + v^2} \ u \quad (4.6)$$

$$G_b = -\frac{K}{h + \eta} \sqrt{u^2 + v^2} \ v \quad (4.7)$$

where u and v are components of velocity u_α (not the depth-averaged velocity) in x and y direction, respectively. In real application, the friction coefficient K should be a function of the bottom roughness and the velocity profile. For simplicity, a constant coefficient $K = 5 \times 10^{-5}$ is used in the model, the same as that used by Zelt (1991).

At the present, the approach of adding a thin layer of water to the dry cell for simulate wave runup does not work to expectation due to the blowup of numerical model. The thickness of the thin layer of water is specified as $d = \delta h_0$, where h_0 is the seaward still water depth and δ is a constant number which is much less than 1 and is adjustable in the model. From computational results prior to the model blowup, large value of δ (i.e., 0.1) resulted in large downward velocity which increases the velocity difference near the shoreline location. On the other hand, too small value of δ (i.e., 0.001) caused strong fluctuation in surface elevation on the areas with the thin layer of water.

Notice that when applying slot-technique for simulating wave runup for the extended Boussinesq equations in an Eulerian description, Madsen *et al.* (1994) applied several other techniques in order to make the model operational. These techniques include switching off dispersive terms at the still water shoreline, changing finite difference scheme from central differences to upwind difference inside slots, and introducing explicit numerical filter near still water shoreline. In order for our model based on thin layer of water to be operational, it maybe necessary to adapt similar techniques.

Chapter 5

RESULTS AND COMPARISONS

To verify the numerical model described in previous chapters, extensive tests have been conducted for a wide range of wave propagation problems. Due to the significant differences in model formulation and required operations, both 1-D and 2-D versions of the numerical model have been developed. Although it is possible to apply the 2-D model for the study of 1-D problems, it is recommended to use the 1-D program to solve 1-D problems due to savings in computer storage and computing time.

For the 1-D model, we first investigate the evolution of solitary waves in constant water depth. Solutions of permanent form corresponding to the model equations are obtained after running the numerical model over a flat bottom for a relatively long time. The solutions for surface elevation for several height to depth ratios are compared with other models to show the importance of high order nonlinear terms included in the model equations.

We then apply the 1-D model to study the shoaling of solitary waves over constant slopes and the propagation of undular bores in constant water depth. Results from the present model with and without high order nonlinear terms are compared with those obtained from the boundary element model (BEM) developed by Grilli *et al.* (1989).

The shoaling and breaking of a random wave train over a constant slope is the next case to be studied using the 1-D version of the present model. Numerical results for the time series of surface elevation and the corresponding power spectrum, root mean square wave height, skewness and asymmetry at various location along the slope are compared in detail with the experimental data of Mase and Kirby (1992).

For the 2-D version of the model, we first study the evolution of waves in a closed rectangular basin. The initial surface elevation is set to be a Gaussian shape. From the computed results, we examine the symmetry of surface elevation and the conservation property of water volume. For linearized conditions, this case admits analytical solutions. We therefore run the model with linear terms only and compare numerical results with these exact solutions.

The 2-D model is then applied to simulate the propagation of monochromatic waves over submerged shoals, corresponding to the experimental studies conducted by Berkhoff *et al.* (1982) and by Chawla (1995). Comparisons of time series of surface elevation and variation of wave height between numerical solutions and experiment data are presented.

5.1 Solitary Wave Evolution over Constant Water Depth

The first case to be studied is the propagation of solitary waves over a long distance in constant water depth. This is a good test for the stability and the conservative properties of any basic numerical scheme. In order to provide the proper initial and boundary conditions to generate the required solitary wave, we need to obtain the corresponding analytical solution (exact or approximate) from the model equations.

Schember (1982) has described a method for obtaining approximate solitary wave solutions for the standard Boussinesq equations, which use depth-averaged velocity as the dependent variables. First, the velocity variable u was replaced with a wave potential ϕ in the equations. Then, to the same order of accuracy as the Boussinesq equations, an ordinary differential equation for wave potential ϕ was obtained by eliminating surface elevation η . The equation of ϕ is a fourth-order nonlinear ordinary differential equation. Applying initial and boundary conditions, a closed-form solution for ϕ was obtained, from which the horizontal velocity u and surface elevation η can be determined. Following the same procedure, we can obtain the corresponding analytical solution for the extended Boussinesq equations of Nwogu (1993), which is the same as the present model equations without high order nonlinear terms. Details of the derivation are included in Appendix A. In the following, only results of the approximate solitary wave solutions are shown. For Nwogu's extended Boussinesq equations, the corresponding solitary wave solutions are given by

$$u = A \operatorname{sech}^2[B(x - Ct)] \quad (5.1)$$

$$\eta = A_1 \operatorname{sech}^2[B(x - Ct)] + A_2 \operatorname{sech}^4[B(x - Ct)] \quad (5.2)$$

where u is the horizontal velocity at depth $z_\alpha = -0.531h$, η is the surface elevation, C is the phase speed of the solitary wave which is a function of wave height to water depth ratio. Definitions for quantities A , B , C , A_1 , A_2 are given in Appendix A.

5.1.1 Evolution of solitary waves

Using the approximate analytical solutions (5.1) and (5.2) for extended Boussinesq equations as initial conditions, we apply the numerical model to investigate the propagation of solitary waves in constant water depth. Notice that due to small nonlinearity, only weakly nonlinear version of the present model is

considered in this section. Both of the weakly and fully nonlinear versions of the model will be studied in the next section. The horizontal length for the computing domain is chosen to be 450 m and the water depth is 0.45 m , which makes the length to depth ratio 1000. Three solitary waves with initial heights $H = 0.045 m$, 0.090 m and 0.135 m are used for the test. The corresponding wave height to water depth ratios were $\delta = 0.1, 0.2$ and 0.3.

Figure 5.1 shows the spatial variations of the solitary wave with initial $\delta = 0.1$ at various time $t = (40, 80, 120, 160, 200 \text{ s})$. The solitary wave is generated at the left boundary ($x=0$) by specifying η and u according to the approximate solutions in (5.1) and (5.2). The grid size and the time step used here are $\Delta x = 0.1 m$ and $\Delta t = 0.02 s$, corresponding to a Courant number of 0.42. Except for the initial deviation in wave height at the start of the channel and the formation of a small dispersive tail (not so obviously seen from Figure 5.1 but illustrated in subsequent figures), the model produced a stable solitary wave propagating across the domain.

Figure 5.2 shows the spatial profiles of a solitary wave with initial $\delta = 0.3$ at $t = (40, 80, 120, 160, 200 \text{ s})$. The solitary wave crests are clipped off in order to accentuate the height of the dispersive tail. Since the propagation speed C for the solitary wave is known from the approximate analytical solution, a radiation boundary condition (3.98) is used at the right end of the domain. At the $t = 200 s$, the main solitary wave has left the domain without significant reflection, indicating the boundary condition worked well. The dispersive tail is seen to lag behind the evolved solitary wave, and shows a distinct ordering with low frequency waves near the front of the wave train and high frequency waves near the back, as would be expected for any dispersive wave train. The amplitude of the dispersive tail increases with initial wave height. This result is partially due

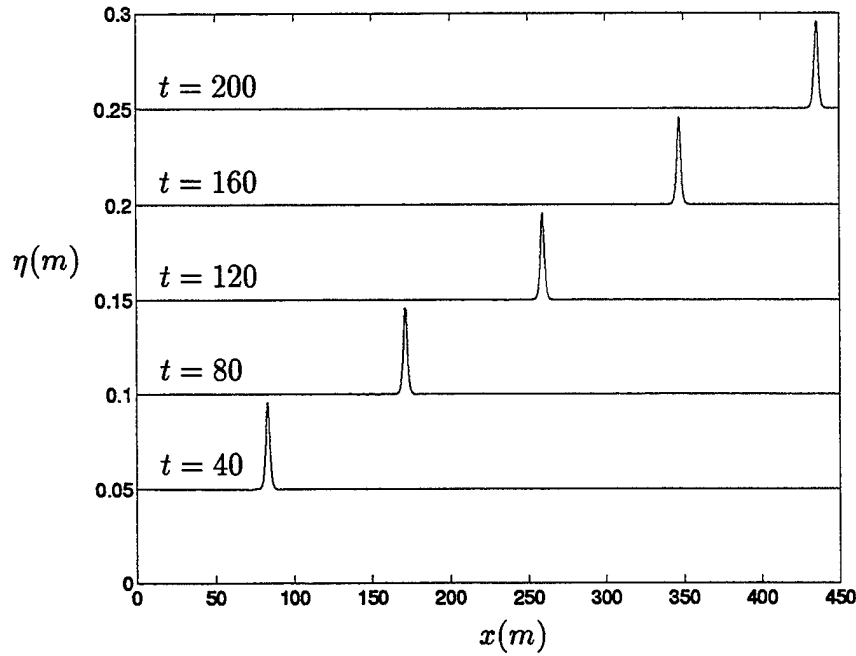


Figure 5.1: Spatial profiles of the solitary wave with initial $\delta = H/h = 0.1$ evolving in a constant water depth of $h = 0.45$ m. The unit of time t is in second.

to the fact that the fourth order equation used to develop the analytical solution is only asymptotically equivalent to the model being solved numerically, so that the wave being input at the boundary of the numerical model does not correspond exactly to a solitary wave form as predicted by the model.

To further illustrate the change in solitary wave height between the initial specified value and the final stable solution resulting from the model, the spatial variation of wave height for all three solitary waves ($\delta = 0.1, 0.2, 0.3$) is shown in Figure 5.3. Except for some numerical noise, all three wave heights were stabilized after traveling a distance of $x/h = 150$. Though the difference in wave height change is proportional to initial wave height, the distance required for solitary wave to reach stable wave height decrease with increasing initial wave height.

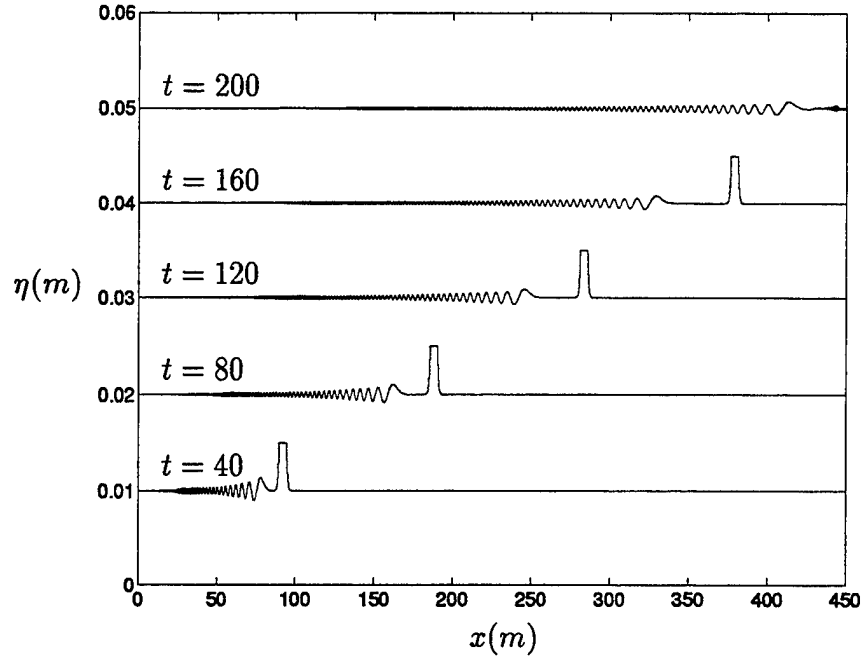


Figure 5.2: Spatial profiles of solitary wave with $\delta = 0.3$ evolving in water of constant depth $h = 0.45\text{ m}$. The unit of time t is in second.

The important feature of the numerical solution is that the solitary wave evolves out of the initial wave form and then propagates for a long distance (about 1000 water depths) without undergoing any significant additional damping or evolution. This indicates that the numerical code is free of unwanted dissipative effects, which would gradually damage the solitary wave form. As indicated in Figure 5.3, the solitary wave height predicted by the model is quite stable.

In Figure 5.4, two numerically predicted wave forms of each of the three solitary waves at times $t = 40\text{ s}$ and $t = 160\text{ s}$ from the numerical model are compared in detail. These wave forms are translated by the analytical phase speed C expressed in equation (A.19) in Appendix A for each of the corresponding solitary waves. Due to the approximation used in the derivation, the analytical

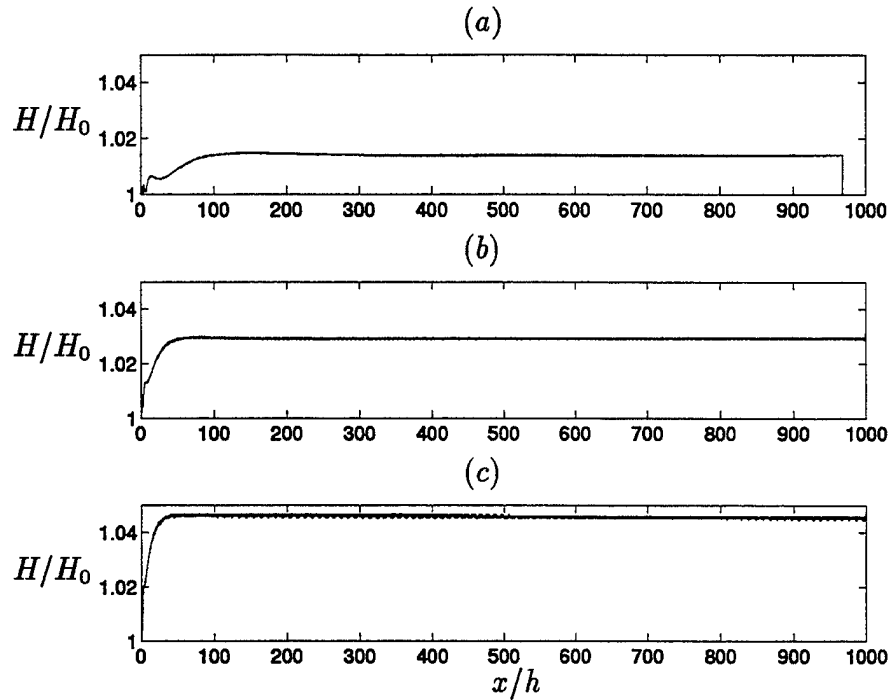


Figure 5.3: Amplitude variations of solitary waves: (a) $\delta = 0.1$; (b) $\delta = 0.2$; (c) $\delta = 0.3$.

phase speed C is not the same as the numerically predicted value. Figure 5.4 indicates that the analytical phase speed is somewhat larger than the numerical one, in contrast to the fact that the numerical wave height is larger than the analytical one. As nonlinearity increases, the discrepancy between analytical and numerical phase speeds increases.

5.1.2 Accuracy of solitary wave with high nonlinearity

Chapter 1 describes general features of some existing nonlinear long wave models. All these models, except for the nonlinear shallow water model, admit permanent form solutions (either analytically or numerically) representing a forcing balance between nonlinearity and dispersion. Due to different assumptions

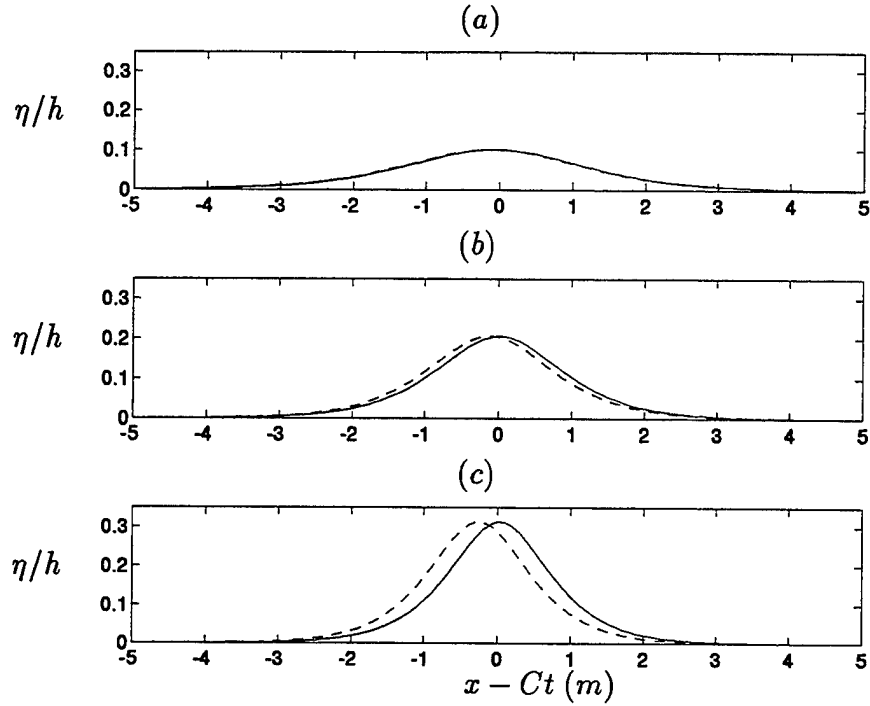


Figure 5.4: Comparison of solitary wave shapes at $t = 40s$ (—) and $t = 160s$ (---): (a) $\delta = 0.1$, (b) $\delta = 0.2$, and (c) $\delta = 0.3$.

made in the derivation of the models, the corresponding permanent wave solutions are not the same. Certain characteristics of the models will be revealed by analyzing their solitary wave solutions with high nonlinearity.

Utilizing a conformal mapping technique to transform the curved surface elevation into a straight line, Tanaka (1986) obtained a closed-form expression for the solitary wave from the original wave equations for irrotational, inviscid and incompressible fluid. Though a numerical method is required to obtain the final results for the close-form expression, Tanaka's solution for the solitary wave is the most accurate result to compare with. For certain approximate wave equations such as the KdV equation and Serre equations, there exist closed-form solutions for permanent waves. For Boussinesq equations, however, no complete analytical

solutions have been found yet. Therefore, we have to obtain the corresponding permanent solutions numerically from these models.

Using the approximate expressions (5.1) and (5.2) as inputs, we ran the present model with and without high-order nonlinear terms over a constant water depth for a long distance. At the beginning of these computations, wave heights and wave shapes changed constantly, and small oscillatory tails developed behind the main waves as they propagated forward. After running the models for a long time, however, the changes of form became negligible and wave shapes stabilized, indicating that a numerical permanent-form solitary wave solution corresponding to each of the Boussinesq models was obtained. Due to the discrepancy between initial and stabilized wave forms, several runs of the models were required to obtain a solitary wave with desired height.

Figure 5.5 shows the computational results from the present model (with and without high-order nonlinear dispersive terms) for three high nonlinear solitary waves (wave height to water depth ratios are $\delta = 0.4, 0.6, 0.8$). The corresponding analytical solution of the Serre equations and the closed-form solution of Tanaka (1986) are also included for comparison.

As shown in Figure 5.5, the results from the present model with high-order nonlinear terms (the fully nonlinear Boussinesq model) match very well Tanaka's solution for all three solitary waves. The corresponding weakly nonlinear model predicted either narrower or wider solitary wave shapes, depending on the wave height. The results imply that these high-order nonlinear dispersive terms are important for simulating wave propagation with strong nonlinearity.

Serre equations were derived under the assumption of a uniform variation of horizontal velocity with depth (Serre, 1953). The solitary wave solution to

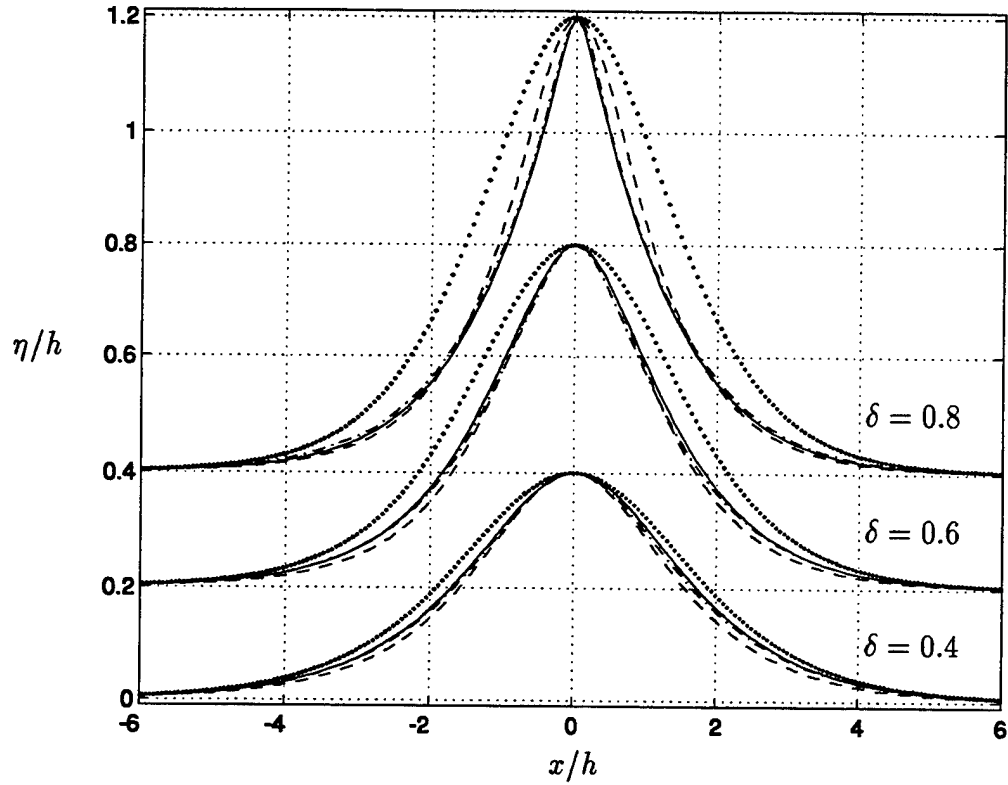


Figure 5.5: Comparison of solitary wave shapes for $\delta = 0.4, 0.6, 0.8$. Tanaka's solution (—); fully nonlinear Boussinesq model (---); Nwogu's Boussinesq model (-.-.-); closed-form solution of Serre's equations (....).

Serre equations was given by Su and Gardner (1969), and by Seabra-Santos *et al.* (1987) who also extended Serre equations to variable water depth. In contrast to the standard derivation of Boussinesq equations or KdV equations, no assumption of small nonlinearity was made in deriving Serre equations. However, as shown in Figure 5.5, the corresponding solitary wave solutions to Serre equations are much wider in shape compared with Tanaka's solutions. The result indicates that the assumption of uniform horizontal velocity with depth is not accurate for solitary waves with high nonlinearity.

As described in Chapter 1, Serre equations are exactly the same as the correction equations to shallow water theory by Su and Gardner (1969), and the same as the fully nonlinear standard Boussinesq equations (using the depth-averaged velocity as the dependent variable) by Mei (1989). Comparisons from Figure 5.5 also indicate that the present model is superior to the standard Boussinesq model, not only for linear dispersion in intermediate water depth but also for high-order nonlinear interaction.

5.2 Solitary Wave Shoaling Over Constant Slopes

After studying the evolution of solitary wave over constant water depth, the next natural step is to investigate the propagation of solitary waves over constant slopes. The solitary wave example is a good test for the model in that it allows for a careful test of the propagation speed of an isolated pulse in the absence of any extra noise sources (such as wave reflection). In addition, the wave height to water depth ratios reached prior to breaking are higher than for most periodic incident waves, and thus a more severe test is made of the nonlinear portion of the model.

In this section, we apply the present model with and without high-order nonlinear terms to simulate solitary wave propagation over four constant slopes. For each slope, three solitary waves with initial wave height to water depth ratios δ between 0.2 to 0.6 are used as model inputs. Results of wave shapes, wave heights, wave celerities and vertical variation of horizontal velocity are compared in detail with those obtained from the boundary element model developed by Grilli *et al.* (1989). Since the boundary element model solves the exact boundary value problem (2.6)–(2.9) for potential flow, we refer to the model to as fully nonlinear potential flow (FNPF) model. For convenience of comparison, we refer to the

present model with and without high order nonlinear terms to as fully nonlinear Boussinesq model (FNBM) and Boussinesq model (BM), respectively.

As shown by Grilli *et al.* (1994), numerical results from FNPF model were quite accurate compared with laboratory data. For solitary wave shoaling over a 1/35 slope, they showed that surface elevations could be calculated to within 1% of the measurements, up to and beyond the theoretical breaking point for which the wave has a vertical tangent on the front face. Therefore, results from the FNPF model serve as accurate data for comparison.

Figure 5.6 shows the computational domain for the study of solitary wave shoaling. Constant water depths of h_0 and h_s are on both ends connected by a constant sloping beach with slope s . Coordinates were set such that the toe of the slope correspond to $x = 0$. For FNBM and BM models, solitary waves were generated at the leftward boundary and propagated to the right. The four slopes are $s=1:100$, 1:35, 1:15 and 1:8, which should cover all natural beaches from gentle to steep. For each slope, the incident wave height is varied from $\delta = 0.2$ to $\delta = 0.6$, which corresponds to a variation from weak to strong nonlinearity. Dimensionless variables are used for showing computing results, with the use of h_0 , $\sqrt{h_0/g}$ and $\sqrt{gh_0}$ to scale the corresponding length, time, and velocity variables. The resulting dimensionless variables are denoted by primes.

The permanent form solitary wave solution obtained for the same initial height in the three models is different due to different levels of approximation in the equations. In the FNPF computations, an exact solution of the fully nonlinear equations, obtained using Tanaka's (1986) method, was used as an initial wave and introduced directly on the free surface. For FNBM and BM, however, numerical experiments were performed to obtain the corresponding solitary wave solutions to be used as model inputs. The detailed method for obtaining the solitary wave with

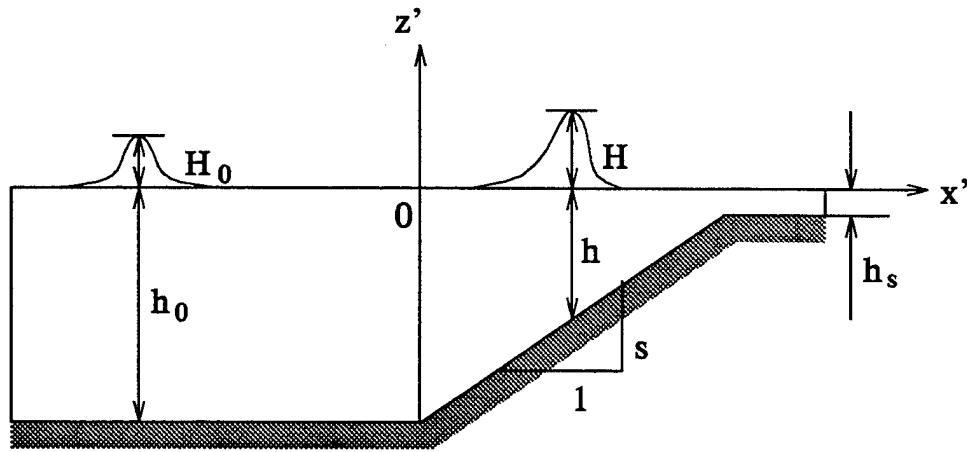


Figure 5.6: Definition sketch for both the FNPF computations and for the Boussinesq models.

the required wave height and comparison of the stable solution forms have been described in the previous section. To account for the slight difference in solitary wave solutions for constant depth in the three models, results of computations were synchronized at $t' = 0$, taken to be the time when wave crests reached the toe of the slope, $x' = 0$. A comparison of evolving solitary wave profiles obtained in the three models is shown in Figure 5.7. The four plots, (a), (b), (c) and (d) correspond to slopes of 1:100, 1:35, 1:15, and 1:8, respectively. The initial wave heights are $\delta = 0.2$ for (a), (b) and (d) but $\delta = 0.3$ for (c). The first profile to the left in each plot corresponds to the waves being at a location roughly half way up the slope. Wave asymmetry is not too pronounced yet, and one can see that both Boussinesq solutions agree quite well with the FNPF solution. The last profile in Figure 5.7 (a), (b), and (c) corresponds to the theoretical breaking points in the FNPF computations, for which the wave has a vertical tangent on the front face. No breaking occurs for the condition in Figure 5.7 (d). Breaking occurs in Figure

5.7(b) for $t' = 25.94$ at $x'_b = 25.90$, and with a breaking index $H_b/h_b = 1.402$. This breaking point was found by Grilli *et al.* (1994) to also closely correspond to measured breaking locations and characteristics in well controlled laboratory experiments.

Results in Figure 5.7 show that, with both the BM and the FNBM models, the wave crests travel almost at the right speed in the early shoaling. For the $s = 1 : 100$ slope, the BM and FNBM wave crests continue to grow in height while the FNPF pitches forward and decreases in height just prior to breaking. The results for the FNPF and FNBM model differ most in this case. For the steeper beaches, the FNBM predicts both the wave height and crest position with much greater accuracy than the BM model. The BM results on the three mildest slopes indicate that the wave significantly overpredicts as compared to the FNPF results, particularly in the upper slope region, and a spurious secondary trough is predicted behind the main crest. With the FNBM, however, overshooting is much less pronounced, and the spurious troughs are almost non-existent.

Results for the relative wave height, H/h , computed with all three models, are given in Figure 5.8 as a function of x' . Symbols (o) denote the FNPF breaking point, determined by the x' location where the wave reaches a vertical tangent on the front face. One can see that, as expected from above, relative wave height is significantly overpredicted at the breaking point in the BM, whereas little or no overprediction occurs in the FNBM. Beyond the theoretical breaking point, wave heights grow in an unbounded fashion in both Boussinesq models. Figure 5.8 also shows that, with the BM, overshooting mostly occurs in the region of high nonlinearity (i.e., high H/h) closer to the breaking point. This is due to insufficient nonlinear effects included in the BM equations; much of the error is eliminated in the FNBM.

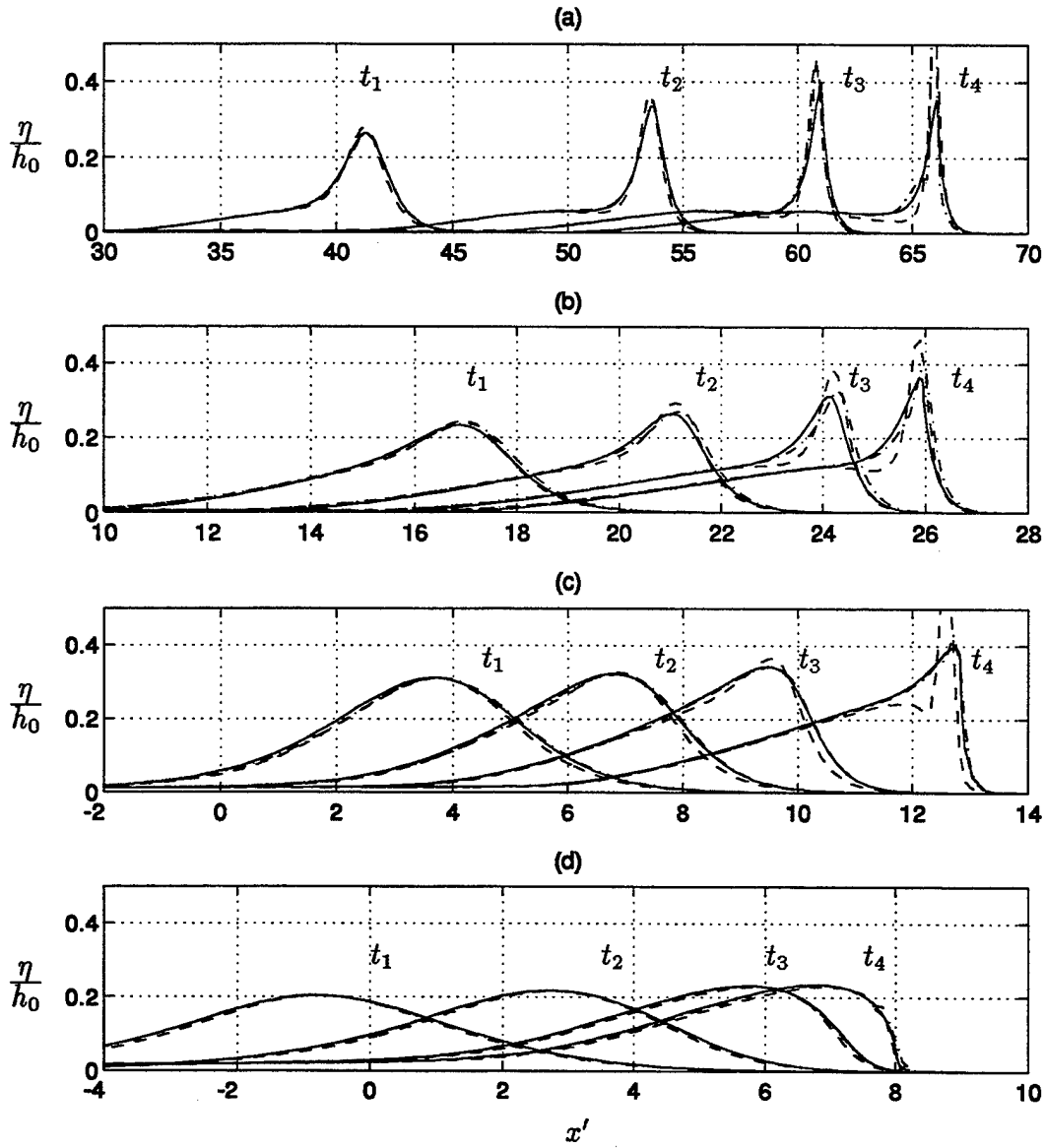


Figure 5.7: Comparison of surface elevations for the shoaling of solitary waves between FNPF (—), BM (----), and FNBM (-·-·).

(a) $s=1:100$, $\delta=0.2$, $(t_1, t_2, t_3, t_4)=(39.982, 53.191, 61.131, 66.890)$;

(b) $s=1:35$, $\delta=0.2$, $(t_1, t_2, t_3, t_4)=(16.243, 20.640, 24.032, 25.936)$;

(c) $s=1:15$, $\delta=0.3$, $(t_1, t_2, t_3, t_4)=(3.230, 6.000, 8.401, 11.320)$;

(d) $s=1:8$, $\delta=0.2$, $(t_1, t_2, t_3, t_4)=(-0.739, 2.575, 5.576, 6.833)$;

The last FNPF profiles in (a), (b) and (c) correspond to the theoretical breaking point for which the wave front face has a vertical tangent.

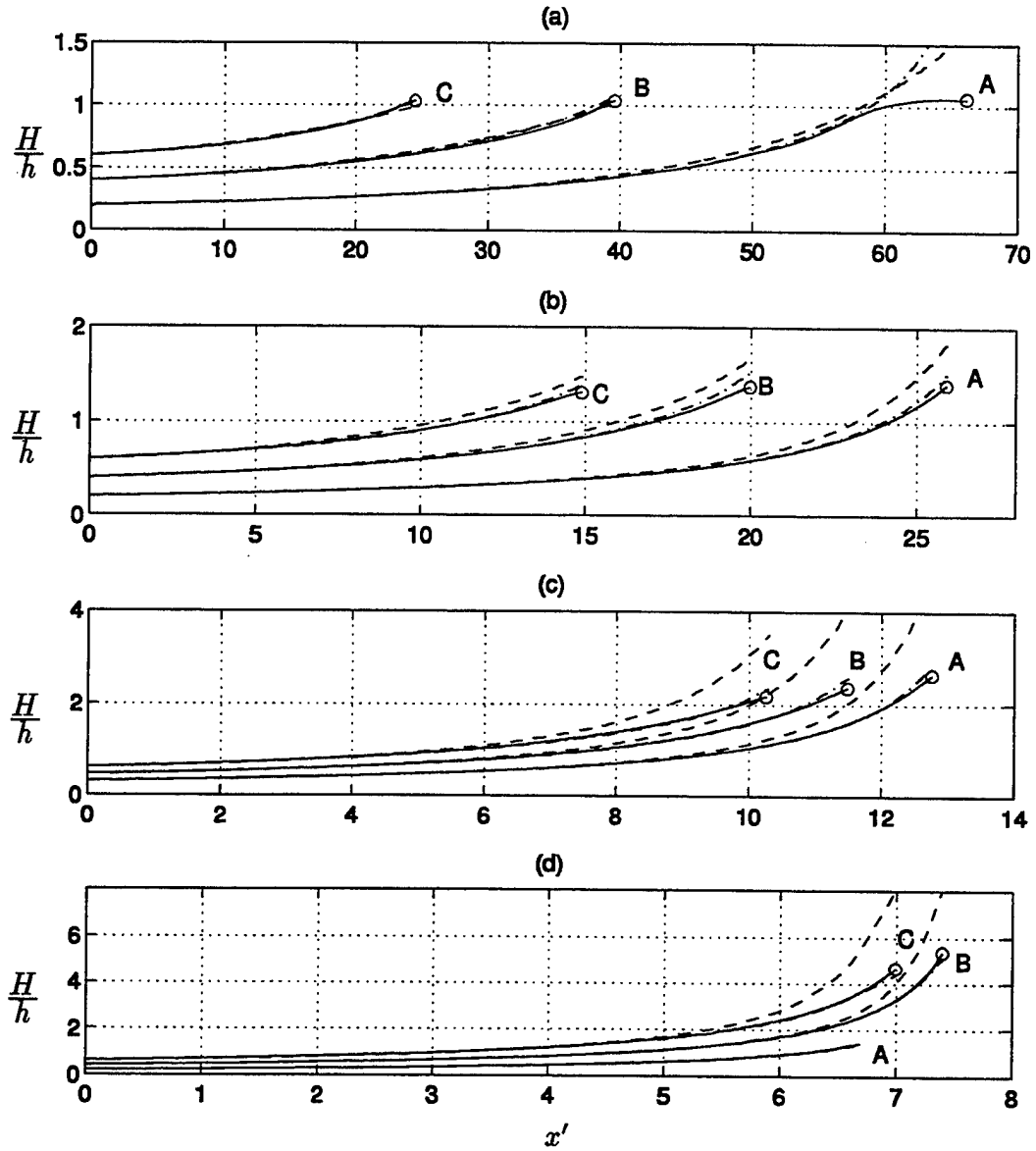


Figure 5.8: Comparison of shoaling rates, H/h , for solitary waves between FNPF (—), BM (----), and FNB (— · —).
 (a) $s=1:100$, $\delta = (0.20, 0.40, 0.60)$ for (A, B, C);
 (b) $s=1:35$, $\delta = (0.20, 0.40, 0.60)$ for (A, B, C);
 (c) $s=1:15$, $\delta = (0.30, 0.45, 0.60)$ for (A, B, C);
 (d) $s=1:8$, $\delta = (0.20, 0.40, 0.60)$ for (A, B, C);
 Symbols (o) denote locations of the breaking point for which the wave has a vertical tangent on the front face.

Wave celerities were calculated for three incident wave heights, for each slope, using all three models. First, we obtained the time series of the crest location x'_c . Then three point finite differencing was applied to compute the crest celerity c'_c . The estimation of the celerity values from the Boussinesq models was fairly straightforward, and the results are well represented by an 11-point running average fit to the values of c'_c . For the FNPF model, the celerity estimates exhibited a great deal of jitter, and also exhibited a much more complex functional dependence on x' due to the rapid change of the wave crest at and just beyond the breaking point. For this model, results are presented in terms of a 25th-order polynomial fit to the original raw data. All data processing was done using Matlab.

Results are reported in Figure 5.9 for the crest celerity $c'_c = \frac{dx'_c}{dt} / \sqrt{gh_0}$, as a function of crest location x'_c . The corresponding incident wave celerity c'_0 is almost identical in all three models. Results show that both Boussinesq models slightly underpredict the wave crest celerity as compared to the FNPF results for most of the shoaling process, with a larger discrepancy close to the breaking point. This was already observed in Figure 5.7.

Particle velocity at the crest is defined as $V'_c = \sqrt{u'^2_c + w'^2_c}$, where u'_c and w'_c are the horizontal and vertical velocity components. The comparison of V'_c for all three models is shown in Figure 5.10(a), (b), (d) for $\delta = 0.2$ and in Figure 5.10(c) for $\delta = 0.3$, where the corresponding crest celerities have also been reproduced from Figure 5.10. The FNPF model predicts, as expected, that $V'_c \geq c'_c$ at breaking on the three milder slopes (in fact slightly beyond the breaking point). The particle velocity at the crest in the BM starts diverging from the FNPF solution about half way up the slope and becomes quite large. This result is due to the overshooting in the BM wave and the resulting overprediction of downward crest

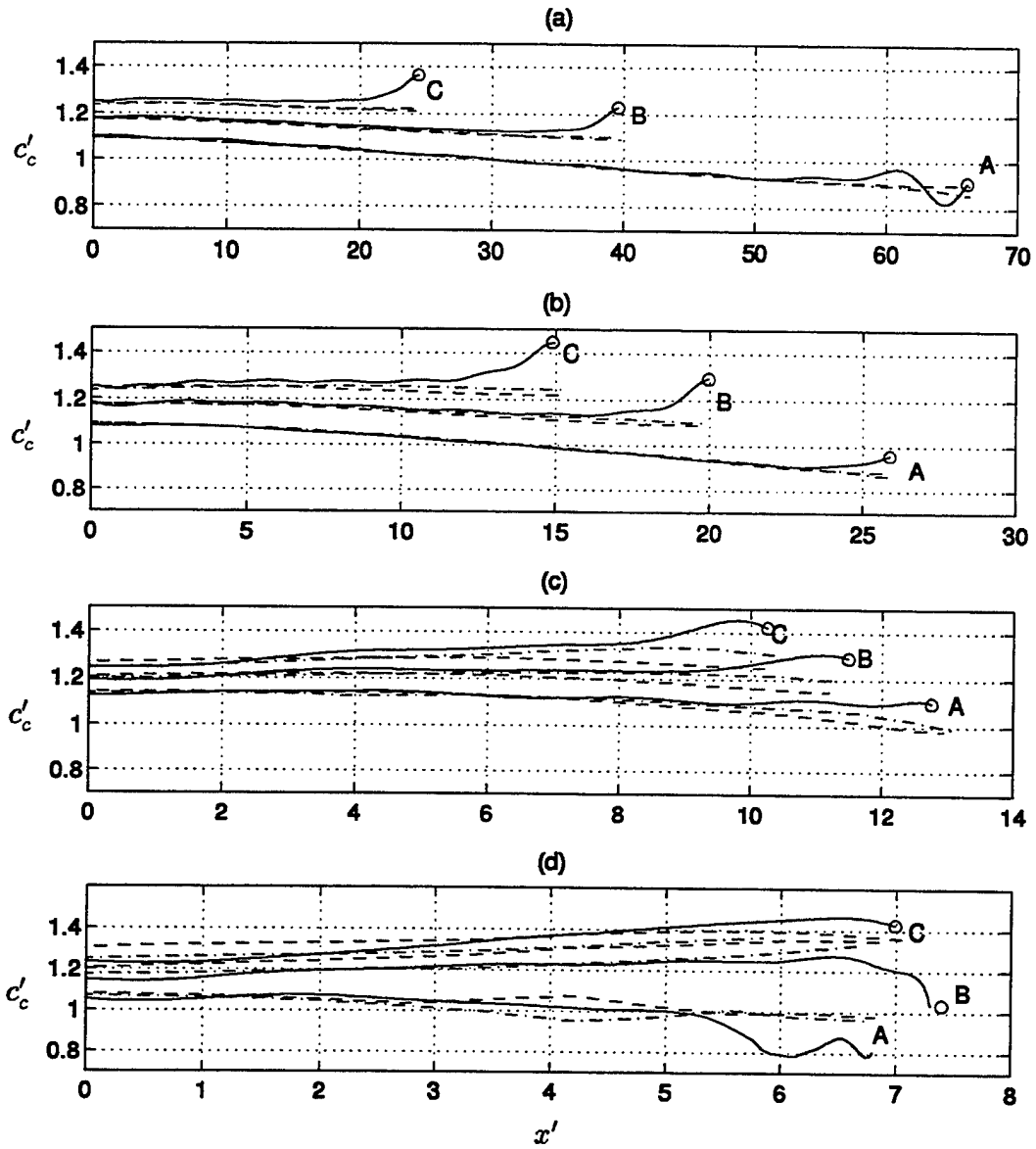


Figure 5.9: Comparison of crest celerity c'_c for the same solitary waves between FNPF (—), BM (----), and FNBM (-·-·-). Legends for the plots are the same as the previous Figure.

curvature. In contrast, the particle velocity in the FNBM stays quite close to the FNPF prediction up to the breaking point for all but the gentlest slopes. In fact, despite the discrepancies at breaking in the FNBM, $V'_c = c'_c$ (i.e., breaking) roughly occurs at the same location as in the FNPF model.

Vertical profiles of horizontal velocity at three different locations are shown in Figure 5.11 for the case of 1:35 slope and wave height $\delta = 0.2$. In the Boussinesq models, the horizontal velocity at a certain depth $z = z_\alpha = -0.531h$, is determined by the model and the corresponding derivatives are computed. Then the variation of horizontal and vertical velocity with water depth z is given by

$$u = u_\alpha + \frac{z_\alpha^2 - z^2}{2}(u_\alpha)_{xx} + (z_\alpha - z)(hu_\alpha)_{xx} \quad (5.3)$$

$$w = -(h + z)(u_\alpha)_x - h_x u_\alpha \quad (5.4)$$

Generally, the velocity profiles of FNBM compare quite well with those of FNPF. The FNBM predict average, surface and bottom velocities reasonably accurately, the main discrepancy being the underprediction of profile curvature owing to the limitation of the quadratic velocity profile used in the model formulation. Most notably, the prediction of the kinematics retains its accuracy up to the wave breakpoint.

The comparison of velocity profiles between BM and FNPF are less satisfactory. The combined effects of incorrectly predicted values of u_α and the overprediction of wave heights and crest curvature in the BM result in larger horizontal velocities, especially at the crest. Horizontal velocities are overpredicted by almost 50% over much of the final stage of shoaling in the BM.

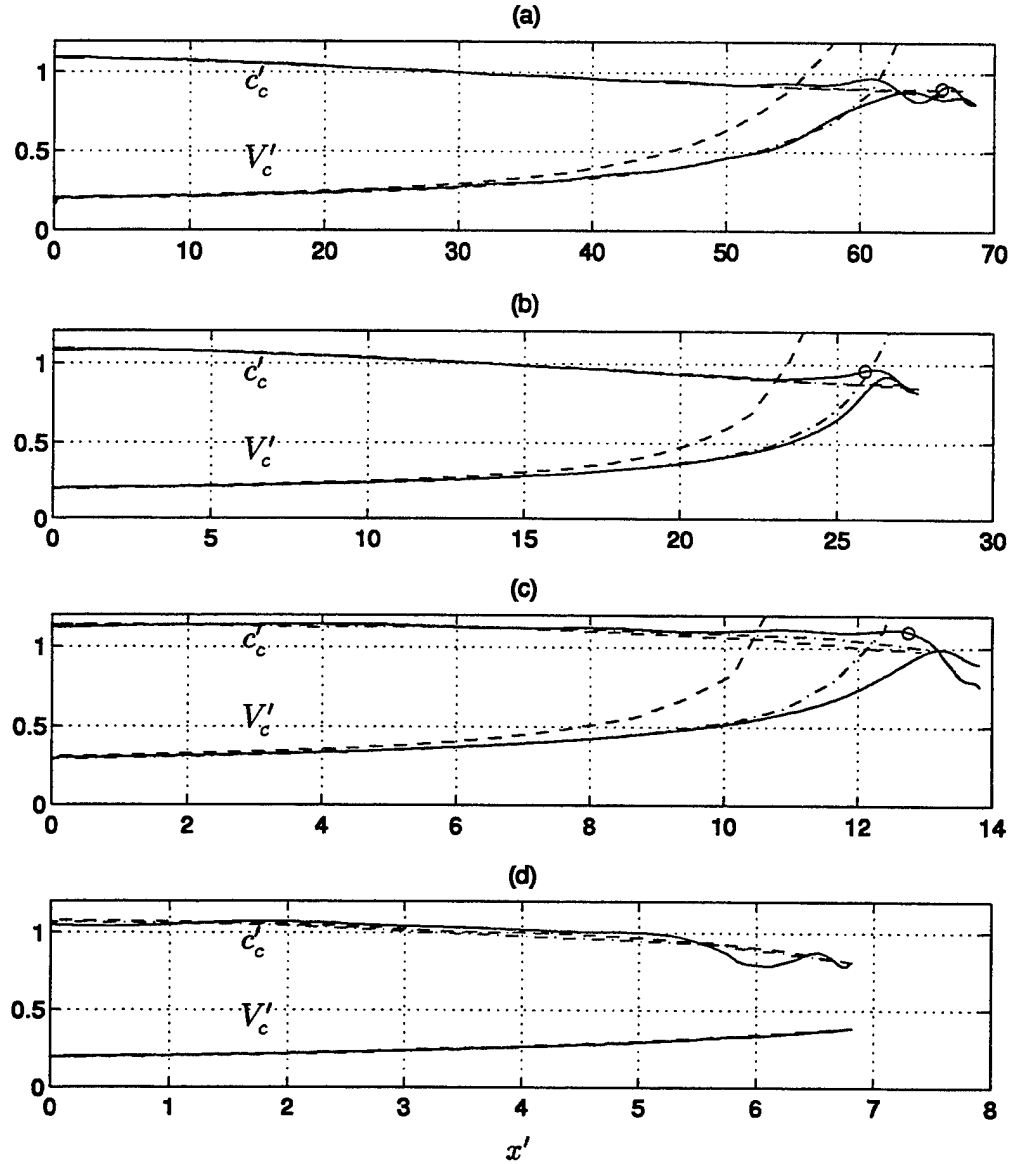


Figure 5.10: Comparison of wave crest celerity c'_c and particle velocity V'_c at the crest between FNPF (—), BM (----), and FNBM (-·-·-). Legends are the same as the previous Figure.

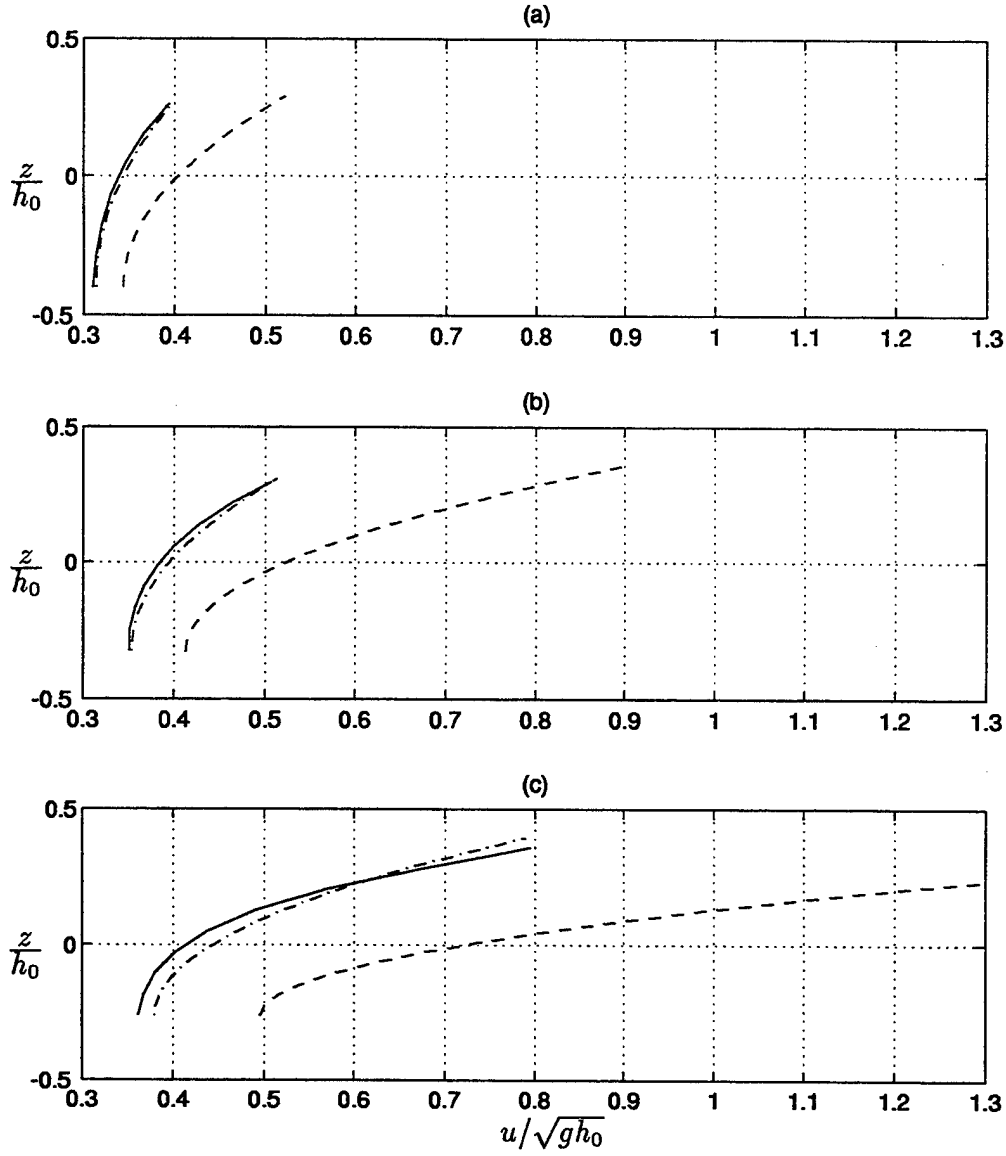


Figure 5.11: Comparison of horizontal velocity profiles between FNPF (—), BM (---), and FNBM (-·-·). The initial wave height is $\delta = 0.2$ and the slope is $s = 1 : 35$. The location for obtaining velocity profiles are at: (a) $x' = 20.96$; (b) $x' = 23.63$; (c) $x' = 25.91$.

5.3 Undular Bore Propagation

When an undular bore propagates into a still water area with constant depth, waves will be generated and propagate out of the bore front. This problem has been studied by a number of investigators and serves as a standard illustration of competing effects of dispersion and nonlinearity. Peregrine (1966) compared the differences between Boussinesq theory and Airy's theory for nonlinear long waves using this example. While results from a Boussinesq model showed wave generation and propagation, results based on Airy's theory only indicated the steepening of the bore front. In this section, we apply the Boussinesq models (FNBM and BM) to study this problem and compare results with those obtained from FNPF model.

As shown in Figure 5.12, the initial conditions for an undular bore is a gentle transition between a uniform flow on the left end and still water on the right, which is defined:

$$u = \frac{1}{2}u_0[1 - \tanh(x/a)] \quad (5.5)$$

$$\eta = u + \frac{1}{4}u^2 \quad (5.6)$$

where η and u are the surface elevation and the horizontal velocity, x is the horizontal coordinate with $x = 0$ corresponding to the center of the initial bore, u_0 is the velocity of uniform flow from the left boundary, and a is a number sufficiently large that the initial motion could be described by Airy's theory (Peregrine, 1966). In all the computation below, we use $a = 5$. Three different values of u_0 are chosen so that the initial heights at the left boundary are $\delta = \eta_0/h_0 = 0.1, 0.2, 0.3$. Due to the presence of vertical acceleration in the transition region between the two uniform depth asymptotes, waves are generated from the initial smooth transition in models incorporating dispersive effects. The number and height of waves increases gradually with time, until a nearly uniform cnoidal wave train is developed.

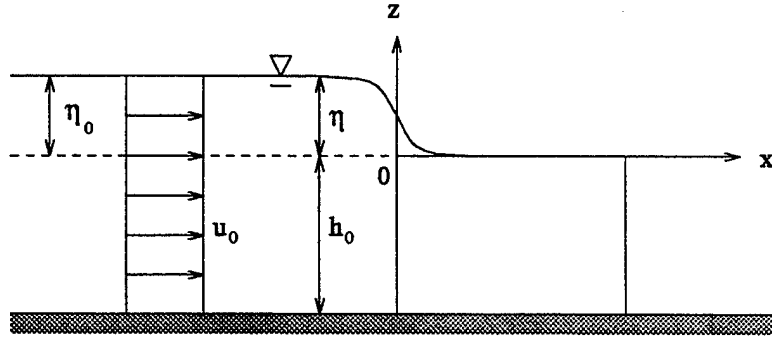


Figure 5.12: Initial conditions for an undular bore.

To compute the evolution of the undular bore, the initial solutions of η and u in expressions (5.5) and (5.6) are introduced as the initial conditions for FNBM and BM. For the FNPF model, the corresponding initial free surface potential $\phi(x)$ is obtained by integrating $u(x)$ as a function of x and the initial normal velocity $\frac{\partial \phi}{\partial n}(x)$ is obtained by projecting $u(x)$ on the normal direction.

Figures 5.13 and 5.14 show the comparison of wave profiles at different times. For small values of δ as in plot (a) results from BM and FNBM are very close, indicating that the effects of the higher order nonlinear terms in FNBM are negligible for small nonlinearity. For large values of δ as in (b) and (c), however, the wave heights predicted by BM are larger than those predicted by FNBM, and the predictions of the FNBM agree more closely with the FNPF model. In addition, the wave crest speeds predicted by FNBM are closer to FNPF model results than are those predicted by BM for all wave crests in the evolving wave train.

In Figure 5.15, we plot the elevations of the first three wave crests and wave troughs as a function of distance traveled for the same three conditions as in

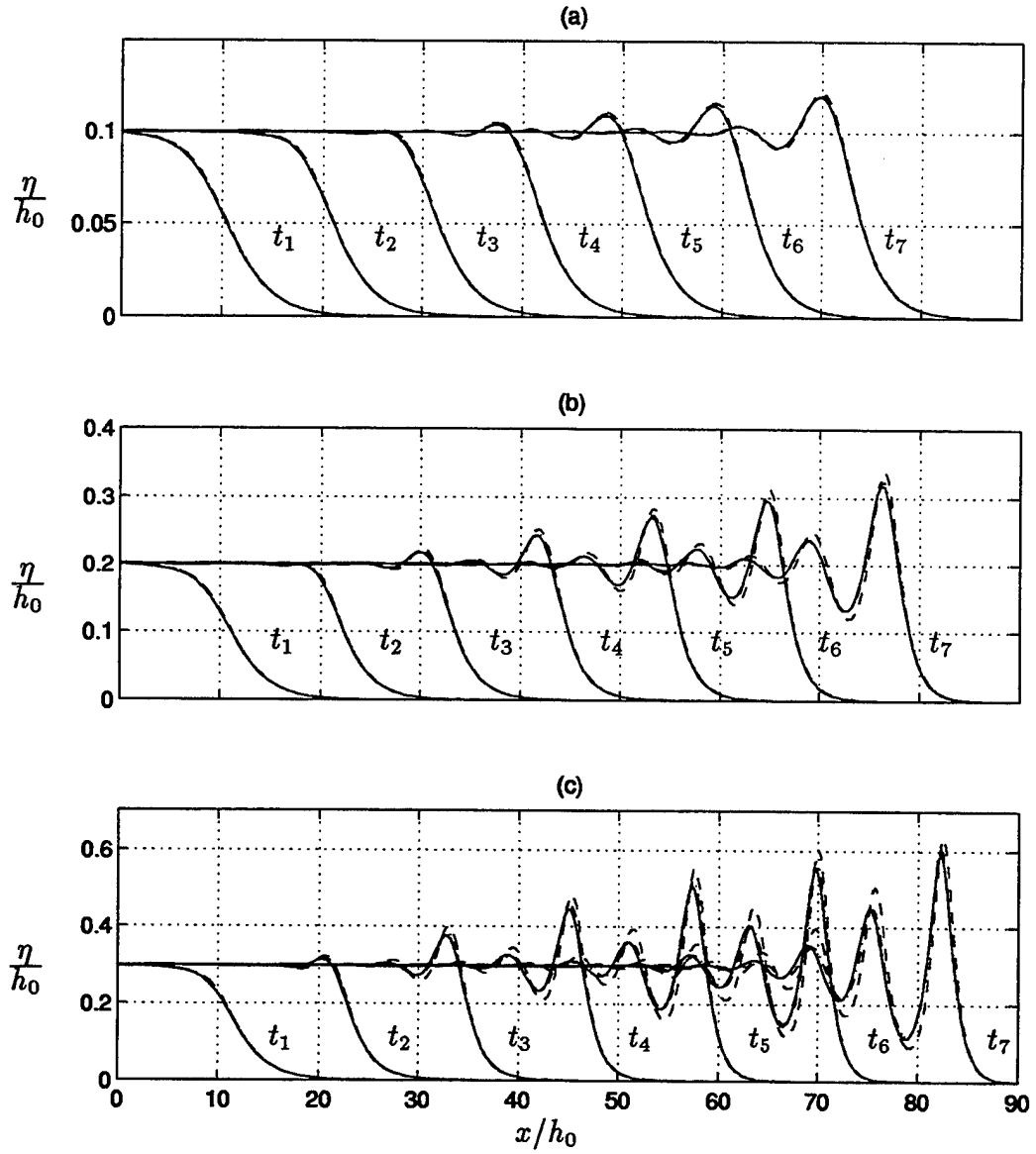


Figure 5.13: Comparison of free surface elevations for undular bores between FNPF (—), BM (----), and FNBM (-·-·-). The initial wave heights are: (a) $\delta = 0.10$; (b) $\delta = 0.20$; and (c) $\delta = 0.30$. The dimensionless time are at $t' = (t_1, t_2, t_3, t_4, t_5, t_6, t_7) = (10, 20, 30, 40, 50, 60, 70)$.

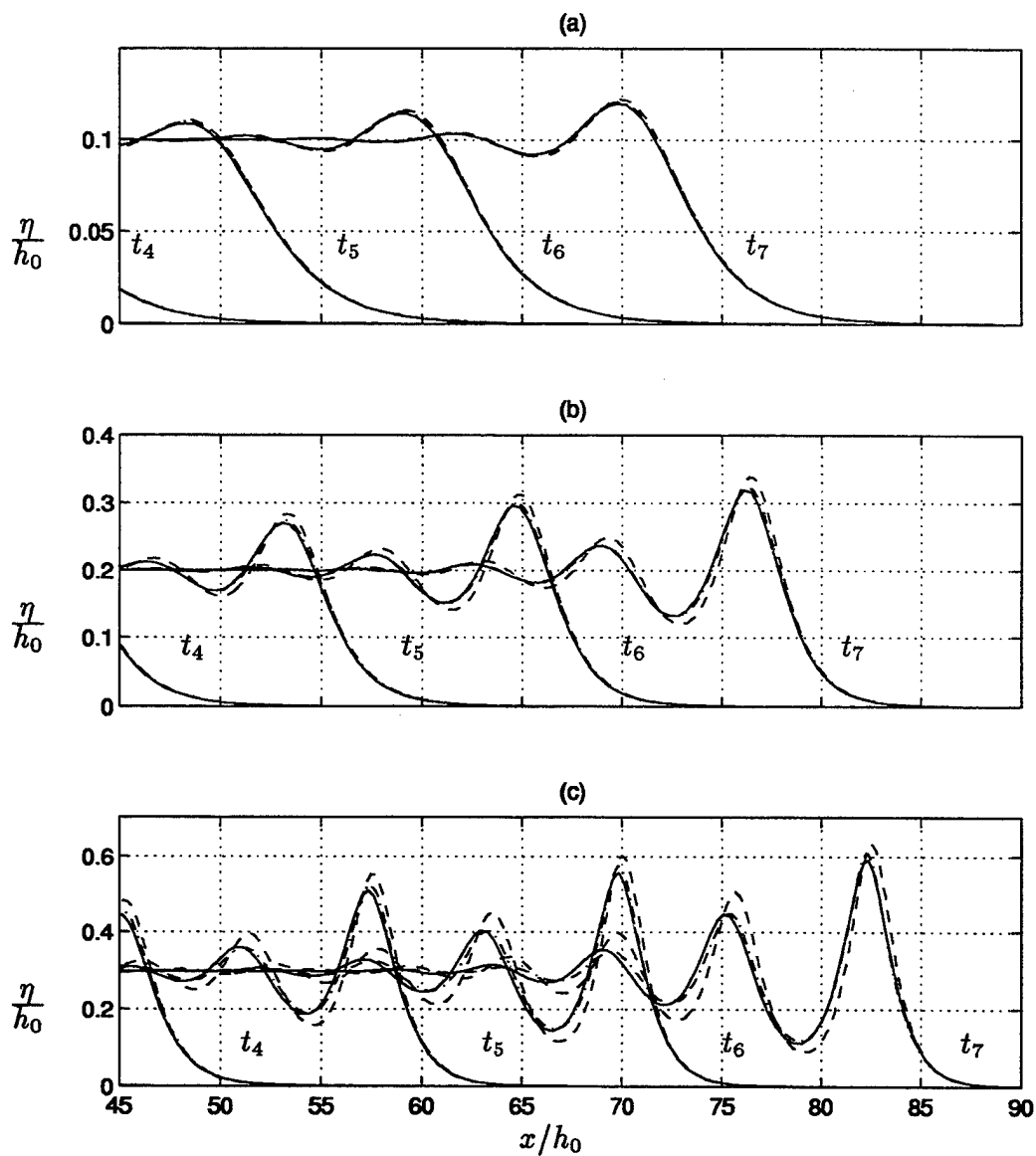


Figure 5.14: Comparison of free surface elevations for undular bores between FNPF (—), BM (---), and FNBM (-·-·-). Legends are the same as previous Figure.

Figures 5.13 and 5.14. We see that, in general, both crest elevations and trough depths increase with time, as was noted by Peregrine (1966) and other investigators. For small nonlinearity (Figure 5.14a), results from BM are similar to those of FNBM, and both Boussinesq models overpredict wave height compared to the FNPF model. However, for large nonlinearity, the FNBM does a reasonable job of predicting the height of the leading wave crest and an excellent job of predicting the subsequent crests and troughs, compared to the FNPF. The wave heights from BM are no longer close to those of FNBM, indicating that the additional nonlinear terms in FNBM are important for this case. The wave crests and troughs from FNBM compare quite well with the predictions of the FNPF.

5.4 Random Wave Propagation Over a Slope

To study random wave shoaling and breaking, Mase and Kirby (1992) conducted a laboratory experiment on random wave propagation over a planar beach. Figure 5.16 shows the experiment layout, where a constant depth on the left connects to a constant slope on the right. Two sets of random waves with peak frequencies 0.6Hz (*run1*) and 1.0Hz (*run2*) are generated by a wavemaker on the left end and propagate through the flat bottom and then over the slope. Starting at the toe, 12 wave gages are deployed along the slope at locations whose water depths are $h = 47, 35, 30, 25, 20, 17.5, 15, 12.5, 10, 7.5, 5, 2.5\text{ cm}$. Time series of surface elevation η at these locations are collected simultaneously for about 14.7 minutes for *run1* and 12.5 minutes for *run2*.

The experiment was conducted in a narrow wave tank so that the 1-D numerical model is sufficient to apply to this case. The values of kh corresponding to peak frequencies at water depth $h = 47\text{ cm}$ are about 0.9 for *run1* and 2.0 for *run2*. Though applicable to the case of *run1*, standard Boussinesq equations are

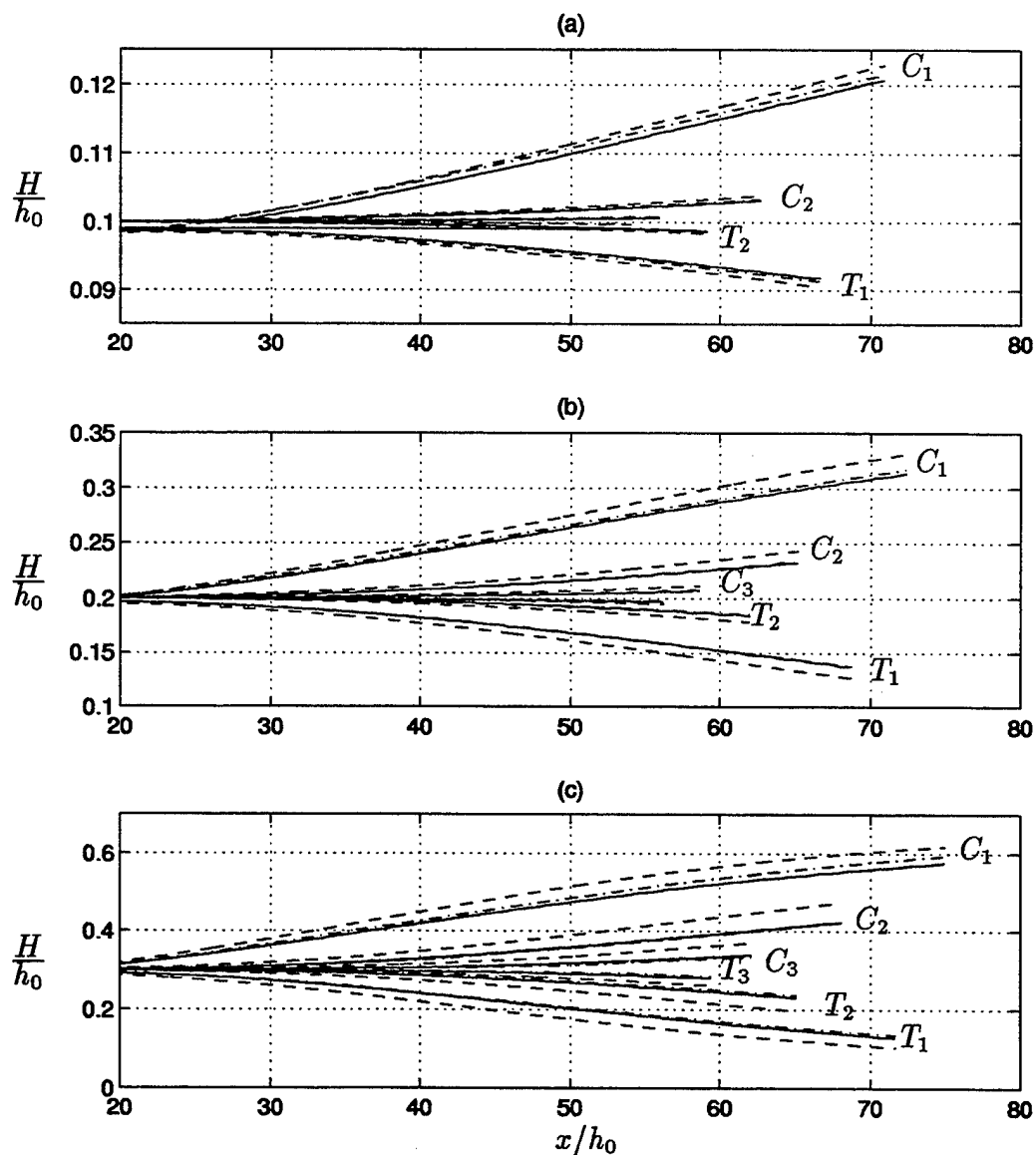


Figure 5.15: Comparison of wave crests and troughs between FNPF (—), BM (----), and FNBM (····). The initial wave height to water depth ratios are: (a) $\delta = 0.10$; (b) $\delta = 0.20$; and (c) $\delta = 0.30$. C_1 , C_2 and C_3 represent the first, second and third wave crests, T_1 , T_2 and T_3 represent the first, second and third wave troughs.

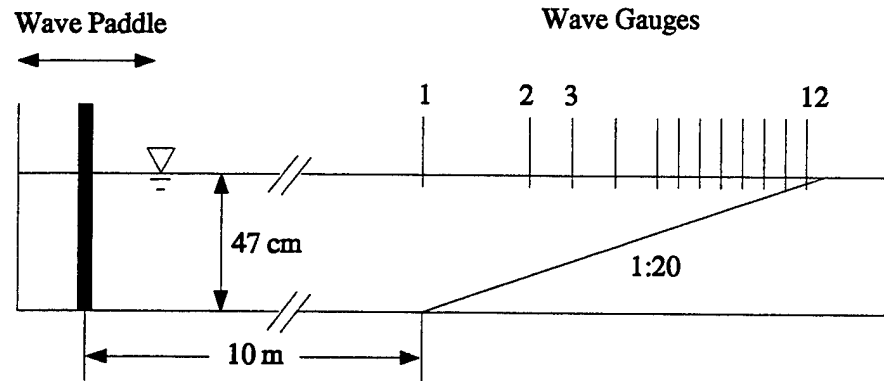


Figure 5.16: Experiment layout of Mase & Kirby (1992).

not valid for the case of *run2* due to large kh value. However, with improved linear dispersion properties in intermediate water depth, the present Boussinesq model should be valid for both cases. In the following, the model will be applied to simulate the propagation of random waves corresponding to the case of *run2*.

Due to the lack of data near the wavemaker and along the region of constant water depth, the computing domain is different from the physical domain. The center of the source region for generating the required random waves in the model is set at the toe of the slope where measured data is available. The shoreline boundary at the high end of the slope is replaced by a constant water depth of 2 cm at the right end of the domain. Sponge layers are added at both ends of the domain to absorb wave energy. The grid size is chosen as $\Delta x = 0.025\text{ m}$ and the time step is $\Delta t = 0.02\text{ s}$, resulting in a Courant number of 1.72 corresponding to a depth of $h = 0.47\text{ m}$.

As described in Chapter 3, it is possible for the present model to choose

four different sets of governing equations by changing certain control parameters. These four sets of equations are nonlinear shallow water equations, standard Boussinesq equation, Nwogu's extended Boussinesq equations, and fully nonlinear Boussinesq equations. Keeping the same numerical scheme and boundary conditions, we will be able compare the characteristics of these four models for the simulation of random waves.

Figure 5.17 shows the time series comparison for surface elevation η between three Boussinesq models, *i.e.* Nwogu's extended Boussinesq model, the fully nonlinear Boussinesq model, and the standard Boussinesq model. For illustration purpose, only the time series obtained at the depth $h = 35\text{ cm}$ are shown. The numerical results are indicated by dashed lines and experiment data by solid lines. With improved linear dispersion property in intermediate water depth, results from the extended Boussinesq model and the fully nonlinear model are in good agreement with the data. The small difference between these two Boussinesq models indicate that those high-order nonlinear terms in fully nonlinear Boussinesq equations have less effect on wave transformation at this location. Results from the standard Boussinesq model, however, match experiment data quite poorly, in both amplitude and phase, indicating that the standard Boussinesq model is not valid for this case due to large value of kh .

For the extended Boussinesq model, we obtained the corresponding time series of surface elevation η at the same locations as those 11 wave gages (deployed at the depths $h=35, 30, 25, 20, 17.5, 15, 12.5, 10, 7.5, 5, 2.5\text{ cm}$) from which experiment data were collected. Figure 5.18 shows the comparison of η from $t = 20\text{ s}$ to $t = 40\text{ s}$ between the model results and the experiment data at those gages. Notice that the data from the first gage (at $h = 47\text{ cm}$) was used as the input for the model to generate the corresponding time series of source function.

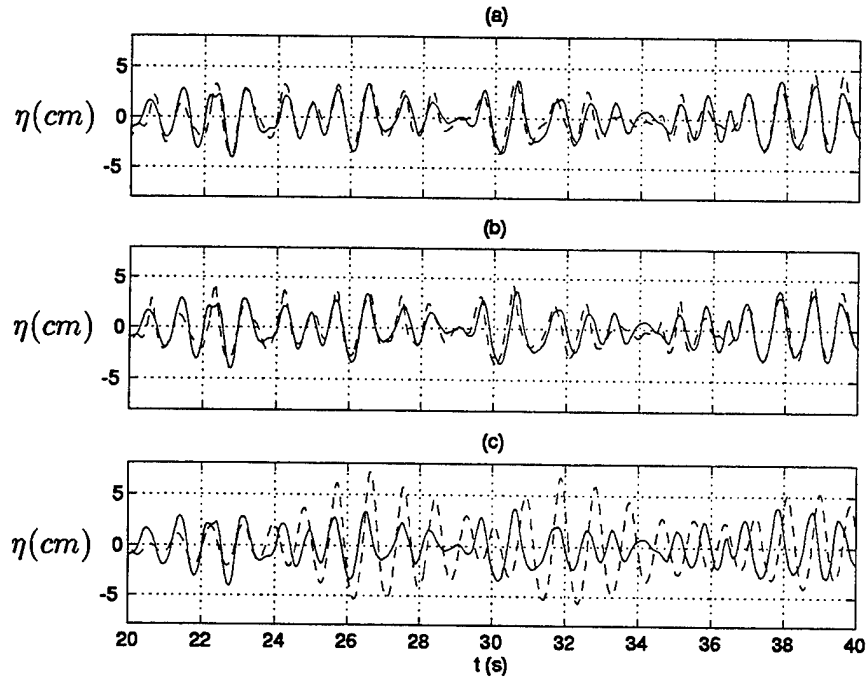


Figure 5.17: Time series comparison of η between three different Boussinesq models (----) and data (—) at $h = 35 \text{ cm}$: (a) Nwogu's extended Boussinesq model; (b) fully nonlinear Boussinesq model; and (c) standard Boussinesq model.

Due to the inclusion of source function inside the source region, it is meaningless to compare the surface elevation obtained from the model with data for this gage. In the model, the actual shoreline condition was replaced by a sponge layer with constant water depth of 2 cm . From the model results, the sponge layer effectively absorbed wave energy and reduced possible wave reflection from the boundary back to the domain. Despite the difference in the setting for the physical and computing domains, surface elevations obtained from the model agree quite well with experimental data.

In the experiment, most of the waves started breaking at the depth $h =$

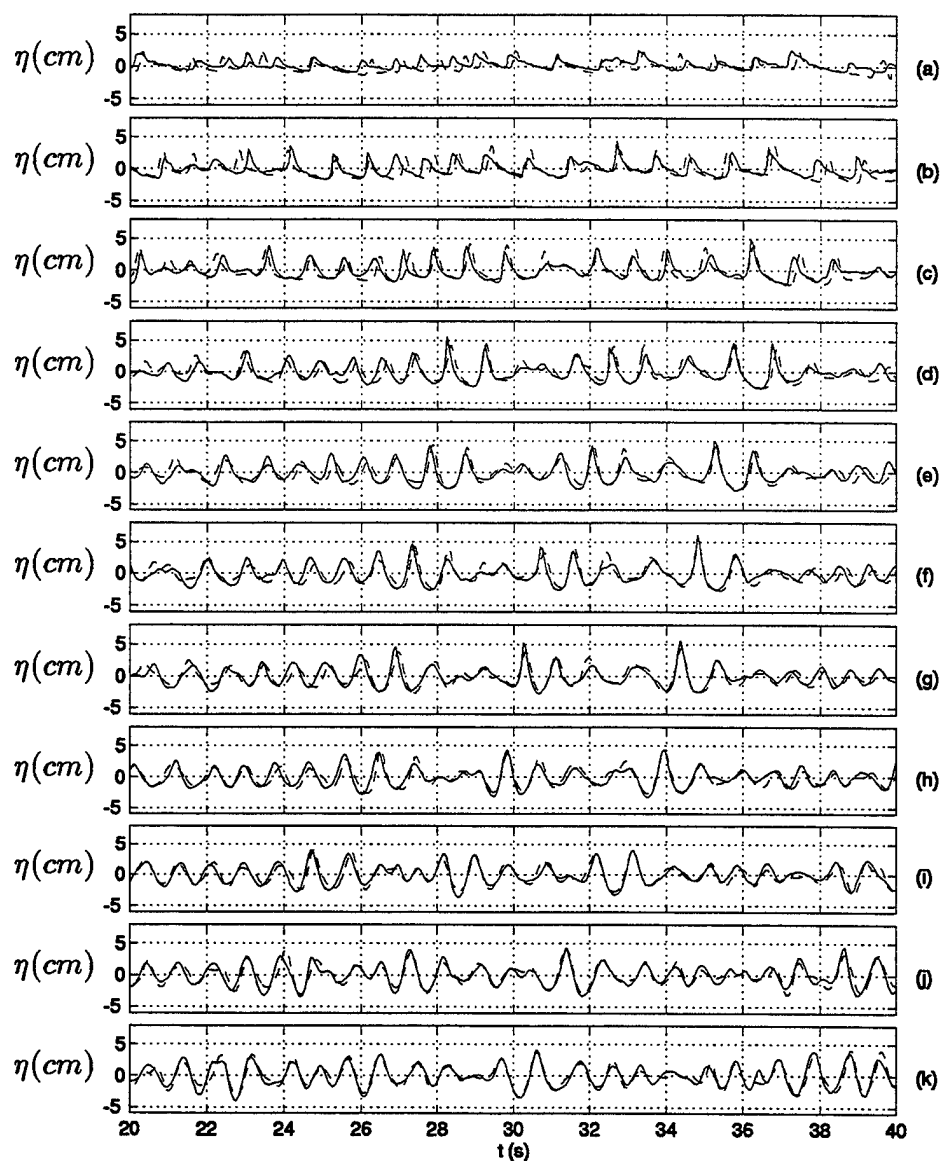


Figure 5.18: Comparison of time series of η between model (----) and data (—) at 11 wave gage locations: (a) $h = 2.5 \text{ cm}$; (b) $h = 5 \text{ cm}$; (c) $h = 7.5 \text{ cm}$; (d) $h = 10 \text{ cm}$; (e) $h = 12.5 \text{ cm}$; (f) $h = 15 \text{ cm}$; (g) $h = 17.5 \text{ cm}$; (h) $h = 20 \text{ cm}$; (i) $h = 25 \text{ cm}$; (j) $h = 30 \text{ cm}$; and (k) $h = 35 \text{ cm}$.

15 cm. To simulate wave breaking, the corresponding eddy viscosity terms described in Chapter 4 were turned on in the numerical model when computed wave properties exceed the breaking criteria. The eddy viscosity terms are quite localized and generate high frequency noises which will eventually cause stability problem for the model. To solve this problem, more frequent use of numerical filtering was employed in the model. This was accomplished first by recording the number of time step when wave breaking occurs. Then the 9 point filtering formula (3.124) was applied to filter surface elevation and horizontal velocity every 50 time steps when wave breaking happens, in addition to the regular filtering for every 100 time steps. With this additional numerical filtering, the model was able to run for the entire time series of data without any stability problem. A sample of time series comparison for surface elevations between the model and data are shown in Figure 5.19, which is corresponding to time interval from $t = 620$ s to $t = 640$ s. Comparisons for other data segments between the model results and the experiment data are as good as those in Figures 5.18 and 5.19.

Instead of comparing the time series of surface elevation obtained from the model and the experiment at each time interval, it is more practical to compute the statistical properties from these time series. In the experiment, the data was collected after the generated random waves have propagated through the domain. In the model, however, the initial conditions for surface elevation and velocity are all set to zero. For meaningful comparison between the model and the data, the first 20 seconds of model results and data must be discarded. Due to the use of FFT in the model to compute the source function, the last portion of data for about 33 seconds was cut off in the model computation. Therefore, the total length of data for statistical calculation between model and data is about 11.5 minutes.

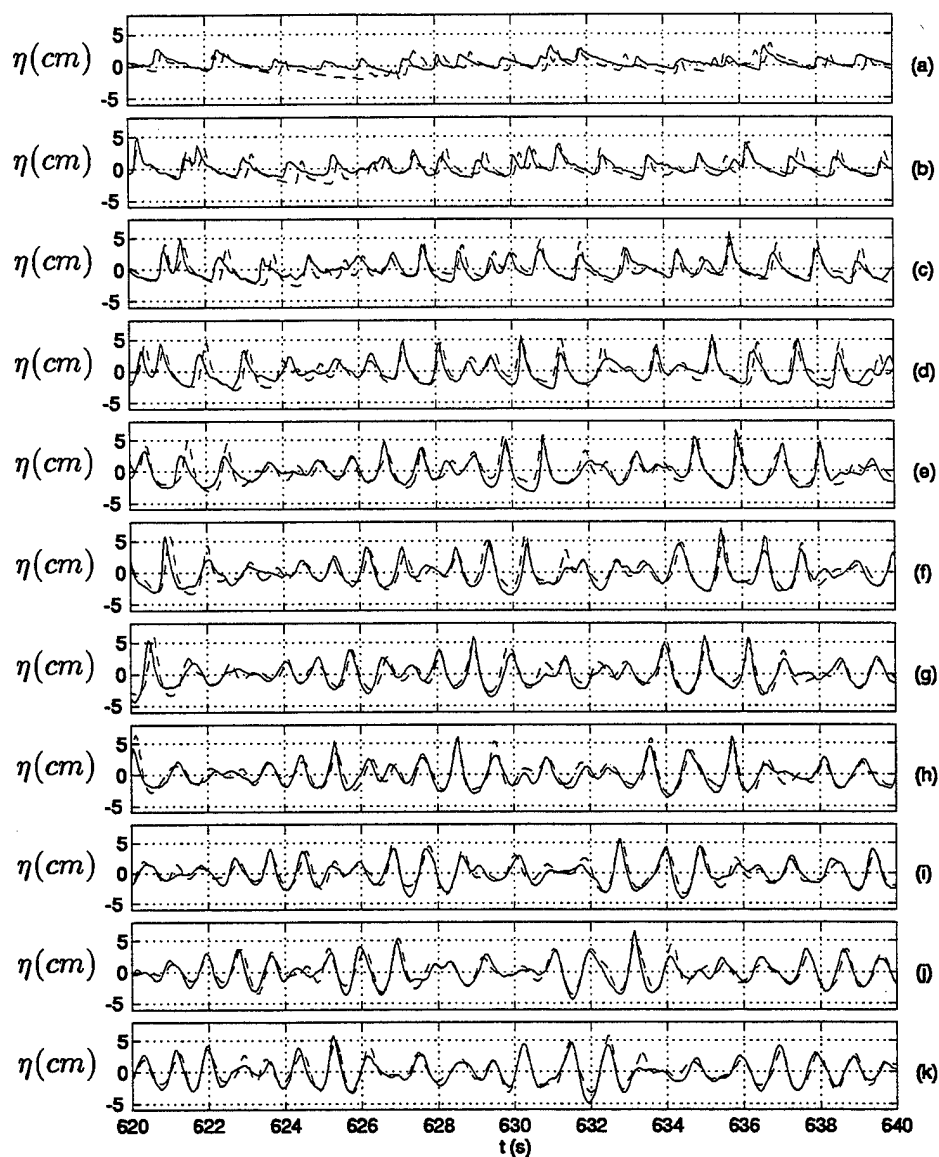


Figure 5.19: Comparison of time series of η between model (----) and data (—) at 11 wave gage locations: (a) $h = 2.5 \text{ cm}$; (b) $h = 5 \text{ cm}$; (c) $h = 7.5 \text{ cm}$; (d) $h = 10 \text{ cm}$; (e) $h = 12.5 \text{ cm}$; (f) $h = 15 \text{ cm}$; (g) $h = 17.5 \text{ cm}$; (h) $h = 20 \text{ cm}$; (i) $h = 25 \text{ cm}$; (j) $h = 30 \text{ cm}$; and (k) $h = 35 \text{ cm}$.

Figure 5.20 shows the comparison of statistical properties between the model and data. The standard deviation σ , as shown in Figure 5.20(a), is straightforward to compute from the corresponding sets of data after the removal of the mean. One of the important statistical property for a random wave train is the root mean square wave height H_{rms} , which is closely related to standard deviation of surface elevation. For random waves with Rayleigh distribution, the relation between the root mean square wave height and standard deviation can be approximated by $H_{rms} = \sqrt{8}\sigma$. Figure 5.20(a) shows that wave height decreases gradually from $h = 47\text{ cm}$ to $h = 10\text{ cm}$ due to shoaling and then drops abruptly, indicating that wave breaking occurs around $h = 10\text{ cm}$.

The corresponding third moment statistics from the data are also computed and shown in Figure 5.20 (b). The skewness and the asymmetry are two quantitative measurements for the irregularity of the shape of a wave train compared to a sinusoidal wave train. As waves approach shallow water areas, wave shapes change accordingly due to shoaling and nonlinear interaction. One change is that wave crests become narrower and higher while wave troughs become broader and flatter. This change is measured by the quantity of skewness. The other change is that the front face of a wave tends to steepen while its back face remains more or less the same. This change is indicated by the quantity of asymmetry. For a given time series of surface elevation $\eta(t)$, the normalized skewness and asymmetry are defined as

$$skew = \frac{E[\eta(t)^3]}{\sigma^3} \quad (5.7)$$

$$asym = \frac{E[\xi(t)^3]}{\sigma^3} \quad (5.8)$$

where E is the expectation value, σ is the standard deviation of $\eta(t)$, and $\xi(t)$ is the Hilbert transform of $-\eta(t)$.

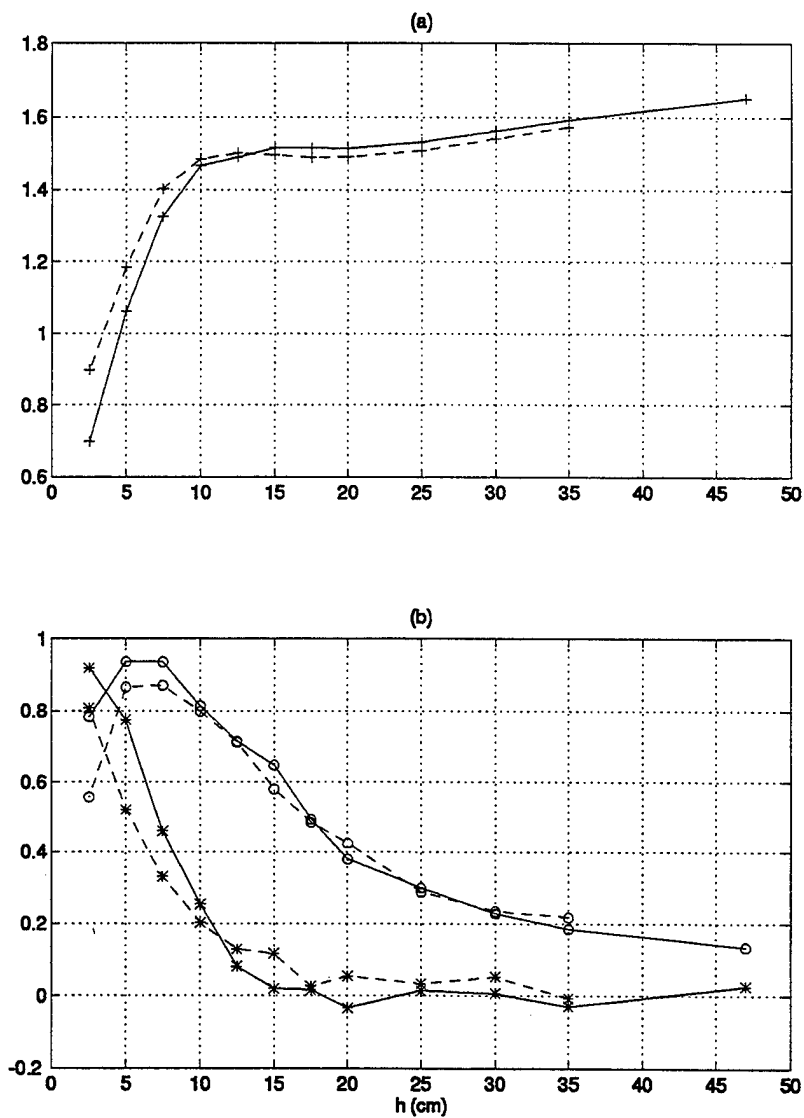


Figure 5.20: Comparison of statistical properties between model (----) and data (—) at various water depths: (a) standard deviation; and (b) skewness (o) and asymmetry (*).

As shown Figure 5.20 (b), skewness increases rather evenly from $h = 47\text{ cm}$ to $h = 10\text{ cm}$ and then decreases. The corresponding asymmetry, on the other hand, remains almost unchanged from $h = 47\text{ cm}$ to $h = 20\text{ cm}$ and then increases sharply all the way to $h = 2.5\text{ cm}$. For the entire range of water depth which includes both the shoaling zone and the breaking zone, the model results agree quite well with the experimental data, except in the very shallow water. For modeling sediment transport, the third moment statistics of skewness and asymmetry are important to accurately compute the corresponding forcing and transport rate. Good agreement of skewness and asymmetry between the model and data indicates that the model could be used for sediment transport modeling.

Figure 5.21 shows the comparisons of power spectrum between the model and the data for various wave gage locations. Notice that the time step used in the model (0.02 s) is not the same as that in the data (0.05 s). In order to use the same number of point for computing the corresponding power spectrum of surface elevation η by FFT, new time series of η with time step 0.05 s were first obtained from the model results by the method of interpolation. The final number of points used for the computation of power spectrum is 13824 and is divided into 27 segments for averaging. Each of the segments has 512 points of data (25.6 s).

Around the peak frequency $f = 1.0\text{ Hz}$, the model spectrum matches quite well with the data spectrum for most of gage locations except for the last one at $h = 2.5\text{ cm}$. Over the frequency range from $f = 2.5\text{ Hz}$ to $f = 5.0\text{ Hz}$, the model spectrum is somehow smaller than the data spectrum. The reason maybe due to the use of numerical filtering in the model. As described in Chapter 3, a numerical filter can effectively eliminate high frequency wave components. However, the filter also decreases the energy of certain short waves. In addition, the present model, though valid for intermediate water depth (about $kh = 3$), is

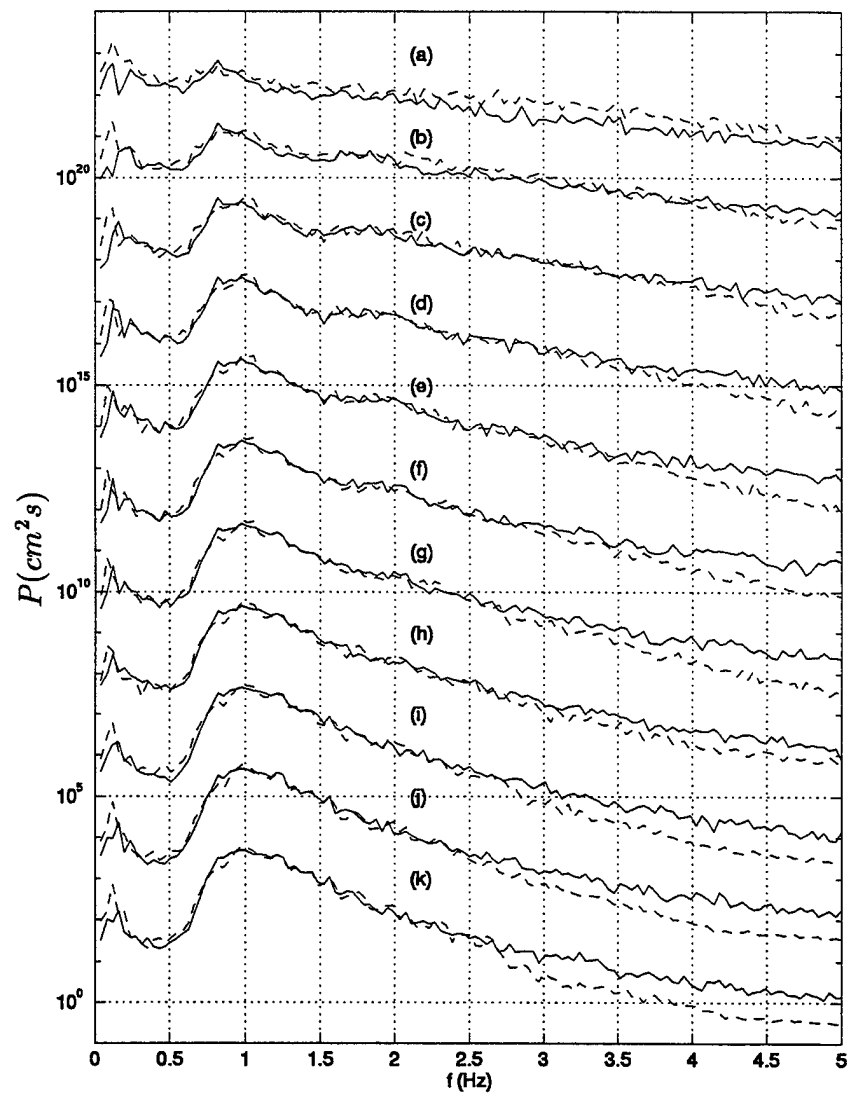


Figure 5.21: Comparison of power spectrum between model (----) and data (—) at 11 wave gage locations: (a) $h = 2.5 \text{ cm}$; (b) $h = 5 \text{ cm}$; (c) $h = 7.5 \text{ cm}$; (d) $h = 10 \text{ cm}$; (e) $h = 12.5 \text{ cm}$; (f) $h = 15 \text{ cm}$; (g) $h = 17.5 \text{ cm}$; (h) $h = 20 \text{ cm}$; (i) $h = 25 \text{ cm}$; (j) $h = 30 \text{ cm}$; and (k) $h = 35 \text{ cm}$.

still not applicable for these high frequency waves whose kh values are quite large ($kh = 7$ for $f = 2.0 \text{ Hz}$). Figure 5.21 also shows that the model overpredicted the data for low frequency motion around $f = 0.2 \text{ Hz}$. This maybe due to the facts that the modeling domain is shorter than the physical domain, and that the shoreline condition in the experiment was replaced by a sponge layer of constant water depth.

5.5 Wave Evolution in a Rectangular Basin

Previous sections describe the simulation of 1-D wave propagation by the 1-D version of the present model. In this and subsequent sections, the corresponding 2-D model will be used to investigate wave propagation in 2-D cases.

The 2-D model equations include many more extra terms, some of which are mixed derivatives in x and y directions. The complexity of the 2-D equations requires careful programming and objective tests to eliminate possible coding errors. One simple yet efficient testing case used for 2-D model was the evolution of waves in a rectangular basin bounded by four vertical side walls.

Figure 5.22 shows a definition sketch of the basin used in the test. The origin of the coordinates is set to be at the left and bottom corner of the basin, with x and y axis coinciding with the corresponding side walls. The basin dimensions are $L_x = 10 \text{ m}$ and $L_y = 10 \text{ m}$, and the water depth is 0.5 m constant over the basin. The initial condition to the model is provided by a motionless Gaussian hump of water with its center align at the center of the basin (x_c, y_c) . For convenience, a new set of coordinates (x', y') is defined, with its the origin at (x_c, y_c) and directions the same as the coordinates (x, y) .

Due to gravitational forcing, the center of the Gaussian hump of water goes

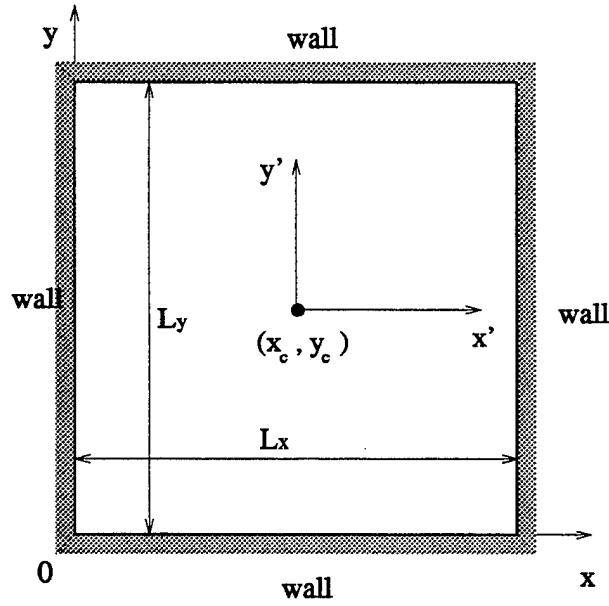


Figure 5.22: Coordinate definition of rectangular basin.

down first and then goes up. As this process repeats, waves are generated at the center and propagate out. These waves are then reflected back to the domain once reaching the vertical side walls. Since energy dissipation terms are not added for this case, waves will propagate inside the domain for as long as the model runs. Though there are no corresponding nonlinear analytical solutions or experimental data to compare with, the resulting surface elevation should be symmetric about x' and y' axis, due to symmetric boundary and initial conditions. Since no water is allowed to escape from the basin, the total water volume inside the domain should also be conserved. The symmetry and conservative properties will be used to examine the corresponding results obtained from the model.

The initial conditions for the Gaussian hump of water are defined as

$$\eta(x, y, t = 0) = H_0 \exp[-\beta[(x - x_c)^2 + (y - y_c)^2]] \quad (5.9)$$

$$u(x, y, t = 0) = 0 \quad (5.10)$$

$$v(x, y, t = 0) = 0 \quad (5.11)$$

where H_0 is the initial height of the hump, β is the shape coefficient which controls the width of the hump, and (x_c, y_c) is the coordinate at the center of the domain. For simplicity, we assume (5.9)-(5.11) to be the values for all three initial time steps. In the testing case shown here, we chose $H_0 = 0.2 \text{ m}$, $\beta = 0.4$, and $x_c = y_c = 5 \text{ m}$. The grid size are specified as $\Delta x = \Delta y = 0.1 \text{ m}$ and time step is $\Delta t = 0.02 \text{ s}$. To eliminate short waves generated from nonlinear interaction, numerical filtering is applied every 100 time steps.

Contour plots of surface elevations obtained from the present model with weak nonlinearity at various times are shown in Figure 5.23. The symmetry of η about the x' and y' axes is apparent, indicating that the finite difference scheme used in the model to discretize the corresponding mixed derivative terms is consistent for both x and y directions.

To verify the property of conserving water mass inside the domain, we apply the following approximate formula in the numerical model to compute the water volume $V(t)$ at any time t

$$V(t) = \frac{1}{4} \Delta x \Delta y \sum_{i=1, j=1}^{M-1, N-1} (\eta_{i,j}^n + \eta_{i+1,j}^n + \eta_{i,j+1}^n + \eta_{i+1,j+1}^n) \quad (5.12)$$

where i and j are the grid index in x and y directions which are related to the coordinates x and y as $x = (i - 1)\Delta x$ and $y = (j - 1)\Delta y$, n is time step index which is related to time t as $t = (n - 1)\Delta t$, Δx and Δy are the grid sizes in x and y directions and Δt is the time step, M and N are total numbers of grid points in x and y , respectively. The relative error $E(t)$ for water volume at any time t compared to its initial value is given by

$$E(t) = \frac{V(t) - V(0)}{V(0)} \quad (5.13)$$

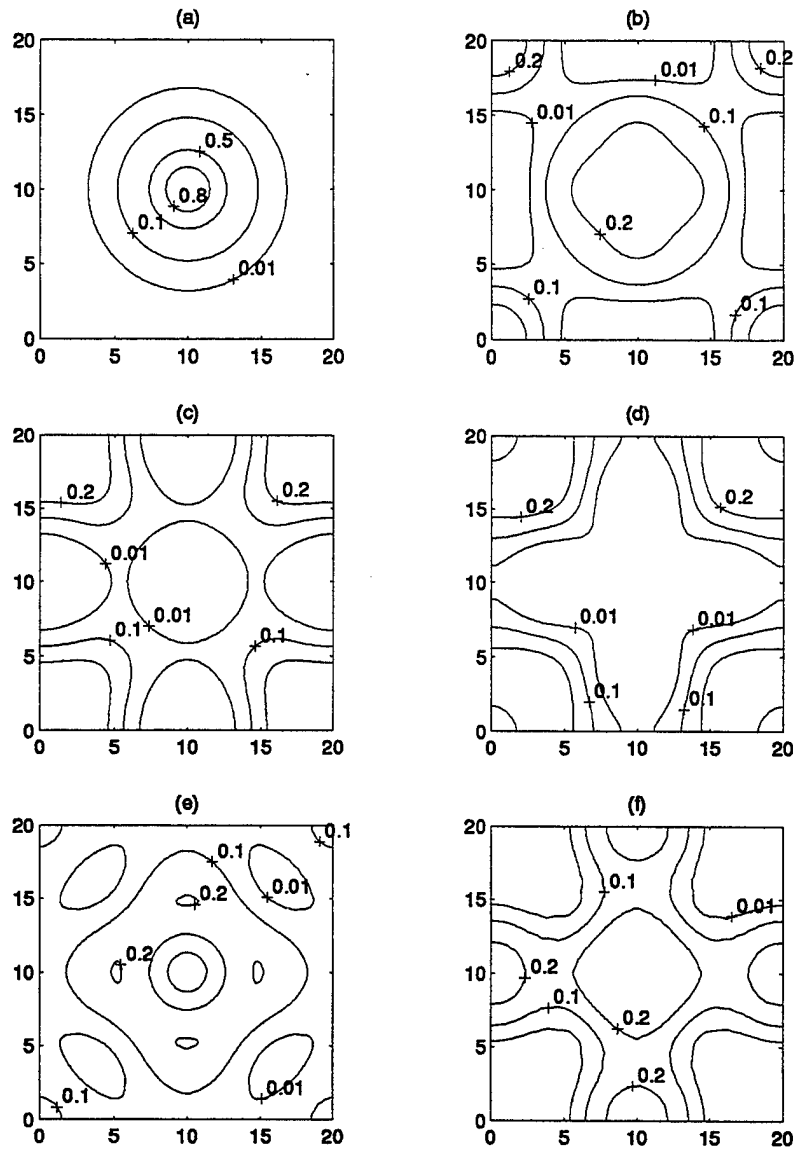


Figure 5.23: Contour plots of surface elevation at time (a) $t=0$; (b) $t=10$; (c) $t=20$; (d) $t=30$; (e) $t=40$; (f) $t=50$ (s).

Since the present model is capable of choosing four different sets of governing equations to simulate wave propagation, we run the model for these four cases and obtained the corresponding time series of E , which are shown in Figure 5.24. The results from the nonlinear shallow water model are not shown since the model blew up at around $t = 23$ s. The boundary conditions used in all three Boussinesq models are same, *i.e.*, zero normal velocity and zero normal derivatives of surface elevation and tangential velocity. Results in Figure 5.24 indicate that the water volumes inside the domain computed from the three Boussinesq models are almost constant, within 1% relative error. Of these three models, the standard Boussinesq model gave the most accurate result. The reason is that depth-averaged velocity is used as the dependent variables in the standard Boussinesq equations. Specifying the normal velocity at the wall boundary to be zero is the exact boundary condition to conserve mass inside the domain. For Nwogu's Boussinesq model or the fully nonlinear Boussinesq model, the dependent variable is velocity at the water depth $z_\alpha = -0.531h$. Specifying zero normal velocity and zero normal derivatives of surface elevation and tangent velocity is only accurate within the model approximation.

If nonlinearity is negligible, linear analytical solution to this problem can be obtained by using a standard Fourier transform method. For simplicity we assume a square domain, *i.e.* $L_x = L_y = L$. Then the transform coefficients for Fourier components are determined from the initial conditions $\eta_0(x, y)$ by

$$\tilde{\eta}_{nm} = \frac{1}{(1 + \delta_{n0})(1 + \delta_{m0})L_x L_y} \int_{-L_x}^{L_x} \int_{-L_y}^{L_y} \eta_0(x, y) \cos(n\lambda x) \cos(m\lambda y) dx dy \quad (5.14)$$

where (n, m) denotes different linear modes for waves in the domain, δ_{nm} is the Kronecker delta function, and $\lambda = \frac{\pi}{L}$. The natural frequency for mode (n, m) is given by the exact linear dispersion relation

$$\omega_{nm}^2 = g k_{nm} \tanh(k_{nm} h_0) \quad (5.15)$$

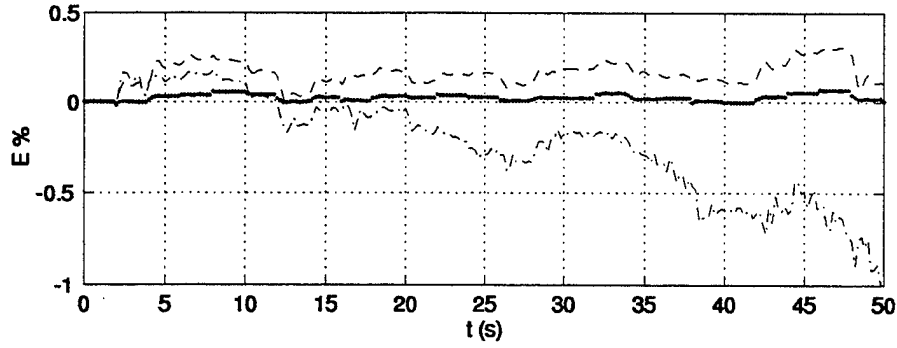


Figure 5.24: Time series comparison of relative error for total water volume inside the domain: Nwogu's Boussinesq model (---) ; the standard Boussinesq model (....); and the fully nonlinear Boussinesq model (-.-.).

where wavenumber k_{nm} is defined as

$$k_{nm}^2 = (n\lambda)^2 + (m\lambda)^2 = \left(\frac{\pi}{L}\right)^2 (n^2 + m^2) \quad (5.16)$$

The corresponding linear analytical solution is

$$\eta(x, y, t) = \sum_{n=0}^{\infty} \sum_{m=0}^{\infty} \tilde{\eta}_{nm} e^{-i\omega_{nm}t} \cos(n\lambda x) \cos(m\lambda y) \quad (5.17)$$

where it is understood that only the real part of the solution is used.

By setting all nonlinear terms into zero, we obtained two linearized numerical models based on standard Boussinesq equations and Nwogu's Boussinesq equations. The time series comparison of surface elevation between the analytical solution and the two linearized numerical models are shown in Figure 5.25, where surface elevation at the center point and at the corner point are plotted. The overall comparisons between three solutions are quite good, for both wave height and wave phase. However, the comparisons of the results from Nwogu's Boussinesq model with the analytical solutions is much better than those from standard Boussinesq model, as evident by the fact that there is almost no visible

difference between the dashed line and the solid line, while the dotted line exhibits discrepancy with the solid line.

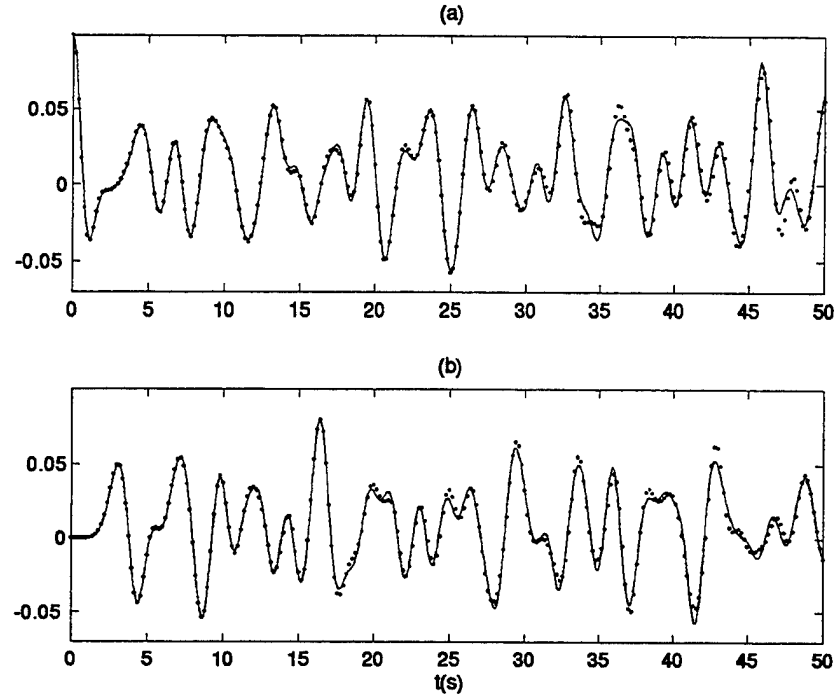


Figure 5.25: Time series comparison of surface elevations between linear analytical solution (—), linearized Nwogu's Boussinesq model (----), and linearized standard Boussinesq model (····): (a) location at center (x_c, y_c) ; and (b) location at the corner $(0, 0)$.

The discrepancy between the two linearized models is due to the effect of errors in the higher frequency portion of the solution, which contributes relatively little variance to the overall surface record. The theoretical natural frequencies corresponding to the two linearized models are given by the linear dispersion relation

$$\omega_{nm}^2 = gk_{nm}^2 h_0 \frac{1 - (\alpha + 1/3)(k_{nm} h_0)^2}{1 - \alpha(k_{nm} h_0)^2} \quad (5.18)$$

where k_{nm} wavenumber for mode (n, m) defined by (5.16), and $\alpha = -0.390$ for Nwogu's model and $\alpha = -1/3$ for standard Boussinesq model. Figure 5.26 shows

the ratios of the Boussinesq natural frequency to the exact natural frequency over the corresponding mode numbers which are represented in the analytic and numerical solutions. The ratio of natural frequency from Nwogu's model to analytical solution for the first 10 modes in each direction is quite close to 1, with the errors in the ratio less than 1%. For the same range of modes, the ratio of frequency from standard Boussinesq model to analytical solution is close to 0.95, and the corresponding errors are on the order of 5%. Results from Figure 5.26 indicate that Nwogu's Boussinesq model is a better representation than standard Boussinesq model for simulating high frequency modes.

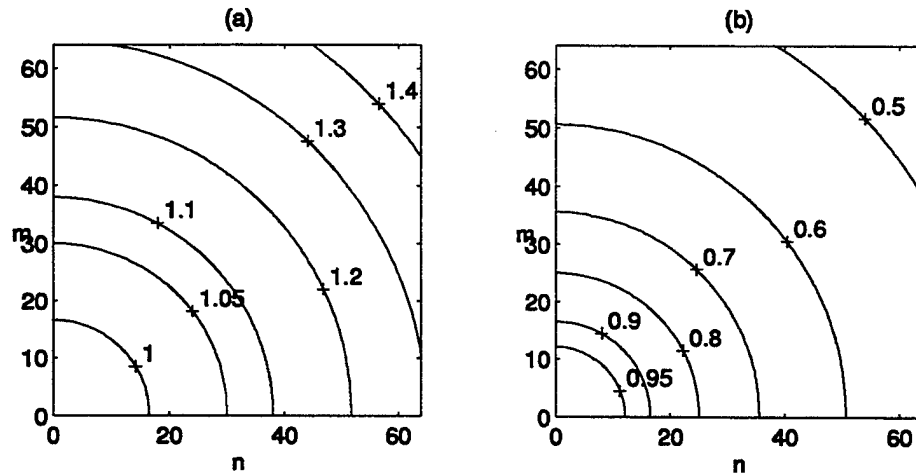


Figure 5.26: Ratios of linearized Boussinesq models natural frequencies to exact natural frequencies for the range of mode numbers considered in the analytic and numerical solution: (a) Nwogu's Boussinesq model; (b) standard Boussinesq model.

5.6 Monochromatic Wave Propagation Over Shoals

To study wave refraction and diffraction patterns and to verify numerical models, laboratory experiments have been conducted in the past by a number of

investigators. The most commonly used bottom geometry for laboratory studies consists a submerged shoal seated on a flat or sloping bottom. In this section, the numerical model is applied to simulate two experiments on wave propagation over shoals. Comparisons between computed results and experimental data are made in detail.

5.6.1 Case 1: experiment of Berkhoff *et al.* (1982)

The experiment conducted by Berkhoff *et al.* (1982) has served for a number of years as a standard test for verifying models based on the mild slope equation. Accurate reproduction of the measured wave heights by numerical models for this experiment depends on a number of factors, including how the model simulates the effects of shoaling, refraction, diffraction, and nonlinear interaction. Though the mild slope model is able to solve the combined refraction-diffraction problem, there are no nonlinear interaction terms included in the equation. Using a third-order Stokes wave dispersion, Kirby and Dalrymple (1984) demonstrated that nonlinearity plays an important role in the accuracy of simulating wave shoaling for this particular experiment.

Due to large kh values in the experiment ($kh = 1.9$ near wavemaker), models based on nonlinear shallow water equations or standard Boussinesq equations are not appropriate to use in this situation, as has been demonstrated in section 5.4 when applying these invalid models to simulate the propagation of the random wave train *run2* of Mase and Kirby (1992). However, the present model based on Nwogu's extended Boussinesq equations or the fully nonlinear Boussinesq equations can be applied to this case and the model results compare quite accurately with the experiment data.

The experimental geometry and the transects for collecting wave data are

shown schematically in Figure 5.27. Notice the non-standard coordinate system for this case where y axis is the wave propagation direction. Monochromatic waves with period 1 s and amplitude 2.32 cm are generated by a wavemaker at $y = -10\text{ m}$. The remaining computational domain includes two side walls (which are located at $x = -10\text{ m}$ and $x = 10\text{ m}$) and an absorbing boundary at $y = 12\text{ m}$. The bottom bathymetry consists of an elliptic shoal resting on a plane beach with a constant slope of $1/50$. The bottom contours on the slope are oriented at an angle of 20° to the x - axis. The slope is described by $h = 0.45\text{ m}$ if $y' < -5.82\text{ m}$ and $h = 0.45\text{ m} - 0.02(5.82 + y')\text{ m}$ if $y' \geq -5.82\text{ m}$. The boundary of the shoal is given by $(x'/4\text{ m})^2 + (y'/3\text{ m})^2 = 1$ and the thickness of the shoal is $d = -0.3\text{ m} + 0.5\text{ m}\sqrt{1 - (x'/5\text{ m})^2 - (y'/3.75\text{ m})^2}$.

The computing domain used in the model is the same as in Figure 5.27 except for two sponge layers with width 2 m and 3 m located behind the wavemaker and on the end of the beach. Instead of a shoreline boundary, a minimum water depth of 0.07 m is used in the model. The center of the source region for generating the corresponding monochromatic wave is located at the experimental wavemaker location. The time step used in the model is $\Delta t = 0.01\text{ s}$ and the grid sizes are chosen as $\Delta x = 0.1\text{ m}$ and $\Delta y = 0.05\text{ m}$, resulting in a maximum Courant number of 0.84 . The total number of time steps for the model to run is 4001 , which corresponds to an elapsed time of 40 wave periods. The 2-D numerical filter described in Section 3.5 was applied for every 100 time steps, which effectively eliminated short wave components generated by the nonlinear interaction. From numerical experiments, it was found that the model became unstable if the same filter was used less frequently. The effect of the high-order filter on other long waves (*i.e.* wavelength longer than 10 grid sizes) was minimal, as shown in Section 3.5 and evident from the resulting wave heights computed from the model.

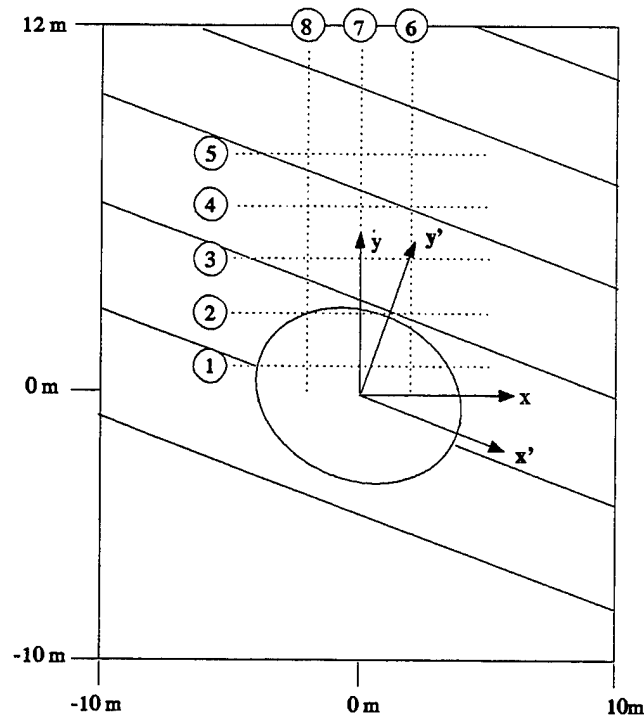


Figure 5.27: Experiment layout for wave focusing experiment of Berkhoff *et al.* (1982).

The computed results obtained from the present model based on Nwogu's Boussinesq equations or the fully nonlinear Boussinesq equations are similar, probably due to relatively small effect of nonlinearity. For this reason, only the results from the Nwogu's model will be shown in the following. Figure 5.28 shows the spatial profile of surface elevation η at the last time step ($it = 4001$) obtained from the model. The light and dark shade regions correspond to positive and negative values of η , respectively. The solid lines in the plot denote the contours of bottom geometry. The surface profile shows very strong focusing of wave energy behind the shoal, indicating the effect of wave diffraction is quite large in that region. For this reason, the traditional ray tracing method which only considers

refraction is not valid here. The mild slope model which includes both refraction and diffraction is applicable to this case. The uniformly grey shade in the two sponge layer regions corresponds to near zero surface elevation, which indicates that wave energy was absorbed properly at these boundaries.

Figure 5.29 shows the time series of surface elevation η at various locations, with their corresponding coordinates (x, y) labeled in the plot. Since the model was started with zero initial conditions for all variables, surface elevations η at $t = 0$ are zero at every location. As waves begin to be generated in the source region and propagate across the domain, surface elevations at these specified points start to increase in magnitude and then approach corresponding stable values. For those points closer to the wavemaker, the transition time from zero to stable values is shorter than that for points far away from the wavemaker. Surface elevations at the points behind the strong focus region show narrower crests and broader troughs, indicating that the effect of nonlinear interaction is important on the transformation of waves in this region. Though no experiment data available to compare with these computed time series of η , Figure 5.29 shows that the computing wave field reaches a stable state at the time $t = 30$ s.

For the numerical model, wave heights at various locations in the domain are computed from the corresponding time series of surface elevations η . Only four segments of data corresponding to the last four periods (*i.e.* from $t = 36$ s to $t = 40$ s) are used for wave height evaluation. First, the wave height for each segment of data is determined by finding the maximum and minimum values of η . Then the averaged value of these four wave heights is the corresponding wave height of the model. The computed wave heights are compared to experimental data along all eight transects where measurements of wave height were available, as shown in Figure 5.30.

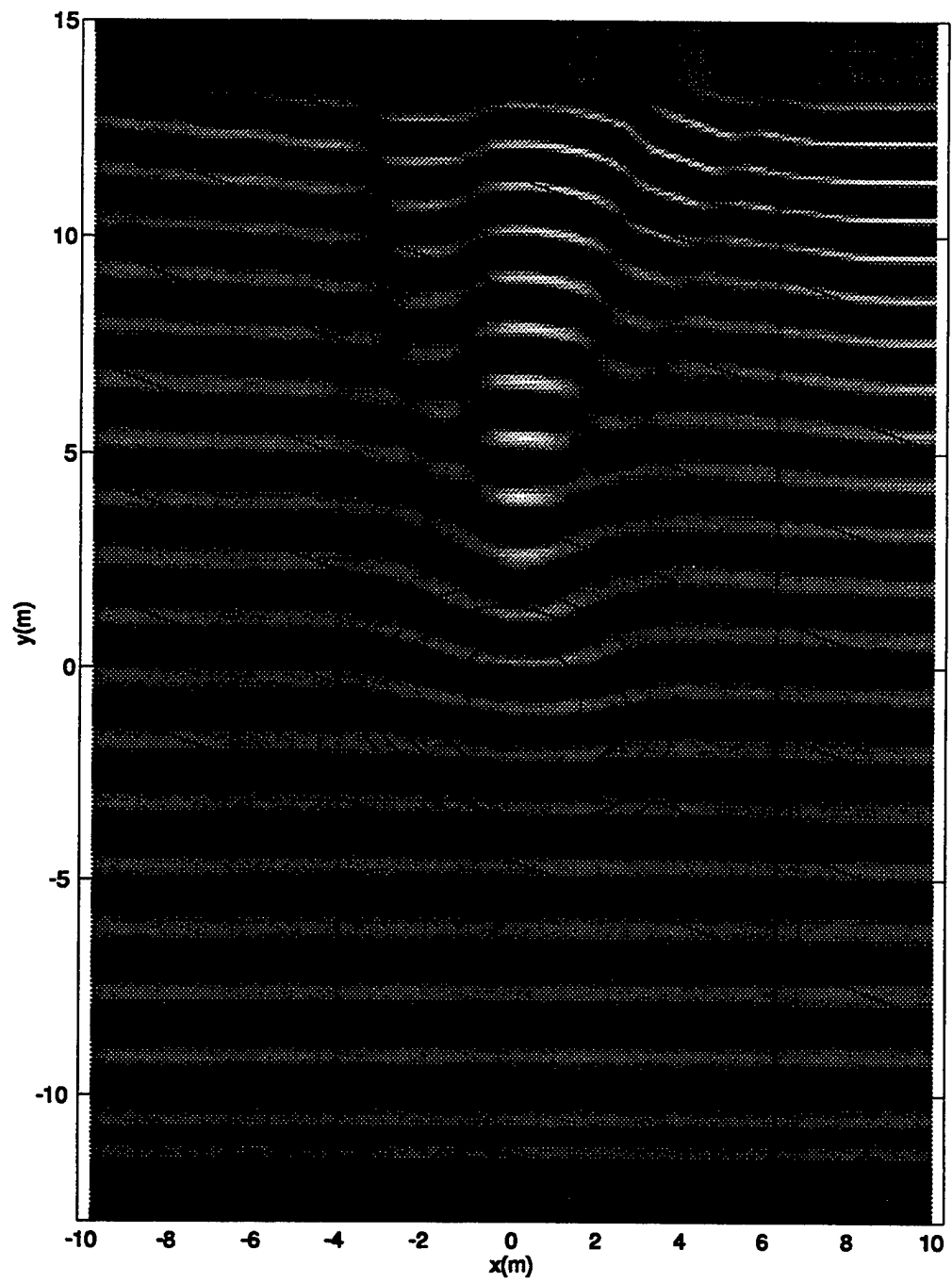


Figure 5.28: Top view of 3-D shaded graph of surface elevation at time step $it = 4001$ ($t = 40s$).

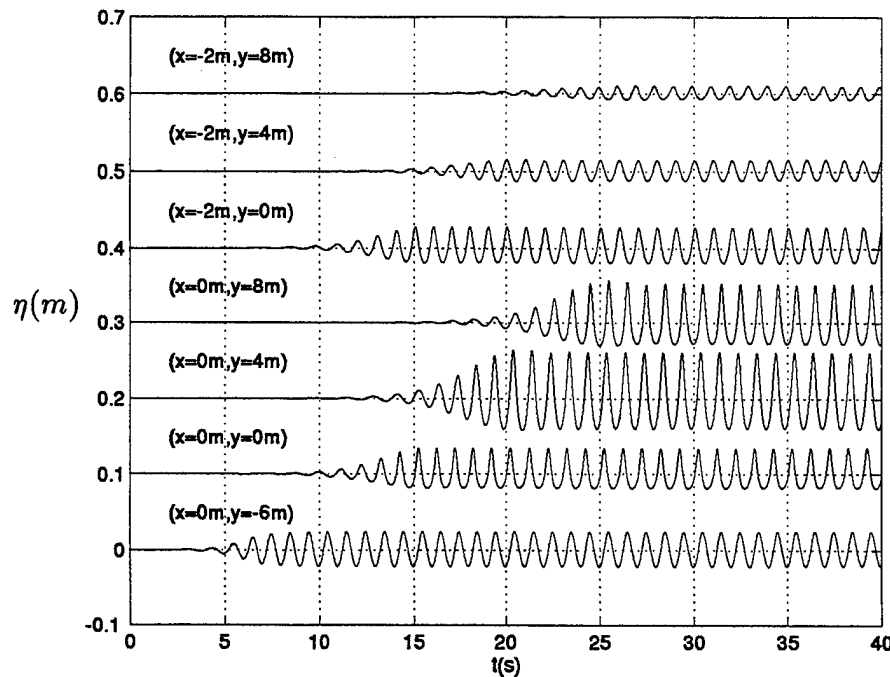


Figure 5.29: Computed time series of surface elevation at various locations.

The computed results of wave heights from the numerical model agree quite well with experiment data, in sections both parallel and normal to the incident wave direction. In the past, models based on the mild slope equation have been applied to simulate wave transformation for this case; see, for example, Berkhoff *et al.* (1982), Kirby and Dalrymple (1984), and Panchang and Kopriva (1989). Though valid for a wide range of water depth including this experiment, the mild slope equation itself does not account for the effect of nonlinearity, which is important for this experiment. Of the mild slope models mentioned above, only the one given by Kirby and Dalrymple (1984) considered the effect of nonlinear interaction by using a third-order Stokes wave dispersion. Not surprisingly, results from the model of Kirby and Dalrymple (1984) compared the best with the data, while other mild slope models based on the usual linear dispersion relation gave

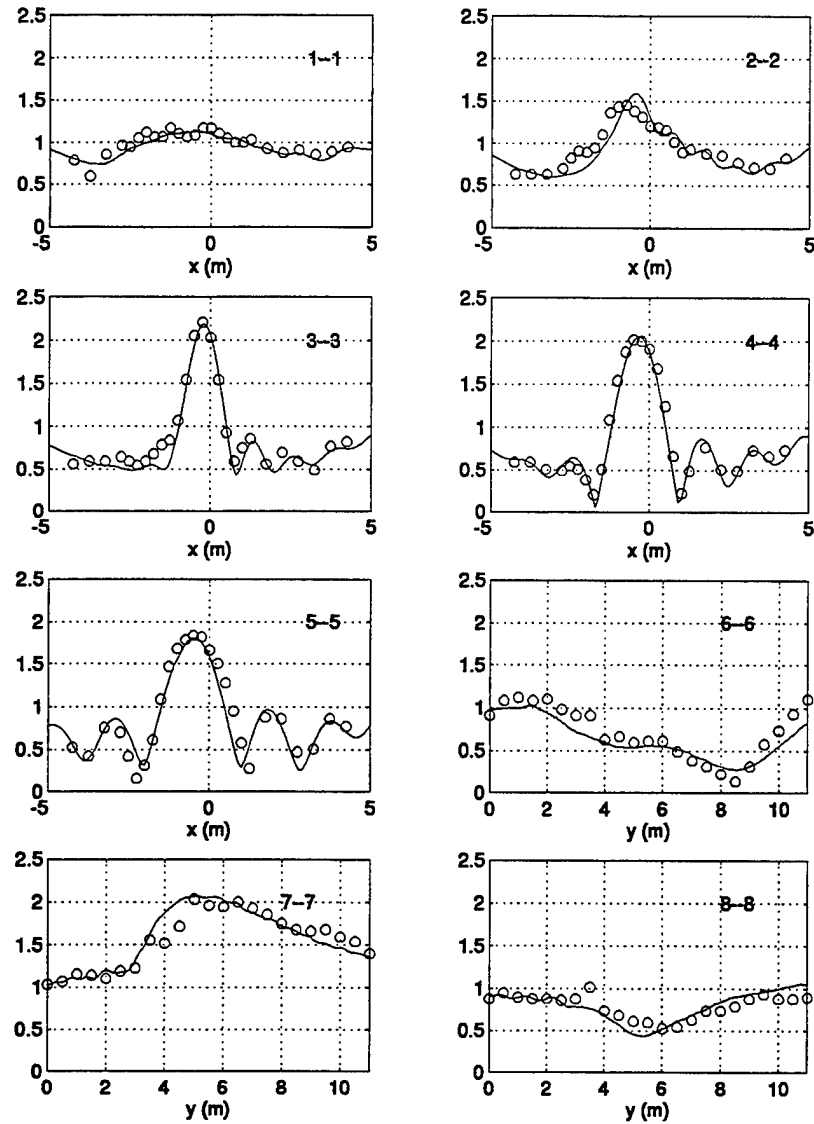


Figure 5.30: Comparisons of normalized wave height (scaled by the incident wave height) along specified sections between the model (—) and experiment data (ooo).

only satisfactory results. The importance of nonlinearity is also verified by the present model which includes the effect of weakly nonlinear interaction. The wave height distribution obtained from the present model is in much better agreement with the experiment data compared to those from linear mild slope models.

5.6.2 Case 2: experiment of Chawla (1995)

To study wave transformation and to provide measured data for the verification with the numerical models of **Ref/Dif 1** (Kirby and Dalrymple, 1994) and of **Ref/Dif S** (Kirby and Özkan, 1992), a series of experiments were conducted in the rectangular basin at the Center for Applied Coastal Research in the University of Delaware (Chawla, 1995; Chawla *et al.*, 1996). The incident waves in the experiment consist of both regular and random waves, with short and long wave periods, small and large wave heights, narrow and broad frequency bands, and narrow and broad directional distributions. The experiment layout and the coordinate system are shown in Figure 5.31. Notice that the coordinate system for this case is a standard one with x axis in the wave propagation direction. A circular shoal with radius of 2.57 m is built on the flat bottom basin whose dimensions are given by $L_x = 18.2\text{ m}$ and $L_y = 20\text{ m}$. The thickness of the shoal is given by

$$\delta_{shoal} = \sqrt{(9.1\text{ m})^2 - r^2} - 8.73\text{ m}, \quad \text{if } r \leq 2.57\text{ m} \quad (5.19)$$

where $r = \sqrt{(x - x_c)^2 + (y - y_c)^2}$ is the horizontal distance from the center of the shoal ($x_c = 5.0\text{ m}$, $y_c = 8.98\text{ m}$) to the point (x, y) . Notice that y_c is not at the exact center line of the basin. As will be shown later from model results and experiment data, the resulting wave field is not symmetric due to this slightly off-center shoal.

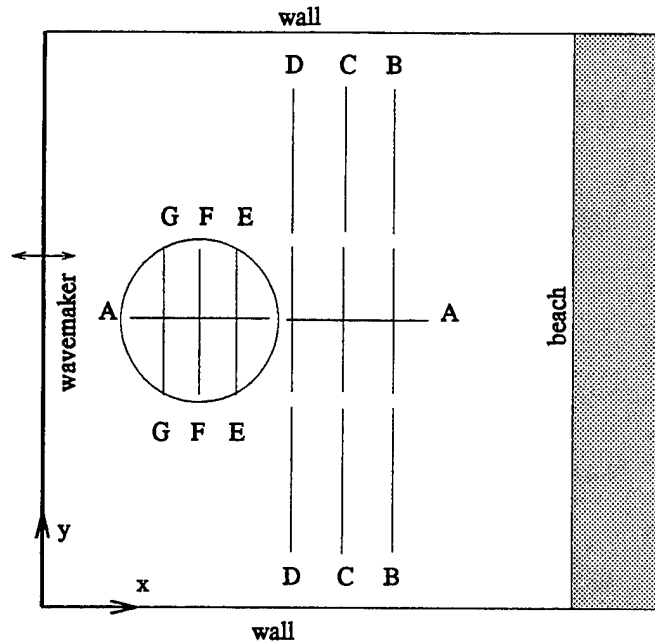


Figure 5.31: Experiment setup of Chawla (1995).

Incident waves are generated by a 3-D paddle-type wavemaker on the left end of the domain and propagate across the basin to the right end, where a beach consisting of small rocks dissipates the incoming wave energy. The top and bottom ends are vertical walls which reflect waves back to the domain. An array of 9 capacitance wave gages were placed at different locations inside the basin to collect time series of surface elevations. These locations are marked by transects $A - A$, $B - B$, $C - C$, $D - D$, $E - E$, $F - F$, and $G - G$ in Figure 5.31. The exact coordinates for each gage are given by Chawla (1995).

Four experiments (TEST 1-4) were conducted for nonbreaking regular waves. Due to data contamination in TEST 3, only three sets of data (TEST 1, TEST 2 and TEST 4) are available from the experiments. The corresponding wave heights, wave periods, and kh values for each test are listed in Table

Table 5.1: Wave heights, wave periods and kh values for the three tests of non-breaking regular waves.

	Wave height (cm)	Wave period (s)	kh
TEST 1	0.98	0.75	3.18
TEST 2	2.01	0.75	3.18
TEST 4	1.18	1.0	1.90

5.1. TEST 1 and TEST 2 are for two waves of shorter period and different wave heights. TEST 4 is for a longer period of wave and a medium wave height. The present model is applied to all these three tests and comparison between model and data will provide detailed information for the model performance.

Though the values of wave period T and water depth at the wavemaker h_0 are close or equal to those in the experiment of Berkhoff *et al.* (1982), the resulting wave fields for these two experiments are quite different, mainly due to variation of bottom geometry. Using ray tracing method, Chawla (1995) computed the corresponding wave ray diagrams. It was found that the focusing of waves in the all the three tests was quite severe (Chawla, 1995) and all of the focusing occur on the top of the shoal. However, the focus of waves in the experiment of Berkhoff *et al.* (1982) is at the area much further behind the shoal. Due to the sloping beach, waves in the experiment of Berkhoff *et al.* (1982) continue shoaling after passing the shoal.

We used the present model with weakly nonlinearity to simulate all three tests of Chawla (1995). The corresponding grid sizes are $\Delta x = 0.05 m$, $\Delta y = 0.1 m$, time step is $\Delta t = 0.01 s$, the total number of time steps is $nt = 4001$, and the numerical filtering is applied every 400 time steps. The time series of surface elevations η from the model results and experiment data for TEST 4 at

selected wave gage locations are shown in Figure 5.32. Good agreements between the model and data are found, not only for wave heights and wave phases, but also for the asymmetry of wave shapes.

Notice that the necessary phase shifting for the data at certain locations had been performed prior to the comparison. In the experiment, there was only one gage array which consists of nine gages to collect data. The gage array was placed at 14 different positions across the domain. Though the same wave condition could be generated for each of these gage positions and the phases for the 9 gage are the same, it is not guaranteed that the phases for different gage array position are the same. Therefore, it is necessary to adjust experiment data by shifting phase for meaningful comparison with the numerical results. For each gage array, only one gage is required to do phase shift due to exact synchronization for the data in the same gage array.

After wave fields reached stable condition, zero-upcrossing method was applied to the corresponding time series of surface elevation to obtain wave heights. For experimental data, a time interval of 10 period data segment was used to compute averaged wave height. Prior to wave height evaluation, a Butterworth fifth-order bandpass filter was applied in order to eliminate noise from the signal. For time series computed from the model, the data segment from $t = 36\text{ s}$ to $t = 40\text{ s}$ was used to compute wave heights. Since numerical filtering has been applied spatially for every 400 time steps in the model simulation, it is not necessary to apply extra filtering to the resulting time series. Comparisons of wave amplitudes between the model and data along all transects from $A - A$ to $G - G$ are shown in Figure 5.33, 5.34 and 5.35 for TEST 1, TEST 2 and TEST 4.

Due to slightly off-center position for the shoal location in the basin, the wave height distributions along y axis are not symmetric. The asymmetry become

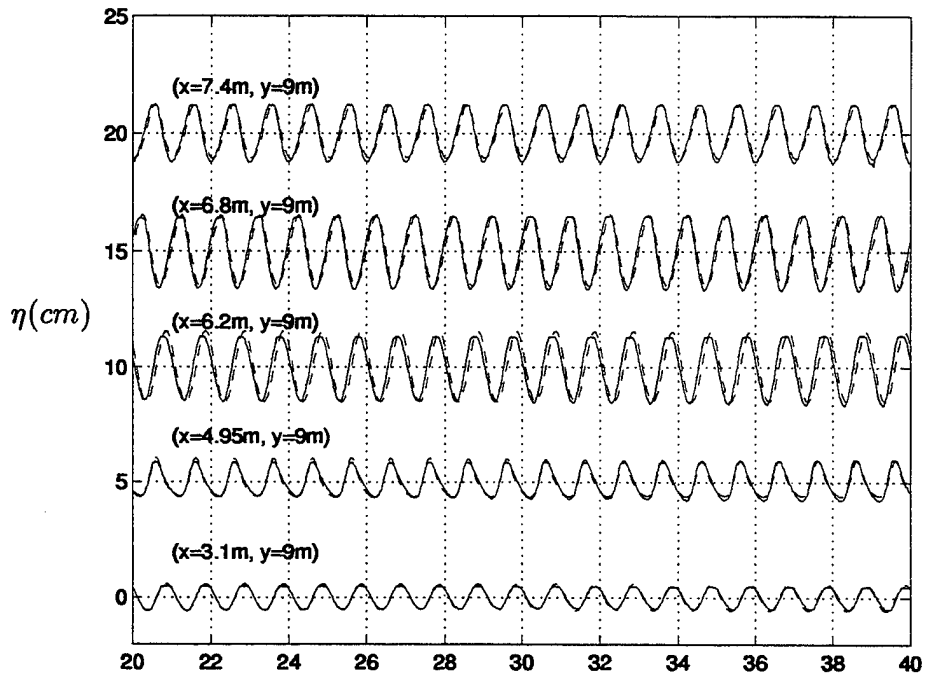


Figure 5.32: Time series comparison of surface elevation between numerical results (----) and experiment data (—) of Chawla (1995).

more apparent for transects away from the wavemaker, indicating increasing effects of side wall reflection. The effect of asymmetry and the zigzag variation of wave height distribution along y axis was accurately predicted by the numerical model.

Chawla (1995) applied two models of **Ref/Dif 1** to simulate all test cases and compared results with experiment data. These two models are all based on the mild slope equation, with one called Stokes model due to the inclusion of nonlinear interaction by using a third order Stokes dispersion (Kirby and Dalrymple, 1984), and the other called linear model which uses the usual linear dispersion relation to compute the wavenumber. As shown by Chawla (1995), the computed results from the Stokes model are in better agreement with the experiment data than

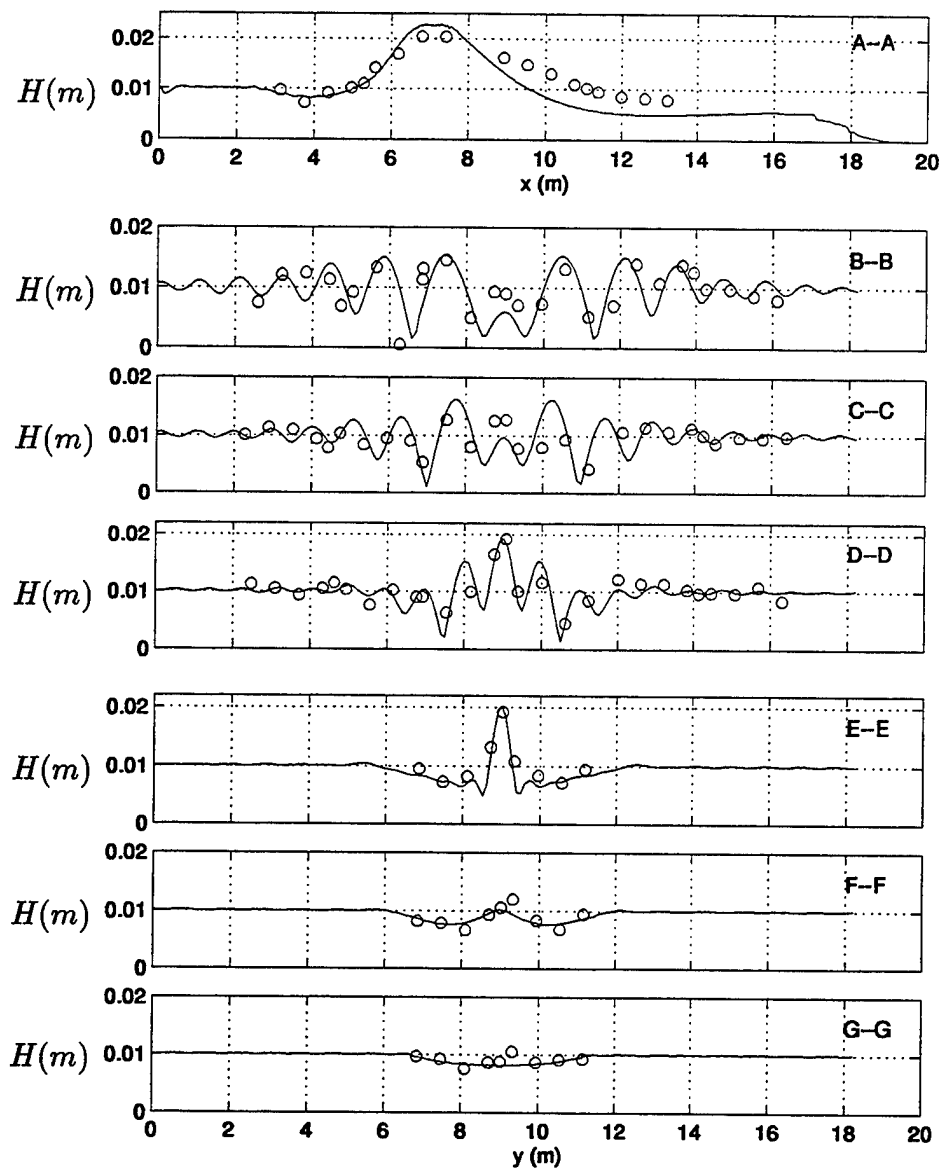


Figure 5.33: Comparison of wave height along specified transects between the present model (—) and data (ooo) of TEST 1.

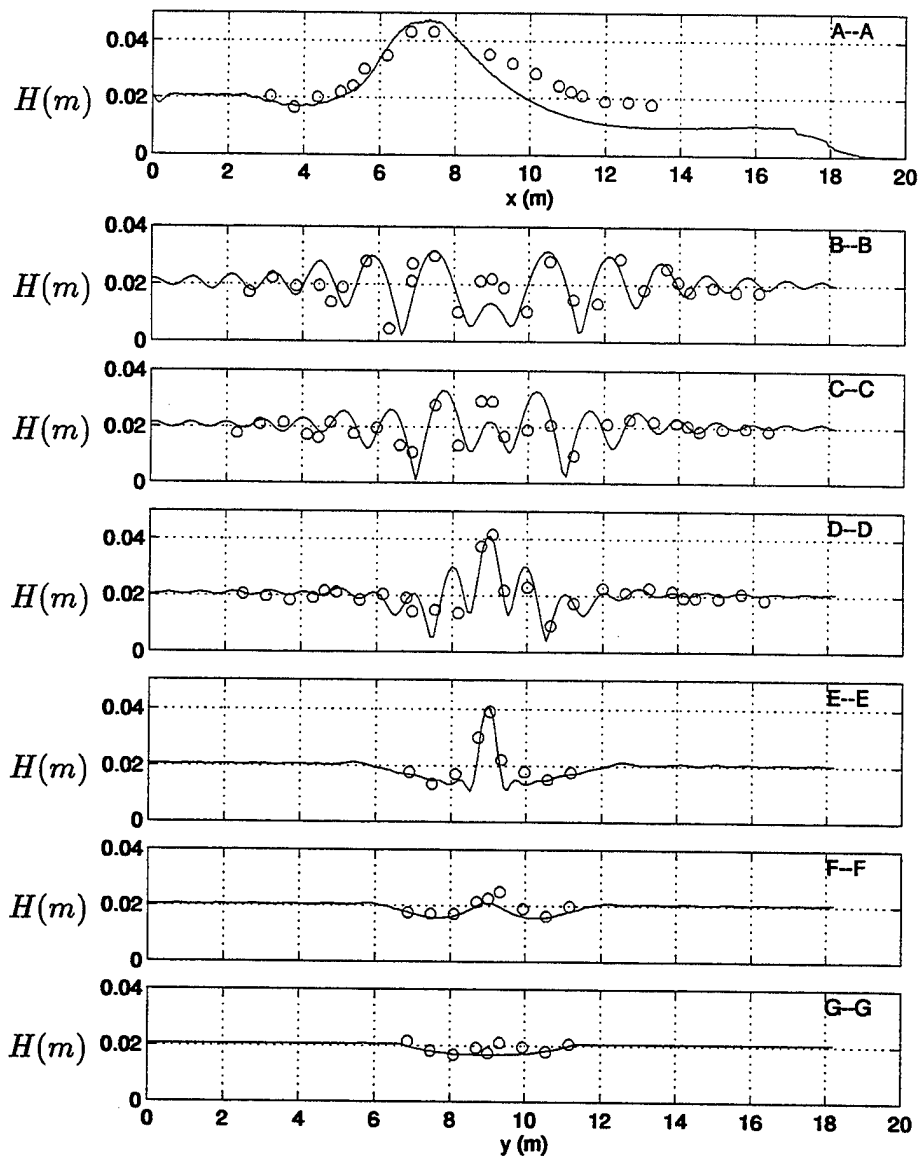


Figure 5.34: Comparison of wave height along specified transects between the present model (—) and data (ooo) of TEST 2.

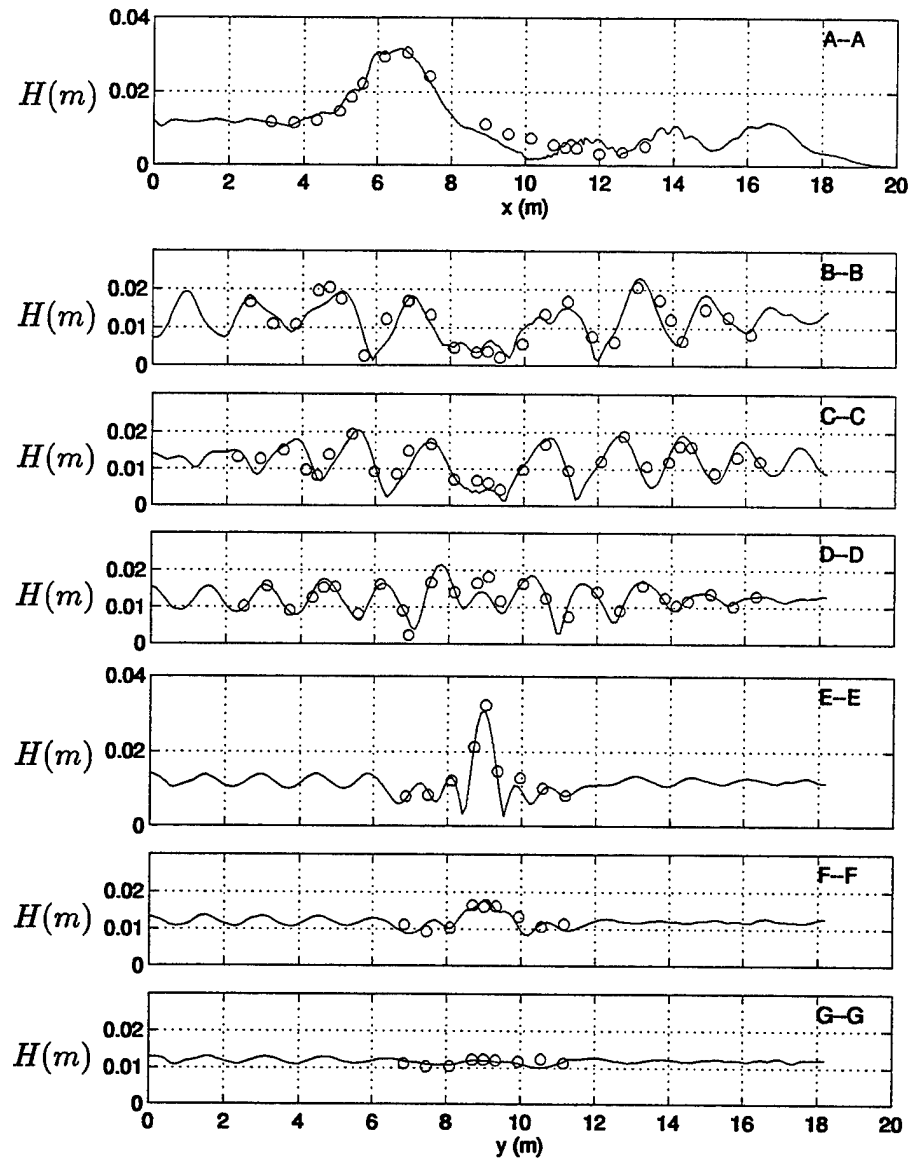


Figure 5.35: Comparison of wave height along specified transects between the present model (—) and data (ooo) of TEST 4.

Table 5.2: Comparisons of index of agreement between data and the three models.

	Present model	Stokes model	Linear model
TEST 1	0.8481	0.7516	0.7257
TEST 2	0.8435	0.8214	0.7064
TEST 4	0.9535	0.8622	0.8369

those obtained from the linear model. However, as will be demonstrated below by computing an index of agreement, the results from the present model compare better with the data than those from the Stokes model.

The index of agreement d_i was proposed by Wilmott (1981) for the objective comparison between two sets of data, which is given by

$$d_i = 1 - \frac{\sum_{j=1}^n [y(j) - x(j)]^2}{\sum_{j=1}^n [|y(j) - \bar{x}| + |x(j) - \bar{x}|]^2} \quad (5.20)$$

where $x(j)$ are the measured data to be compared with, $y(j)$ are the predicted values from the model, and \bar{x} is the mean value of $x(j)$. A perfect agreement between data and model corresponds to $d_i = 1$, while a completely disagreement results in $d_i = 0$. Instead of comparing results for each transect, we compute the index of agreement for all transects for the present model and the two **Ref/Dif** models. The corresponding index of agreement for each of the three tests (TEST 1, TEST 2 and TEST 4) are all computed and the corresponding results are given in Table 5.2.

For all the three testing cases, the resulting indices of agreement from the present model are better than those from the two **Ref/Dif 1** models, especially for the cases of TEST 1 and TEST 4, the differences between these results are

about 10%. Among two **Ref/Dif 1** models, the computed indices of agreement from the Stokes model are larger than those from the linear model. These results indicate that the effect of nonlinearity is important for wave transformation in all the testing cases. Because of the strong focusing and the limitation of the parabolic approximation for the two **Ref/Dif 1** models, the present model gives the best predictions for wave transformation.

Further analysis from the results of TEST 2 shows that the wave height distributions along the transect $A - A$ after the shoal predicted by the Stokes model are in better agreement than those from the present model. However, for other transects which are parallel to the wavemaker, agreements between the computed results from the present model are better than those from the Stokes model.

Chapter 6

CONCLUSIONS

In this study, we have derived a set of fully nonlinear Boussinesq equations and developed the corresponding numerical model for simulating wave transformation in coastal regions. Following the approaches of Nwogu (1993) and of Chen and Liu (1995), the internal flow field is expanded with respect to the velocity potential at a depth z_α in the water column. By substituting the power series expansion into the original governing equations and by keeping all nonlinear terms, the fully nonlinear Boussinesq equations are obtained. Due to the use of velocity potential at the optimum water depth as the dependent variable, the resulting equations have improved linear dispersion properties in intermediate depth water, similar to the results obtained by Nwogu (1993) and by Chen and Liu (1995). In addition, since no assumption of small nonlinearity is made in the derivation, the model is valid for simulating cases of wave propagation involving strong nonlinear interaction, such as wave shoaling prior to wave breaking.

To gain insight into the fully nonlinear Boussinesq equations, we have obtained the superharmonic and subharmonic coefficients for the second order bound waves whose wavenumber vectors and frequency are the sum and difference of the primary waves. We also have derived the corresponding cubic Schrödinger equation which governs the long term evolution of a wave train with a narrow band of frequencies and wavelengths. Comparisons are made between the model results

and the exact solutions by Dean and Sharma (1981) and by Mei (1989). The higher order nonlinear terms in equations are found to be important for studying nonlinear interaction between waves and waves, and waves and currents.

A high order numerical model has been developed to obtain solutions to the fully nonlinear Boussinesq equations. The fourth order Adams-Bashforth-Moulton predictor-corrector scheme is employed in the model for time stepping. For spatial derivatives, the fourth order and second order finite difference schemes are applied to discretize the first order derivative terms and the second or higher order terms in the equations, respectively. Due to the use of fourth order schemes for first order derivative terms, the corresponding truncation errors are smaller than the dispersive terms, making it unnecessary to substitute the truncation errors back into the discretized equations, as required by other low order schemes for a typical time step and grid size. To increase the stability range and the efficiency of the model, the momentum equations are rearranged so that the solutions for velocity variables are based on a system of tridiagonal matrices.

Linear stability analysis has been performed based on von Neumann's method. For the case of constant water depth and 1-D flow, the stability range is determined numerically by evaluating the eigenvalues from the corresponding amplification matrix. The moduli of the eigenvalues are related to the Courant number C_r , the dimensionless wavenumber $k\Delta x$, and the ratio of water depth to grid size $h/\Delta x$. For the case of using one predictor and one corrector at each time step, the scheme will be stable if the Courant number is less than 0.8, regardless the magnitude of the other two parameters.

The present model utilizes three boundary conditions, which include the wall (reflecting) boundary, the radiation (absorbing) boundary, and the incident (generating) boundary. Since the model uses the velocity at a certain depth as the

dependent variable, it is not sufficient to make the volume flux zero by specifying zero normal velocity at a reflecting boundary. The extra condition is that the normal derivative of the surface elevation be zero at the boundary. With these two conditions, the resulting volume flux across the reflecting boundary is, to the order of approximation in the model equations, essentially zero. In addition, the model also utilizes the no-shear condition at the reflecting boundary, requiring that the normal derivative of the tangent velocity be zero.

For the absorbing boundary, the present model uses a sponge layer to dissipate the energy for outgoing waves. Though it is sufficient to use the radiation conditions proposed by Sommerfeld (1949) and by Engquist and Majda (1977) for some special cases, the generally unknown property of phase speed for the outgoing waves in real applications makes the use of these radiation conditions problematic. Following the approach by Israeli and Orszag (1981), terms representing the effect of linear friction or viscosity have been included in the momentum equations and the energy of outgoing waves was dissipated over the areas of sponge layer.

To take advantage of using a sponge layer for absorbing the energy of outgoing waves, it is necessary to generate waves inside the computing domain. We first added a source function with unknown amplitude to the continuity equation. We then obtained, based on the method of Green function, the exact linearized solution to the source function from the given characteristics of the desirable wave. Several examples of generating sinusoidal waves have been shown.

The 9 point 1-D filter proposed by Shapiro (1970) is employed in the model to eliminate short wave components which are generated by the nonlinear interaction and might cause stability problems. Two versions of the model, one with a numerical filter applying every 100 time steps and the other without any filtering, were applied to study the evolution of waves in a closed basin. The asymmetric

surface elevation resulted from the version of the model without filtering indicated that the existence of short waves affects the accuracy of the computing results.

Models for simulating wave breaking and wave runup have been reviewed briefly. The eddy viscosity breaking model, which was employed by Heitner and Housner (1970) and by Zelt (1991), is used here to simulate wave breaking. Corresponding eddy viscosity terms are added into the model equations to dissipate wave energy due to breaking. The breaking criterion is based on the horizontal gradient of velocity. In the long wave limit, the gradient of velocity is equivalent to the slope of surface elevation. The 1-D breaking model has been applied to study the shoaling and breaking of random waves. The model results agree well with experimental data. For the 2-D breaking model, however, more research work is needed.

To overcome the difficulties for the Eulerian system to specify moving a boundary for simulating wave runup, it is proposed in this study to maintain a thin layer of water over those physically dry grids. However, due to the abrupt change of variables around the moving shoreline, this model experiences stability problems at present and is left for future investigation.

To examine its validity, the present model has been applied to study a number of wave propagation cases. For the one dimensional case, the model has been applied to study the evolution of solitary waves in constant water depth, the permanent form solutions of solitary waves with large nonlinearity, the shoaling of solitary waves over constant slopes, the propagation of undular bores over constant water depth, and the shoaling and breaking of random waves over a beach. For the two dimensional case, the model has been used to study the evolution of waves with an initial Gaussian shape of surface elevation in a rectangular basin, the transformation of monochromatic waves over submerged shoals. The model

results have been compared with available analytical solutions, experimental data, or other numerical results. The close agreements for the results between these models showed that the present model is capable of simulating shallow water wave propagation for general coastal engineering practice.

REFERENCES

- Abbott, M. B., Damsgaard, A., and Rodenhuis, G.S. (1973) "System 21, Jupiter, a design system for two-dimensional nearly horizontal flows", *J. Hydr. Res.*, Vol. 11, 1-28.
- Abbott, M. B., McCowan, A. D. and Warren, I. R. (1981) "Numerical modelling of free-surface flows that are two-dimensional in plan", *Transport Models for Inland and Coastal Water*, Academic Press, New York, 222-283.
- Abbott, M. B., McCowan, A. D. and Warren, I. R. (1984) "Accuracy of short-wave numerical model", *J. Hydr. Eng.*, 110, 1287-1301.
- Airy, G.B. (1845) "Tides and waves", *Encycl. Metrop.*, Section VI.
- Benjamin, T.B. and Feir, J.E. (1967) "The disintegration of wave trains on deep water", *J. Fluid Mech.*, 27, 417-430.
- Benny, D.J. and Roskes, G.J. (1969) "Wave instabilities", *Studies Appl. Math.*, 48, 377-385.
- Berkhoff, J. C. W., Booy, N. and Radder, A. C. (1982) "Verification of numerical wave propagation models for simple harmonic linear water waves", *Coastal Engineering*, 6, 255-279.
- Boussinesq, J.V. (1872) "Théorie des ondes et des remous qui se propagent le long d'un canal rectangulaire horizontal, en communiquant au liquide contenu dans ce canal des vitesses sensiblement pareilles de la surface au fond", *J. Math. Pures Appliq.*, 17, 55-108.
- Broer, L.J.F. (1974) "On the Hamiltonian theory of surface waves", *Appl. Sci. Res.*, 30, 430-446.

- Broer, L.J.F. (1975) "Approximate equations for long water waves", *Appl. Sci. Res.*, 31, 377-395.
- Broer, L.J.F., van Groesen, E.W.C., and Timmers, J.M.W. (1976) "Stable model equations for long water waves", *Appl. Sci. Res.*, 32, 619-636.
- Carrier, G. F. and Greenspan, H. P. (1958) "Water waves of finite amplitude on a sloping beach", *J. Fluid Mech.*, 4, 97-109.
- Casulli, V. and Cheng, R.T. (1992) "Semi-implicit finite difference methods for three-dimensional shallow water flow", *Intl. J. Numer. Meth. Fluids*, 15, 629-648.
- Chawla, A. (1995) "Wave transformation over a submerged shoal", *MS Thesis*, Department of Civil Engineering, University of Delaware, Newark, 240pp.
- Chawla, A. , Özkan-Haller, H. T., and Kirby, J. T. (1996) "Experimental study of breaking waves over a shoal", *Proc. 25th Intl. Conf. Coast. Eng.*, Orlando (in press).
- Chen, Y. and Liu, P.L.F. (1995) "Modified Boussinesq equations and associated parabolic models for water wave propagation", *J. Fluid Mech.*, 288, 351-381.
- Chu, V.C. and Mei, C.C. (1971) "The nonlinear evolution of Stokes waves in deep water", *J. Fluid Mech.*, 47, 337-352.
- Dean, R. G. and Sharma, J.N. (1981) "Simulation of wave systems due to non-linear directional spectra", *Proc. Intl. Symp. Hydrodynamics Ocean Eng.*, Trondheim, 1211-1222.
- Demirbilek, Z. and Webster, W.C. (1992) "Application of the Green-Naghdi theory of fluid sheets to shallow water wave problems", *Technical Report CERC-92-11*, U.S. Army Corps of Engineers, Vicksburg, MS, 45pp.
- Dingemans, M.W. (1994) "Comparison of computations with Boussinesq-like models and laboratory measurements", *Report H1648.12*, Delft Hydraulics, 32pp.

- Elgar, S. and Guza, R. T. (1985) "Shoaling gravity waves: comparisons between field observations, linear theory and a nonlinear model", *J. Fluid Mech.*, 158, 47-70.
- Elgar, S. and Guza, R. T. (1986) "Nonlinear model predictions of bispectra of shoaling surface gravity waves", *J. Fluid Mech.*, 167, 1-18.
- Elgar, S., Freilich, M. H. and Guza, R. T. (1990) "Model-data comparisons of moments of nonbreaking shoaling surface gravity waves", *J. Geophys. Res.*, 95(C9), 16055-16063.
- Engquist, B. and Majda, A. (1977) "Absorbing boundary conditions for the numerical simulation of waves", *Math. Comp.*, 31, 629-65.
- Freilich, M. H., and Guza, R. T. (1984) "Nonlinear effects on shoaling surface gravity waves", *Philos. Trans. R. Soc. London, Ser. A*, 311, 1-41.
- Freilich, M. H., Guza, R. T., and Elgar, S. L. (1993) "Field test of two-dimensional Boussinesq shoaling wave model", *MEET'N'93- First Joint ASCE/ASME /SES MEETING*, Herakovich, C.T. and Duva, J.M. (Eds.), Charlottesville, VA, USA (abstract only).
- Galvin, C.J. (1972) "Wave breaking in shallow water", *Waves on Beaches and Resulting Sediment Transport*, Meyer, R.E. (Ed.), Academic, New York.
- Gardner, C.S., Greene, J.M., Kruskal, M.D., and Miura, R.M. (1967) "Method for solving the Korteweg-de Vries equation", *Phys. Rev. Lett.*, 19, 1095-1096.
- Gobbi, M. and Kirby, J.T. (1996) "A fourth order Boussinesq-type wave model", *Proc. 25th Intl. Conf. Coast. Eng.*, Orlando (in Press).
- Goring, D. G. (1978) "Tsunamis—the propagation of long waves onto a shelf", *Ph.D Dissertation*, California Institute of Technology, Pasadena, California.
- Green, A.E., Laws, N., and Naghdi, P.M. (1974) "On the theory of water waves", *Proc. Roy. Soc. A*, 338, 43-55.
- Green, A.E. and Naghdi, P.M. (1976) "A derivation of equations for wave propagation in water of variable depth", *J. Fluid Mech.*, 78, 237-246.

- Grilli, S. T., Skourup, J., and Svendsen, I. A. (1989) "An efficient boundary element method for nonlinear water waves", *Engineering Analysis with Boundary Elements*, 6(2), 97-107.
- Grilli, S. T., Subramanya, R., Svendsen, I. A., and Veeramony, J. (1994) "Shoaling of solitary waves on plane beaches", *J. Waterway, Port, Coast. and Ocean Eng.*, 120, 609-628.
- Hammack, J. L., Scheffner, N. W., and Segur, H. (1989) "Two-dimensional periodic waves in shallow water", *J. Fluid Mech.*, 209, 567-589.
- Hasselmann, K. (1962) "On the non-linear energy transfer in a gravity-wave spectrum. Part 1. General theory", *J. Fluid Mech.*, 12, 481-500.
- Heitner, K. L. and Housner, G. W. (1970) "Numerical model for tsunami runup", *J. Waterway, Port, Coast. and Ocean Eng.*, 96, 701-719.
- Hansen, J.B. and Svendsen, I.A. (1979) "Regular waves in shoaling water, experimental data", *Series Paper 21*, ISVA, Techn. Univ. Denmark, 233pp.
- Hibberd, S. and Peregrine, D.H. (1979) "Surf and runup on a beach: a uniform bore", *J. Fluid Mech.*, 95, 323-345.
- Hinwood, J.B. and Wallis, I.G. (1975a) "Classification of models of tidal waters", *J. Hydr. Div., ASCE*, Vol. 101, No. HY10, 1315-1331.
- Hinwood, J.B. and Wallis, I.G. (1975b) "Review of models of tidal waters", *J. Hydr. Div., ASCE*, Vol. 101, No. HY11, 1405-1421.
- Hoffman, J.D. (1992) *Numerical Methods for Engineers and Scientists*, McGraw-Hill, New York, 825pp.
- Israeli, M. and Orszag, S. A. (1981) "Approximation of radiation boundary conditions", *J. Comp. Phys.*, 41, 115-13.
- Karambas, Th.V. and Koutitas, C.A. (1992) "A breaking wave propagation model based on the Boussinesq equations", *Coastal Engineering*, 18, 1-19.
- Karjadi, E. and Kobayashi, N. (1994) "Numerical modelling of solitary wave breaking, runup and reflection", *Intl. Symp.: Waves - Phys. Numer. Modelling*, 426-435, Vancouver.

- Kirby, J. T. (1990) "Modelling shoaling directional wave spectra in shallow water", *Proc. 22nd Intl. Conf. Coast. Eng.*, Delft, 109-121.
- Kirby, J. T. (1996) "Nonlinear, dispersive long waves in water of variable depth", *Research Report No. CACR-96-02*, Center for Applied Coastal Research, University of Delaware, 71pp.
- Kirby, J. T. and Dalrymple, R. A. (1984) "Verification of a parabolic equation for propagation of weakly-nonlinear waves", *Coastal Engineering*, 8, 219-232.
- Kirby, J.T. and Dalrymple, R. A. (1994) "Combined refraction/diffraction model: **REF/DEF 1** (Version 2.5)", *Research Report No. CACR-94-22*, Center for Applied Coastal Research, University of Delaware, 171pp.
- Kirby, J.T. and Özkan, H.T. (1992) "Combined refraction/diffraction model for spectral wave conditions: **REF/DIF S** (Version 1.0) ", *Research Report No. CACR-92-06*, Center for Applied Coastal Research, University of Delaware, 118pp.
- Kobayashi, N., DeSilva, G.S., and Watson, K.D. (1989) "Wave transformations and swash oscillations on gentle slopes", *J. Geophys. Res.*, 94(C1), 951-966.
- Kobayashi, N. and Watson, K.D. (1987) "Wave reflection and runup on smooth slopes", *Proc. Coast. Hydrodynamics*, ASCE, University of Delaware, 548-562.
- Kobayashi, N. and Wurijanto, A. (1992) "Irregular wave setup and runup on beaches", *J. Waterway, Port, Coast. and Ocean Eng.*, 118, 235-251.
- Korteweg, D.J and de Vries, G. (1895) "On the change of form of long waves advancing in a rectangular canal, and on a new type of long stationary waves", *Phil. Mag.*, 39, 422-443.
- Lamb, H. (1932) *Hydrodynamics* (6th ed.), University Press, Cambridge, 738pp.
- Larsen, J. and Dancy, H. (1983) "Open boundaries in short-wave simulations — A new approach", *Coastal Engineering*, 7, 285-297.
- Liu, P. L-F., Yoon, S. B. and Kirby, J. T. (1985) "Nonlinear refraction-diffraction of waves in shallow water", *J. Fluid Mech.*, 153, 185-201.

- Liu, P.L-F., Cho, Y.S., Briggs, M.J., Kanoglu, U., and Synolakis, C.E. (1995) "Runup of solitary waves on a circular island", *J. Fluid Mech.*, 302, 259-285.
- Longuet-Higgins, M. S. and Stewart, R. W. (1964) "Radiation stress in water waves; a physical discussion, with applications", *Deep Sea Research*, 11, 529-562.
- Madsen, P. A., Murray, R. and Sørensen, O.R. (1991) "A new form of Boussinesq equations with improved linear dispersion characteristics", *Coastal Engineering*, 15, 371-388.
- Madsen, P. A., Sørensen, O. R. (1992) "A new form of Boussinesq equations with improved linear dispersion characteristics. Part 2. A slowly-varying bathymetry", *Coastal Engineering*, 18, 183-204.
- Madsen, P. A., Sørensen, O. R. (1993) "Bound waves and triad interaction in shallow water", *Coastal Engineering*, 20, 359-388.
- Madsen, P. A., Sørensen, O. R., and Schäffer, H. A. (1994) "Time domain modelling of wave breaking, runup, and surf beats", *Proc. 24th Intl. Conf. Coast. Eng.*, Kobe, 399-411.
- Mase, H. and Kirby, J. T. (1992) "Hybrid frequency-domain KdV equation for random wave transformation", *Proc. 23rd Intl. Conf. Coast. Eng.*, Venice, 474-487.
- McCowan, A.D. (1978) "Numerical simulation of shallow water waves", *Proc. 4th Austr. Conf. on Coast. and Ocean Eng.*, Perth.
- McCowan, A.D. (1981) "Developments in numerical short waves modelling", *Proc. 5th Austr. Conf. on Coast. and Ocean Eng.*, Adelaide.
- McCowan, A.D. (1987) "The range of application of Boussinesq type numerical short wave models". *Proc. 22nd IAHR Congr.*, Lausanne.
- Mei, C.C. (1989) *The Applied Dynamics of Ocean Surface Waves*, Wiley, New York, 740 pp.
- Mei, C.C. and Le Méhauté, B. (1966) "Note on the equations of long waves over an uneven bottom", *J. Geophys. Res.*, 71, 393-400.

- Miles, J.W. and Salmon, R. (1985) "Weakly dispersive nonlinear gravity waves", *J. Fluid Mech.*, 157, 519-531.
- Mooiman, J. (1991) "Boussinesq equations based on a positive definite Hamiltonian", *Report Z294*, Delft Hydraulics, 103pp.
- Murray, R. J. (1989) "Short wave modelling using new equations of Boussinesq type", *Proc. 9th Austr. Conf. on Coast. and Ocean Eng.*, Adelaide, 331-336.
- Nwogu, O. (1993) "An alternative form of the Boussinesq equations for nearshore wave propagation", *J. Waterway, Port, Coast. and Ocean Eng.*, 119(6), 618-638.
- Nwogu, O. (1994) "Nonlinear evolution of directional wave spectra in shallow water", *Proc. 24th Intl. Conf. Coast. Eng.*, Kobe, 467-481.
- Özkan, H.T. and Kirby, J.T. (1996) "Finite amplitude shear wave instabilities", *Coastal Dynamics'95*, Gdańsk, Poland, 465-476.
- Packwood, A.R. and Peregrine, D.H. (1981) "Surf and run-up on beaches: models of viscous effects", *Rep. AM-81-07*, School Math., University of Bristol, Bristol, 34pp.
- Panchang, V. G. and Kopriva, D. A. (1989) "Solution of two-dimensional water-wave propagation problems by Chebyshev collocation", *Math. Comput. Modelling*, 12(6), 625-640.
- Pedersen, G. and Gjevik, B. (1983) "Run-up of solitary waves", *J. Fluid Mech.*, 135, 283-299.
- Peregrine, D. H. (1966) "Calculations of the development of an undular bores", *J. Fluid Mech.*, 25, 321-330.
- Peregrine, D. H. (1967) "Long waves on a beach", *J. Fluid Mech.*, 27, 815-82.
- Peregrine, D. H. (1983) "Breaking waves on beaches", *Ann. Rev. Fluid Mech.*, 15, 149-178.
- Press, W. H., Flannery, B. P., Teukolsky, S. A. and Vetterling, W. T. (1992) *Numerical Recipes in Fortran* (2nd ed.), University Press, Cambridge, 963pp.

- Rygg, O. B. (1988) "Nonlinear refraction-diffraction of surface waves in intermediate and shallow water", *Coastal Engineering*, 12, 191-211.
- Schäffer, H. A., Madsen, P. A., and Deigaard, R. (1993) "A Boussinesq model for wave breaking in shallow water", *Coastal Engineering*, 20, 185-202.
- Schember, H. R. (1982) "A new model for three-dimensional nonlinear dispersive long waves", *Ph.D. Dissertation*, California Institute of Technology, Pasadena, California, 141pp.
- Seabra-Santos, F. J., Renouard, D. P., and Temperville, A. M. (1987) "Numerical and experimental study of the transform of a solitary wave over a shelf or isolated obstacle", *J. Fluid Mech.*, 176, 117-134.
- Serre, F. (1953) "Contribution a l'etude des ecoulements permanents et variables dans les canaux", *Houille Blanche*, 3, 374-385.
- Shapiro, R. (1970) "Smoothing, filtering, and boundary effects", *Rev. Geophys. and Space Phys.*, 8(2), 359-387.
- Shields, J.J. (1986) "A direct theory for waves approaching a beach", *Ph.D. Dissertation*, University of California at Berkley, 137pp.
- Shields, J.J. and Webster, W.C. (1988) "On direct methods in water-wave theory", *J. Fluid Mech.*, 197, 171-199.
- Shields, J.J. and Webster, W.C. (1989) "Conservation of mechanical energy and circulation in the theory of inviscid fluid sheets", *J. Eng. Math.*, 23, 1-15.
- Sommerfeld, A. (1949) *Partial Differential Equations in Physics*, (E.G. Straus Trans.), Academic Press, New York, 335pp.
- Sørensen, O.R., Schäffer, H.A., Madsen, P.A., and Deigaard, R. (1994) "Wave breaking and induced nearshore circulations", *Proc. 24th Intl. Conf. Coast. Eng.*, Kobe, 2583-2594.
- Synolakis, C.E. (1986) "The run-up of long waves", *Ph.D. Dissertation*, California Institute of Technology, 228pp.

- Su, C.H. and Gardner, C.S. (1969) "Korteweg-de Vries equation and generalizations. III. Derivation of the Korteweg-de Vries equation and Burgers equation", *J. Math. Phys.*, 10, 536-539.
- Tanaka, M. (1986) "The stability of solitary waves", *Phys. Fluids*, 29(3), 650-655.
- Tao, J. (1983) "Computation of wave run-up and wave breaking", *Internal Report*, Danish Hydraulic Institute, 40pp.
- Thacker, W. C. (1981) "Some exact solutions to the nonlinear shallow-water wave equations", *J. Fluid Mech.*, 107, 499-508.
- Twizell, E.H. (1984) *Computational Methods for Partial Differential Equations*, Ellis Horwood Limited, West Sussex, England, 276pp.
- Ursell, F. (1953) "The long wave paradox in the theory of gravity waves", *Proc. Cambridge Phil. Soc.*, 49, 685-694.
- Van der Veen, W.A. and Wubs, F.W. (1993) "A Hamiltonian approach to fairly low and fairly long gravity waves", *Report W-9314*, Department of Mathematics, University of Groningen, 25pp.
- Von Neumann, J. and Richtmyer, R.D. (1950) "A method for the numerical calculation of hydrodynamic shocks", *J. Appl. Phys.*, 21, 232-237.
- Webster, W.C. and Wehausen, J.V. (1995) "Bragg scattering of water waves by Green-Naghdi theory", *Z. angew Math. Phys.*, 46, Special issue, S566-S583.
- Wei, G. and Kirby, J. T. (1995) "A time-dependent numerical code for the extended Boussinesq equations", *J. Waterway, Port, Coast. and Ocean Eng.*, 121(5), 251-261.
- Wei, G., Kirby, J. T., Grilli, S. T., Subramanya, S. (1995) "A fully nonlinear Boussinesq model for surface waves. I. Highly nonlinear, unsteady waves", *J. Fluid Mech.*, 294, 71-92.
- Wei, G. and Kirby, J. T. (1997) "Generation of waves in Boussinesq models using a source function method", in preparation.

- Whalin, R. W. (1971) "The limit of applicability of linear wave refraction theory in a convergence zone", *Res. Rept. H-71-3*, Hydraulics Laboratory, U. S. Army Corps of Engineers Waterways Experiment Station, Vicksburg.
- Whitham, G.B. (1958) "On the propagation of shock waves through regions of non-uniform area or flow", *J. Fluid Mech.*, 4, 337-360.
- Wilmott, C.J. (1981) "On the validation of models", *Physical Geography*, 2(2), 219-232.
- Witting, J. M. (1984) "A unified model for the evolution of nonlinear water waves", *J. Comp. Phys.*, 56, 203-239.
- Wu, T.Y.T. (1981) "Long waves in ocean and coastal waters", *J. Eng. Mech.*, 107, 501-522.
- Yu, K. and Svendsen, I.A. (1995) "Breaking waves in surfzones", *Coastal Dynamics '95*, Gdańsk, Poland, 329-340.
- Zakharov, V.E. (1968) "Stability of periodic waves of finite amplitude on the surface of a deep fluid", *J. Appl. Mech. Tech. Phys.*, 2, 190-194.
- Zelt, J. (1991) "The runup of breaking and non-breaking solitary waves", *Coastal Engineering*, 15, 205-246.

Appendix A

SOLITARY WAVE SOLUTION FOR EXTENDED BOUSSINESQ MODEL

Following the approach of Schember (1982) who obtained the approximate solution for solitary waves from the standard Boussinesq equations, we seek the corresponding solution from the extended Boussinesq equations derived by Nwogu (1993).

For convenience, the dimensionless form of Nwogu's equations for the case of 1-D horizontal flow and in constant depth is rewritten here as

$$\eta_t + u_x + \delta(\eta u)_x + \mu^2(\alpha + 1/3)u_{xxx} = 0 \quad (\text{A.1})$$

$$u_t + \eta_x + \delta u u_x + \mu^2 \alpha u_{xxt} = 0 \quad (\text{A.2})$$

where η is the surface elevation, u the horizontal velocity at the elevation $z = z_\alpha$, α is the coefficient related to reference water depth z_α , subscripts t and x denote partial derivatives respect to time t and spatial coordinate x , and $\mu = kh$ and $\delta = H/h$ (k is the wavenumber, H the amplitude) are dimensionless parameters which represent the effects of dispersion and nonlinearity, respectively.

Instead of the velocity u , we use the velocity potential ϕ (such that $u = \phi_x$) as an dependent variable. Then equations (A.1) and (A.2) become

$$\eta_t + \phi_{xx} + \delta(\eta \phi_x)_x + \mu^2(\alpha + 1/3)\phi_{xxxx} = 0 \quad (\text{A.3})$$

$$\phi_t + \eta + \frac{\delta}{2}(\phi_x)^2 + \mu^2 \alpha \phi_{xxt} = 0 \quad (\text{A.4})$$

Substituting η from (A.4) into (A.3) and retaining terms which are consistent with the ordering in the Boussinesq equations, we have

$$-\phi_{tt} + \phi_{xx} - \delta(2\phi_x\phi_{xt} + \phi_t\phi_{xx}) + \mu^2[(\alpha + 1/3)\phi_{xxxx} - \alpha\phi_{xxtt}] = O(\delta^2, \delta\mu^2) \quad (\text{A.5})$$

The truncated terms on the right hand side of the above equation are

$$O(\delta^2, \delta\mu^2) = \frac{3}{2}\delta^2\phi_x\phi_{xx} + \delta\mu^2\alpha(\phi_{xxt}\phi_x)_x \quad (\text{A.6})$$

which is responsible for the fact that the analytic solitary waves differ by a small amount from their numerical counterparts, even in the limit of small grid size Δx and small time step Δt . We introduce a new coordinate ξ as

$$\xi = x - Ct \quad (\text{A.7})$$

where C is the phase speed of the solitary waves. The relation between the old and new coordinates are

$$\phi_x = \phi', \quad \phi_t = -C\phi' \quad (\text{A.8})$$

where primes denote differentiation with respect to the new variable ξ . Then equation (A.5) is transformed into an ordinary differential equation

$$(1 - C^2)\phi'' + 3\delta C\phi'\phi'' + \mu^2[(\alpha + 1/3) - \alpha C^2]\phi'''' = 0 \quad (\text{A.9})$$

Integrating the equation (A.9) once results in

$$(1 - C^2)\phi' + \frac{3}{2}\delta C(\phi')^2 + \mu^2[(\alpha + 1/3) - \alpha C^2]\phi''' = G_1 \quad (\text{A.10})$$

Multiplying equation (A.10) by $2\phi''$ and integrating once yields

$$(1 - C^2)(\phi')^2 + \delta C(\phi')^3 + \mu^2[(\alpha + 1/3) - \alpha C^2](\phi'')^2 = 2G_1\phi' + G_2 \quad (\text{A.11})$$

where the integration constants G_1 and G_2 are zero for solitary waves since $\phi' = \phi'' = \phi''' = 0$ as $|\xi| \rightarrow \infty$. Assume the solution form of ϕ' to be

$$\phi' = A \operatorname{sech}^2(B\xi) \quad (\text{A.12})$$

The quantities A and B are obtained by substituting expression (A.12) into equation (A.11)

$$A = \frac{C^2 - 1}{\delta C} \quad (\text{A.13})$$

$$B = \left\{ \frac{C^2 - 1}{4\mu^2[(\alpha + 1/3) - \alpha C^2]} \right\}^{\frac{1}{2}} \quad (\text{A.14})$$

With the solution of ϕ' , we obtain the corresponding solution for the surface elevation from equation (A.4)

$$\eta = A_1 \operatorname{sech}^2(B\xi) + A_2 \operatorname{sech}^4(B\xi) \quad (\text{A.15})$$

where

$$A_1 = \frac{C^2 - 1}{3\delta[(\alpha + 1/3) - \alpha C^2]} \quad (\text{A.16})$$

$$A_2 = -\frac{(C^2 - 1)^2 [(\alpha + 1/3) + 2\alpha C^2]}{2\delta C^2 [(\alpha + 1/3) - \alpha C^2]} \quad (\text{A.17})$$

The solitary wave crest is located at the origin of the new coordinate system, from which we have $\eta = 1$ at $\xi = 0$ and equation (A.15) becomes

$$1 = A_1 + A_2 \quad (\text{A.18})$$

The above equation is equivalent to

$$2\alpha(C^2)^3 - (3\alpha + 1/3 + 2\alpha\delta)(C^2)^2 + 2\delta(\alpha + 1/3)(C^2) + \alpha + 1/3 = 0 \quad (\text{A.19})$$

which is a third order polynomial equation for C^2 . The corresponding solution is evaluated once the wave height to water depth ratio δ is given.

It is convenient to write the solitary wave solutions in original coordinates and in dimensional form, which are summarized here:

$$\eta = \eta = A_1 \text{sech}^2[B(x - Ct)] + A_2 \text{sech}^4[B(x - Ct)] \quad (\text{A.20})$$

$$u = A \text{sech}^2[B(x - Ct)] \quad (\text{A.21})$$

$$A = \frac{C^2 - gh}{C} \quad (\text{A.22})$$

$$B = \left\{ \frac{C^2 - gh}{4[(\alpha + 1/3)gh^3 - \alpha h^2 C^2]} \right\}^{\frac{1}{2}} \quad (\text{A.23})$$

$$A_1 = \frac{C^2 - gh}{3[(\alpha + 1/3)gh - \alpha C^2]} h \quad (\text{A.24})$$

$$A_2 = -\frac{(C^2 - gh)^2}{2ghC^2} \frac{[(\alpha + 1/3)gh + 2\alpha C^2]}{[(\alpha + 1/3)gh - \alpha C^2]} h \quad (\text{A.25})$$

Appendix B

WAVE GENERATION BY SOURCE FUNCTION

For waves in two horizontal directions and constant depth, the generalized form of the linearized Boussinesq and shallow water equations may be written as

$$\eta_t + h \nabla \cdot \mathbf{u} + \alpha_1 h^3 \nabla^2 (\nabla \cdot \mathbf{u}) = 0 \quad (\text{B.1})$$

$$\mathbf{u}_t + g \nabla \eta + \alpha h^2 \nabla^2 \mathbf{u}_t = 0 \quad (\text{B.2})$$

where h is the water depth, g is the gravitational acceleration, η is the surface elevation and \mathbf{u} is a velocity vector in the horizontal plane. The values of α_1 and α have different definitions depending on the form of equations. For Nwogu's (1993) extended Boussinesq equations, \mathbf{u} is the velocity at the elevation $z = z_\alpha$, and $\alpha_1 = \alpha + 1/3$, with α determined by:

$$\alpha = \frac{z_\alpha}{h} \left(\frac{1}{2} \frac{z_\alpha}{h} + 1 \right) \quad (\text{B.3})$$

For the Boussinesq equations of Peregrine (1967), \mathbf{u} is the depth-averaged velocity, $\alpha_1 = 0$, and $\alpha = -1/3$. For shallow water equations, \mathbf{u} is depth-averaged velocity and $\alpha_1 = \alpha = 0$.

Alternatively, we may introduce a velocity potential ϕ defined such that $\mathbf{u} = \nabla \phi$, which gives the model equations

$$\eta_t + h \nabla^2 \phi + \alpha_1 h^3 \nabla^2 \nabla^2 \phi = 0 \quad (\text{B.4})$$

$$\phi_t + g \eta + \alpha h^2 \nabla^2 \phi_t = 0 \quad (\text{B.5})$$

The linear dispersion relation for these equations may be obtained by considering a plane wave solution in 1-D

$$\begin{aligned}\eta &= \eta_0 \exp[i(kx - \omega t)] \\ \phi &= \phi_0 \exp[i(kx - \omega t)]\end{aligned}$$

and is given by

$$\omega^2 = gk^2 h \frac{1 - \alpha_1(kh)^2}{1 - \alpha(kh)^2} \quad (\text{B.6})$$

where ω is the angular frequency and k the wavenumber. The amplitude of the potential is given in terms of the wave amplitude η_0 by

$$\phi_0 = \frac{ig}{\omega(1 - \alpha(kh)^2)} \eta_0 \quad (\text{B.7})$$

B.1 Source function in continuity equation

We first add a source function $f(x, y, t)$ to (B.1) and find the corresponding solution of the following equations

$$\eta_t + h \nabla \cdot \mathbf{u} + \alpha_1 h^3 \nabla^2 (\nabla \cdot \mathbf{u}) = f(x, y, t) \quad (\text{B.8})$$

$$\mathbf{u}_t + g \nabla \eta + \alpha h^2 \nabla^2 \mathbf{u}_t = 0 \quad (\text{B.9})$$

We introduce a velocity potential ϕ , integrate (B.9) once, and eliminate η in favor of ϕ to obtain the equation

$$\phi_{tt} - gh \nabla^2 \phi + \alpha h^2 \nabla^2 \phi_{tt} - \alpha_1 gh^3 \nabla^2 \nabla^2 \phi = -gf(x, y, t) \quad (\text{B.10})$$

We now assume that the y dependence of ϕ and f is suitable for a Fourier transform and introduce

$$\phi(x, y, t) = \frac{1}{2\pi} \int_{-\infty}^{\infty} \tilde{\phi}(x, \lambda, t) \exp(i\lambda y) d\lambda \quad (\text{B.11})$$

$$f(x, y, t) = \frac{1}{2\pi} \int_{-\infty}^{\infty} \tilde{f}(x, \lambda, t) \exp(i\lambda y) d\lambda \quad (\text{B.12})$$

leading to an equation for $\tilde{\phi}$ in x, t . We further introduce a Fourier transform in time

$$\tilde{\phi}(x, \lambda, t) = \frac{1}{2\pi} \int_{-\infty}^{\infty} \hat{\phi}(x, \lambda, \omega) \exp(-i\omega t) d\omega \quad (\text{B.13})$$

$$\tilde{f}(x, \lambda, t) = \frac{1}{2\pi} \int_{-\infty}^{\infty} \hat{f}(x, \lambda, \omega) \exp(-i\omega t) d\omega \quad (\text{B.14})$$

$$(\text{B.15})$$

and obtain the fourth order ODE

$$A\hat{\phi}^{(4)} + B\hat{\phi}'' + C\hat{\phi} = g\hat{f} \quad (\text{B.16})$$

where

$$\begin{aligned} A &= \alpha_1 g h^3 \\ B &= gh + \alpha \omega^2 h^2 - 2\alpha_1 g h^3 \lambda^2 \\ C &= \omega^2 - gh\lambda^2 - \alpha \omega^2 h^2 \lambda^2 + \alpha_1 g h^3 \lambda^4 \end{aligned} \quad (\text{B.17})$$

The governing equation reduces to a second-order equation for either the long wave or Peregrine models, where $A = 0$. Homogeneous solutions of (B.16) corresponding to progressive waves are given by

$$\hat{\phi}_h(x) = \exp(\pm ilx) \quad (\text{B.18})$$

where $l = \sqrt{k^2 - \lambda^2}$. In order to obtain the particular solution for $\hat{\phi}$, we seek a Green function $G(x, x')$ which satisfies

$$AG^{(4)} + BG''' + CG = \delta(x - x') \quad (\text{B.19})$$

We impose the boundary conditions on the Green function to correspond to the condition that waves are radiating away from the source region.

$$\begin{aligned} G^{(n)} &\rightarrow (+il)^n G, & \hat{\phi}^{(n)} &\rightarrow (+il)^n \hat{\phi}; & x &\rightarrow +\infty \\ G^{(n)} &\rightarrow (-il)^n G, & \hat{\phi}^{(n)} &\rightarrow (-il)^n \hat{\phi}; & x &\rightarrow -\infty \end{aligned} \quad (\text{B.20})$$

Integrating equation (B.19) with respect to x from $x' - 0$ to $x' + 0$, we have

$$AG'''(x, x')|_{x=x'-0}^{x=x'+0} + BG'(x, x')|_{x=x'-0}^{x=x'+0} + C \int_{x'-0}^{x'+0} G(x, x') dx = 1 \quad (\text{B.21})$$

The solution for the Green function takes different forms depending on whether the value of A is equal to zero.

B.1.1 Case 1: $A = 0$

If $A = 0$ ($\alpha_1 = 0$), equation (B.21) becomes

$$BG'(x, x')|_{x=x'-0}^{x=x'+0} + C \int_{x'-0}^{x'+0} G(x, x') dx = 1 \quad (\text{B.22})$$

In addition to boundary conditions (B.20), we require G to be continuous at $x = x'$. Equation (B.22) then reduces to

$$BG'(x, x')|_{x=x'-0}^{x=x'+0} = 1 \quad (\text{B.23})$$

We assume the Green function to be given by

$$G(x, x') = \begin{cases} a \exp[i l(x - x')] & \text{if } x > x' \\ a \exp[i l(x' - x)] & \text{if } x < x' \end{cases} \quad (\text{B.24})$$

which automatically satisfies the boundary conditions (B.20) and is continuous at $x = x'$. Substituting (B.24) into (B.23) results in

$$a = -\frac{i}{2lB} \quad (\text{B.25})$$

For normally incident waves ($\lambda = 0$) this reduces to

$$a = -\frac{i}{2kB} = -\frac{ik}{2\omega^2} \quad (\text{B.26})$$

B.1.2 Case 2: $A \neq 0$

For $A \neq 0$ ($\alpha = -0.39, A < 0$), we require that G, G', G'' are continuous at $x = x'$. Thus the second and third terms in equation (B.21) drop out and we have

$$AG'''(x, x')|_{x=x'+0}^{x=x'-0} = 1 \quad (\text{B.27})$$

We assume the form of Green function to be

$$G(x, x') = \begin{cases} a \exp[il_1(x - x')] + b \exp[il_2(x - x')] & \text{if } x > x' \\ a \exp[il_1(x' - x)] + b \exp[il_2(x' - x)] & \text{if } x < x' \end{cases} \quad (\text{B.28})$$

where l_1 and l_2 are the positive real and imaginary wavenumbers which satisfy the homogeneous form of the governing equation (B.16), given by

$$\begin{aligned} l_1 &= \left(\frac{B - \sqrt{B^2 - 4AC}}{2A} \right)^{\frac{1}{2}} = l \\ l_2 &= \left(\frac{B + \sqrt{B^2 - 4AC}}{2A} \right)^{\frac{1}{2}} = iL \end{aligned} \quad (\text{B.29})$$

with $l > 0$ and $L > 0$. The definition of G in equation (B.28) automatically satisfies the boundary conditions (B.20) and the continuity of G and G'' at $x = x'$.

The continuity of G' at $x = x'$ results in

$$b = i \left(\frac{l}{L} \right) a \quad (\text{B.30})$$

Substituting equation (B.28) into equation (B.27) gives

$$A[(il)^3 a + (-L)^3 b - (-il)^3 a - L^3 b] = 1 \quad (\text{B.31})$$

From equations (B.30) and (B.31), we obtain solution for a and b ,

$$a = \frac{i}{2Al(l^2 + L^2)} \quad (\text{B.32})$$

$$b = \frac{-1}{2AL(l^2 + L^2)} \quad (\text{B.33})$$

In summary, the general form of solution for Green's function is

$$G(x, x') = \begin{cases} G_+(x, x') = a \exp[il(x - x')] + b \exp[-L(x - x')] & \text{if } x > x' \\ G_-(x, x') = a \exp[il(x' - x)] + b \exp[-L(x' - x)] & \text{if } x < x' \end{cases} \quad (\text{B.34})$$

B.1.3 Solution and choice of source function f

Now we seek solution of $\hat{\phi}$ by using Green's function G . Multiplying (B.19) by $\hat{\phi}(x')$ and integrating with respect to x' from $-\infty$ to $+\infty$ gives

$$\int_{-\infty}^{+\infty} \hat{\phi}(x') [AG(x, x')^{(4)} + BG(x, x')'' + CG(x, x')] dx' = \int_{-\infty}^{+\infty} \hat{\phi}(x') \delta(x - x') dx' \quad (\text{B.35})$$

Integration by parts, use of the boundary conditions (B.20), and use of the definition of the delta function then gives

$$\begin{aligned} \hat{\phi}(x) &= \int_{-\infty}^{+\infty} G(x, x') g \hat{f}(x') dx' \\ &= \int_{-\infty}^x G_+(x, x') g \hat{f}(x') dx' + \int_x^{+\infty} G_-(x, x') g \hat{f}(x') dx' \end{aligned} \quad (\text{B.36})$$

In principle, the source function \hat{f} can be of any shape. For the examples that follow, we have adopted a smooth Gaussian shape for \hat{f} ,

$$\hat{f}(x) = D \exp(-\beta x^2) \quad (\text{B.37})$$

which keeps the source function fairly well localized and which does not introduce the need for any additional numerical filtering. The amplitude D is a constant to be determined by matching the source to a desired progressive wave amplitude η_0 far away, while β controls the width of the source region. Then for sufficiently large value of x , the solution approaches

$$\begin{aligned} \hat{\phi}(x) &= \int_{-\infty}^x G_+(x, x') g \hat{f}(x') dx' \\ &\simeq gD [aI_1 \exp(ilx) + bI_2 \exp(-Lx)] \end{aligned} \quad (\text{B.38})$$

where I_1 and I_2 are defined by

$$\begin{aligned} I_1 &= \int_{-\infty}^{\infty} \exp(-\beta x'^2) \exp(-ilx') dx' \\ &= \sqrt{\frac{\pi}{\beta}} \exp\left(-\frac{l^2}{4\beta}\right) \end{aligned} \quad (\text{B.39})$$

$$\begin{aligned} I_2 &= \int_{-\infty}^{\infty} \exp(-\beta x'^2) \exp(Lx') dx' \\ &= \sqrt{\frac{\pi}{\beta}} \exp\left(\frac{L^2}{4\beta}\right) \end{aligned} \quad (\text{B.40})$$

For sufficiently large x , the contribution of last term in (B.38) is negligible. Therefore, the velocity potential away from source regions becomes

$$\hat{\phi}(x) = gDaI_1 \exp(ilx) \quad (\text{B.41})$$

The corresponding surface elevation is

$$\hat{\eta}(x) = -i\omega DaI_1[1 - \alpha(kh)^2] \exp(ilx) = \eta_0 \exp(ilx) \quad (\text{B.42})$$

which gives the relation between the source amplitude D and the desired wave amplitude η_0 ,

$$D = \frac{i\eta_0}{\omega a I_1 (1 - \alpha(kh)^2)} \quad (\text{B.43})$$

In many cases, wave data is available in terms of a frequency-direction spectrum. In order to provide the model coefficients in this representation, we may take $\lambda = k \sin \theta$ and $l = k \cos \theta$, where θ is the angle between the wave vector and the x axis in a right handed sense. Using these, we obtain

$$a = -\frac{ik}{2 \cos \theta (\omega^2 - \alpha_1 g k^4 h^3)} \quad (\text{B.44})$$

$$D = \frac{2\eta_0 \cos \theta (\omega^2 - \alpha_1 g k^4 h^3)}{\omega I_1 k (1 - \alpha(kh)^2)} \quad (\text{B.45})$$

B.2 Source function in momentum equation

Alternately, let us add a source term in the vector momentum equation according to

$$\mathbf{u}_t + g\nabla\eta + \alpha h^2 \nabla^2 \mathbf{u}_t = -g\nabla P \quad (\text{B.46})$$

where P is a normalized pressure distribution having units of length. Using the velocity potential, (B.46) may be integrated to give

$$\phi_t + g\eta + \alpha h^2 \phi_{xxt} = P \quad (\text{B.47})$$

Combining the continuity and Bernoulli equations then gives

$$\phi_{tt} - gh\nabla^2\phi + \alpha h^2 \nabla^2 \phi_{tt} - \alpha_1 gh^3 \nabla^2 \nabla^2 \phi = -P_t \quad (\text{B.48})$$

Comparing (B.47) and (B.10) gives

$$P = g \int f dt \quad (\text{B.49})$$

Introducing the Fourier transform for P ,

$$P = \frac{1}{4\pi^2} \int \int \hat{P} \exp[i(\lambda y - \omega t)] d\lambda d\omega \quad (\text{B.50})$$

we obtain

$$\hat{P} = \frac{ig}{\omega} \hat{f} \quad (\text{B.51})$$

The remainder of the solution for this case follows from the previous section.